Angle Dependent Magnetoresistance in $Tl_2Ba_2CuO_{6+\delta}$

Matthew Malcolm James French

April 2009

A thesis submitted to the University of Bristol in accordance with the requirements of the degree of Doctor of Philosophy in the Faculty of Science, Department of Physics.

34414 words

Abstract

The interlayer resistivity of the high temperature cuprate superconductor $Tl_2Ba_2CuO_{6+\delta}$ has been measured in a high magnetic field as a function of field angle and temperature. Angle dependent magnetoresistance (ADMR) was observed over a larger doping, azimuthal angle and temperature range than in previous work. Similar ADMR data were observed on crystals from a second sample grower, confirming this effect is intrinsic to the material. The need for anisotropy in the scattering rate is confirmed and a new term in the temperature dependence of this anisotropy is uncovered. This form of the scattering rate provides a qualitative explanation of the doping and temperature dependence of not only of the c-axis resistivity but also for the in-plane resistivity, Hall effect and magnetoresistance. Further work on samples with a higher T_c shows significant changes in ADMR over a narrow doping range, possibly due to the presence of the pseudogap. In a separate experiment, both Shubnikov-de Haas and de Haas-van Alphen oscillations have been observed for the first time in an overdoped cuprate superconductor. They reveal a Fermi surface area in excellent agreement with that determined from the ADMR work presented here as well as from photoemission experiments and bandstructure calculations.

Author's declaration

I declare that the work in this thesis was carried out in accordance with the Regulations of the University of Bristol. The work is original, except where indicated by special reference in the text, and no part of the thesis has been submitted for any other academic award. Any views expressed in the thesis are those of the author.

M. M. J. French

April 2009

...

In memory of my Mum

...

"Science without religion is lame, religion without science is blind"
Albert Einstein

"Great are the works of the Lord, studied by all who delight in them"
Psalm 111

Acknowledgements

I am very grateful for the help and guidance provided by my supervisor, Nigel Hussey, throughout my PhD. Helpful suggestions and advice were provided by many members of the low temperature group including Jon Fletcher, Tony Carrington, Edward Yelland, Amalia Coldea, Ali Bangura, Alessandro Narduzzo, Araz Enayati Rad, James Analytis, Liam Malone, Rosie Cooper and Caroline Andrew. The experiments performed at NHMFL, Tallahassee were aided by the help of James Analytis and Luis Balicas. Experiments were performed at LNCMP, Toulouse by Nigel Hussey and Rosie Cooper. I thank Laurence French for proof reading this work. Many enlightening and entertaining conversations were had with members of the low temperature group and the department in the coffee room, the lab and the pub — occasionally they were also relevant to the work presented here.

Other academic staff who have been helpful include Neil Fox; Jon Charmant for help with X-ray crystallography measurements; Richard Brooker (UCL) for help with high pressure annealing; Todor Mishonov (Sofia University, Bulgaria) and Mike Smith (University of Queensland, Australia) for useful discussions on the $T_c = 45\,\mathrm{K}$ data. The many technical and administrative staff who have gone out of their way to help and are greatly appreciated include Dick, Bob, John, Adrian, Richard, Mike, Frances, Yvonne and Carol.

Finally, I thank my parents, Margaret and Malcolm and my brother, Laurence, for their support and encouragement.

Matt French

April 2009

Contents

Chapter 1

Introduction

From the early eighteenth century it was known that there were types of material that conducted electricity and types which acted as electrical insulators. Throughout the nineteenth century a great deal of thought and research went into trying to understand electricity and in 1827 G. S. Ohm published the now familiar relation $V = IR$ showing, perhaps, the first understanding of resistance in conductors. Following on from the work of J. Dewar on the reduction of electrical resistance at low temperatures, superconductivity (when all resistance to the flow of electric current disappears) was first observed in mercury by Onnes [1] in 1911. It was not until Bardeen, Cooper and Schrieffer [2] developed BCS theory in 1957 that it was understood to result from bound (Cooper) pairs of electrons with wavefunctions that are coherent throughout the material. Cooper showed that the electrons would pair in the presence of even the weakest attractive potential which arises due to an interaction between the crystal lattice and the electron.

The maximum T_c (the temperature below which superconductivity occurs) known in any element or compound was around 23 K until 1986 when Bednorz and Muller discovered 'high temperature' superconductivity in a cuprate system [3]. A flurry of work soon led to T_c values up to 133 K in a mercury based cuprate (Hg1223) [4] (and even higher under pressure). Despite the common observation of a zero in electrical resistance, the Meissner effect and pairing units with charge $-2e$ [5] in both the cuprates and conventional BCS superconductors, due to their other unusual properties (which shall be described later) we still lack a theory to fully describe the cuprates.

The cuprates have the common feature of at least one CuO_2 plane per unit cell, so this is seen as the key structural component to their superconductivity. They are quasi-two dimensional, that is, they have a much larger resistivity measured perpendicular to the CuO_2 planes than within the plane — sometimes up to a factor of 1000.

The T_c of the cuprates can be tuned from zero up to a maximum by doping electrons or holes into the CuO_2 planes. Chemically this involves changing the structure and/or the elements in the charge reservoir layers between the planes. Figure 1.1 shows the temperature-doping phase diagram which

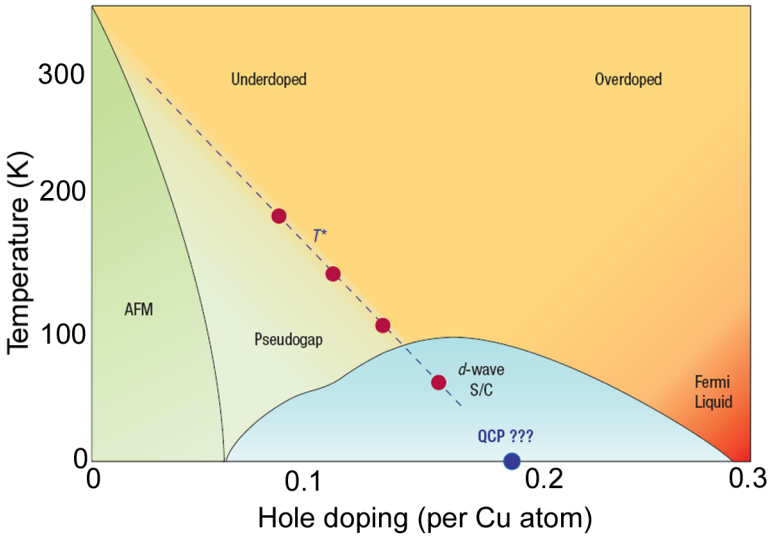

Figure 1.1: Doping-temperature phase diagram for hole doped cuprate superconductors showing the antiferromagnetic region (AFM) in green, and the superconducting (S/C) dome in blue. Figure from [6].

is generic for hole doped systems. At zero doping the cuprates are Mott insulators and below a few hundred Kelvin are also antiferromagnetic. As the doping is increased above around $p = 0.05$ (holes per formula unit) the antiferromagnetic state disappears and the pseudogap region is entered. At very low temperatures there is the first appearance of superconductivity. This is called the 'underdoped' side as the doping is less than that which optimises T_c. As the doping is further increased up to around $p = 0.16$, the optimum T_c is reached which varies between compounds. On the 'overdoped' side, moving towards a doping of around $p = 0.27$ sees T_c decrease to zero. Tallon *et al.* [7] gave a phenomenological model for hole doped cuprate superconductors which links the fraction of holes per Cu atom in the CuO_2 sheet, p, to T_c:

$$\frac{T_c}{T_{c,\max}} = 1 - 82.6(p - 0.16)^2 \tag{1.1}$$

When superconducting, an ordinary BCS superconductor has an energy gap. That is, if photons are fired at the material no excitations of the electron states occur unless the photon energy rises above a certain value, E_g. This is the energy required to break apart a Cooper pair. The gap disappears above T_c as Cooper pairs are no longer present. The cuprates also have an energy gap below T_c, but its magnitude depends on the direction. The superconducting gap turns out to be d-wave i.e. it has 4-fold symmetry with minima along the diagonals of the Brillouin zone. This suggests that the BCS electron-phonon pairing mechanism does not apply since this normally leads to s-wave pairing.

In underdoped cuprates, above T_c there is still a gap which is called the pseudogap. This region

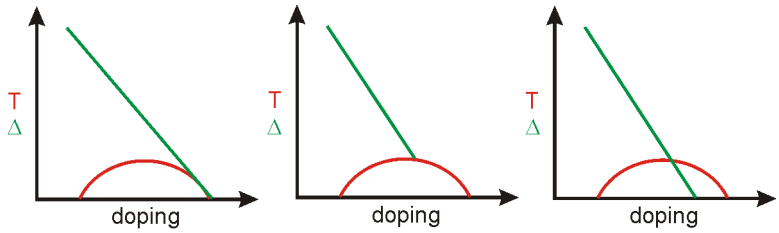

Figure 1.2: Three suggestions for the pseudogap on the overdoped side of the phase diagram [9]. Red line is the superconducting dome, green line is magnitude of the pseudogap.

of the phase diagram is characterised by broad (rather than sharp) peaks in the Angle Resolved Photoemission Spectroscopy (ARPES) energy distribution, a decrease in the normal state electronic contribution to the specific heat as the temperature is reduced and a S-shaped in-plane resistivity (see below). Reference [8] provides a good review of these and other methods for observing the pseudogap. The magnitude of the pseudogap ($\Delta_p(p)$) is quite large and varies with doping between about 20 meV at optimal doping and extrapolates to around 100 meV at zero doping. Its variation with T_c ($\approx [\Delta_p(p)^2 + \mu^2 k T_c(p)^2]^{(1/2)}$ with $\mu = 5$) suggests that the pseudogap might have a different physical origin to the superconducting gap. As the doping is increased beyond $p \approx 0.16$ it is not yet clear what happens to the pseudogap. As shown in figure 1.2 it has been suggested to continue right up to the edge of the superconducting dome with a steadily decreasing magnitude [10]; to come to and end at T_c at a particular doping level or to continue to exist below T_c and to terminate at a possible quantum critical point [11],[12]. The origin of the pseudogap remains unclear, although it has been associated with stripes of charge and/or spin [13], antiferromagnetic fluctuations [14] due to the proximity of the antiferromagnetic phase at low doping and preformed pairs [15] where the temperature is still too high for the phase coherence necessary for superconductivity to set in.

Further differences between BCS superconductors and the cuprates includes the in-plane coherence length which is found to be small (~ 20 Å) in the cuprates compared to several hundred Å in conventional BCS superconductors. The out-of-plane coherence length in the cuprates is also very small, indicating that the superconducting state can almost be viewed as being confined to the planes. Even so, the presence of a coupling indicates the superconducting state is a three-dimensional long range order.

One way to study these materials is to consider their electrical transport properties. The temperature dependence of the zero field in-plane resistivity shows a systematic evolution with doping above T_c — see figure 1.3. On the underdoped side ρ_{ab} is S-shaped with a downward deviation presumably due to the partial removal of a dominant scattering mechanism. This deviation was initially interpreted as a 'kink' corresponding to the pseudogap [16], although more recent work suggests that the deviation may occur at a much higher temperature [17]. At very low temperatures, $\rho_{ab}(T)$ in underdoped cuprates develops an upturn which suggests some kind of electronic localisation. In a

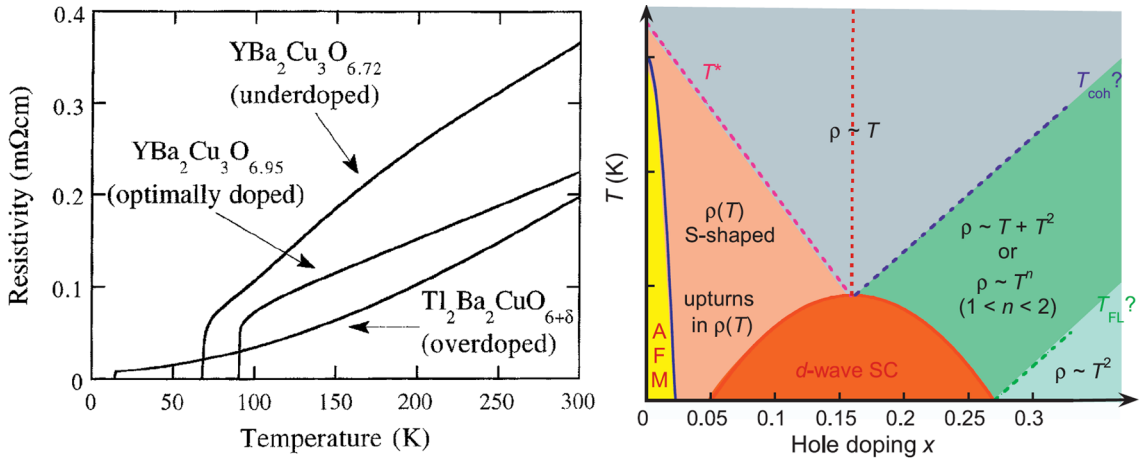

Figure 1.3: Left panel shows representative $\rho_{ab}(T)$ for underdoped, optimally doped and overdoped cuprates. Figure from [19]. Right panel shows the phase diagram of (hole doped) cuprates mapped out in terms of the temperature and doping evolution of the in-plane resistivity $\rho_{ab}(T)$. Solid lines are phase boundaries and the dashed lines indicate ill defined crossovers. Figure from [20].

'V' shaped region above the superconducting dome ρ_{ab} is linear, with this linearity persisting down to T_c at optimal doping. The confinement of this linearity to a narrow doping range is regarded as the signature of a potential quantum critical point beneath the superconducting dome, as seen in heavy fermion compounds [18]. Increasing the doping further leads to a $\rho_{ab} \sim T + T^2$ or $\sim T^n$ dependence (with $1 \leq n \leq 2$). Going beyond the superconducting dome on the overdoped side gives the $\rho_{ab} \sim T^2$ characteristic of a Fermi liquid. The fact that Fermi liquids (see §2.1.4) are well explained theoretically, suggests it may be possible to gain further insight into the cuprates by tracking their behaviour as the doping is gradually reduced from the overdoped side. This unusual temperature and doping dependence of the resistivity cannot yet be explained, but it is interesting to study as its eventual explanation may also hold the key to a full understanding of the cuprates and their superconductivity.

The in-plane Hall coefficient R_H shows significant changes with doping and temperature. The behaviour is captured across a large doping range by LSCO — see figure 1.4. At optimal doping ($p \sim 0.16$) R_H has a $1/T$ dependence across a large temperature range. In the underdoped region R_H retains its $1/T$ dependence but develops a downturn at low temperatures. The carrier density ($n_h = 1/R_H e$) at low temperatures approaches the hole concentration (p) given by the valence of the Cu atoms and not the $(1 + p)$ predicted by bandstructure calculations. On the overdoped side, the magnitude of R_H falls by an order of magnitude, probably as the Fermi surface evolves into a large cylinder. At doping higher than $p \approx 0.25$ R_H becomes negative at high temperatures. ARPES measurements support the evolution of the Fermi surface implied by R_H (i.e. the carrier number increases as the Fermi arcs lengthen) in the underdoped region. On the overdoped side ARPES suggests the Fermi surface in LSCO is electron-like for $p \geq 0.18$ but R_H remains positive up to

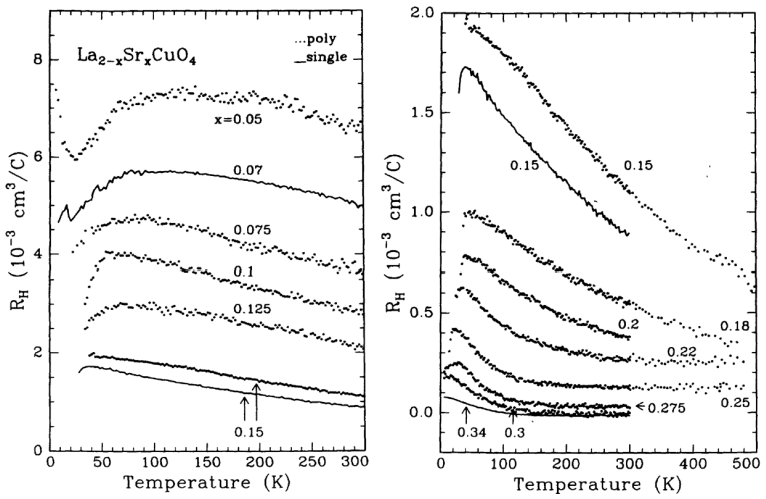

Figure 1.4: $R_H(T)$ at different dopings for LSCO. Figure from [21].

$p = 0.34$. This is problematic as $R_H(0)$ for a 2D single-band metal should reflect the sign of the dominant carrier.

Despite the linearity of ρ_{ab}, the inverse Hall angle, $\cot\theta_H = \rho_{ab}/R_H B$, is found to have a quadratic temperature dependence over a large temperature and doping range. This clear difference in the T dependencies led Anderson [22] to suggest that at optimal doping the resistivity reflects the temperature dependence of $1/\tau_{\rm tr}$ while $\cot\theta_H$ is sensitive to $1/\tau_H$. In this 'separation of lifetimes' picture R_H is sensitive to $\tau_H/\tau_{\rm tr}$ [23]. Gaining an understanding of the normal state transport properties such as $\rho_{ab}(T)$ and $R_H(T)$ is seen as a key way to uncover the pairing mechanism and a full understanding of the cuprate superconductors.

The electronic structure of the cuprates, resulting from the highest partially filled bands with Cu3$d_{x^2-y^2}$ and O2$p_{x,y}$ character, can be expressed as a 2D energy dispersion in a tight-binding representation as:

$$\varepsilon(\mathbf{k}) = \varepsilon_0 - 2t(\cos k_x + \cos k_y) + 4t'(\cos k_x \cdot \cos k_y) - 2t''(\cos 2k_x + \cos 2k_y) \tag{1.2}$$

Pavarini *et al.* [24] identified a correlation between the maximum T_c and the ratio of t'/t (where t represents a nearest neighbour interaction and t' a next-nearest neighbour interaction). The low $T_{c,\max}$ cuprates like $La_{2-x}Sr_xCuO_4$ (LSCO) and $Bi_2Sr_{2-x}La_xCuO_6$ (Bi2201) have a relatively low t'/t corresponding to a diamond-like Fermi surface. Those with higher $T_{c,\max}$ values such as $Bi_2Sr_2CaCu_2O_{8+\delta}$ (Bi2212), $YBa_2Cu_3O_{7-\delta}$ (YBCO) and $Tl_2Ba_2CuO_{6+\delta}$ (Tl2201) have much more rounded Fermi surfaces characteristic of higher t'/t values. This is illustrated in figure 1.5 where a representative 2D projection of the Fermi surface is shown for a doping of $p = 0.15$ (near optimal) and $p = 0.30$ (beyond the superconducting dome). Notice that on the left of figure 1.5, for the lower t'/t the Fermi level

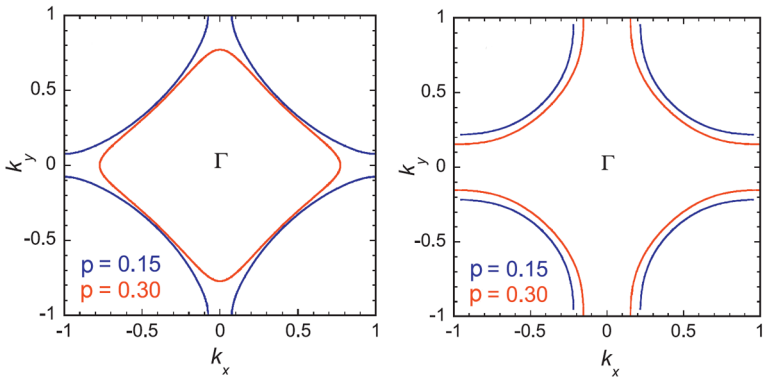

Figure 1.5: Left panel shows schematic 2D projection of the Fermi surface in LSCO for $p = 0.15$ ($t'/t = 0.15$) and $p = 0.30$ ($t'/t = 0.12$). Right panel shows similar projections for $Tl_2Ba_2CuO_{6+\delta}$ for $p = 0.15$ ($t'/t = 0.22$) and 0.30 ($t'/t = 0.22$).

has been reduced below the van Hove singularity and there is a cross-over to an electron-like Fermi surface (seen only in LSCO).

The shape and size of the Fermi surface in overdoped $Tl_2Ba_2CuO_{6+\delta}$ has been measured by ARPES [25] and ADMR [26] and more recently confirmed by quantum oscillations [27]. All these experimental probes as well as bandstructure calculations [28] are in good agreement. In the underdoped region, ARPES measurements show most of the spectral intensity is concentrated in small regions near the nodes in the superconducting gap (i.e. along (π,π)), suggesting the Fermi surface is broken up into disconnected Fermi arcs [29]. However, recent work on underdoped ortho-II ordered $YBa_2Cu_3O_{6.5}$ [30] and $YBa_2Cu_4O_8$ [31],[32] show quantum oscillations at a frequency corresponding to a very small Fermi surface pocket. The origin of this pocket, its location in the Brillouin zone and its relation to the ARPES Fermi arcs remains controversial.

Recently, a number of authors have proposed that quasiparticle scattering in the cuprates may be anisotropic. Suggestions of 'hot spots', that is, local regions of the Fermi surface where scattering is intense were made by considering NMR data where the antiferromagnetic spin correlation function is strongly peaked along a specific $\mathbf{Q}$ vector [33]. Although, the regions where the scattering rate is lower are now thought to short-circuit the 'hot spots' leading to conventional transport [34]. A model based on 'cold spots' where only the (π,π) quasiparticles are long lived was proposed citing optical conductivity data and quasiparticle lifetimes measured by ARPES as an experimental basis [35]. Both these models explain the behaviour of $\rho_{ab}(T)$ and $\cot\Theta_H(T)$ through the inclusion of an anisotropic mean free path. Hussey [36] found that a simple (trigonometric) four-fold anisotropic form for the scattering rate was sufficient to accurately explain the normal state transport properties in $Tl_2Ba_2CuO_{6+\delta}$ and $Bi_2Sr_2CaCu_2O_{6+x}$ and went on to use it to successfully model the temperature dependence of angle dependent magnetoresistance (ADMR) data on $Tl_2Ba_2CuO_{6+\delta}$ [37].

The underdoped side of the phase diagram is complicated by the pseudogap and possible antiferro-

magnetic, spin, charge or superconducting fluctuations. In contrast, the overdoped cuprates provide a fresh angle to study these interesting materials by approaching from the well understood Fermi liquid starting point. Magnetotransport measurements such as the Hall effect and quantum oscillations have been used for many years to investigate the electronic properties and Fermi surface of metals. Over recent years, the measurement of angle dependent magnetoresistance (ADMR) in both organic superconductors and now the cuprates have become an increasingly important experimental tool. In this thesis, ADMR measurements are performed on the overdoped cuprate $Tl_2Ba_2CuO_{6+\delta}$ and used to gain a deeper understanding of the temperature and doping dependence and the anisotropy of the quasiparticle scattering rate.

Previous work by Hussey and Adbel-Jawad includes the application of the Boltzmann transport equation to model ADMR data on $Tl_2Ba_2CuO_{6+\delta}$ at 4.2 K [26] and then the application of an anisotropic scattering rate to model ADMR data measured at a single azimuthal angle and doping level at temperatures up to 55 K [37]. Analysis of these data provided the first evidence of a 3D Fermi surface in the cuprates. Further data were taken across a range of azimuthal angles at a single temperature for samples at two lower doping levels [38].

The work in this thesis significantly extends previous ADMR work on $Tl_2Ba_2CuO_{6+\delta}$, extending the number of azimuthal angles measured to five, increasing the temperature range of the data to 110 K and obtaining a doping dependence down to a T_c of 45 K. This has added robustness to the determination of the Fermi surface and confirmed the need for an anisotropic scattering rate. The magnitude of the anisotropic component of the scattering rate is shown to have a direct correlation with doping (T_c). Recent work on LSCO has found the same anisotropic scattering rate form using both transport [39] and ARPES measurements [40]. This previous work along with this thesis have identified the temperature and doping dependence of this anisotropic scattering rate, but what remains now is to identify its microscopic origin as this may provide a vital piece in the puzzle of the cuprates. The thesis also reports new quantum oscillations measurements on $Tl_2Ba_2CuO_{6+\delta}$ which provide an analysis free confirmation of the existence of a Fermi surface in overdoped cuprates. Here the Fermi surface is found to be a large cylinder which is in contrast to recent work [30],[31],[32] on the underdoped cuprates where one or more small Fermi surface pockets are observed by the same experimental technique. One of the most interesting problems in the cuprates is to uncover how these two distinct Fermi surfaces evolve towards optimal doping.

This thesis is structured as follows: chapter two gives a general introduction to the behaviour of electrons in metals, the origin of resistivity & magnetoresistance and an introduction to the theory behind angle dependent magnetoresistance. Chapter 3 gives an introduction to $Tl_2Ba_2CuO_{6+\delta}$ including its bandstructure and transport properties. The experimental methods used in this work are explained in detail in chapter 4. In chapter 5 there is an explanation of the analysis techniques used in this work including a derivation of the form of the Boltzmann transport equation used to

fit the ADMR data in $Tl_2Ba_2CuO_{6+\delta}$ along with simulated examples of ADMR data showing the effect of different parameterisations. Chapter 6 reports high quality experimental ADMR data taken at up to 110 K on $Tl_2Ba_2CuO_{6+\delta}$ samples with T_c up to 38 K from two different crystal growers. A scattering rate which is anisotropic around the Fermi surface is confirmed to be necessary to explain the temperature evolution of the data. This scattering rate is separated into two components, one which is isotropic with a T^2 dependence and the other which has 4-fold anisotropy with the minima corresponding to the minima in the superconducting gap and T-linear. There is a discussion of the agreement and reliability of other data (ARPES and magnetoresistance) on the same material. Also shown is the ability of the ADMR fitting parameters to accurately reproduce in-plane transport properties. In chapter 7 a study of quantum oscillations (both Shubnikov-de Haas (SdH) and de Haas-van Alphen (dHvA)) on $Tl_2Ba_2CuO_{6+\delta}$ is presented. This provides good agreement of the size of the Fermi surface with the ADMR work. Chapter 8 looks at markedly different ADMR data taken on samples with $T_c \approx 45$K and attempts to explain this sudden change for only a small change in doping. Finally, the appendix provides a little more depth on a number of points discussed elsewhere in this thesis. For transparency and to aid easy reproduction of this work the computer code used in the data analysis is also shown here.

Chapter 2

Resistance & Magnetoresistance and its Characteristics in Quasi-2D Systems

2.1 Electrons in Metals

The early Drude and Sommerfeld models treat the electrons in a metal as free. This allows some progress towards understanding the electrical properties of metals, but to progress further the electrons need to modelled in a periodic potential arising from the crystal lattice.

2.1.1 Drude Model

The Drude model uses the idea of a gas of electrons which are able to move freely between the positively charged ionic cores. The electrons collide instantaneously with ions with a probability per unit time τ^{-1}. Between collisions the electrons are assumed not to interact with each other or with the ions. The conductivity, σ_0 can be shown to be:

$$\sigma_0 = \frac{ne^2\tau}{m} \tag{2.1}$$

where n is the electron number density, e is the electron charge, τ is the scattering time — the probability per unit time that the electron scatters and m is the electron mass. Substituting a typical room temperature conductivity of a metal ($\rho = 1/\sigma = 1 - 20\,\mu\Omega$cm) and then calculating the mean free path $v\tau$ (where v is the velocity) using the idea that the electrons have a mean kinetic energy $\frac{1}{2}m\langle v\rangle^2 = \frac{3}{2}k_BT$ gives a value of the order of the interatomic distance which is consistent with the idea of electrons colliding with the ionic cores. A further partial success of this model is in predicting the magnitude of the Wiedemann-Franz ratio, $L = \kappa/\sigma T$. At room temperature it was noticed that this was a constant value of $2.5 \times 10^{-8}\mathrm{W\Omega K^{-2}}$ for many metals. κ is the thermal conductivity given by $\kappa = \frac{1}{3}\langle v\rangle^2\tau C_{\mathrm{el}}$ where C_{el} is the electronic heat capacity. The Drude model

predicts C_{el} is the classical equipartition of energy result $\frac{3}{2}nk_B$. Despite these partial successes, a major failing of the model is that it predicts C_{el} to be two orders of magnitude too large and independent of temperature (rather than proportional to temperature as found experimentally at low temperatures).

2.1.2 Sommerfeld Model

The Sommerfeld model improved upon the Drude model by realising that the Pauli exclusion principle applies to the electrons which means that the electron velocity distribution should be the quantum-mechanical Fermi-Dirac distribution rather than the classical Maxwell-Boltzmann distribution:

$$f(\varepsilon) = \frac{1}{e^{(\varepsilon-\varepsilon_F)/k_BT}+1} \tag{2.2}$$

With the simple parabolic form $\varepsilon(\mathbf{k}) = \hbar^2\mathbf{k}^2/2m$ for the energy dispersion as a function of $\mathbf{k}$ consider adding free electrons into a metal. Initially they will occupy the lowest energy state but will then be forced into higher energy states by the Pauli exclusion principle. A sphere of $\mathbf{k}$ states of radius $k_F = \left(3\pi^2 n\right)^{\frac{1}{3}}$ will then be occupied where n is the electron density in $\mathbf{k}$-space. The surface of this sphere is the Fermi surface — the division between occupied and unoccupied states at $T = 0\,\text{K}$. The Fermi energy, ε_F is then defined as:

$$\varepsilon_F = \frac{\hbar^2 k_F^2}{2m} = \frac{\hbar^2}{2m}\left(3\pi^2 n\right)^{\frac{2}{3}} \tag{2.3}$$

This modification by Sommerfeld successfully explained the temperature dependence and magnitude of $C_{\mathbf{el}}$, but still couldn't explain the Hall coefficient, magnetoresistance or the more complex Fermi surface shape of many metals. To make further progress the interactions between the ionic cores and the electrons need to be taken into account, that is a periodic potential must be introduced.

2.1.3 Electrons in Periodic Potentials

The translational periodicity of the crystal is given by:

$$\mathbf{R} = n_1 a\hat{\mathbf{x}} + n_2 b\hat{\mathbf{y}} + n_3 c\hat{\mathbf{z}} \tag{2.4}$$

where n_1, n_2 and n_3 are integers and a, b, c are the lattice dimensions. So the potential $V(\mathbf{r})$ must be periodic i.e. $V(\mathbf{r}+\mathbf{R}) = V(\mathbf{r})$. With this in mind Bloch's theorem shows that the eigenstates, ψ, of the one-electron Hamiltonian $H = -\hbar^2\nabla^2/2m + V(\mathbf{r})$ can be chosen to be a plane wave multiplied by a function with the periodicity of the lattice:

$$\psi(\mathbf{r}+\mathbf{R}) = e^{i\mathbf{k}\cdot\mathbf{R}}\psi(\mathbf{r}) \tag{2.5}$$

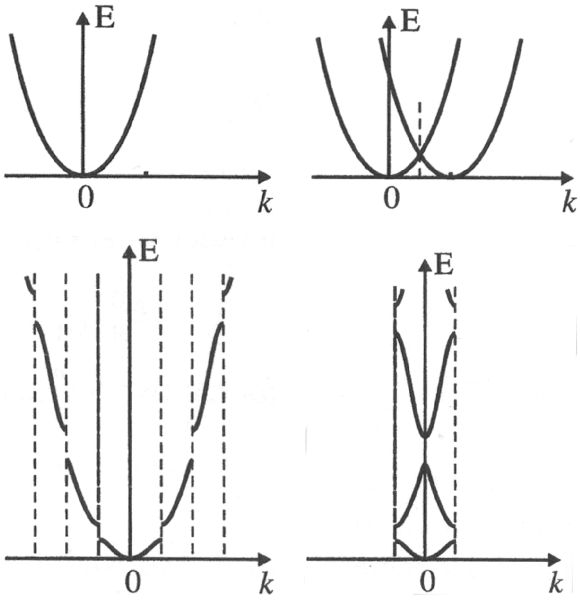

Figure 2.1: Top left panel shows the free electron dispersion relation — see equation 2.3. Top right panel shows the free electron dispersion repeated due to periodicity of **k**-space. Bottom left panel shows the changes to the free electron dispersion as a band gap opens at each Brillouin zone boundary. This is the extended zone scheme. Bottom right panel shows the same dispersion as the extended zone scheme but with corresponding translations by an integer number of wave vectors the size of the Brillouin zone. This is the reduced zone scheme. Figure adapted from [43].

The two limiting cases, a very weak potential (the nearly free electron model) or a very strong potential (the tight binding model), both give rise to very similar energy bands with band gaps so real potentials which lie somewhere in between must also give qualitatively similar bandstructure.

The energy dispersion is now modified as **k** values which lie outside the first Brillouin zone can be translated back into it by subtracting reciprocal lattice vectors. It can also be shown that gaps in this dispersion open up at the zone boundaries. This allows much more complex and realistic Fermi surfaces to be constructed when the translation into the first Brillouin zone is applied. Much more detailed description of the various models of electrons in metals can be found in books by Kittel [41], Ashcroft and Mermin [42] and Singleton [43].

2.1.4 Fermi Liquids

Ideas by Lev Landau were originally designed to explain the liquid state of ^{3}He and became known as Fermi liquid theory. These ideas have found an additional application in explaining electron-electron interactions in metals. Consider a set of non-interacting electrons where an interaction is gradually turned on which causes electrons to be scattered. Landau applied the idea of adiabatic continuity i.e. by turning on an interaction slowly the eigenstates of the non-interacting system evolve with one-to-one correspondence into eigenstates of the interacting system. Suppose a system consists of a filled

Fermi sphere with a single excited electron in a level with $\varepsilon_1 > \varepsilon_F$. In order to scatter this electron must interact with an electron with energy ε_2 which must be less than ε_F since these are the only other occupied states. The Pauli exclusion principle ensures that these electrons can only scatter into unoccupied levels with energy ε_3 and ε_4 which both must be $> \varepsilon_F$. Phase space is available for this interaction as the energies ε_2, ε_3 and ε_4 can vary within a shell of thickness of order $|\varepsilon_1 - \varepsilon_F|$. This leads to a scattering rate of order $(\varepsilon_1 - \varepsilon_F)^2$. The quantity appears squared rather than cubed, because once ε_2 and ε_3 have been chosen within the shell of allowed energies, energy conservation allows no further choice for ε_4. If the system with the excited state is not a filled Fermi sphere, but a thermal equilibrium distribution of electrons, then there will be partially occupied levels in a shell of width $k_B T$ about ε_F. This provides an additional range of choice for the energies ε_2 and ε_3 and therefore leads to a scattering rate going as $(k_B T)^2$ [42]:

$$\frac{1}{\tau} = a(\varepsilon_1 - \varepsilon_F)^2 + b(k_B T)^2 \tag{2.6}$$

A rough estimate of the magnitude of this lifetime can be calculated by assuming the temperature dependence is fully accounted for by the $b(k_B T)^2$ factor; where b can be given by the Born approximation to be the square of the Fourier transform of the interaction potential which can be estimated by the Thomas-Fermi screened potential. At room temperature this leads to a scattering rate around a factor of 10^4 lower than a typical metallic scattering rate, suggesting that electron-electron interactions do not invalidate the independent electron picture.

This indicates that if the independent electron picture is a good approximation then electron-electron scattering will not invalidate this picture even if the interactions are strong. But, if these interactions are strong then it is unlikely that the independent electron picture will be appropriate. Landau approached this problem by accepting that the independent electron picture was not valid, but suggested the above ideas could still be applied providing that an independent 'something' picture was still a valid starting point. These 'somethings' were labeled 'quasiparticles'. A good review of Fermi liquid ideas applied to the cuprates can be found in reference [44].

2.2 Resistance

Electrical resistance is caused by the scattering of electrons from phonons, other electrons, lattice defects or impurities.

2.2.1 Electron-Phonon Scattering

Electrons can be scattered from phonons by two processes. Elastic scattering is where both the electron and phonon change wavevector. Secondly, inelastic scattering occurs when a phonon is emitted or absorbed by an electron causing a change in the electron wavevector and energy. The

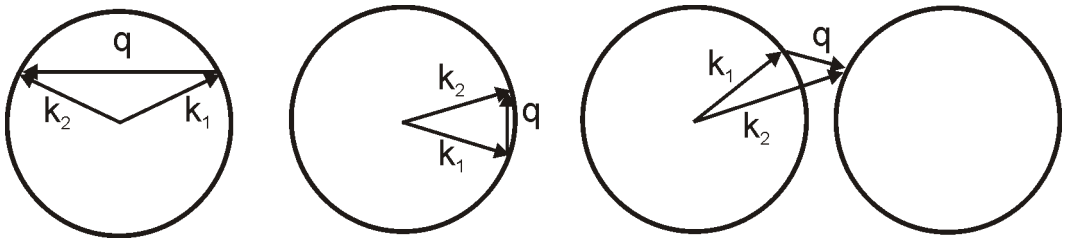

Figure 2.2: Electron-phonon scattering geometry, $\mathbf{k_1}$ is the initial state, $\mathbf{k_2}$ is the final state, $\mathbf{q}$ is the phonon wavevector and the circle represents the Fermi surface. Left panel shows large $\mathbf{q}$ for $T \sim \Theta_D$. Middle panel shows that for $T \ll \Theta_D$ $\mathbf{q}$ is small and forward scattering dominates. Right panel shows Umklapp scattering — scattering with small $\mathbf{q}$ from one Brillouin zone into an adjoining zone.

Debye temperature, Θ_D, corresponds to the energy of the most energetic phonons ($\hbar\omega_D = k_B\Theta_D$) and for a typical metal is of the order of room temperature. At temperatures $T \sim \Theta_D$ phonons will have wavevectors, $\mathbf{q}$, of the order of the width of the Brillouin zone so electrons are scattered to the opposite side of the Fermi surface — see left of figure 2.2. This scattering is proportional to the number of phonons with energy $\hbar\omega_D \approx k_B\Theta_D$ which is $\propto T$. At lower temperatures the phonons will have energies $\ll k_B\Theta_D$ and therefore wavevectors much less than the Brillouin zone size and will be unable to scatter across the Fermi surface. The scattering will be proportional to the number of phonons ($\propto T^3$) multiplied by a factor to account for the fact that the scattering events become more concentrated in the forward direction ($\propto T^2$) — see middle of figure 2.2. This T^5 dependence is rarely exactly obeyed experimentally as there are extra $\mathbf{k}$-states into which small $\mathbf{q}$ scattering can occur such as those present due to lobes of Fermi surface. Small $\mathbf{q}$ scattering can also occur to the Fermi surface in the next Brillouin zone as these states are accessible due to the periodicity of $\mathbf{k}$-space. This is often labelled 'Umklapp' or U-process scattering — see right of figure 2.2. Both these effects tend to give a resistivity which is approximately linear at high temperature and exponential at low temperatures i.e. $e^{-\Theta_F/T}$ where Θ_F is a characteristic temperature dependent on the Fermi surface geometry — see left of figure 2.3.

2.2.2 Residual Resistivity

As the temperature drops to zero in the absence of crystal impurities and defects the resistivity would also drop to zero as the electron-phonon resistivity becomes negligible. Real crystals are not free from lattice defects or impurities so as temperature drops a resistivity minimum is reached; at $T = 0\,\mathrm{K}$ this is the residual resistivity, ρ_0:

$$\rho = \rho_0 + \rho_{e-p}(T) \tag{2.7}$$

This form is found to fit experimental data on good metals such as copper very accurately — see reference [45] and the left of figure 2.3.

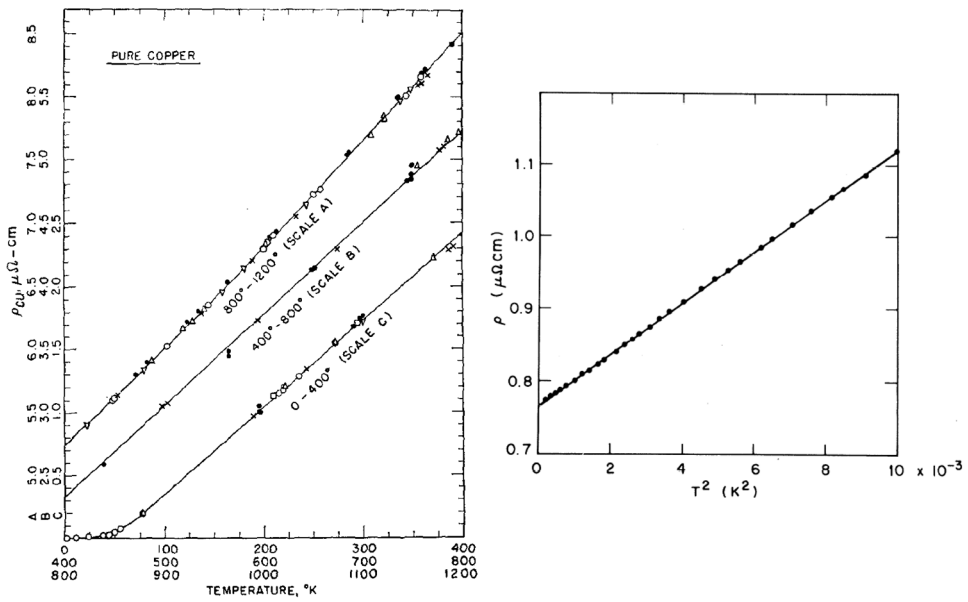

Figure 2.3: Left panel shows the electrical resistivity of pure copper between 4 K and 1100 K. Figure from [49]. Right panel shows the electrical resistivity of the heavy fermion compound $CeAl_3$ below 100 mK showing the T^2 dependence from electron-electron scattering — this continues up to ≈ 0.3 K. Figure from [50].

2.2.3 Electron-Electron Scattering

The resistivity due to electron-electron scattering is theoretically found to be given by:

$$\rho_{e-e} = A_{e-e}T^2 \tag{2.8}$$

where A_{e-e} is a material specific constant related to the strength of the screening of the Coulomb potential by the electrons. It arises from scattering of electrons with initial and final states with energy close to the Fermi level and wavevectors close to k_F. Its magnitude is such that the T^2 component of the resistivity is usually only noticeable at very low temperatures. It can also be significant when the density of states at the Fermi energy is very large (i.e. a large effective electron mass) as there are more possible states for scattering from/to or when there is a complex Fermi surface again making more states available with the correct energy and momentum. This T^2 resistivity appears to be most relevant to materials where electron correlations are very strong such as at very low temperatures in heavy fermion compounds (see right of figure 2.3), below 60 K in Sr_2RuO_4 [46], below 50 K in $PrBa_2Cu_4O_8$ [47], various organic superconductors [48] and probably the cuprate high temperature superconductors.

2.3 The Boltzmann Transport Equation

The Boltzmann transport equation provides a method of calculating the conductivity of a metal taking into account various effects on the quasiparticles when the system is not at equilibrium. It is a semiclassical model since the periodic potential is treated with quantum mechanics but the theory describes the evolution of the Bloch states due to applied fields in a classical manner. The function $f_{\mathbf{k}}(\mathbf{r})$ is the local concentration of quasiparticles in the state $\mathbf{k}$ near the point $\mathbf{r}$ in space. With time, $f_{\mathbf{k}}(\mathbf{r})$ changes because of quasiparticle diffusion due to a temperature gradient, the effect of external electric and magnetic fields on the quasiparticles and because of scattering of the quasiparticles to another state. The net effect at any point and for any $\mathbf{k}$ is zero:

$$\left.\frac{\partial f_{\mathbf{k}}}{\partial t}\right|_{\text{total}} = \left.\frac{\partial f_{\mathbf{k}}}{\partial t}\right|_{\text{scattering}} + \left.\frac{\partial f_{\mathbf{k}}}{\partial t}\right|_{\text{field}} + \left.\frac{\partial f_{\mathbf{k}}}{\partial t}\right|_{\text{diffusion}} = 0 \tag{2.9}$$

$f_{\mathbf{k}}$ is the steady state; the equilibrium state is $f^0_{\mathbf{k}}$ and exists when all fields and temperature gradients are absent. It can be assumed that the steady state distribution is close to equilibrium so that:

$$g_{\mathbf{k}} = f_{\mathbf{k}} - f^0_{\mathbf{k}} \tag{2.10}$$

Working at constant temperature the diffusion term can be neglected. The term due to external fields can be written as:

$$\left.\frac{\partial f_{\mathbf{k}}}{\partial t}\right|_{\text{field}} = \frac{\partial f_{\mathbf{k}}}{\partial \mathbf{k}}\frac{\partial \mathbf{k}}{\partial t} = -\frac{e}{\hbar}\left[\mathbf{E} + \mathbf{v}\times\mathbf{B}\right]\frac{\partial f_{\mathbf{k}}}{\partial \mathbf{k}} \tag{2.11}$$

The final term, due to scattering, is in general quite complex so is often approximated using the 'relaxation time approximation' where a relaxation time τ is introduced such that if the field was turned off then $g_{\mathbf{k}}$ would decay to zero as $g_{\mathbf{k}}(t) = g_{\mathbf{k}}(0)e^{-t/\tau}$:

$$\left.\frac{\partial f_{\mathbf{k}}}{\partial t}\right|_{\text{scattering}} = -\frac{g_{\mathbf{k}}}{\tau} \tag{2.12}$$

Combining these gives:

$$-\frac{e}{\hbar}\left[\mathbf{E} + \mathbf{v}\times\mathbf{B}\right]\frac{\partial f_{\mathbf{k}}}{\partial \mathbf{k}} = \frac{g_{\mathbf{k}}}{\tau} \tag{2.13}$$

Substituting equation 2.10:

$$-\frac{e}{\hbar}\left[\mathbf{E} + \mathbf{v}\times\mathbf{B}\right]\frac{\partial g_{\mathbf{k}}}{\partial \mathbf{k}} - \frac{e}{\hbar}\left[\mathbf{E} + \mathbf{v}\times\mathbf{B}\right]\frac{\partial f^0_{\mathbf{k}}}{\partial \mathbf{k}} = \frac{g_{\mathbf{k}}}{\tau} \tag{2.14}$$

Using:

$$\mathbf{v} = \frac{1}{\hbar}\frac{\partial \varepsilon}{\partial \mathbf{k}} \tag{2.15}$$

$$\frac{\partial f^0_{\mathbf{k}}}{\partial \mathbf{k}} = \frac{\partial f^0_{\mathbf{k}}}{\partial \varepsilon}\frac{\partial \varepsilon}{\partial \mathbf{k}} = \frac{\partial f^0_{\mathbf{k}}}{\partial \varepsilon}\hbar\mathbf{v} \tag{2.16}$$

and noting that $\mathbf{v}\cdot\mathbf{v}\times\mathbf{B}=0$ and dropping the $\mathbf{E}\cdot dg_{\mathbf{k}}/d\mathbf{k}$ term (as it represents an order E^2 deviation from Ohm's Law), equation 2.13 can be written as the linearised Boltzmann transport equation:

$$e\mathbf{E}\cdot\mathbf{v}\left(-\frac{\partial f^0_{\mathbf{k}}}{\partial\varepsilon}\right)=\frac{g_{\mathbf{k}}}{\tau}+\frac{e}{\hbar}\left[\mathbf{v}\times\mathbf{B}\right]\frac{\partial g_{\mathbf{k}}}{\partial\mathbf{k}} \tag{2.17}$$

2.4 The Resistivity Tensor

The resistivity is represented by a tensor, with the first subscript referring to the direction of the applied current and the second to the direction of the measured voltage drop:

$$\rho=\begin{pmatrix}\rho_{xx}&\rho_{xy}&\rho_{xz}\\\rho_{yx}&\rho_{yy}&\rho_{yz}\\\rho_{zx}&\rho_{zy}&\rho_{zz}\end{pmatrix}=\begin{pmatrix}\sigma_{xx}&\sigma_{xy}&\sigma_{xz}\\\sigma_{yx}&\sigma_{yy}&\sigma_{yz}\\\sigma_{zx}&\sigma_{zy}&\sigma_{zz}\end{pmatrix}^{-1} \tag{2.18}$$

In the case of cubic crystal symmetry and a spherical Fermi surface the resistivity may be isotropic i.e. its magnitude is unaffected by the direction along which the current is applied. Alternatively, the resistivity may be anisotropic. The general case of inverting a 3×3 matrix leads to a complex result. In real materials some of the conductivity tensor components are zero or small which simplifies the calculation of the resistivity tensor.

2.5 Zero Field Resistivity Tensor

Taking the Boltzmann transport equation (equation 2.17) when $\mathbf{B}=0$ gives:

$$e\mathbf{E}\cdot\mathbf{v}\left(-\frac{\partial f^0_{\mathbf{k}}}{\partial\varepsilon}\right)=\frac{g_{\mathbf{k}}}{\tau} \tag{2.19}$$

Noting that the current density, J_i is given by:

$$J_i=\sigma_{ij}E_j=\frac{1}{4\pi^3}\int ev_i g_{\mathbf{k}}d^3k \tag{2.20}$$

$g_{\mathbf{k}}$ can be substituted from equation 2.19 giving:

$$\sigma_{ij}=\frac{1}{4\pi^3}\int e^2\tau v_i v_j\left(-\frac{\partial f^0_{\mathbf{k}}}{\partial\varepsilon}\right)d^3k \tag{2.21}$$

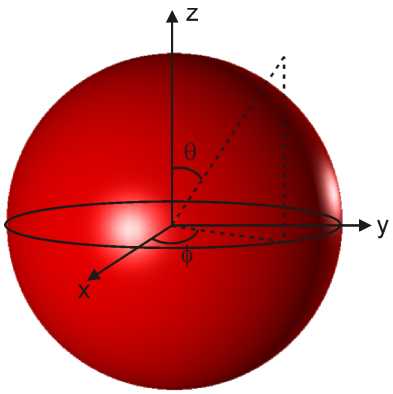

Figure 2.4: Spherical Fermi surface and coordinates

Due to the vector dot product the components where v_i and v_j are perpendicular are zero leaving only the diagonal terms in the conductivity tensor:

$$\rho = \begin{pmatrix} \sigma_{xx} & 0 & 0 \\ 0 & \sigma_{yy} & 0 \\ 0 & 0 & \sigma_{zz} \end{pmatrix}^{-1} = \begin{pmatrix} \frac{1}{\sigma_{xx}} & 0 & 0 \\ 0 & \frac{1}{\sigma_{yy}} & 0 \\ 0 & 0 & \frac{1}{\sigma_{zz}} \end{pmatrix} \tag{2.22}$$

2.5.1 Spherical Fermi Surface

In the case of a spherical Fermi surface (see figure 2.4), spherical polar coordinates are appropriate where $d^3k = k_F^2 \sin\theta \partial\theta\partial\phi\partial k_F$ and $\partial k_F = \partial\varepsilon/\hbar v_F$. Fermions obey Fermi-Dirac statistics with a distribution function given in equation 2.2. At low temperatures the derivative of the distribution function can be approximated by a delta function so $\int -\left(\partial f^0_{\mathbf{k}}/\partial\varepsilon\right)\partial\varepsilon$ is 1 at the Fermi level and zero elsewhere. So equation 2.21 becomes:

$$\sigma_{ij} = \frac{1}{4\pi^3}\int_0^{\pi}\int_0^{2\pi} \frac{e^2\tau v_i v_j}{\hbar v_F} k_F^2 \sin\theta \partial\theta\partial\phi \tag{2.23}$$

Now in spherical polar coordinates $v_x = v_F \sin\theta\cos\phi$, $v_y = v_F \sin\theta\sin\phi$ and $v_z = v_F\cos\theta$ and it can be shown (see §10.1.1) that $\sigma_{xx} = \sigma_{yy} = \sigma_{zz}$. In fact, noting the carrier number for a free electron system is $n = 2/(2\pi)^3 \times 4\pi k_F^3/3 = k_F^3/(3\pi^2)$, σ_{xx}, σ_{yy} and σ_{zz} reduce to the Drude result:

$$\sigma_0 = \frac{e^2\tau k_F^3}{3\pi^2 m^*} = \frac{ne^2\tau}{m^*} \tag{2.24}$$

so:

$$\rho = \begin{pmatrix} \frac{1}{\sigma_0} & 0 & 0 \\ 0 & \frac{1}{\sigma_0} & 0 \\ 0 & 0 & \frac{1}{\sigma_0} \end{pmatrix} \tag{2.25}$$

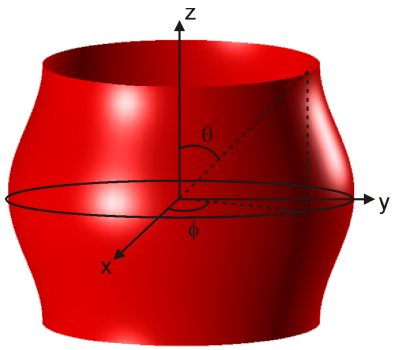

Figure 2.5: Barrel shaped Fermi surface

2.5.2 Cylindrical Fermi Surface

In the case of a strictly 2D cylindrical Fermi surface where the axis of the Fermi surface is along the z direction, cylindrical polar coordinates can be used leading to the same result for σ_{xx} and σ_{yy} as for the spherical case. On the other hand σ_{zz} will be zero since the velocity is zero as it is always perpendicular to the Fermi surface giving:

$$\rho = \begin{pmatrix} \frac{1}{\sigma_0} & 0 & 0 \\ 0 & \frac{1}{\sigma_0} & 0 \\ 0 & 0 & 0 \end{pmatrix} \tag{2.26}$$

2.5.3 Barrel Shaped Fermi Surface

If there is a small barrel shaped warping to this cylindrical Fermi surface — see figure 2.5:

$$\varepsilon(\mathbf{k}) = \frac{\hbar^2 k_{\parallel}^2}{2m^*} - 2t_{\perp}\cos\left(\frac{k_z c}{2}\right) \tag{2.27}$$

where c is the c-axis lattice parameter and $t_{\perp}$ is the interlayer transfer integral then:

$$v_z = \frac{1}{\hbar}\frac{\partial\varepsilon}{\partial k_z} = \frac{ct_{\perp}}{\hbar}\sin\left(\frac{k_z c}{2}\right) \tag{2.28}$$

In cylindrical polar coordinates where the volume element $d^3k = k_F \partial k_F \partial\phi \partial k_z$ and $v_x = v_F\cos\phi$, $v_y = v_F\sin\phi$, $v_z = v_z$ and considering the carrier number for this system is given by $n = 2/(2\pi)^3 \times \pi k_F^2 \times 4\pi/c = k_F^2/\pi c$ the resistivity tensor is (see §10.1.2):

$$\rho = \begin{pmatrix} \frac{1}{\sigma_0} & 0 & 0 \\ 0 & \frac{1}{\sigma_0} & 0 \\ 0 & 0 & \frac{\pi\hbar^4}{e^2\tau m^* c t_{\perp}^2} \end{pmatrix} \tag{2.29}$$

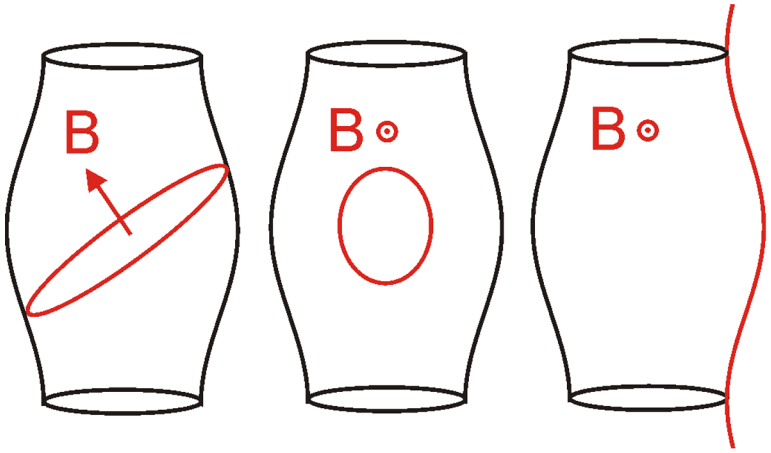

Figure 2.6: Left and centre panels show possible closed orbits of quasiparticles on a barrel shaped Fermi surface in the presence of a magnetic field. Right panel shows an example of an open orbit.

Later in §5.5 σ_{xx} is derived for the case when the barrel shaped Fermi surface does not have a circular cross section and τ is not isotropic around the Fermi surface.

2.6 Measurements in Magnetic Fields

Two major changes occur to the conductivity tensor when a sample is subject to a magnetic field. The well known Hall effect emerges as a result of the cross terms (i.e. σ_{xy}, σ_{yx} etc) and the magnitude of the σ_{xx}, σ_{yy} and σ_{zz} terms also change. The change in resistance of a sample when it is placed in a magnetic field is the sample's magnetoresistance. The magnitude of the magnetoresistance is usually expressed as $\Delta\rho/\rho_0 = (\rho(B) - \rho_0)/\rho_0$ where $\rho(B)$ is the resistivity when the magnetic field is applied and ρ_0 is the resistivity when no field is applied. In metals with a long relaxation time, τ, the effect of a magnetic field is usually to deviate the trajectory of the carriers from their electric field induced path. As the carrier path length is now longer the additional scattering results in a positive magnetoresistance. This occurs due to the Lorentz force caused by the magnetic field:

$$F = \frac{\partial \mathbf{k}}{\partial t} = -\frac{e}{\hbar}\mathbf{v} \times \mathbf{B} \tag{2.30}$$

which is always perpendicular to the field which causes the quasiparticles to have paths (or orbits) on the Fermi surface in planes perpendicular to the magnetic field. Depending upon the shape of the Fermi surface and the orientation of the magnetic field the Lorentz force creates two types of orbits — closed orbits and open orbits. An example of both types are shown in figure 2.6.

To describe the conductivity of closed orbits the Shockley-Chambers tube-integral can be used.

2.6.1 Shockley-Chambers Tube-Integral

The Boltzmann transport equation (equation 2.3) is modified for closed orbits by considering the Lorentz force (equation 2.30) giving:

$$e\mathbf{E}\cdot\mathbf{v}\left(-\frac{\partial f^0_{\mathbf{k}}}{\partial\varepsilon}\right)=\frac{g_{\mathbf{k}}}{\tau}+\frac{\partial g_{\mathbf{k}}}{\partial t} \tag{2.31}$$

The phase angle around the orbit is defined as $\partial\phi{=}\omega\partial t$ where ω is the angular frequency so equation 2.31 becomes:

$$e\mathbf{E}\cdot\mathbf{v}\left(\frac{-\partial f^0_{\mathbf{k}}}{\partial\varepsilon}\right)=\frac{g_{\mathbf{k}}}{\tau}+\omega\frac{\partial g_{\mathbf{k}}}{\partial\phi} \tag{2.32}$$

Taking $G{=}\int\frac{1}{\omega_c\tau}\partial\phi$ this can be re-written as:

$$e\mathbf{E}\cdot\mathbf{v}\left(\frac{-\partial f^0_{\mathbf{k}}}{\partial\varepsilon}\right)=\frac{g_{\mathbf{k}}}{\tau}+\omega_c\frac{\partial g_{\mathbf{k}}}{\partial\phi}=\omega_c e^{-G}\frac{\partial}{\partial\phi}(e^G g_{\mathbf{k}}) \tag{2.33}$$

Equation 2.33 can be rearranged to make $g_{\mathbf{k}}$ the subject also noting that $\mathbf{v}$ may have ϕ dependence:

$$g_{\mathbf{k}}=\left(\frac{-\partial f^0_{\mathbf{k}}}{\partial\varepsilon}\right)e^{-\frac{\phi}{\omega_c\tau}}\int_{-\infty}^{\phi}\frac{e}{\omega_c}e^{\frac{\phi'}{\omega_c\tau}}E_j v_j(\phi')\partial\phi' \tag{2.34}$$

(where the integration limits $-\infty$ to ϕ is a sum over history of the phase variable ϕ). The integration variable ϕ' can now be changed $\phi'\rightarrow\phi-\phi''$ so the upper limit $\phi\Rightarrow\phi''=0$ and the lower limit $-\infty\Rightarrow\phi''=\infty$ (note switching the limits introduces a factor of -1, but $\partial\phi'=-\partial\phi''$ so the two factors of -1 cancel) so that:

$$g_{\mathbf{k}}=\left(\frac{-\partial f^0_{\mathbf{k}}}{\partial\varepsilon}\right)\int_{0}^{\infty}\frac{e}{\omega_c}e^{-\frac{\phi''}{\omega_c\tau}}E_j v_j(\phi-\phi'')\partial\phi'' \tag{2.35}$$

Now:

$$d^3k=\partial k_B\partial k_\perp\partial k_\parallel \tag{2.36}$$

where $\partial k_\perp$ is parallel to $v_\perp$, ∂k_B is parallel to the $\mathbf{B}$ field and $\partial k_\parallel$ is perpendicular to $v_\perp$ and the $\mathbf{B}$ field. For free electrons where $v_\perp$ is perpendicular to the $\mathbf{B}$ field:

$$\hbar v_\perp\partial k_\perp=\hbar\left(\frac{1}{\hbar}\frac{\partial\varepsilon}{\partial k_\perp}\right)\partial k_\perp=\partial\varepsilon \tag{2.37}$$

Using $\partial\phi=\omega_c(\phi)\partial t$ and $\omega_c=eB/m^*$:

$$\partial k_\parallel=\frac{ev_\perp B}{\hbar}\partial t=\frac{ev_\perp B}{\omega_c\hbar}\partial\phi=\frac{v_\perp m^*}{\hbar}\partial\phi \tag{2.38}$$

therefore using equations 2.36 and 2.37:

$$d^3k = \partial k_B \partial k_\perp \frac{v_\perp m^*}{\hbar} \partial\phi = \frac{m^*}{\hbar^2} \partial k_B \partial\varepsilon \partial\phi \tag{2.39}$$

so using equation 2.20:

$$J_i = \frac{e}{4\pi^3} \int \partial\varepsilon \int \partial k_B \int_0^{2\pi} \frac{m^*}{\hbar^2} v_i(\phi) g_{\mathbf{k}} \partial\phi \tag{2.40}$$

Therefore:

$$\sigma_{ij} = \frac{e}{4\pi^3} \int \partial\varepsilon \int \partial k_B \int_0^{2\pi} \partial\phi \left[\frac{m^*}{\hbar^2} v_i(\phi) \left(\frac{-\partial f^0_{\mathbf{k}}}{\partial\varepsilon} \right) \int_0^\infty \frac{e}{\omega_c} e^{-\frac{\phi''}{\omega_c\tau}} \frac{E_j}{E_j} v_j(\phi - \phi'') d\phi'' \right] \tag{2.41}$$

$$\sigma_{ij} = \frac{e^2}{4\pi^3\hbar^2} \int \partial\varepsilon \left(\frac{-\partial f^0_{\mathbf{k}}}{\partial\varepsilon} \right) \int \partial k_B \int_0^{2\pi} \partial\phi \int_0^\infty \partial\phi'' v_i(\phi) v_j(\phi - \phi'') \frac{m^*}{\omega_c} e^{-\frac{\phi''}{\omega_c\tau}} \tag{2.42}$$

If $k_B T \ll \varepsilon_F$ then the Fermi-Dirac distribution is a step function at the Fermi level and so its derivative is a δ function at the Fermi energy. Therefore $\int_0^\infty d\varepsilon \delta(\varepsilon - \varepsilon_F) = 1$ so equation 2.42 becomes the Shockley-Chambers tube-integral form of the Boltzmann transport equation:

$$\sigma_{ij} = \frac{e^2}{4\pi^3\hbar^2} \int \partial k_B \int_0^{2\pi} \partial\phi \int_0^\infty \partial\phi'' v_i(\phi) v_j(\phi - \phi'') \frac{m^*}{\omega_c} e^{-\frac{\phi''}{\omega_c\tau}} \tag{2.43}$$

2.6.2 Spherical Fermi Surface

Using equation 2.43 for a spherical Fermi surface the magnetoconductivity can be calculated for each of the tensor components (see §10.1.3) so:

$$\rho = \sigma^{-1} = \begin{pmatrix} \frac{\sigma_0}{1+(\omega_c\tau)^2} & -\frac{\sigma_0\omega_c\tau}{1+\omega_c^2\tau^2} & 0 \\ \frac{\sigma_0\omega_c\tau}{1+\omega_c^2\tau^2} & \frac{\sigma_0}{1+(\omega_c\tau)^2} & 0 \\ 0 & 0 & \sigma_0 \end{pmatrix}^{-1} = \begin{pmatrix} \frac{1}{\sigma_0} & \frac{\omega_c\tau}{\sigma_0} & 0 \\ -\frac{\omega_c\tau}{\sigma_0} & \frac{1}{\sigma_0} & 0 \\ 0 & 0 & \frac{1}{\sigma_0} \end{pmatrix} \tag{2.44}$$

This shows there is no transverse or longitudinal magnetoresistance. Generally, isotropic metallic systems have a small positive magnetoresistance due to slight distortions of the Fermi surface from a perfect sphere or the presence of more than one band which crosses the Fermi level. In the case of multiband systems the transverse and longitudinal resistivities are given by the inverse of the sum of the individual band conductivities which will not necessarily cancel out the $\omega_c\tau$ terms. The only change from the zero field conductivity tensor is in the ρ_{xy} and ρ_{yx} terms where a field dependent magnetoresistance occurs. This is the Hall effect where the Hall coefficient is defined as:

$$R_H = \frac{\rho_{xy}}{B} = \frac{\omega_c\tau}{\sigma_0 B} = \frac{e\tau}{m^*\sigma_0} = \frac{1}{ne} \tag{2.45}$$

This suggests that the Hall coefficient is negative if the charge carriers are electrons and positive if they are holes.

2.6.3 Barrel Shaped Fermi Surface

Using the dispersion relation for a barrel shaped Fermi surface (equation 2.27) gives the Fermi velocity components in cartesian coordinates as:

$$v_x = \frac{\hbar k_{F\|}}{m^*}\cos\phi \tag{2.46}$$

$$v_y = \frac{\hbar k_{F\|}}{m^*}\sin\phi \tag{2.47}$$

$$v_z = \frac{ct_\perp}{\hbar}\sin\frac{k_z c}{2} \tag{2.48}$$

If the magnetic field is parallel to the axis of the cylinder the resistivity tensor can be shown (see §10.1.4) to be:

$$\rho = \sigma^{-1} = \begin{pmatrix} \frac{\sigma_0}{1+(\omega_c\tau)^2} & -\frac{\sigma_0\omega_c\tau}{1+(\omega_c\tau)^2} & 0 \\ \frac{\sigma_0\omega_c\tau}{1+(\omega_c\tau)^2} & \frac{\sigma_0}{1+(\omega_c\tau)^2} & 0 \\ 0 & 0 & \frac{e^2 ct_\perp m^*\tau}{\pi\hbar^4} \end{pmatrix}^{-1} = \begin{pmatrix} \frac{1}{\sigma_0} & \frac{\omega_c\tau}{\sigma_0} & 0 \\ -\frac{\omega_c\tau}{\sigma_0} & \frac{1}{\sigma_0} & 0 \\ 0 & 0 & \frac{\pi\hbar^4}{e^2 ct_\perp m^*\tau} \end{pmatrix} \tag{2.49}$$

In this case the resistivity tensor is the same as for the spherical case in a magnetic field with the exception of the ρ_{zz} term which is the same as for the barrel shaped Fermi surface when no magnetic field is present. As with the spherical case, this is only valid for single band systems and for a perfectly circular barrel cross section.

If the magnetic field is tilted away from the axis of the cylinder, things change slightly as open orbits are now possible. A more general form of the Shockley-Chambers tube-integral needs to be applied:

$$\sigma_{ij} = \frac{e^2}{4\pi^3}\int d^3k \left(-\frac{\partial f^0_{\mathbf{k}}}{\partial\varepsilon}\right) v_i(k,0)\int_{-\infty}^{0} v_j(k,t)e^{-t/\tau}dt \tag{2.50}$$

where t is time. In the case where the magnetic field is rotated in the x-z plane the resistivity tensor can be shown (see §10.1.4) to be:

$$\rho = \sigma^{-1} = \begin{pmatrix} \sigma_0 & 0 & 0 \\ 0 & \sigma_0 & 0 \\ 0 & 0 & \frac{\sigma^0_{zz}}{\sqrt{1+\left(\frac{eBv_F\tau}{\hbar}\right)^2}} \end{pmatrix}^{-1} = \begin{pmatrix} \frac{1}{\sigma_0} & 0 & 0 \\ 0 & \frac{1}{\sigma_0} & 0 \\ 0 & 0 & \frac{\sqrt{1+\left(\frac{eBv_F\tau}{\hbar}\right)^2}}{\sigma^0_{zz}} \end{pmatrix} \tag{2.51}$$

Expanding this for small B gives $\rho_{zz} \propto B^2$ and for large B gives $\rho_{zz} \propto B$.

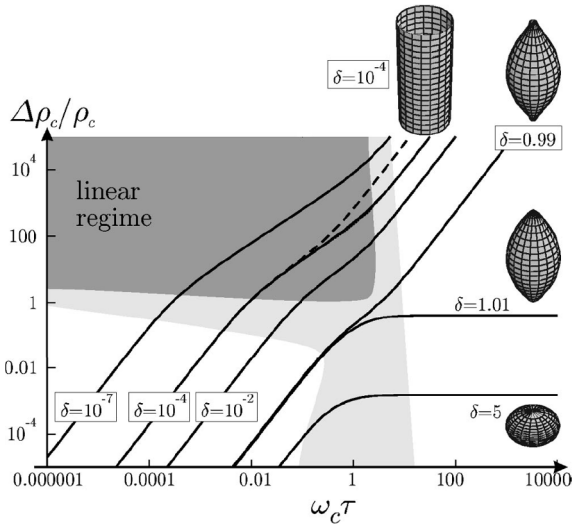

Figure 2.7: Numerical evaluation of the magnetoresistance for arbitrary magnetic fields ($\omega_c\tau$) and Fermi surface anisotropy (δ). Figure from [51].

2.6.4 Magnetoresistance - ρ_c or ρ_{zz}

As shown above for a perfectly isotropic material (i.e. with a spherical Fermi surface) the magnetoresistance is zero. In the case of a highly anisotropic system (such as $Tl_2Ba_2CuO_{6+\delta}$) at low fields ($\omega_c\tau < 1$) the c-axis magnetoresistance is found to vary as B^2. In the high field limit ($\omega_c\tau \gg 1$) the magnetoresistance saturates in the presence of closed orbits or maintains its quadratic dependence if open orbits are present. Schofield and Cooper [51] derive an analytic formula for the c-axis magnetoresistance which is valid for all magnetic fields in the limit of high anisotropy. They generalised this to apply to arbitrary levels of anisotropy allowing the graph in figure 2.7 to be drawn. Referring to the figure, in the case of $\delta = 4t_\perp/\varepsilon_F > 1$ the Fermi surface is closed. For $\delta = 5$ corresponding to an almost spherical Fermi surface there is almost no magnetoresistance — as derived above in equation 2.44. The high field limits discussed earlier can be seen on the right of the figure — saturation for closed orbits ($\delta > 1$) and $\propto B^2$ for open orbits ($\delta < 1$). In the presence of open orbits the low field B^2 variation is observed along with the linear regime at higher fields as shown by equation 2.51.

2.7 Resistivity Tensor for a Quasi-2D System

In the case of $Tl_2Ba_2CuO_{6+\delta}$ the Fermi surface cross section in the x-y plane is not perfectly circular so the cross terms will be non-zero. But the z conductivity is three orders of magnitude smaller than

the x or y so any mixed terms involving a z component can be neglected leaving:

$$\rho = \sigma^{-1} = \begin{pmatrix} \sigma_{xx} & \sigma_{xy} & 0 \\ \sigma_{yx} & \sigma_{yy} & 0 \\ 0 & 0 & \sigma_{zz} \end{pmatrix}^{-1} = \begin{pmatrix} \frac{\sigma_{yy}}{\sigma_{xx}\sigma_{yy}-\sigma_{xy}\sigma_{yx}} & -\frac{\sigma_{xy}}{\sigma_{xx}\sigma_{yy}-\sigma_{xy}\sigma_{yx}} & 0 \\ -\frac{\sigma_{yx}}{\sigma_{xx}\sigma_{yy}-\sigma_{xy}\sigma_{yx}} & \frac{\sigma_{xx}}{\sigma_{xx}\sigma_{yy}-\sigma_{xy}\sigma_{yx}} & 0 \\ 0 & 0 & \frac{1}{\sigma_{zz}} \end{pmatrix} \tag{2.52}$$

Examining the components of interest, firstly the simple case for ADMR gives $\rho_{zz} = 1/\sigma_{zz}$. For the inplane zero field resistivity there is no magnetic field present so the cross terms will be zero or very small compared to σ_{xx} and σ_{yy}:

$$\rho_{xx} = \frac{\sigma_{yy}}{\sigma_{xx}\sigma_{yy} - \sigma_{xy}\sigma_{yx}} = \frac{\sigma_{yy}}{\sigma_{xx}\sigma_{yy}} = \frac{1}{\sigma_{xx}} \tag{2.53}$$

For the case of the inplane Hall effect, the cross terms (σ_{xy} and σ_{yx}) in the denominator can be neglected as they are much smaller than σ_{xx} and σ_{yy} and due to the crystal symmetry $\sigma_{xx} = \sigma_{yy}$ so:

$$\rho_{xy} = -\frac{\sigma_{xy}}{\sigma_{xx}\sigma_{yy} - \sigma_{xy}\sigma_{yx}} = -\frac{\sigma_{xy}}{\sigma_{xx}^2} \tag{2.54}$$

and:

$$R_H = \frac{-\sigma_{xy}}{\sigma_{xx}^2 B} \tag{2.55}$$

2.8 Ong Construction for the Hall Conductivity

In a quasi-2D system Ong [52] showed that the Hall conductivity, σ_{xy} has a simple geometric interpretation: when normalised to e^2/h it is equal to twice the number of flux quanta, ϕ_0, threading the Stokes area, $\mathbf{A_l} = \int \partial\ell \times \ell$, swept out around the Fermi surface by the mean free path length vector, $\ell(\mathbf{k}) = \mathbf{v} \cdot \tau$. Taking the two Fermi surfaces in figure 2.8 as examples where the magnitude of the mean free path, ℓ, varies as shown, it is easy to see the path traced out by the ℓ vector due to the local curvature of the Fermi surface. The different circulations of the primary and secondary loops give rise to contributions to σ_{xy} which sum with different signs. This shows the crucial role of anisotropy in ℓ and therefore also in the velocity and/or the scattering time in determining the Hall conductivity.

2.9 Angular Magnetoresistance Oscillations (AMRO)

Oscillations in the magnetoresistivity periodic in $\tan\theta$ (where θ is defined in figure 2.9) were observed in organic superconductors by Kajita [53]. Yamaji [54] showed that these peaks in the interlayer magnetoresistance could be explained by considering magnetic field induced electron orbits on a corrugated cylindrical Fermi surface. At certain angles of the field the areas of all these orbits are

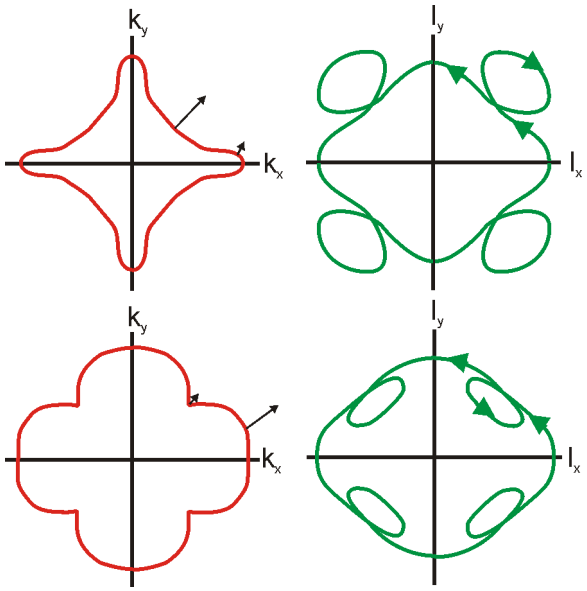

Figure 2.8: Left panel shows two Fermi surface geometries. The arrows indicate the variation of ℓ which is short on the high curvature segments. Right panel shows the corresponding ℓ curves. The arrows show the direction of the circulation. If ℓ has the opposite variation (long on high curvature segments) then the ℓ curves will be interchanged.

the same so the electron energies near the Fermi energy are completely discretised into Landau levels enhancing the low temperature magnetoresistance at this angle.

Assuming a simple band energy of the form:

$$\varepsilon = \frac{\hbar^2(k_x^2 + k_y^2)}{2m} - 2t\cos\left(\frac{ck_z}{2}\right) \tag{2.56}$$

where t is the transfer energy, c is the c-axis lattice parameter and k_z is the component of the wavevector along the axis of the cylinder, so:

$$k_f^2 = k_x^2 + k_y^2 - 4mt\cos\left(\frac{ck_z}{2}\right) \tag{2.57}$$

figure 2.9 shows the geometry of the orbits induced by a magnetic field and that:

$$k_z = k_0 - k_F\tan\theta\cos\phi \tag{2.58}$$

The area, A, of an orbit is given by:

$$A\cos\theta = \int_0^\pi d\theta(k_x^2 + k_y^2) \tag{2.59}$$

$$= \int_0^\pi d\theta k_F^2 + 4mt\cos\left[\frac{c}{2}\left(k_0 - k_F\tan\theta\cos\phi\right)\right] \tag{2.60}$$

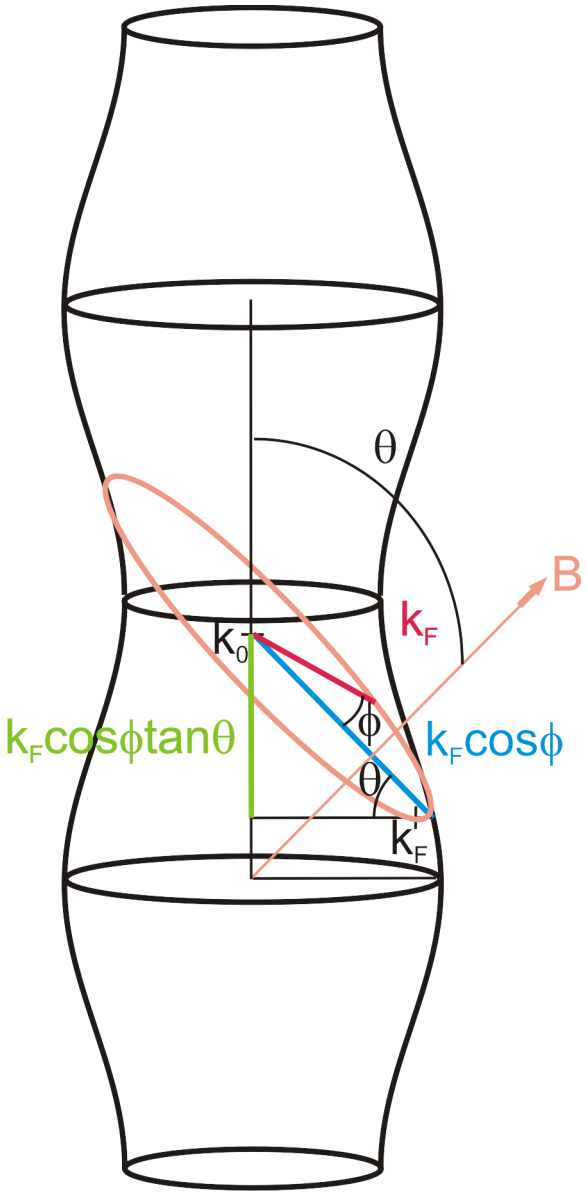

Figure 2.9: Diagram showing the geometry of magnetic field induced orbits on the Fermi surface. θ is defined as the angle from the cylinder axis to the magnetic field. ϕ is the angle between the magnetic field and the CuO bond.

Integrating and using $\cos(A-B) = \cos A \cos B + \sin A \sin B$:

$$A\cos\theta = \pi k_F^2 + 4mt\cos\left(\frac{ck_0}{2}\right)\int_0^\pi \cos\left(\frac{c}{2}k_F\tan\theta\cos\phi\right)d\theta + 4mt\sin\left(\frac{ck_0}{2}\right)\int_0^\pi \sin\left(\frac{c}{2}k_F\tan\theta\cos\phi\right)d\theta \quad (2.61)$$

Noting that $\cos x = 1 - x^2/2! + x^4/4! - ...$ and $\sin x = x - x^3/3! + x^5/5! - ...$ and taking $a = \frac{c}{2}k_F\tan\theta$:

$$\int_0^\pi \cos(a\cos\theta) = \int_0^\pi 1 - \frac{(a\cos\theta)^2}{2!} + \frac{(a\cos\theta)^4}{4!} \quad (2.62)$$

$$= \pi\left(1 - \frac{a^2}{2!} + \frac{a^4}{4!}\right) = \pi J_0(a) \quad (2.63)$$

and:

$$\int_0^\pi \sin(a\cos\theta) = \int_0^\pi a\cos\theta - \frac{(a\cos\theta)^3}{3!} + \frac{(a\cos\theta)^5}{5!} = 0 \quad (2.64)$$

so:

$$A\cos\theta = \pi k_F^2 + 4mt\cos\left(\frac{ck_0}{2}\right)\pi J_0\left(\frac{ck_F\tan\theta}{2}\right) \quad (2.65)$$

where J_0 is the Bessel function which can be approximated as $J_0(a) \approx (2/\pi a)^{1/2}\cos(a - \pi/4)$ for large a (see [55]). The k_0 dependent term in equation 2.65 vanishes periodically with θ for integer n when:

$$\frac{c}{2}k_F\tan\theta = \pi\left(n - \frac{1}{4}\right) \quad (2.66)$$

This means that the area for all the orbits is identical and gives the peaks seen in the magnetoresistance data. Figure 2.10 shows a number of simulations of the Yamaji oscillations in magnetoresistance. On the top left, the magnetoresistance is shown as a function of θ with $\omega_c\tau$ ranging from 4 for the oscillations with the largest amplitude to 0.5 when the oscillations have disappeared, in steps of $\omega_c\tau$ of 0.5. This is shown for a purely barrel shaped Fermi surface (like that shown in figure 2.9) which occupies roughly 12 % of the Brillouin zone. In the top right of figure 2.10 this simulation is reproduced for a Fermi surface which occupies 32 % of the Brillouin zone and in the bottom right it is again reproduced for a Fermi surface occupying 62 % of the Brillouin zone. Notice that the number of oscillations (i.e. the number of times the distribution in the areas of planes perpendicular to the field vanishes) increases as the diameter of the barrel Fermi surface increases. This can be confirmed from the geometry. The magnitude of the magnetoresistance generally increases as both the angle and $\omega_c\tau$ increase due to the increase in the length of the path the electrons travel and therefore their chances of scattering. The small decrease in the maximum amplitude of the oscillations at large angles occurs because of the $\cos\theta$ factor which attenuates $\omega_c\tau$. The bottom right of figure 2.10 shows a magnetoresistance simulation for the parameters that will later be found to be the most appropriate for $Tl_2Ba_2CuO_{6+\delta}$ with $T_c = 15\,\mathrm{K}$ ($\omega_c\tau = 0.45$ and occupying 65 % of the Brillouin zone). Notice the

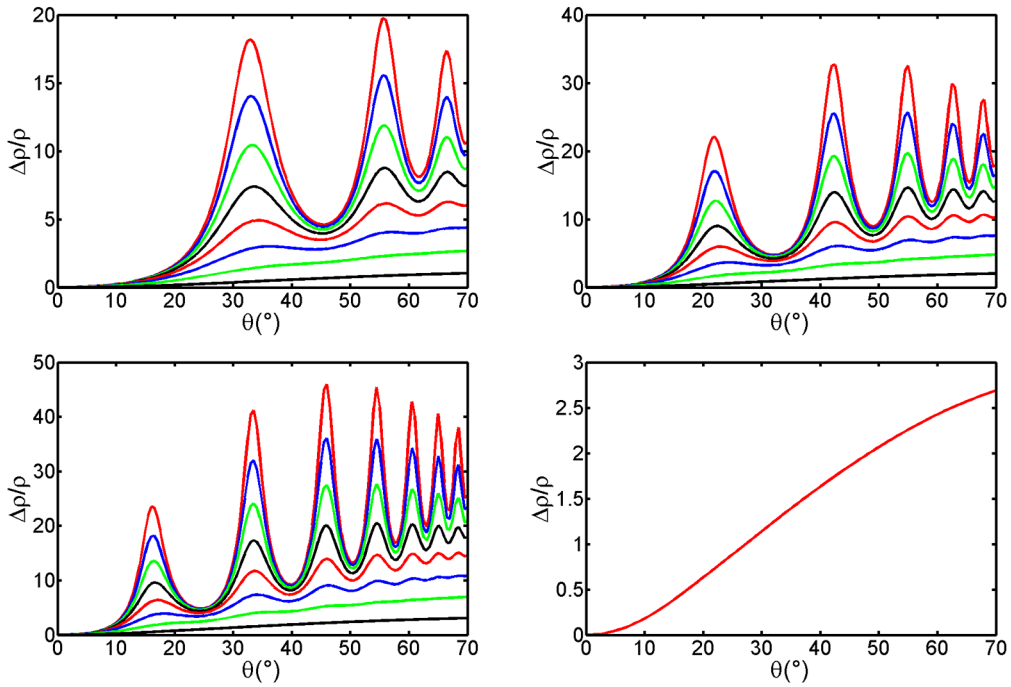

Figure 2.10: Simulations of the Yamaji oscillations in magnetoresistance expected for a quasi-2D barrel shaped Fermi surface. Top left panel shows $\omega_c\tau$ varying from 4 (largest oscillations) to 0.5 in 0.5 steps. Fermi surface occupies 12 % of the Brillouin zone. Top right panel shows the same but with a larger Fermi surface (32 %). Bottom left panel shows the same but with Fermi surface occupying 62 % of the Brillouin zone. Bottom right panel shows a simulation of the magnetoresistance expected for the parameters which best fit $Tl_2Ba_2CuO_{6+\delta}$ for a purely barrel shaped Fermi surface ($\omega_c\tau = 0.45$ and occupying 65 % of the Brillouin zone). Simulated using code in §10.7.1.

Yamaji oscillations in the magnetoresistance, from considering only a barrel shaped Fermi surface, have completely disappeared leaving only a monotonic dependence on angle.

2.10 Quantum Oscillations

In 1930 de Haas and van Alphen measured the magnetisation (M) of bismuth as a function of magnetic field (B) and observed oscillations in M/B which were periodic in 1/B — the dHvA effect [56]. A similar oscillatory effect (SdH) was observed in the resistivity measured as a function of magnetic field by Shubnikov and de Haas. Onsager later showed that the frequency of these oscillations is directly related to the extremal area of the Fermi surface in the plane perpendicular to the magnetic field. This allows the topology of a Fermi surface to be explored in great detail by varying the orientation of the magnetic field with respect to the sample:

$$F = \frac{\hbar}{2\pi e} A \tag{2.67}$$

where F is the frequency in T, $e = 1.6 \times 10^{-19}$ C and A is the extremal area of the orbit in **k**-space in m^{-2}. Equation 1.1 with $T_{c,\max} \approx 93$ K [57] and equation 3.8 suggests for overdoped $Tl_2Ba_2CuO_{6+\delta}$ with $T_c = 10$ K that F = 17.6 kT which decreases to 17.4 kT for $T_c = 25$ K.

In the presence of a magnetic field the electrons can be thought of as quantised onto Landau levels (or cylinders) in **k**-space. As the magnetic field increases the electrons are drawn up to the Fermi level so their energy increases. When the Landau level passes through the Fermi level it empties and the electrons' energies drop. These oscillations in the electron energy cause oscillations in the (density of states dependent) physical properties of a material. These effects are only visible in materials that are clean enough, at high magnetic fields (which avoids the quantisation of electron orbits being blurred by collisions) and at low temperatures (which avoids oscillations in the electron population being thermally averaged out). A detailed derivation and explanation of these effects can be found in books by Ziman [58] or Shoenberg [59].

At finite temperature the probability of an electron occupying a state is given by the Fermi-Dirac distribution function. An actual metal at finite temperature (with Fermi energy ε) can be thought of as equivalent to a distribution of hypothetical metals all at $T = 0$ K with a range of Fermi energies spread around ε. Since the dHvA frequency is a function of ε, a spread of (hypothetical) Fermi energies is equivalent to a phase smearing. This has the effect of multiplying the amplitude of the oscillations by a (temperature) reduction factor, R_T:

$$R_T = \frac{X}{\sinh X} \tag{2.68}$$

where $X = (2\pi^2 k_B/\hbar e)(m^* T/B)$ and m^* is the quasi-particle effective mass.

If the electrons have a finite relaxation time due to scattering the otherwise sharp quantum levels become broadened. This broadening can be described by a Lorentzian distribution function and causes a spread of Fermi energies around ε. Again this leads to a phase smearing and a further amplitude reduction factor — often called the Dingle factor [60], R_D:

$$R_D = e^{(-\pi/\omega_c \tau)} = e^{[-(\pi \hbar k_F)/(eB\ell)]} \tag{2.69}$$

where ℓ is the appropriately orbitally averaged quasiparticle mean free path, τ refers only to impurity scattering and k_F is the average Fermi wavevector.

The Lifshitz-Kosevich formula (see [59]) incorporates these reduction factors and may be applied to calculate a value for the effective mass, m^*, of the quasiparticles:

$$\frac{\Delta\rho}{\rho_0} = C B^{\frac{1}{2}} R_T R_D \sin\left(\frac{2\pi F}{B} + \phi\right) \tag{2.70}$$

where C is a constant, B is the magnetic field strength and F is the SdH frequency.

Chapter 3

$Tl_2Ba_2Ca_0Cu_1O_{6+\delta}$

$Tl_2Ba_2CuO_{6+\delta}$ is one of a series of hole doped cuprate high temperature superconductors. It has a T_c which can be varied between 93 K and non-superconducting and a much higher $T_{c,\max}$ than other common single CuO_2 layer cuprates such as $La_{2-x}Sr_xCuO_4$ [61] and $Bi_2Sr_2CuO_{6+x}$ [62] where $T_{c,\max} \approx 40$ K. However, its $T_{c,\max}$ is the same as that of $YBa_2Cu_3O_7$ and lower than for other multilayer thallium [63] or mercury based compounds [4]. $Tl_2Ba_2CuO_{6+\delta}$, unlike $YBa_2Cu_3O_7$ or $HgBa_2CuO_{4+x}$, can be formulated across the whole overdoped side of the phase diagram giving access to compositions which aren't complicated by antiferromagnetic, spin, charge or superconducting fluctuations. Neither does it suffer from the disorder introduced by the strontium ions that occurs in $La_{2-x}Sr_xCuO_4$. The superconducting gap in $Tl_2Ba_2CuO_{6+\delta}$ is found to have $d_{x^2-y^2}$ symmetry, in agreement with other cuprates [64]. Additionally, an inelastic neutron scattering magnetic resonance peak, previously only seen in multilayer cuprates, was observed for the first time in a single layer cuprate in $Tl_2Ba_2CuO_{6+\delta}$ [65]. This has restricted the range of theoretical models for the origin of the resonant mode and its role in the mechanism of high temperature superconductivity.

The rest of this chapter provides an introduction to the structure, transport properties and Fermi surface of $Tl_2Ba_2CuO_{6+\delta}$.

3.1 Structure of Tl2201

$Tl_2Ba_2CuO_{6+\delta}$ is a member of a series of layered compounds $Tl_mBa_2Ca_{n-1}Cu_nO_{2(n+1)+m}$ where m=2 and n=1 and is often shorted to $Tlm2(n-1)n$ or Tl2201. It has been reported to have either a tetragonal and orthorhombic structure [67]. As an introduction, consider the body centred tetragonal phase with lattice parameters $a = b = 3.8608$ Å and $c = 23.1332$ Å and I4/mmm (139) space group as determined by Liu *et al.* [57] using electron probe microanalysis (EPMA) and X-ray diffraction — see table 3.1. They show that the Tl and O(3) atoms are not in a symmetric position in the unit cell and also that the occupancy of the Tl site is $0.233 \times 4 = 0.932$, and not 1, which was attributed to

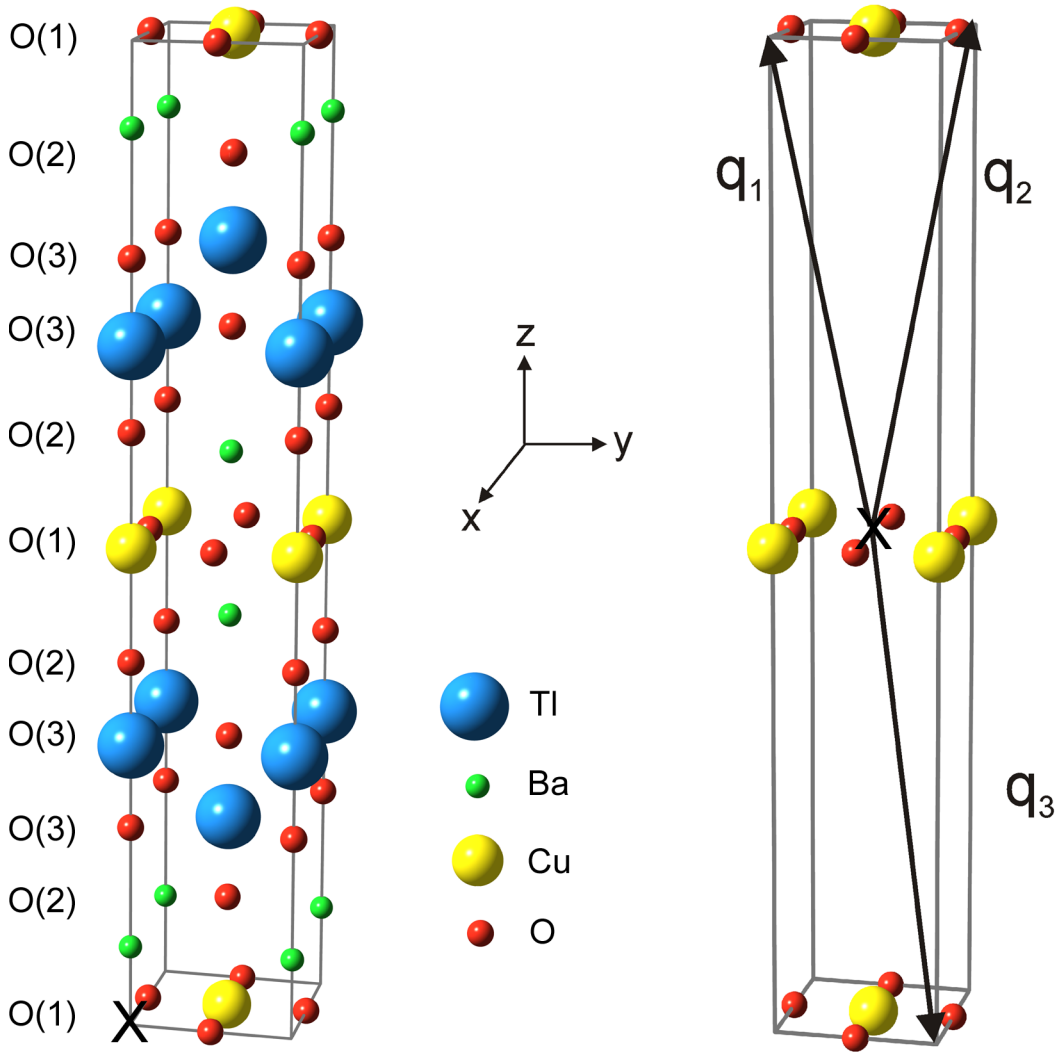

Figure 3.1: Left panel shows one unit cell of $Tl_2Ba_2CuO_{6+\delta}$ showing the crystal structure, height is c and planar square is $a \times a$. Oxygen labels refer to their origin in table 3.1. Right panel shows a unit cell with only Cu and O atoms present (others removed for clarity) showing real space primitive lattice translation vectors. Drawn using [66].

Site	Occupancy	x	y	z	Sym-x	Sym-Occupancy
Tl	0.233	0.5406	0.5	0.20304	0.5	1
Ba	1	0	0	0.08426	0	1
Cu	1	0.5	0.5	0	0.5	1
O(1)	1	0	0.5	0	0	1
O(2)	1	0.5	0.5	0.1168	0.5	1
O(3)	0.25	0.401	0.5	0.289	0.5	1

Table 3.1: Position and occupancy of atoms in the $Tl_2Ba_2CuO_{6+\delta}$ unit cell [57].

copper substitution onto Tl sites giving $Tl_{1.86}Ba_2Cu_{1.14}O_{6+\delta}$. Figure 3.1 shows the crystal structure with the x position of the Tl and O(3) atoms symmetrised and the occupancy altered as shown in the last two columns of table 3.1 and the additional δ oxygen set to zero. The extra δ oxygen atoms are situated on interstitial (O(4)) sites between the two TlO layers [68].

The size of the orthorhombic distortion, c-axis lattice parameter and the Cu/Tl substitution as well as the excess δ oxygen all show a correlation with T_c [67]. The orthorhombic distortion of the lattice yields slightly different a and b lattice parameters and depends on the Cu/Tl and δ oxygen substitution. The size of this distortion is indicated by an orthorhombicity parameter $2(b-a)/(b+a)$ which decreases as T_c increases although its magnitude is very sample dependent. A maximum of 0.01 is reported, giving a very small difference between a and b of $<1\,\%$. Greater Cu substitution onto Tl sites suggests a more tetragonal structure [69] and therefore a higher T_c. Below $T_c = 60\,\mathrm{K}$ as T_c decreases the c axis lattice parameter is found to decrease but this reverses for $T_c > 60\,\mathrm{K}$. For a given sample with a set Cu:Tl ratio, the T_c dependence comes from an increase in δ of around 0.1 which is enough to change the T_c across the whole range from 93 K to 0 K. With the application of hydrostatic pressure up to 6 kbar at room temperature the T_c is broadened and depressed [70]. The location of the O(4) away from the CuO_2 plane suggests that there is very little disorder within the plane and this is backed up by the very low residual in-plane resistivity of $< 10\,\mu\Omega$cm [19] meaning that $Tl_2Ba_2CuO_{6+\delta}$ is one of the cleanest and least disordered cuprates.

3.1.1 Reciprocal Lattice & Brillouin Zone

Adopting the body-centred tetragonal structure the real space primitive lattice translation vectors can be taken with reference to figure 3.1 as:

$$\mathbf{q_1} = \frac{a}{2}\hat{\mathbf{x}} - \frac{a}{2}\hat{\mathbf{y}} + \frac{c}{2}\hat{\mathbf{z}} \tag{3.1}$$

$$\mathbf{q_2} = -\frac{a}{2}\hat{\mathbf{x}} + \frac{a}{2}\hat{\mathbf{y}} + \frac{c}{2}\hat{\mathbf{z}} \tag{3.2}$$

$$\mathbf{q_3} = \frac{a}{2}\hat{\mathbf{x}} + \frac{a}{2}\hat{\mathbf{y}} - \frac{c}{2}\hat{\mathbf{z}} \tag{3.3}$$

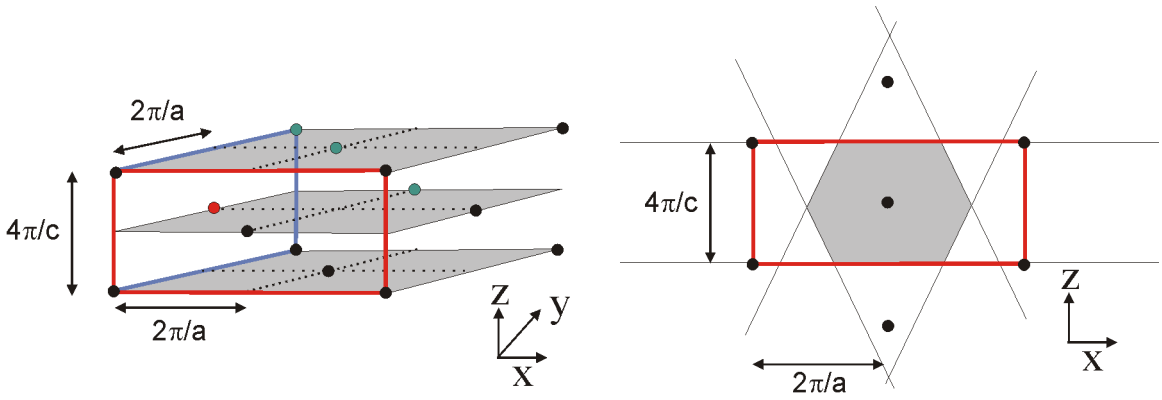

Figure 3.2: Left panel shows selected reciprocal lattice points for the body-centred tetragonal phase of $Tl_2Ba_2CuO_{6+\delta}$. Taking the red point as the origin, the green points are given directly by the reciprocal lattice vectors. Right panel shows a z-x reciprocal space slice with perpendicular bisectors and the first Brillouin zone shaded in grey.

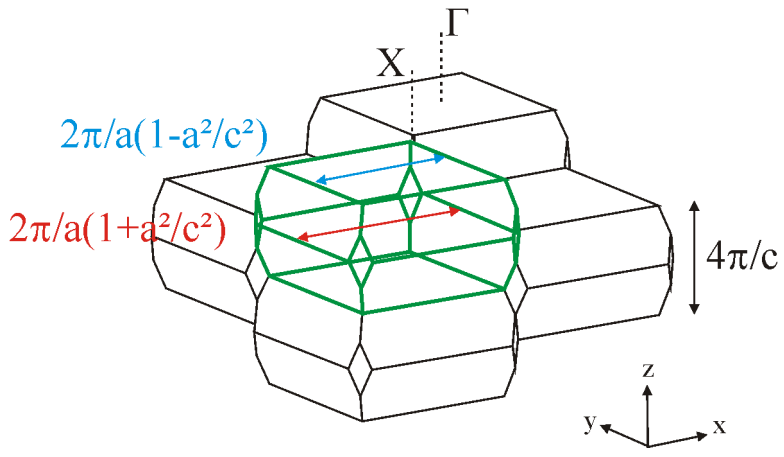

Figure 3.3: The $Tl_2Ba_2CuO_{6+\delta}$ Brillouin zone shown in green. The minimum and maximum x-y plane dimensions due to the facets are shown in blue and red. Also shown is the stacking arrangement of the Brillouin zones.

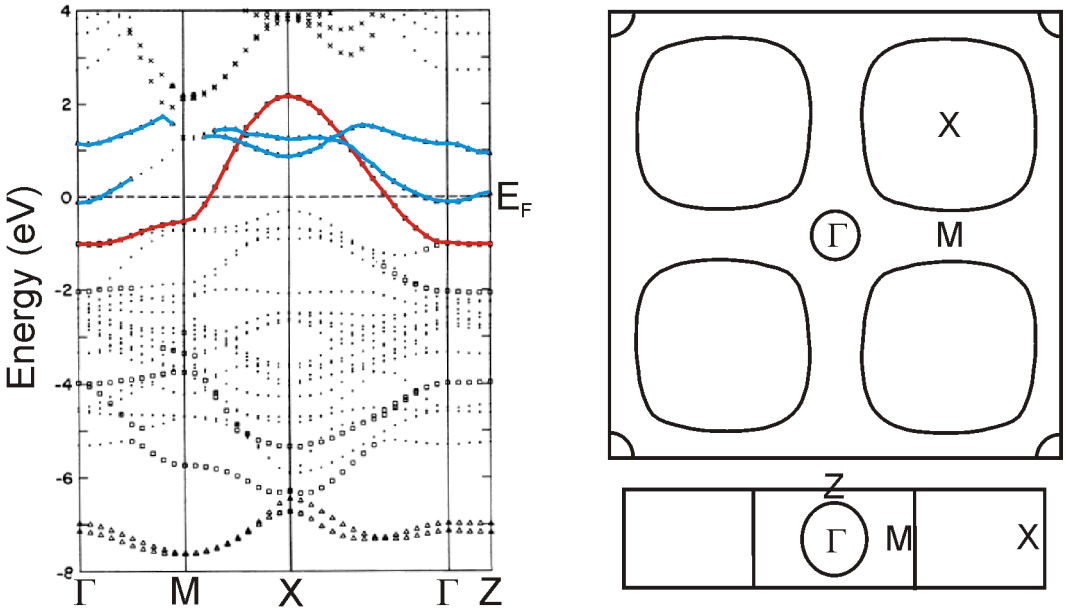

Figure 3.4: Left panel shows the bandstructure of $Tl_2Ba_2CuO_{6+\delta}$ along symmetry lines of the Brillouin zone. Figure from [71]. Right panel shows the Fermi surface cross section in the basal plane showing the X-centred barrel and the Γ centred spheroid. Bottom right panel shows the (110) plane cross section showing the flatness of the barrel and the spheroid. Figure from [72].

and the reciprocal lattice vectors are now defined as:

$$\mathbf{q_1}^* = 2\pi \frac{\mathbf{q_2} \times \mathbf{q_3}}{\mathbf{q_1} \cdot \mathbf{q_2} \times \mathbf{q_3}} = \frac{2\pi}{a}\hat{\mathbf{x}} + \frac{2\pi}{c}\hat{\mathbf{z}} \tag{3.4}$$

$$\mathbf{q_2}^* = 2\pi \frac{\mathbf{q_3} \times \mathbf{q_1}}{\mathbf{q_1} \cdot \mathbf{q_2} \times \mathbf{q_3}} = \frac{2\pi}{a}\hat{\mathbf{y}} + \frac{2\pi}{c}\hat{\mathbf{z}} \tag{3.5}$$

$$\mathbf{q_3}^* = 2\pi \frac{\mathbf{q_1} \times \mathbf{q_2}}{\mathbf{q_1} \cdot \mathbf{q_2} \times \mathbf{q_3}} = \frac{2\pi}{a}\hat{\mathbf{x}} + \frac{2\pi}{a}\hat{\mathbf{y}} \tag{3.6}$$

Selected reciprocal lattice points are plotted on the left in figure 3.2. A two dimensional (z-x) slice of reciprocal space is plotted on the right in figure 3.2 along with perpendicular bisectors of lines joining a reciprocal lattice point to its nearest and next nearest neighbouring points. The area enclosed is defined as the first Brillouin zone. Slices taken in the z-y plane and a similar plane 45° to the x axis reveal the 3D shape of the first Brillouin zone and the stacking arrangement to be that shown in figure 3.3. The z dimension of the zone is $4\pi/c$ but the x and y dimensions are between a maximum of $\frac{2\pi}{a}\left(1+\frac{a^2}{c^2}\right)$ and a minimum of $\frac{2\pi}{a}\left(1-\frac{a^2}{c^2}\right)$ which are different from the average value of $\frac{2\pi}{a}$ by 2.8 %.

3.2 Bandstructure and Fermi Surface

Using a symmetrised version of the atomic positions similar to those in table 3.1 the bandstructure and Fermi surface were calculated by Hamann [71] and Singh [72] and are shown in figure 3.4 where $\Gamma = (0,0,0)$, X$= (\pi/a, \pi/a, 0)$, M$= (\pi/a, 0, 0)$ and Z$= (0, 0, 2\pi/c)$. The bandstructure shows two bands which cross the Fermi level. The red band, which has $\mathrm{Cu}(3d_{x^2-y^2}) - \mathrm{O}(1)(p_{x,y})$ character, is highly two-dimensional with very little dispersion in the c-axis direction (see $\Gamma-$Z section) and gives the hole-like barrel shaped part of the Fermi surface. The blue band has $\mathrm{Tl} - \mathrm{O}(3), \mathrm{O}(2p_z), \mathrm{Cu}(3d_{z^2})$ character and crosses the Fermi level near Γ giving the electron-like spheroidal Fermi surface pocket. At the M point there is a saddle point — i.e. in one direction the energy band goes up and in the orthogonal direction the energy band goes down. The extremely high resistive anisotropy (see figure 3.9) is not consistent with the presence of this spheroidal pocket. More recent work on the Fermi surface was performed using the ADMR technique described in this work by the Bristol group which confirmed the existence of a barrel shaped Fermi surface centred at the X point but found no evidence for the Γ centred spheroidal pocket [26]. Further confirmation of this later came from angle-resolved-photoemission spectroscopy (ARPES) work [25] where a large X-centred Fermi surface pocket was observed with an approximately circular cross-section. No evidence of the TlO pocket was found in the ARPES work despite a detailed search. The ARPES derived Fermi surface is shown in figure 3.5 along with a red line showing a tight binding model fit [25]:

$$\varepsilon_k = \mu + \frac{t_1}{2}(\cos k_x + \cos k_y) + t_2 \cos k_x \cos k_y + \frac{t_3}{2}(\cos 2k_x + \cos 2k_y) + \frac{t_4}{2}(\cos 2k_x \cos k_y + \cos k_x \cos 2k_y) + t_5 \cos 2k_x \cos 2k_y \quad (3.7)$$

where the lattice constant a has been set to 1 and $\mu = 0.2438$, $t_1 = -0.725$, $t_2 = 0.302$, $t_3 = 0.0159$, $t_4 = -0.0805$ and $t_5 = 0.0034$.

The TlO pocket has also remained elusive in ADMR and dHvA/SdH (§7) work done by the present author and the Bristol group. It was noted by the author that these bandstructure calculations were performed on the undoped structure i.e. $Tl_2Ba_2Cu_1O_6$ rather than $Tl_2Ba_2CuO_{6+\delta}$ and the effect of including the doping might alter the bandstructure and Fermi surface by shifting some of the bands. Band structure calculations were therefore performed using *Wien2K* and doping was simulated using the virtual crystal approximation (§5.6) and shown in figures 3.6 and 3.7. Similar calculations were also performed separately by Sahrakorpi [28]. When $\delta = 0$, the X hole pocket is present along with the electron pocket at Γ which is consistent with earlier bandstructure calculations (see figure 3.4). When the virtual crystal approximation (VCA) is used to simulate $\delta = 0.02$ the band which causes the electron pocket at Γ rises in energy slightly. This rise is more visible in the $\delta = 0.04$ graph, and for $\delta = 0.06$ it has risen significantly to a position above the Fermi level, but the band responsible for the X hole pocket remains in nearly the same place with only a very slight rise. By using *Wien2K* and

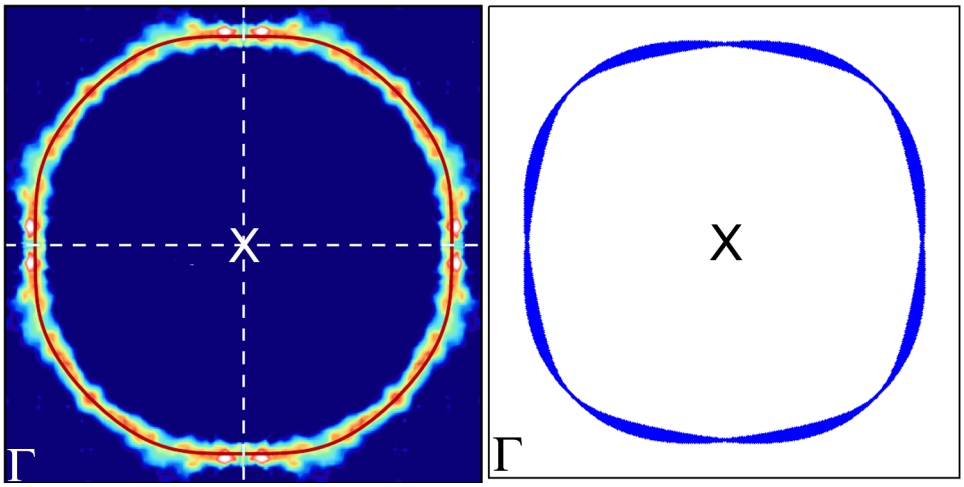

Figure 3.5: Left panel shows an ARPES derived Fermi surface with tight binding fit in red. Figure from [25]. Right panel shows LCAO Fermi surface described by Mishonov [73].

xcrysden to calculate the area of the Fermi surface a doping of δ extra oxygen atoms can be related to a doping of p holes using a simple hole counting procedure as no direct algebraic relationship exists between p and δ:

$$A = \frac{1+p}{2}\left(\frac{2\pi}{a}\right)^2 \tag{3.8}$$

where A is the area of the cylindrical Fermi surface and a is the in-plane lattice dimension. The area can be calculated from the *Wien2K* output using *Matlab* [74]. For $\delta = 0.09$ this suggests $p \approx 0.18$. Further doping of $\delta = 0.11$ suggests $p \approx 0.22$ and $\delta = 0.12$ suggests $p \approx 0.24$. As doping increases, the band responsible for the pocket at Γ continues to rise in energy and band responsible for the hole cylinder only moves up slightly which is consistent with the addition of holes. For $\delta = 0.13$, $p \approx 0.26$ and $\delta = 0.15$ corresponds to $p \approx 0.30$. A simple *Matlab* program can be written to plot the bandstructure from the *Wien2K* output — see §10.7.2.

Using *Wien2K* the Fermi surface can be calculated. For a simulated doping of $\delta = 0.12$ this is shown in figure 3.8. In the 2D projection a small eight fold broadening can be seen in the *Wien2K* Fermi surface, corresponding to positions of zero interplane dispersion. This corresponds with what was seen as a result of analysis of ADMR data [26].

It should also be noted that any Tl^{3+} and Cu^{2+} non-stoichiometry will also have an effect on the number of holes in the system. $Tl_{1.86}Ba_2Cu_{1.14}O_{6+\delta}$ contributes 0.14 extra holes per formula unit which is sufficient to empty the TlO band [25]. With bandstructure calculations in mind, it is possible that if Tl2201 was made stoichometric and with no excess oxygen, then the TlO band would be partially occupied giving an electron pocket in the Fermi surface.

A further method of modelling the Fermi surface was given by Mishonov [73] using the LCAO (Linear Combination of Atomic Orbitals) approximation over the Cu3$d_{x^2-y^2}$, Cu4s, O2p_x and O2p_y

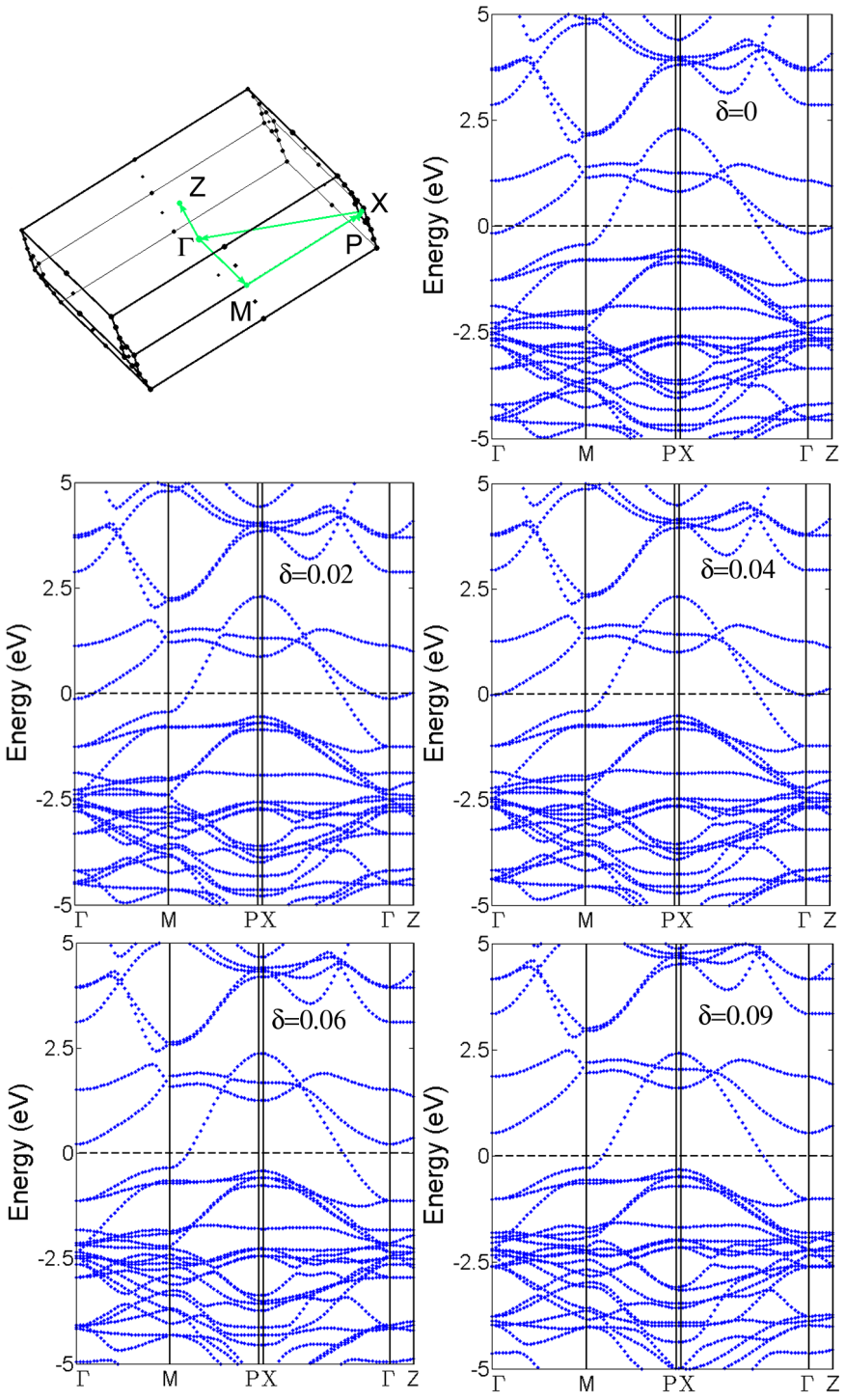

Figure 3.6: Diagram of the **k**-path through the Brillouin zone and *Wien2K* calculations of the $Tl_2Ba_2CuO_{6+\delta}$ bandstructure with δ as shown.

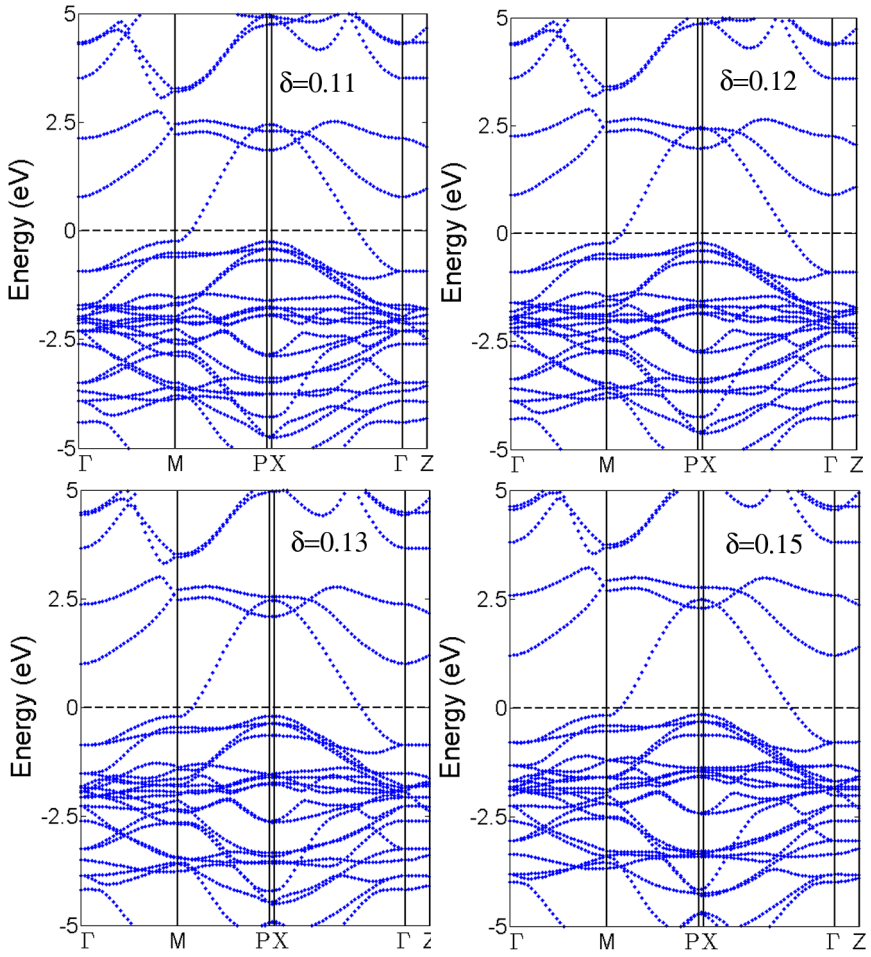

Figure 3.7: *Wien2K* calculations of the $Tl_2Ba_2CuO_{6+\delta}$ bandstructure with δ as shown.

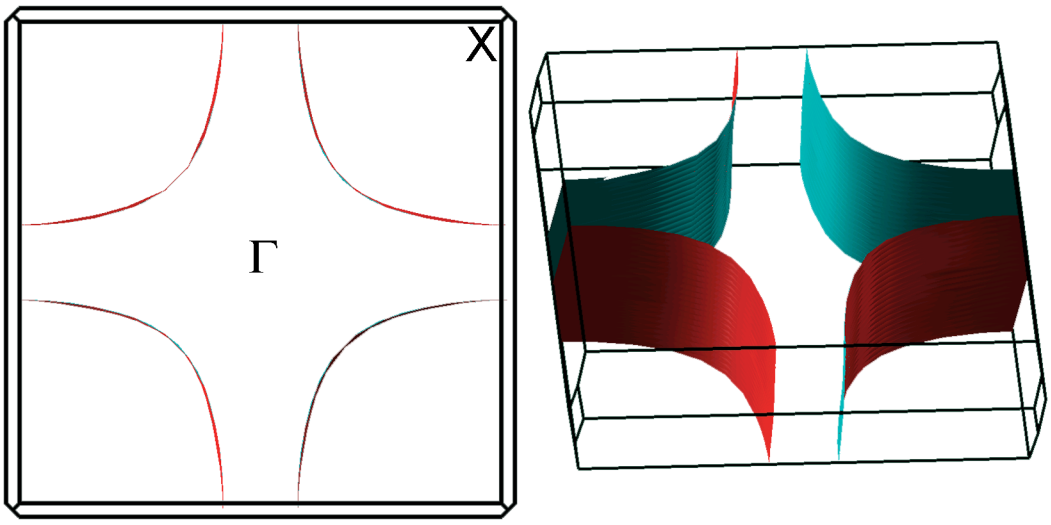

Figure 3.8: *Wien2K* calculated Fermi surface for a doping of $\delta = 0.12$ corresponding to $p \approx 0.24$. Left panel shows a 2D projection. Right panel shows the 3D Fermi surface.

Sample	T_c	δ	n
A	81	0.01	0.95
B	62	0.03	1.26
C	47	0.05	1.49
D	16	0.08	1.67
E	0	0.10	1.88

Table 3.2: Samples, T_c, δ and n for the samples in figures 3.9 and 3.10.

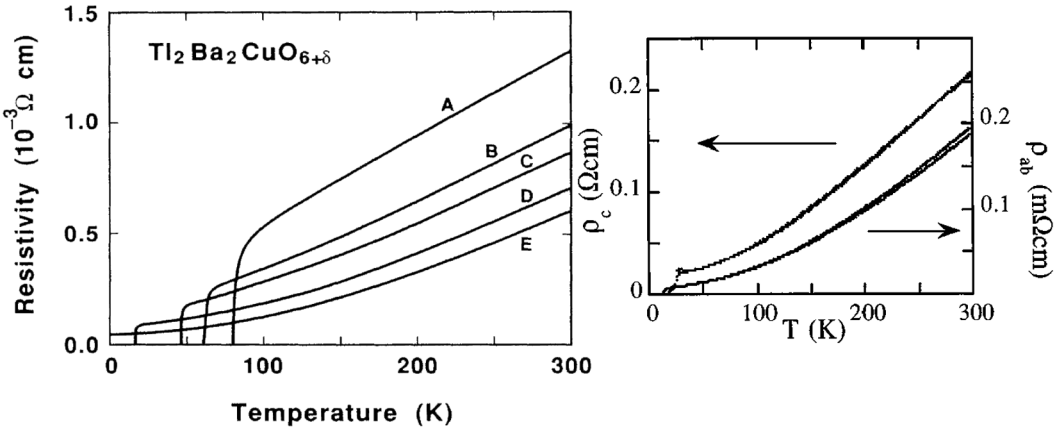

Figure 3.9: Left panel shows the temperature dependence of the in-plane resistivity. Figure from [76]. Right panel shows the zero field ρ_c and ρ_{ab} showing factor of ~ 1000 anisotropy at 300 K. Figure from [77].

orbitals. This is shown in figure 3.5 which is drawn using the code in §10.7.3. This also shows the broadening in the projection indicating a k_z dependent change in size of the Fermi surface.

3.3 Transport Properties

3.3.1 Zero Field Resistivity

The in-plane zero field resistivity measurements of samples with a high T_c shows that the resistivity is approximately linear with temperature. As the T_c decreases (doping increases) the resistivity gradually becomes more T^2. This form is consistent with other cuprate superconductors. The left of figure 3.9 shows the resistivity of a single polycrystalline sample that was repeatedly annealed to achieve different transition temperatures. In an attempt to analyse this data Kubo *el al.* fitted it to the form $\rho = \rho_0 + AT^n$. The values for n (see table 3.2) vary from approximately 1 to 2 with overdoping. They also estimated the δ value for each sample which is shown in table 3.2 from the approximately linear relationship obtained in reference [75]. In other work the temperature dependence of the resistivity has also been fitted to the form $\rho = \rho_0 + AT + BT^2$.

Hussey *et al.* [77] compared the c-axis resistivity (ρ_c) to the in-plane resistivity (ρ_{ab}) and showed

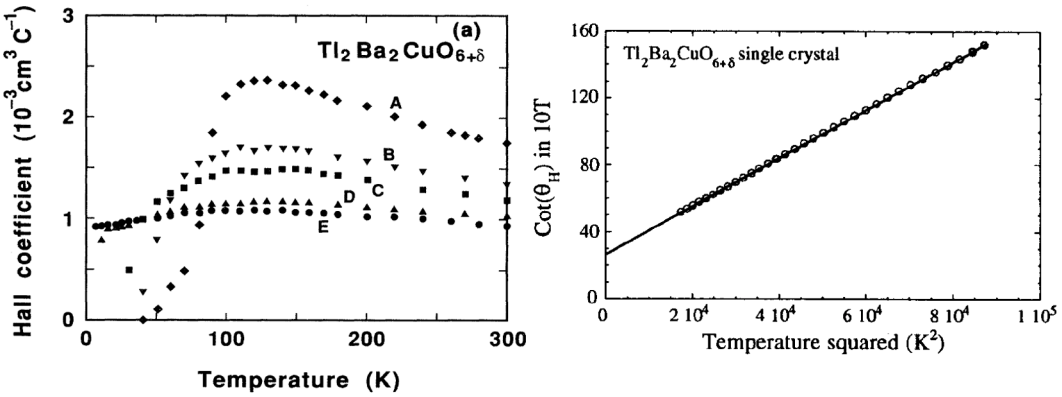

Figure 3.10: Left panel shows the Hall coefficient R_H for the samples in table 3.2. Figure from [76]. Right panel shows the cotangent of the Hall angle for a sample with $T_c = 80\,\mathrm{K}$ circles, solid line is a linear 'guide to the eye'. Figure from [78].

the anisotropy ratio ρ_c/ρ_{ab} rises from 1000 at 300 K to 2500 at 30 K — see figure 3.9 right.

3.3.2 Hall Effect

The Hall coefficient changes in a non-systematic way with temperature which is not consistent with a real change in carrier concentration as the number of carriers would be required to increase with decreasing temperature below 30 K. The magnitude and doping dependence is broadly consistent with similar overdoped cuprates like LSCO — see figure 1.4. Alternatively the cotangent of the hall angle $\cot\Theta_H = \rho_{ab}/R_H B$ can be plotted against T^2 (see figure 3.10) giving a linear relationship that is only very weakly doping dependent.

A model by Anderson suggested at optimal doping this arises due to a separation of scattering lifetimes as the resistivity ($\propto T$) reflects the temperature dependence of $1/\tau_{\mathrm{tr}}$ and $\cot\Theta_H$ ($\propto T^2$) is sensitive to $1/\tau_H$ whereas R_H is dependent on $\tau_H/\tau_{\mathrm{tr}}$. This apparent lifetime separation is dramatically illustrated by figures 3.9 and 3.10.

An alternative model for fitting ρ_{ab} and $\cot\Theta_H$ is suggested by Hussey [36] where a single scattering rate is applied which has a strong doping dependent in-plane anisotropy. Furthermore, a maximum scattering rate is assumed corresponding to the Mott-Ioffe-Regel criterion which states that the quasiparticle mean free path can't become smaller than the lattice spacing. These scattering rates are added in a parallel resistor form. This model successfully fits both the resistivity and cotangent of the Hall angle across a range of doping.

3.3.3 Magnetoresistance

Magnetoresistance measurements above T_c when $I \parallel c$ and $B \parallel ab$ show that the magnetoresistance is large and positive and varies as $\rho = \rho_0 + \rho_2 B^2 - \rho_4 B^4$ [77] where the B^4 term is associated with the

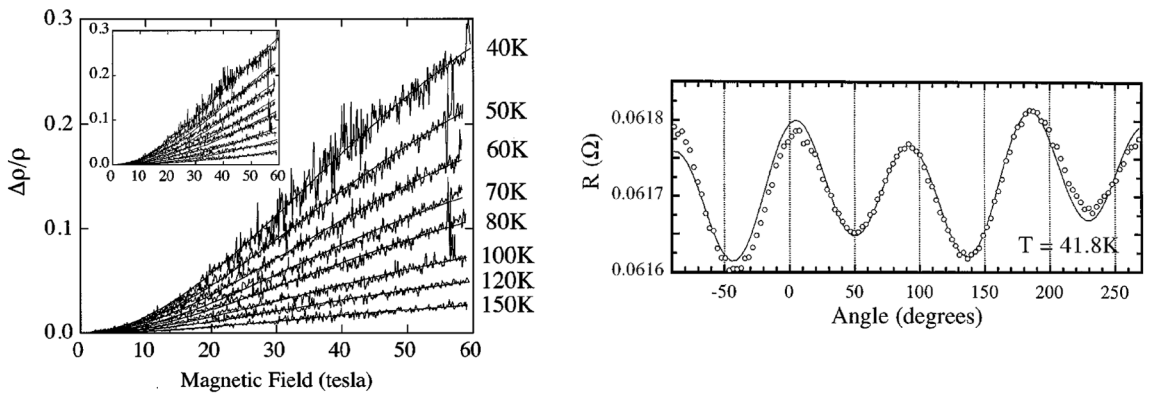

Figure 3.11: Left panel shows the c axis magnetoresistance of $Tl_2Ba_2CuO_{6+\delta}$, showing a large positive effect and non-saturating behabiour up to 60 T. Figure from [79]. Right panel shows the angle dependence of c-axis magnetoresistance for $I \parallel c$ and B rotated in-plane on a crystal with $T_c = 25$ K taken at 42 K. Figure from [77].

crossover from B^2 at low temperatures to non-saturating behaviour in the high-field limit. The left of figure 3.11 shows magnetoresistance data up to 60 T taken from reference [79].

In Boltzmann transport theory the transverse magnetoresistance $\Delta\rho/\rho \propto (\omega_c\tau)^2$. Assuming the only effect of a change of temperature or purity of the material is to alter τ by a constant factor then $\Delta\rho/\rho$ is unchanged if B is reduced by the same factor. This means that the product $\Delta\rho \times \rho$ is independent of τ and a plot of $\Delta\rho/\rho$ versus $(B/\rho)^2$ is expected to fall on a straight line with a slope independent of temperature; this is known as Kohler's rule. In common with other cuprates such as $YBa_2Cu_3O_{7-x}$ and $La_{2-x}Sr_xCuO_4$ Kohler's rule is violated in $Tl_2Ba_2CuO_{6+\delta}$ [79], [80]. This is an indicator of a non-conventional temperature or magnetic field dependence of the scatting rate.

Hussey [77] showed that rotating the field within the ab plane with $I \parallel c$ gave a strongly angle dependent resistivity which is periodic every 90° and gradually decreases in magnitude as the temperature is increased — see the right of figure 3.11. Further work when the magnetic field was rotated from $B \parallel c$ to $B \parallel ab$ produced the first ADMR data on $Tl_2Ba_2CuO_{6+\delta}$ [26] — see figure 3.13. This data was accurately simulated by assuming an intricate 3D warping of the Fermi surface (see reference [26] and described in detail in chapter 5), as shown in figure 3.12 and provided the first direct evidence of a Fermi surface in a high temperature superconductor.

3.3.3.1 Upper Critical Field H_{c2}

The upper critical field in $Tl_2Ba_2CuO_{6+\delta}$ is lower than in many other cuprates meaning that superconductivity can be suppressed using an experimentally achievable magnetic field. Mackenzie [82] showed that as the temperature drops a larger magnetic field is required to suppress superconductivity and that the transition broadens — see figure 3.13. H_{c2} is also found to be anisotropic: for $H \parallel c$ it is a minimum and for $H \perp c$ it is a maximum. Furthermore, H_{c2} is doping dependent. Samples

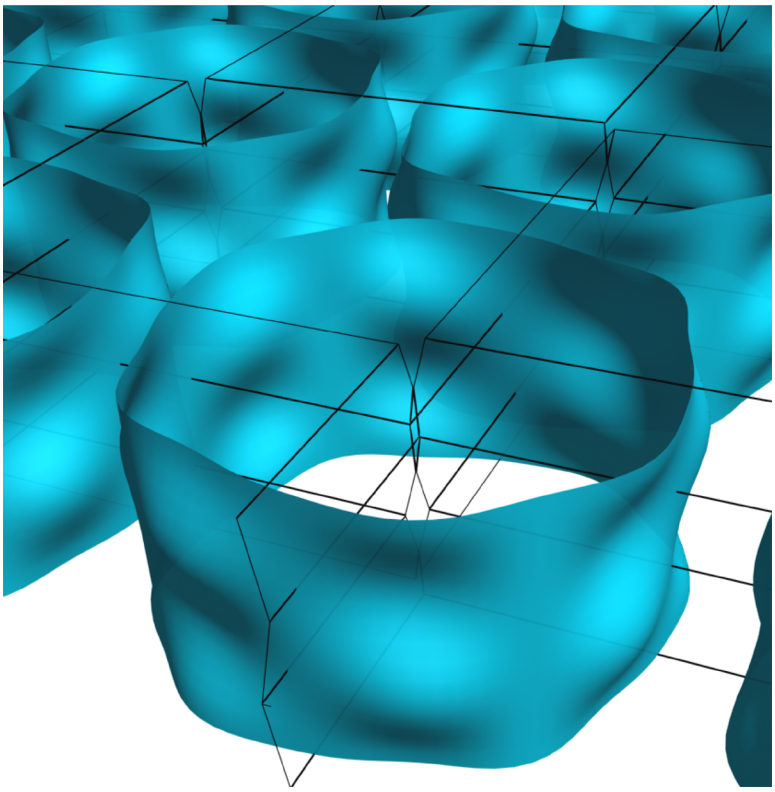

Figure 3.12: Fermi surface of $Tl_2Ba_2CuO_{6+\delta}$ implied by fit to ADMR data. Shown in repeated zone scheme. Figure from [81].

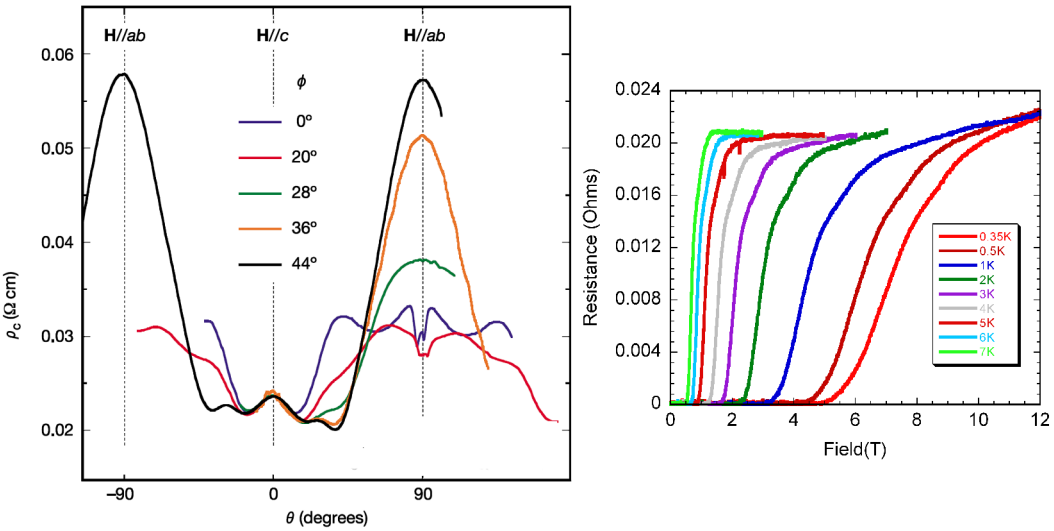

Figure 3.13: Left panel shows ADMR data on $Tl_2Ba_2CuO_{6+\delta}$. θ is angle of field with respect to c-axis and ϕ is angle of field with respect to CuO bond. Taken at 4.2 K and $B = 45$ T on a crystal with $T_c = 20$ K. Figure from [26]. Right panel shows the broadening and shift of superconducting transition to higher field as temperature is lowered for a $T_c = 10$ K sample.

with a higher T_c require a larger field to suppress superconductivity.

Chapter 4

Experimental Techniques

4.1 $Tl_2Ba_2CuO_{6+\delta}$ Samples

4.1.1 Origin and Growth

The samples used in this work were grown by André Tyler working with Andy Mackenzie (formerly at Cambridge, now at St. Andrews) and Walter Hardy (University of British Columbia, Canada). Their growth is described in detail in [83], but for convenience is summarised here. $Tl_2Ba_2CuO_{6+\delta}$ can be grown using a special flux where crystallisation is promoted by additives, e.g. KCl [84], but has the disadvantage of potential inclusion of flux impurities in the crystals. An alternative method which doesn't suffer the impurity problem is a self-flux method where the starting composition is different from that of the crystal being grown; it is rich in one or more of the component elements. It should be noted that thallium and its oxides are poisonous materials and special safety precautions must be taken. Tl_2O_3, BaO_2 and CuO powders are weighed out in ratios of $2.5739 : 1.4192 : 1$. The BaO_2 and CuO powders are ground in a pestle and mortar for 15 minutes. The Tl_2O_3 powder is then added to the BaO_2 and CuO along with a small amount of acetone and ground for a further 15 minutes. The final powder is then pressed into pellets of 15 mm diameter. A small number of pellets are then placed into an alumina crucible (17 mm diameter and 14 mm height) and any gaps filled with further powder. Above 850 °C Tl_2O_3 decomposes into $TlO_2 + \frac{1}{2}O_2 + Tl$. To reduce the loss of thallium, oxygen gas can be passed through the furnace to slow the decomposition and a gold lid is tightly fixed on the crucible. The crucible is placed in a quartz boat in a tube furnace at room temperature. The furnace is then heated as follows: 600 °C/hr between room temperature and 850 °C, dwell at 850 °C for 1 hour, 200 °C/hr up to 893.5 °C, dwell at 893.5 °C for 25 minutes, cool at 0.5 °C/hr to 850 °C, then cool at 200 °C/hr to room temperature. The crystals are then extracted individually under a microscope by smashing the crucible into pieces between sheets of white paper.

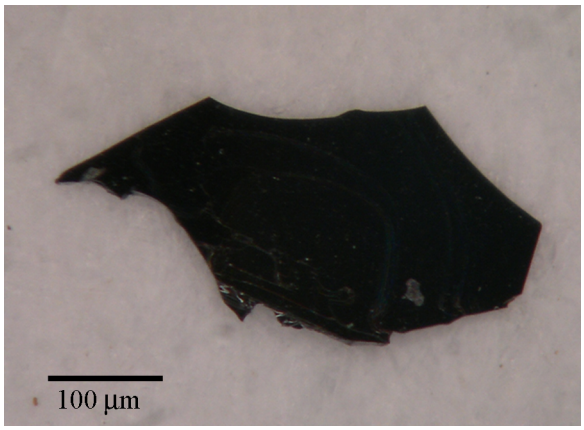

Figure 4.1: A typical Tl2201 crystal.

4.1.2 Characteristics

In common with other cuprates Tl2201 single crystals are black and shiny — see Figure 4.1. Typical as grown crystals have a T_c around 15 K and dimensions 300 μm × 300 μm × 20 μm (where the sample is thinnest along the crystallographic c-axis).

4.1.3 Storage and Handling of Samples

When a sample is not being annealed or measured it is stored in a desiccator to prevent exposure to moisture from the air. After growth, samples are stored loose in a small plastic container and once mounted on quartz platforms (see §4.5) they are stored in larger plastic containers with the quartz platforms fixed down with double sided sticky tape. This prevents damage to the samples or the electrical contacts caused by samples banging into each other or the walls of the container. Quarts platforms are picked up from the sticky tape and transferred to experimental probes with fine tweezers or a scalpel.

The samples are extremely thin and fragile so they cannot be simply picked up with a pair of tweezers as they would frequently break into small pieces. Therefore a 'crystal stick' is used to move or manipulate samples under the microscope. This consists of a stick or small paint brush with bristles removed with a small piece of soft plastic attached to one end and relies on static to attract and pick up samples. A gentle knock of the stick drops the sample.

4.2 Reversibility of T_c - Setting by Annealing

The superconducting transition temperature of Tl2201 samples can be reversibly set between 'non-superconducting' on the heavily overdoped side of the phase diagram and 93 K at optimal doping by annealing or re-annealing in various conditions. An oxygen or argon atmosphere in a tube furnace

gives a T_c in the range approximately 10 K to 70 K, an oxygen atmosphere in a high pressure furnace gives $T_c < 10$ K and annealing in a vacuum (10^{-5} mbar) gives $T_c > 70$ K [83].

4.2.1 Tube Furnace

A quartz tube was thoroughly cleaned using propanol and then baked at 700 °C (higher than the temperature at which subsequent sample annealing will take place) overnight in a box furnace to remove any contamination from inside the tube. The tube is then placed in the tube furnace as shown in figure 4.3. One end of the tube has a gas bottle attached with a flow meter. The other has a flask of diffusion pump oil (which doesn't react dangerously with hot gas and also has a low vapour pressure so doesn't evaporate quickly). This allows gas to flow out of the furnace and prevents air entering.

To help preserve the quality of the sample surfaces, small boxes were cut and folded from thick gold foil (typical dimensions 3 mm × 3 mm × 3 mm) to contain them during annealing. Before use these were placed in a small clean alumina crucible and baked in the tube furnace in flowing oxygen overnight, again to remove any contamination.

To prevent contamination after baking the tube and crucible were only handled with tweezers or when wearing latex gloves. Either bottled argon gas (N5 quality, BOC order code 270050-L) or oxygen gas (N5.5 quality, BOC order code 284916-L) were flowed through the tube furnace during the anneal at a rate of 100 cm^3/min. Reference [83] shows that a one hour anneal in flowing oxygen gas at 400 °C gives a $T_c \approx 20$K, 500 °C gives $T_c \approx 30$K, 600 °C gives $T_c \approx 40$ K and 700 °C gives $T_c = 50$ K. A one hour anneal in flowing argon gas at 500 °C gives $T_c \approx 50$ K and 600 °C gives $T_c \approx 60$K — this illustrated in figure 4.2. Very long anneals tend to give a sharper superconducting transition as the doping is more homogenous, but this additional annealing time causes increased damage to the crystal surfaces which adversely affects the quality of electrical contacts that can be made. A typical anneal is between 4 and 24 hours.

4.2.2 High Pressure Annealing

Annealing samples in a high pressure oxygen atmosphere was attempted. Working with Richard Brooker at UCL, a home-built high pressure rapid quench cold-seal furnace [87] was used to try to get samples that were non-superconducting. The samples were tightly wrapped in gold foil before being placed in a tantalum, zirconium, molybdenum bomb and then into the furnace. To comply with safety regulations a mixture of 20 % O_2 and 80 % Ar gas had to be used at a pressure of around 1000 bar giving a partial O_2 pressure of 200 bar. The furnace was heated to a temperature in the range 300-500 °C for 1-2 hours.

Following annealing, the crystal surfaces were somewhat degraded and measurements of their T_c indicated it was around 5 K. A higher furnace temperature or a longer anneal led to increased

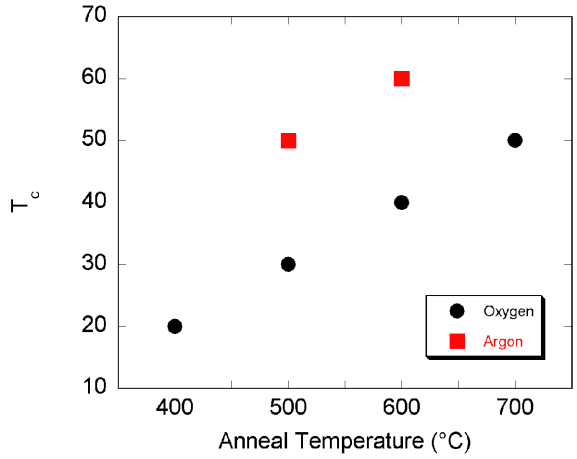

Figure 4.2: The T_c of samples annealed under different conditions. Data from [83].

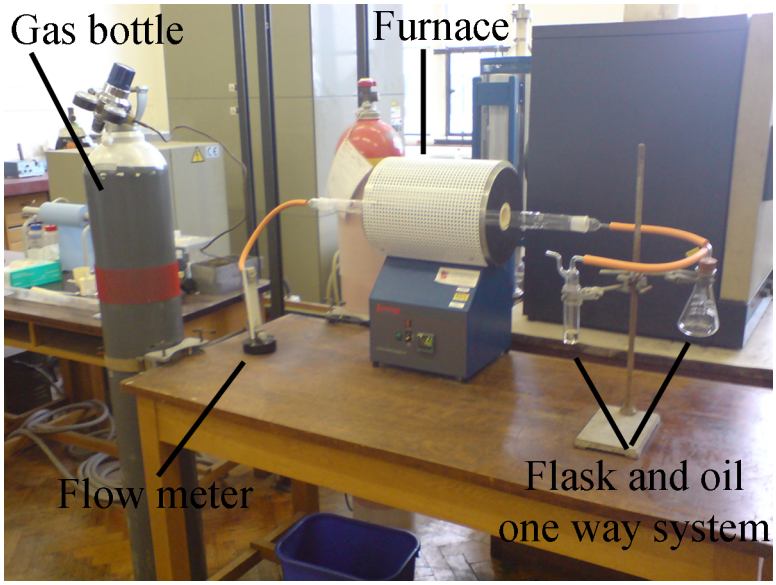

Figure 4.3: Furnace used to anneal crystals. Model is Lenton [85] LTF 12/50/300 tube furnace with Eurotherm [86] 2216 PID temperature controller.

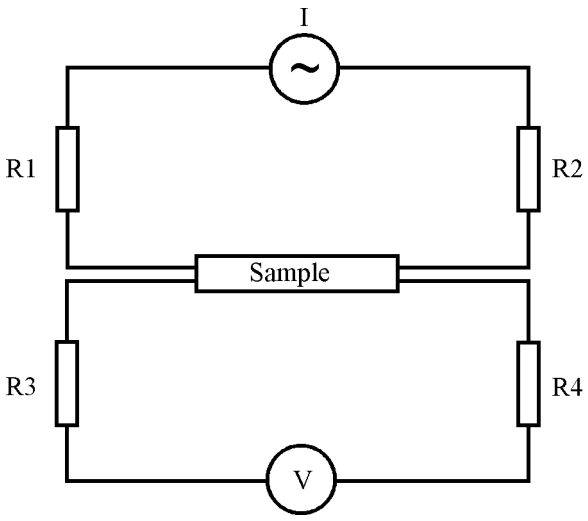

Figure 4.4: Simple diagram of a four-wire method of measuring the sample resistance. R1, R2, R3 and R4 are resistances which represent the contact and lead resistances.

damage to the crystal surfaces. The surface damage was probably due to it not being possible to clean the furnace thoroughly enough prior to the annealing and the failure to suppress T_c due to not using pure O_2 gas.

4.3 Four Wire Resistivity Measurements

All resistivity measurements were performed using the four wire method (figure 4.4) where four wires are separately attached to the sample. Two are used to pass current through the sample and a further two are used to measure the voltage drop across the sample. The simpler method of attaching only two wires to the sample (passing current and measuring the voltage drop through the same wires) has the disadvantage of measuring the sum of the sample resistance, contact resistance and the resistance of the leads. In some cases where the sample resistance is much higher than the lead resistance this is acceptable as the additional resistance only forms a very small part of the measurement. In the case of $Tl_2Ba_2CuO_{6+\delta}$ the resistance of a typical sample is $O(\mathrm{m}\Omega)$. The typical wiring on an experimental probe is $O(10\,\Omega)$ due to the thin wires used to reduce the heat load on the cold end of the probe.

4.4 Electrical Contact Configuration

Figure 4.5 shows a contact configuration which measures the resistivity parallel to the current. The current is passed through the sample via the two surfaces at each end and the voltage drop is measured over a distance ℓ between the other two contacts. The voltage contacts should be far away

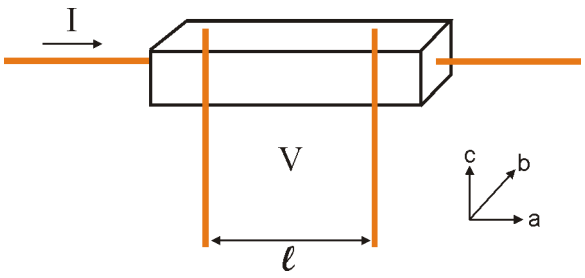

Figure 4.5: Simple four-wire mounting configuration of a sample to measure resistance along in the direction of the current flow.

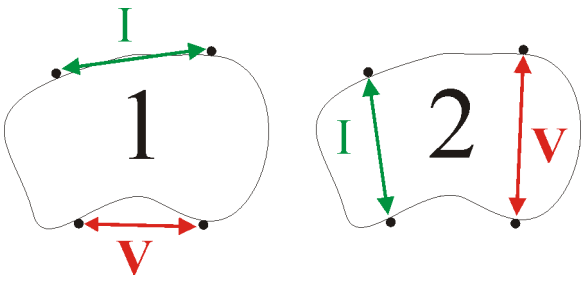

Figure 4.6: The van der Pauw method of measuring the resistance of an arbitrary shaped flat sample. R_1 is measured first followed by R_2.

from the current contacts to ensure the current flow is uniform and parallel between the voltage contacts. The current contacts should cover the whole of the end surfaces as a misalignment would cause a component of current flow in the c direction and will introduce an additional contribution to the measured resistivity. This method provides a way to measure the in-plane resistivity of $Tl_2Ba_2CuO_{6+\delta}$ samples, but due to their shape and size contacts cannot be easily attached to measure the c-axis resistivity in this way, although approximations can be made which allow this measurement in a different configuration.

4.4.1 van der Pauw Method

Not all crystals can be cut or cleaved along their crystallographic axes so the van der Pauw [88] method can be used to measure the resistivity of flat disk-like isotropic samples of a non-uniform shape. Four contacts are attached to the edges of a sample, ideally equally spaced. These must be small compared to the sample dimensions and must be uniform in the direction perpendicular to the plane of the sample. Two measurements (R_1 and R_2) are performed as shown in figure 4.6. The resistivity is found to be:

$$\rho = \frac{\pi d}{2ln2}\left(R_1 + R_2\right) f\left(\frac{R_1}{R_2}\right) \tag{4.1}$$

where d is the sample thickness and the function f is given by:

$$\cosh\left(\frac{R_1/R_2 - 1}{R_1/R_2 + 1}\frac{\ln 2}{f}\right) = \frac{1}{2}\exp\left(\frac{\ln 2}{f}\right) \tag{4.2}$$

4.4.2 Montgomery Method

The above van der Pauw method applies to materials that are isotropic; that is they have the same resistance along all three crystallographic axes so the orientation of the sample in not important. However other materials (including $Tl_2Ba_2CuO_{6+\delta}$ see figure 3.9) are anisotropic which means that consideration must be given to the direction along which a measurement is being made and how accurately the measured component of the resistivity has been isolated.

Wasscher [89] and van der Pauw [90] showed that an anisotropic sample can be related by a simple transformation to an equivalent isotropic sample (equivalent means that identical currents flow and the potential differences are the same between corresponding contacts on the anisotropic sample and the equivalent isotropic sample). An anisotropic sample with dimensions l'_1, l'_2, l'_3 in the directions of ρ_1, ρ_2 and ρ_3 respectively, maps to an equivalent isotropic sample with dimensions l_1, l_2, l_3 and resistivity ρ by

$$l_i = l'_i\left(\frac{\rho_i}{\rho}\right)^{\frac{1}{2}} \tag{4.3}$$

where

$$\rho^3 = \rho_1\rho_2\rho_3 \tag{4.4}$$

Using this, Montgomery [91] generalised the van der Pauw method to the case of anisotropic conductors. Four small contacts are placed near the corners of a sample which has edges in directions along which the resistivity is determined — see figure 4.7. If these edges are initially in the 1 and 2 directions two measurements are performed in the same way as the van der Pauw method giving $\rho_1 = HER_1$ and $\rho_2 = HER_2$ where H is a function of l_2/l_1 and E is the effective thickness of the sample (see [91]). ρ_3 can be measured in the same way by rearranging the contacts. Once it is established that a material is extremely anisotropic, approximations can be made which allow samples to be mounted in a quasi-Montgomery configuration when measuring the c axis resistivity — see figure 4.7. One current contact and one voltage contact are applied to the top face of the sample and the same to the bottom face so that current is passed through the thickness of the sample and the voltage drop is also measured across the thickness of the sample. The error in the technique is negligible as long as the length of the equivalent isotropic sample in the c direction is much greater than the in-plane dimension of the sample ($l_c \gg l_{ab}$ where l_{ab} is an average of l_a and l_b). From equation 4.3

$$\frac{l_c}{l_{ab}} = \frac{l'_c}{l'_{ab}}\sqrt{\frac{\rho_c}{\rho_{ab}}} \tag{4.5}$$

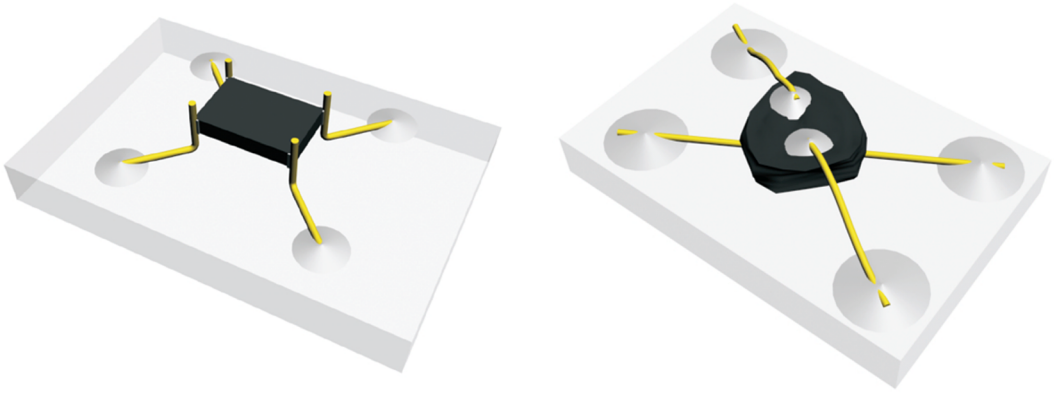

Figure 4.7: Left panel shows the Montgomery configuration for electrical contacts on an anisotropic crystal. Right panel shows the quasi-Montgomery configuration for attaching electrical contacts on to a $Tl_2Ba_2CuO_{6+\delta}$ crystal to measure the c-axis electrical transport. Figure from [38].

For $Tl_2Ba_2CuO_{6+\delta}$, $\rho_c/\rho_{ab} = 1000$ and the typical dimensions of a sample used for measurement are $a = 200\,\mu$m $b = 200\,\mu$m $c = 30\,\mu$m so $l_c/l_{ab} \approx 5$ which implies the quasi-Montgomery method can be applied with $< 3\,\%$ error [92]. The quasi-Montgomery configuration of electrical contacts was used for all c-axis resistivity measurements presented in this thesis.

4.5 Techniques for Attaching Contacts to Samples

For c-axis resistivity measurements a sample is first selected for its size, shape and quality of its surfaces. Depending on the desired T_c it may be annealed as described in §4.2. A small platform of quartz is cut to around $2\,\text{mm} \times 2\,\text{mm} \times 0.4\,\text{mm}$. Quartz is used as it is electrically insulating, can survive from 4.2 K to over 800 K, has a small difference in thermal expansion compared to the other materials used and has a reasonable thermal conductivity. Using an Olympus SZX12 microscope (with up to 90× magnification and a resolution of 800 lines/mm) and working on white paper (which makes small black samples more easily visible) both the sample and quartz platform are washed in acetone with a cotton bud to remove any grease or dirt. Gold wire is cut into pieces approximately the correct length. Usually 25 μm diameter wire is used, although for smaller crystals 10 μm wire must be used. Dupont 6838 conducting silver paint is thinned with hexylacetate until it flows a little. A gold wire approximately 1 mm long is held with tweezers and one end is dipped into the 6838. Some will adhere to the wire which is then brought gently into contact with the crystal to attach the first contact. This is repeated for the second contact on the same face. Using one of the wires already attached, the sample is carefully picked up, turned over and placed onto the quartz platform. A 'wire stick' (which is a cocktail stick that has a small piece of wire (approximately 300 μm diameter) fixed to one end using PTFE tape) is used to pick up some 6838 and then to create two separate puddles which attach the free ends of the wires on the crystal to the quartz platform. While doing this it

is helpful to hold the quartz platform with a pair of tweezers to prevent movement. The remaining two wires are then attached to the crystal and then to the platform in the same way. A photograph of a mounted sample is shown in figure 4.8.

Dupont 6838 needs to be heated in a tube furnace in order to cure so the quartz platform is placed in a crucible and then into a furnace. The lowest contact resistances (around $1\,\Omega$) are achieved by annealing for 10 minutes in flowing O_2 gas at $450\,^\circ$C. When the sample is removed from the furnace it is quench-cooled by placing the crucible onto a thick brass block. The contact resistance can then be checked using a multimeter and needle probes (wires from the multimeter with sewing needles soldered to the ends) placed on the puddles of 6838 on the platform.

In order to get low contact resistances with 6838 the surfaces of the samples need to be of very high quality which is why so much care is taken to keep the furnaces clean when annealing samples. It is most likely that the annealing causes some of the silver to diffuse into the surface of the sample providing the excellent electrical contact.

Before the sample goes into the furnace, if a mistake is made with the 6838 it can be easily removed with acetone and a cotton bud and the mounting process started again. Following annealing if the contacts are of poor quality they can sometimes be successfully scraped off with a razor blade. When this is done all contacts need to be removed as a second 10 minute anneal will significantly degrade any original contacts which remain.

An alternative conducting silver paint called Epotec H20E (2-parts which are mixed in a $1:1$ ratio by weight) was used on some samples. This is less sensitive to the quality of the sample surfaces but the contacts are more brittle and susceptible to breaking meaning larger contacts and therefore larger samples are needed. Samples may or may not be initially annealed and are mounted in the same way described above. The annealing process to set the T_c can be done at the same time as the contacts are annealed following mounting. Typically 1 hour in flowing O_2 at $600\,^\circ$C gives a sample with $T_c \approx 30\,\mathrm{K}$. A higher $T_c \approx 38\,\mathrm{K}$ was achieved by annealing the sample in argon at $400\,^\circ$C for 90 minutes. If the Epotec is annealed at too low a temperature ($250\,^\circ$C) or for too short a time (< 10 minutes) the contact resistances are very high.

The crystals from the high pressure annealing described in §4.2.2 were mounted using 6838 but this gave poor contacts due to the surface damage. When mounted with Epotec, good contact resistances were achieved ($\approx 4\,\Omega$), but the annealing conditions (10 minutes in O_2 at $500\,^\circ$C) resulted in a $T_c \approx 14\,\mathrm{K}$.

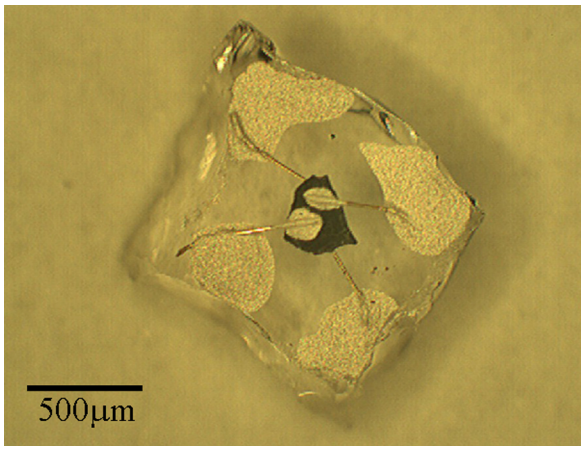

Figure 4.8: Photograph of a $Tl_2Ba_2CuO_{6+\delta}$ sample mounted in the quasi-Montgomery configuration for c-axis resistivity.

4.6 The Sample Measurement Circuit

4.6.1 Electrical Connections to Sample

In order to measure the mounted sample in a experiment it is stuck to an experimental probe using double sided sticky tape. From a connector at the top of the probe thin (usually copper or phosphor-bronze) wires (diameter $\sim 40-100\,\mu$m) run down the probe to small solder pads spread around the area where samples are stuck. Gold wires (usually $50\,\mu$m diameter) are then carefully soldered to four of these pads and using tweezers are bent into position each just touching one of the puddles of silver paint on the quartz platform. A wire stick is used to place Dupont 4929 silver paint (thinned with hexylacetate) to make a connection between the gold wire and puddle of 6838. 4929 silver paint sets in $5-10$ minutes at room temperature to give a good electrical contact. From the connector at the top of the probe a wire then runs to a breakout box usually with a series of BNC sockets each connected to one of the solder pads at the bottom of the probe. Standard BNC cables are then used to make connections between the sample, lock-in amplifier and the current source. A consideration of the standard techniques to reduce the noise in the measurement is given in §10.4.

4.6.2 Lock-In Amplifier

At a very simplistic level this can be thought of as a voltmeter. It accurately measures very small AC signals by using phase-sensitive detection to extract the signal from an often huge background that would otherwise obscure the signal.

The sample is excited by an AC current at fixed frequency, ω_r, and the lock-in detects the response of the sample at the same frequency along with any background noise, $\sum_f V_{f,\mathrm{sig}} \sin(\omega_f t + \theta_{f,\mathrm{sig}})$. It uses a phase sensitive multiplier to multiply this by a self generated reference signal at the same

frequency as the current $V_L \sin(\omega_r t + \theta_{\text{ref}})$.

$$V_{\text{psdoutput}} = \sum_f V_{f,\text{sig}} V_L \sin(\omega_f t + \theta_{f,\text{sig}}) \sin(\omega_r t + \theta_{\text{ref}}) \tag{4.6}$$

$$V_{\text{psdoutput}} = \sum_f \frac{1}{2} V_{\text{sig}} V_L \cos([\omega_r - \omega_f]t + \theta_{\text{sig}} - \theta_{\text{ref}}) - \frac{1}{2} V_{\text{sig}} V_L \cos([\omega_r + \omega_f]t + \theta_{\text{sig}} - \theta_{\text{ref}}) \tag{4.7}$$

For each component frequency, ω_f, that is detected this output is two AC signals, one at the difference frequency $\omega_r - \omega_f$ and the other at the sum frequency $\omega_r + \omega_f$, which are then passed through a low pass filter. In the general case for ω_r and ω_f there is no signal from the low pass filter as both signals are AC and are filtered out. If $\omega_r = \omega_f$ then part of the signal is no longer AC, but DC and proportional to the signal amplitude $V_{\text{lpfoutput}} = \frac{1}{2} V_{\text{sig}} V_L \cos(\theta_{\text{sig}} - \theta_{\text{ref}})$. This gives the X output of the lock-in. The Y output is obtained by using a second phase sensitive detector to multiply the detected signal by the reference frequency shifted by 90° which gives an output $V_{\text{lpfoutput}} = \frac{1}{2} V_{\text{sig}} V_L \sin(\theta_{\text{sig}} - \theta_{\text{ref}})$.

Changing the offset of the reference frequency, θ_{ref}, alters 'the phase' $(\theta_{\text{sig}} - \theta_{\text{ref}})$ of the measurement. For a pure resistor in an AC circuit the voltage response is exactly in phase with the current so the phase should be set to zero $(\theta_{\text{sig}} - \theta_{\text{ref}} = 0)$ meaning that the X ('in phase') output of the lock-in gives the measured signal $(\cos(0) = 1)$ and the Y ('out of phase') output is zero $(\sin(0) = 0)$.

The frequency of the excitation current, ω_r, can be altered on the lock-in. Typically it would be in the region 50 – 100 Hz — but being careful to avoid the mains electricity frequency (50 Hz in UK and 60 Hz in USA) and its harmonics.

The lock-in used for all measurements in this thesis was a Stanford Research Systems [93] SR830.

4.6.3 Current Source

An ideal current source should output the same current regardless of the resistance of the sample or the leads. A number of different methods of generating constant current were used.

The most straight forward method is to use a normal resistor mounted into a metal box with BNC connectors attached. The SR830 has an internal oscillator which outputs an AC voltage in the range 0 – 5 V at a frequency in the range 1 Hz – 102 kHz. Typically a 1 kΩ or 10 kΩ resistor is connected to the SR830 front panel oscillator output and to the sample as shown on the left in figure 4.9. It is easily seen that the current flowing through the sample is given by:

$$I = \frac{V}{R} = \frac{V}{R + R_{\text{sample}}} \tag{4.8}$$

$R \gg R_{\text{sample}}$ otherwise as the sample resistance changes with temperature or magnetic field the current going through the sample will also change leading to ambiguous results. The value of R

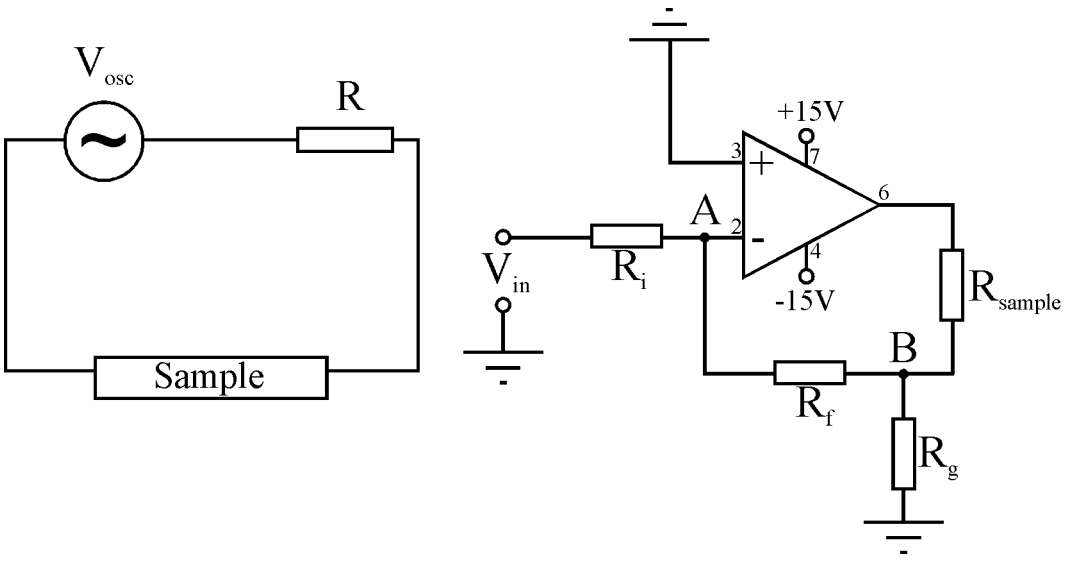

Figure 4.9: Left panel shows a circuit layout of a resistor (typically R = 1 kΩ or 10 kΩ) used as a constant current source. It is connected in series with the sample and the oscillator sin out on a SR830 lock-in amplifier. Right panel shows a circuit diagram of a voltage controlled constant current source used for some measurements. The op-amp used is an Linear Technology LTC1150CN8#PBF (RS order number 5455629).

used is limited by the fact that the lock-in can only output 5 V; when a larger R is used, the current decreases. Inevitably passing a current through a sample with resistance will cause some heating ($\mathrm{P}_{\mathrm{dissipated}} = I^2 R_{\mathrm{sample}}$). The use of a lock-in amplifier is beneficial as it allows the measurement of very small voltages meaning that small currents can be used to limit sample heating. Currents need to be sufficiently large to produce a high quality signal above any background noise as well as sufficiently low so that no self heating is detectable in measurements. Typically they are in the range 2.4 μA – 5 mA depending upon the sample environment and temperature.

An alternative method is to use the voltage controlled current source circuit as shown on the right in figure 4.9. For an op-amp with the non-inverting(+) input connected to ground, the voltage at the inverting(-) input is also zero. An ideal op-amp has an infinite input impedance so draws no current from its input circuit implying the sum of the currents (Kirchoff's First Law) at point A should be zero:

$$\frac{V_{\mathrm{in}}}{R_i} = -\frac{V_B}{R_f} \tag{4.9}$$

Where V_{in} is the voltage from the SR830 oscillator output; R_i and R_f are the values of the resistors and V_B is the voltage at point B. Summing the currents going through the sample gives:

$$I_{\mathrm{sample}} = \frac{V_B}{R_g} + \frac{V_B}{R_f} \tag{4.10}$$

Combining equations 4.9 and 4.10 gives I_{sample} which is independent of the sample resistance and is

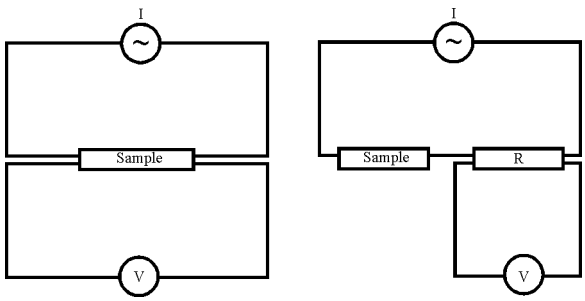

Figure 4.10: Left panel shows the circuit setup for a normal 4-wire measurement configuration. Right panel shows the circuit setup when setting the phase. Current is passed though the sample and a series resistor, R. The voltage drop is measured across only the resistor.

proportional to V_{in}.

$$I_{\text{sample}} = -\frac{R_f + R_g}{R_i R_g} V_{\text{in}} \tag{4.11}$$

The lock-in oscillator output is connected to V_{in} and the sample current contacts are those attached to the op-amp output. The current in the sample is given by equation 4.11.

A final method of generating a constant current used for some experiments was with a Keithley [94] 6221 AC and DC current source. This has two current output leads which are connected to the sample. It also has its own internal oscillator (the lock-in oscillator output is not used) so a trigger link cable carrying a reference signal is connected to the reference input on the lock-in.

4.6.4 Setting the Phase

As a first approximation, assuming the sample is purely resistive and the experimental equipment is sufficiently well designed that it doesn't cause large capacitive or inductive signals, the phase of the measurement can be set using the auto-phase button on the lock-in. This sets the phase such that the Y output is zero. In most cases this is a perfectly adequate assumption to make. In some cases, either when a low-noise transformer (Princeton Applied Research model 1900) is used to amplify a very small voltage signal before it goes into the lock-in or when the sample contacts are not of optimal quality the phase of the measurement needs to be set to account for the phase shift of the true resistive component of the signal. Firstly the normal measurement circuit shown in the left of figure 4.10 is modified to include a series resistor, approximately of the same resistance as the sample. The voltage drop across this resistor is then measured with the lock-in. In the ideal case this is a pure resistor so the auto-phase button is pressed to set the phase such that the out-of-phase component, Y, is zero, the phase is then kept at this value when the circuit is then returned to the original configuration (figure 4.10) for the measurement.

4.7 Zero Field Measurements

In order to make the measurements reported in this thesis, samples of the highest possible quality are needed. The most practical way to determine the quality of the samples is to attach contacts and make a measurement of their zero field resistivity between 300 K and 4.2 K. The best samples have a low resistivity at 4.2 K and also a high residual resistivity ratio (RRR) of ≈ 15 given by $\rho(T = 300\,\mathrm{K})/\rho(T = T_c)$. This screening process also allows samples to be selected with the desired T_c. The relatively small number of samples measured in high magnetic field labs for this thesis were selected from over 100 initial samples.

These measurements were performed in Bristol using equipment developed by Prof. Nigel Hussey. A simple stick probe is slowly pushed into a dewar of liquid helium using a motor — see figure 8.1. There are trip switches positioned at the top and bottom to switch off the motor preventing the probe being pushed or pulled too far. The tip of the probe is made from copper due to its high thermal conductivity ($400\,\mathrm{Wm^{-1}K^{-1}}$ at 300 K) which ensures the sample and thermometer are well coupled — it is stuck well to the copper with a thin layer of GE varnish. The temperature was measured using a SRS SIM922A instrument from a four-wire measurement of the forward voltage drop across a p-n junction diode carrying a constant current of $10\,\mu$A. The voltage drop increases as temperature decreases and is converted to temperature using a calibration table. The shaft of the probe is made from hollow stainless steel tube which has a relatively low thermal conductivity ($\approx 20\,\mathrm{Wm^{-1}K^{-1}}$ at 300 K) and the sample/thermometer wires are thin ($100\,\mu$m) preventing an excess heat load which causes unnecessary liquid helium boil off. No temperature control or heater was required with this apparatus as a acceptable temperature gradient was maintained by slowly pushing the probe into the liquid helium and then pulling it back out again over the course of 3 – 4 hours.

4.8 In-Field Measurements at NHMFL, Tallahassee

Once the best samples were selected in Bristol, ADMR measurements were carried out at the 45 T hybrid magnet at the United States National High Magnetic Field Laboratory (NHMFL) in Tallahassee, Florida [95]. The strength of the magnetic field produced by superconducting magnets like those used in Bristol is limited by the critical field (H_{c2}) and the critical current density (J_{c2}) of the magnet wire. To get to fields significantly higher than the 19 T available in Bristol a different technology needs to be used. A hybrid magnet combines a superconducting outsert magnet coil (11.5 T) and a resistive insert magnet coil (33.5 T) — see figure 4.12. The superconducting magnet has a very large bore and is kept at 1.8 K using liquid helium. The Florida bitter resistive magnet has a 32 mm bore and is made from many perforated copper disks clamped together with discontinuous electrical insulation between the disks. A current of approximately 73 kA is then passed through the coil along with 23,000 l/min of chilled water to dissipate the heat. To change the orientation of the sample with

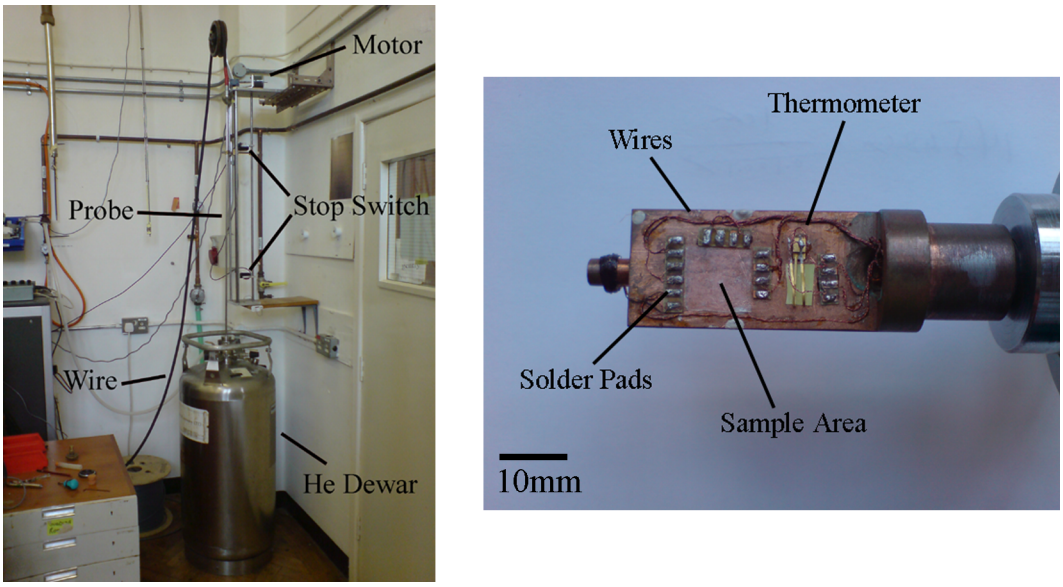

Figure 4.11: Left panel shows the experimental equipment setup for zero field measurements. Right panel shows the sample end of the probe used for zero field measurements.

respect to the magnetic field in order to make ADMR measurements a probe is used which allows in-situ rotation at low temperature and high magnetic field. A simple version would allow rotation is one axis, but a more complex version, like the one used here developed by Dr. Luis Balicas, allows rotation about two axes. This is achieved by having one drive mechanism permanently connected to the rotation platform (the θ or polar rotation) and connected to a computer controlled motor. A removable drive shaft is used for the second rotation (the ϕ or azimuthal rotation) which has to be engaged when the θ rotation is specially aligned. The required ϕ rotation is then performed by hand and the drive shaft disengaged before any further θ rotation can occur. Due to the ratio of the cogs and worms used, one 360° turn of the ϕ rotation screwdriver at the top of the probe corresponds to rotating the samples by 13.3°.

The end of probe used is shown in the left in figure 4.13. This is made from brass as it is easier to machine/cut into intricate shapes than copper but still has a good thermal conductivity ($100\,\mathrm{Wm^{-1}K^{-1}}$ at $300\,\mathrm{K}$). The probe shaft is stainless steel. Up to 5 samples were mounted on this probe (see right of figure 4.13). The $100\,\mu$m wires from the top of the probe emerge in a fountain from the centre of the sample area. They are fairly stiff copper wires which don't move very much during the rotation. The flexibility necessary is provided by attaching $50\,\mu$m gold wires to the copper wires by winding them together and then using 4929 silver paint. The gold wires are then attached to the puddles of silver paint on the individual sample platforms, also using 4929. The wires need to be carefully positioned prior to the measurement to allow for the rotation and also not to short circuit each other. The probe is placed in a jacket which is a stainless steel tube which seals around the probe and allows the air to be pumped away; usually down to a pressure of 10^{-5} mbar ensuring no air

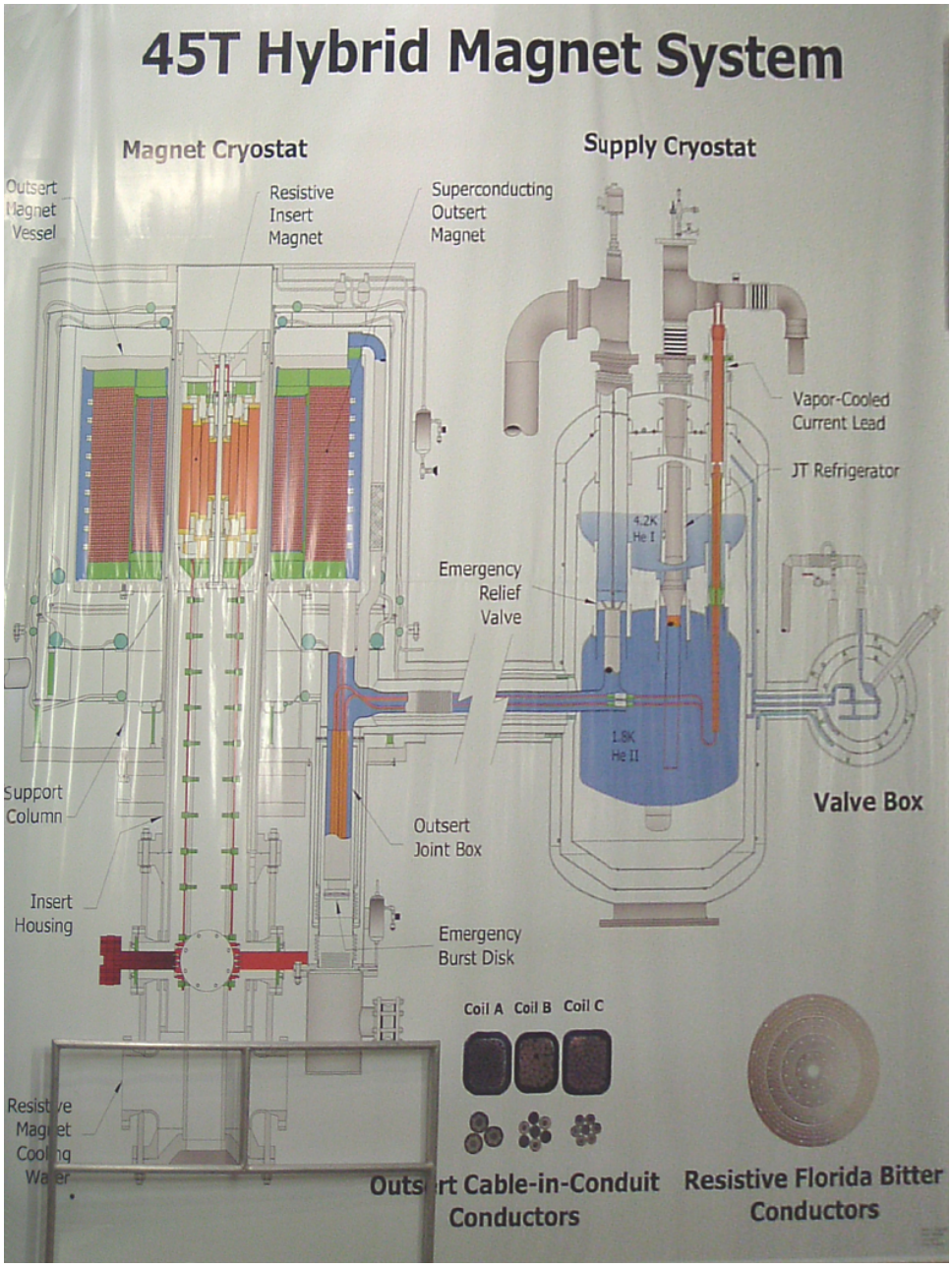

Figure 4.12: Diagram of 45T Hybrid Magnet at NHMFL. Superconducting and resistive magnets are shown on the left. The supply cryostat for the superconducting magnet is shown on the right. At the bottom is the resistive magnet cooling water pipe.

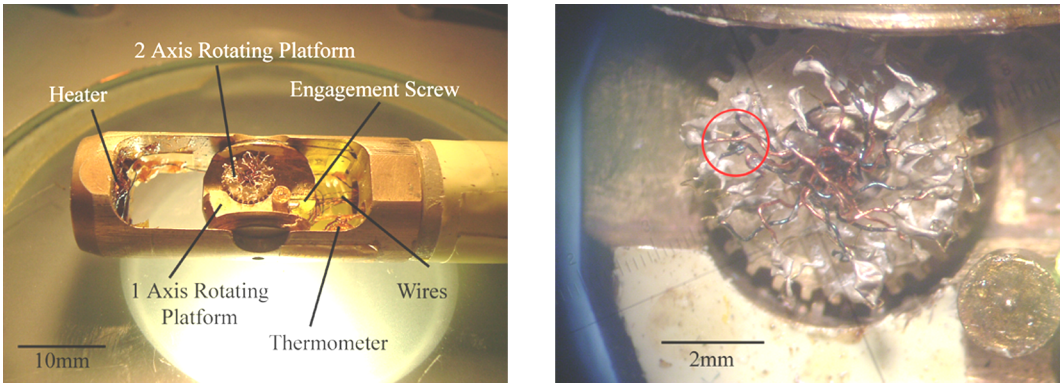

Figure 4.13: Left panel shows the tip of the two axis rotator probe used. The drive mechanism for the 1 axis platform is permanently connected. A screwdriver is pushed down from the right hand side to engage with the engagement screw in order to operate the second rotation axis. Right panel shows four samples mounted on the 2 axis platform. One of these samples in circled in red.

freezes inside which could lock the rotation mechanism. The bottom 6 inches of the jacket, around the samples, has an additional outer sealed jacket in which all air freezes when at low temperatures, nearly isolating the samples. By controlling the pressure of the ^{3}He exchange gas (i.e. varying the thermal contact with the 4.2 K helium bath) and using a heater, the jacket allows the temperature of the samples to be controlled between 4.2 K and up to 110 K.

Heat can be supplied by using a small heater fixed well to the probe near the samples using GE varnish. This is normally a non-inductively wound coil (i.e. fold the length of wire in half before winding the coil) of high-resistance wire with a typical resistance around 100 Ω. A Cernox negative temperature coefficient resistance thermometer was connected with the heater to a Lakeshore [96] 340 temperature controller instrument. This maintains the temperature of the samples using a PID (proportional-integral-derivative) algorithm to control the current supplied to the heater (in this case corresponding to a power up to 3 W) based on the desired temperature set point and feedback from the thermometer. Before the temperature comes to stability it usually overshoots the desired value and oscillates. The speed of temperature change is accelerated by increasing the P value, although this also tends to increase the overshoot. The rate at which the oscillations decay is controlled by the I value and is minimised by setting I to 1000 divided by the time period in seconds of any oscillations. The D value decreases the overshoot but slows the response. Typical values are $P = 80-150$, $I = 3-10$ and $D = 0$. The Cernox is affected by magnetoresistance but a number of factors come together to minimise its impact on these measurements. The measurement taken at 4.2 K is not affected since no heat was applied, the sample was just in good thermal contact with the ^{4}He bath which remained at 4.2 K. Brandt [97] showed that at 15 K the change in resistance of the Cernox is linear in field and it can easily be shown to extrapolate to 2.5 % at 45 T. Using the thermometer calibration file at 15 K a 2.5 % change in resistance corresponds to a temperature error of 0.7 K. But for $Tl_2Ba_2CuO_{6+\delta}$ at

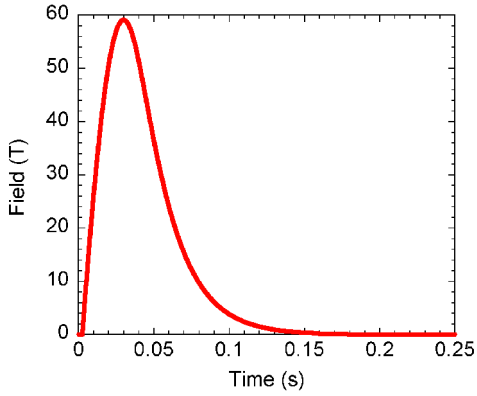

Figure 4.14: Pulse profile of a 60 T long pulse magnet at LNCMP.

15 K $\frac{dR}{dT}$ is small resulting in a minimal error in the ADMR data. By 50 K, the resistance error has decreased to 0.3 %, and the temperature error has dropped to 0.3 K, although $\frac{dR}{dT}$ is higher at 50 K the error in the ADMR data remains small.

Measurements can also be made down to approximately 0.5 K. First the space above the liquid ^{4}He in the bath is continuously pumped using a large vacuum pump. This reduces the temperature of the helium and samples to approximately 1.25 K which is below the boiling temperature of ^{3}He causing it it liquefy. The liquid ^{3}He is then also pumped reducing its temperature to around 0.5 K depending on the strength of the pump and the heat load from the probe.

The samples were connected to SR830 lock-in amplifiers using Princeton Applied Research low noise transformers. The excitation currents were provided by Keithley 6221's.

4.9 In-Field Measurements at LNCMP, Toulouse

Fields higher than 45 T can only currently be achieved for a very short period of time in a pulsed magnetic field system. The 'Laboratoire National des Champs Magnétiques Pulsés' (LNCMP) is based in Toulouse and provides a long pulse magnetic field to 60 T. A typical pulse profile is shown in figure 4.14. To create the field pulse the fibre reinforced coil is pre-cooled with liquid nitrogen then 14 MJ of energy from a capacitor bank is discharged into the coil. Both magnetoresistance measurements (in a standard ^{4}He cryostat) and torque measurements (in a dilution refrigerator) were performed on samples of $Tl_2Ba_2CuO_{6+\delta}$ in the search for quantum oscillations. Magnetoresistance measurements were performed using the standard 4-point technique described above. For torque measurements the sample was mounted onto a sensitive piezoresistive cantilever. Electrical connections were made so that the cantilever was part of a Wheatstone bridge arrangement of resistors which allowed very small changes in piezoresistance (and therefore torque) to be detected using a lock-in amplifier.

4.10 In-Field Measurements in Bristol

4.10.1 14 T 'Green' Magnet

This superconducting magnet (Nb_3Sn, $T_c = 18\,K$) was used for measurements up to 14 T. A single axis rotation probe with up to 2 samples and a thermometer and heater was used in the same way as described above. This was placed directly into a variable temperature insert (VTI) which allows accurate temperature control and stabilisation from 1.8 K to 300 K (± 0.1 K) by controlling the flow of helium continually pumped through a needle valve from the cryostat bath and the use of heaters on the VTI helium inlet and the probe. The VTI has a vacuum insulation jacket and is placed into the bore of the magnet which is placed in a green coloured dewar with a 100 l capacity of helium and a vacuum insulation jacket. A computer program was written by the author to allow this experiment to automatically perform a series of field sweeps, temperature sweeps and sample rotations which can be defined in a simple text input file.

4.10.2 19 T 'Yellow' Magnet

This 19 T superconducting magnet was used mainly to get to temperatures as low as 300 mK which are not possible in the 'green' magnet. It has a ^{3}He top-loading cryostat and takes a 3 m insert with interchangeable Hysol end-pieces on which samples are mounted along with a thermometer. Measurements are performed either in liquid ^{3}He or at higher temperatures in ^{3}He exchange gas. For temperatures between 1.4 K and 4.2 K a ^{4}He pot is used where ^{4}He is sucked in using a pump and then continuously pumped to reduce its temperature and also that of the sample. For temperatures below 1.4 K, ^{3}He is released from the sorption pump by heating it and is condensed by the cooling power of the ^{4}He pot, falling to the tail of the cryostat. The sorption pump is then cooled using a flow of ^{4}He from the bath and the ^{3}He is then reabsorbed effectively pumping on the ^{3}He liquid and lowing the temperature. Samples were connected in the way described above to a lock-in amplifier and the thermometers and heaters were connected to a Neocera temperature controller.

4.11 Computer Data Recording and Control Programs

All instruments are connected to a computer using either a GPIB (General Purpose Interface Bus or IEEE-488) or serial port interface. Computer programs can then be written to record all the required data — in Bristol the programs are written in the *Borland Delphi* language and in Tallahassee the software provided for users is written in *LabVIEW* [98]. With *Delphi* it is also possible to create programs which control experiments. This is often very useful when a list of tasks can be set and the computer will preform experiments overnight while the user is not present. A brief tutorial on setting up *Delphi* is provided in §10.5.

4.11.1 Remote Monitoring

This same method of saving information from instruments to files can be used in a further interesting way. The current parameters such as the temperature, magnetic field, helium level in the magnet and sample resistances can be saved to a simple *html* file along with a time stamp using the rewrite command so that the file only contains the latest information. A copy of the *Apache* [99] web-server is then installed and configured on the computer which must be connected to the internet. The file is saved in the special directory which is also the one *Apache* uses to serve documents to the internet for remote access (it's usually called *htdocs*). This can then be accessed via the internet by a PC to monitor the experiment. Of course, in many cases *Windows XP Pro* remote desktop can be used, but this method also allows access from a WAP enabled mobile phone meaning an experiment can be monitored from almost anywhere! The code is given in §10.5.3.

4.12 X-ray Crystal Orientation

As will be explained in detail in chapter 6 it was important to know the alignment of the sample crystallographic axes with respect to the magnetic field. This was done by taking photographs of the samples when they were mounted on the experimental probe before and after measurement. Later on, the same crystals had their electrical contacts carefully removed and were placed in a X-ray crystal diffractometer using vacuum grease to attach them to a glass fibre. This identifies the reciprocal space directions of the faces of the $Tl_2Ba_2CuO_{6+\delta}$ crystals which usually form/break along well defined, low index directions. The CuO bond is along [100] type directions (i.e. 100, 010, $\bar{1}00$ or $0\bar{1}0$ depending on the specific bond in question). The direction at 45° to the CuO bond is then a [110] type direction (i.e. 110, $\bar{1}10$, $1\bar{1}0$ or $\bar{1}\bar{1}0$) as the unit cell is square in the two short dimensions. The X-ray results were then compared with the photos to calculate the ϕ orientation of the samples with respect to the magnetic field.

Chapter 5

Analysis Techniques

This chapter provides a detailed mathematical and computational explanation of how the Boltzmann transport equation described in §2.3 can be applied to model ADMR experimental data obtained on $Tl_2Ba_2CuO_{6+\delta}$ of the form shown in figure 5.1.

5.1 ADMR Equation Derivation

The experimental data taken during the course of this thesis can be analysed using the ideas described in §2.9 but do not strictly contain oscillations so have been termed angular dependent magnetoresistance (ADMR).

Without making the case for any anisotropy at this stage, this section generalises the derivation of the Shockley-Chambers Tube-Integral (equation 2.43) to give the angle (θ and ϕ) dependent conductivity for a quasi-2D cylindrical Fermi surface using an anisotropic scattering time, $\tau(\psi)$, and angular frequency, $\omega(\theta, \psi)$. The simplifications which can be made if $\tau(\psi)$ and $\omega(\psi)$ are isotropic are explained in §5.1.1.

The linearised Boltzmann transport equation (equation 2.17):

$$e\mathbf{E}\cdot\mathbf{v}\left(-\frac{\partial f^0_{\mathbf{k}}}{\partial\varepsilon}\right) = \frac{g_{\mathbf{k}}}{\tau} + \frac{e}{\hbar}\left[\mathbf{v}\times\mathbf{B}\right]\frac{\partial g_{\mathbf{k}}}{\partial\mathbf{k}} \tag{5.1}$$

is modified for a cylindrical Fermi surface by considering magnetic field induced closed orbits on the Fermi surface so that the Lorentz force is given by:

$$\frac{\partial\mathbf{k}}{\partial t} = \frac{e}{\hbar}\left[\mathbf{v}\times\mathbf{B}\right] \tag{5.2}$$

and so:

$$e\mathbf{E}\cdot\mathbf{v}\left(-\frac{\partial f^0_{\mathbf{k}}}{\partial\varepsilon}\right) = \frac{g_{\mathbf{k}}}{\tau} + \frac{\partial g_{\mathbf{k}}}{\partial t} \tag{5.3}$$

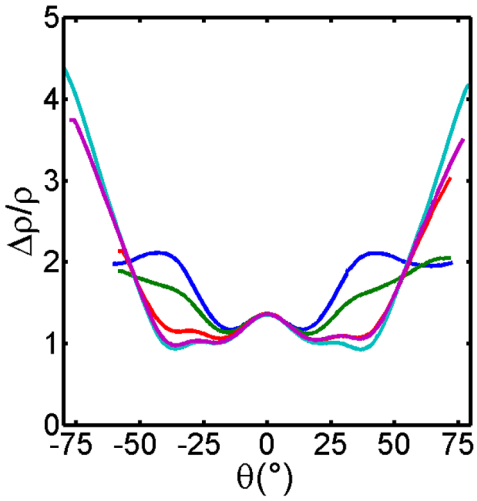

Figure 5.1: Example of ADMR data taken on a $Tl_2Ba_2CuO_{6+\delta}$ sample ($T_c = 17\,\mathrm{K}$) at 4.2 K. Each colour represents ADMR taken at a different azimuthal (ϕ) angle.

The phase angle around the orbit is defined as $\partial\psi = \omega\partial t$ where ω is the angular frequency so equation 5.3 becomes:

$$e\mathbf{E}\cdot\mathbf{v}\left(\frac{-\partial f^0_{\mathbf{k}}}{\partial\varepsilon}\right) = \frac{g_{\mathbf{k}}}{\tau} + \omega\frac{\partial g_{\mathbf{k}}}{\partial\psi} \tag{5.4}$$

In the general case τ has ψ dependence and ω has θ and ψ dependence. θ is the angle between the magnetic field and the axis of the cylinder so $\omega(\theta,\psi)$ can be written as $\omega_c(\psi)$ where the $\cos\theta$ factor is not explicitly written:

$$e\mathbf{E}\cdot\mathbf{v}\left(\frac{-\partial f^0_{\mathbf{k}}}{\partial\varepsilon}\right) = \frac{g_{\mathbf{k}}}{\tau(\psi)} + \omega_c(\psi)\frac{\partial g_{\mathbf{k}}}{\partial\psi} = \omega_c(\psi)e^{-G}\frac{\partial}{\partial\psi}(e^G g_{\mathbf{k}}) \tag{5.5}$$

where:

$$G = \int \frac{1}{\omega_c(\psi)\tau(\psi)}\partial\psi \tag{5.6}$$

This can be proved by differentiation by parts:

$$\omega_c(\psi)e^{-G}\frac{\partial}{\partial\psi}(e^G g_k) = \omega_c(\psi)e^{-G}\left(e^G\frac{\partial g_k}{\partial\psi} + \frac{e^G g_k}{\omega_c(\psi)\tau(\psi)}\right) = \omega_c(\psi)\frac{\partial g_k}{\partial\psi} + \frac{g_k}{\tau(\psi)} \tag{5.7}$$

This anisotropy is parameterised using γ and β in the simplest form that fits the crystal symmetry:

$$G(\psi) = \int \frac{1+\beta\cos 4\psi}{\omega_c}\frac{1+\gamma\cos 4\psi}{\tau^0}d\psi \tag{5.8}$$

Equation 5.5 can be rearranged noting that v may have ψ dependence:

$$\frac{e}{\omega_c(\psi)}e^{G(\psi)}\left(-\frac{\partial f^0_{\mathbf{k}}}{\partial\varepsilon}\right)E_j v_j(\psi) = \frac{\partial}{\partial\psi}(e^{G(\psi)}g_{\mathbf{k}}) \tag{5.9}$$

$$\left(\frac{-\partial f^0_{\mathbf{k}}}{\partial \varepsilon}\right)\int_{-\infty}^{\psi}\frac{e}{\omega_c(\psi')}e^{G(\psi')}E_j\_jpsi')\partial\psi' = e^{G(\psi)}g_{\mathbf{k}} \tag{5.10}$$

making $g_{\mathbf{k}}$ the subject (where the integration limits $-\infty$ to ψ is a sum over history of the phase variable ψ):

$$g_{\mathbf{k}} = \left(\frac{-\partial f^0_{\mathbf{k}}}{\partial \varepsilon}\right)e^{-G(\psi)}\int_{-\infty}^{\psi}\frac{e}{\omega_c(\psi')}e^{G(\psi')}E_j v_j(\psi')\partial\psi' \tag{5.11}$$

The integration variable ψ' can now be changed $\psi' \rightarrow \psi - \psi''$ so the upper limit $\psi \Rightarrow \psi'' = 0$ and the lower limit $-\infty \Rightarrow \psi'' = \infty$ (note switching the limits introduces a factor of -1, but $\partial\psi' = -\partial\psi''$ so the two factors of -1 cancel) so that:

$$g_{\mathbf{k}} = \left(\frac{-\partial f^0_{\mathbf{k}}}{\partial \varepsilon}\right)e^{-G(\psi)}\int_{0}^{\infty}\frac{e}{\omega_c(\psi-\psi'')}e^{G(\psi-\psi'')}E_j v_j(\psi-\psi'')\partial\psi'' \tag{5.12}$$

Using equation 2.40 gives

$$J_i = \frac{e}{4\pi^3}\int\partial\varepsilon\int\partial k_B\int_0^{2\pi}\frac{eB}{\omega_c(\psi)\hbar^2}v_i(\psi)g_{\mathbf{k}}\partial\psi \tag{5.13}$$

Therefore:

$$\sigma_{ij} = \frac{e}{4\pi^3}\int\partial\varepsilon\int\partial k_B\int_0^{2\pi}\partial\psi \left[\frac{eB}{\omega_c(\psi)\hbar^2}v_i(\psi)\left(\frac{-\partial f^0_{\mathbf{k}}}{\partial\varepsilon}\right)e^{-G(\psi)}\int_0^{\infty}\frac{e}{\omega_c(\psi-\psi'')}e^{-G(\psi-\psi'')}\frac{E_j}{E_j}v_j(\psi-\psi'')d\psi''\right] \tag{5.14}$$

$$\sigma_{ij} = \frac{e^3}{4\pi^3\hbar^2}\int\partial\varepsilon\left(\frac{-\partial f^0_{\mathbf{k}}}{\partial\varepsilon}\right)\int\partial k_B B\int_0^{2\pi}\partial\psi\int_0^{\infty}\partial\psi''\frac{v_i(\psi)}{\omega_c(\psi)}\frac{v_j(\psi-\psi'')}{\omega_c(\psi-\psi'')}e^{-G(\psi)}e^{G(\psi-\psi'')} \tag{5.15}$$

Fermions obey Fermi-Dirac statistics with a distribution function given in equation 2.2. So if $k_BT \ll \varepsilon_F$ then the distribution is a step function at the Fermi level. Its derivative is a δ function at the Fermi energy so $\int_0^{\infty} d\varepsilon\delta(\varepsilon-\varepsilon_F) = 1$ and equation 5.15 becomes:

$$\sigma_{zz} = \frac{e^3}{4\pi^3\hbar^2}\int\partial k_B B\int_0^{2\pi}\partial\psi\int_0^{\infty}\partial\psi''\frac{v_z(\psi)}{\omega_c(\psi)}\frac{v_z(\psi-\psi'')}{\omega_c(\psi-\psi'')}e^{-G(\psi)}e^{G(\psi-\psi'')} \tag{5.16}$$

where the z-axis conductivity (σ_{zz}) is considered. Substituting $dk_B = dk_z\cos\theta$ into equation 5.16 gives:

$$\sigma_{zz} = \frac{e^3}{4\pi^3\hbar^2}\int_{-\frac{\pi}{d}}^{\frac{\pi}{d}}\partial k_z B\cos\theta\int_0^{2\pi}\partial\psi\int_0^{\infty}\partial\psi''\frac{v_z(\psi)}{\omega_c(\psi)}\frac{v_z(\psi-\psi'')}{\omega_c(\psi-\psi'')}e^{-G(\psi)}e^{G(\psi-\psi'')} \tag{5.17}$$

Now:

$$G(\psi) = \int \frac{1+\beta\cos 4\psi}{\omega_c}\frac{1+\gamma\cos 4\psi}{\tau^0}\partial\psi$$
$$= \frac{1}{\omega_c\tau^0}\left[\psi + \frac{\gamma}{4}\sin 4\psi + \frac{\beta}{4}\sin 4\psi + \frac{\gamma\beta}{4}\left(\frac{1}{2}\cos 4\psi\sin 4\psi + 2\psi\right)\right] \quad (5.18)$$

Concentrating on the two exponential terms in equation 5.17 and expanding them so:

$$e^{-G(\psi)}e^{G(\psi-\psi'')} = \exp\left\{\frac{1}{\omega_c\tau^0}\left[-\psi - \frac{\gamma}{4}\sin 4\psi - \frac{\beta}{4}\sin 4\psi - \frac{\gamma\beta}{4}\left(\frac{1}{2}\cos 4\psi\sin 5\psi + 2\psi\right)\right.\right.$$
$$+ \frac{\gamma\beta}{4}2\psi - \frac{\gamma\beta}{4}2\psi'' + \psi - \psi'' + \frac{\gamma}{4}\sin 4(\psi-\psi'') + \frac{\beta}{4}\sin 4(\psi-\psi'')$$
$$\left.\left. + \frac{\gamma\beta}{4}\left(\frac{1}{2}\cos 4(\psi-\psi'')\sin 4(\psi-\psi'') + 2\psi - 2\psi''\right)\right]\right\} \quad (5.19)$$

Grouping terms with the same periodicity:

$$e^{-G(\psi)}e^{G(\psi-\psi'')} = \exp\left\{\frac{1}{\omega_c\tau^0}\left[-\frac{\gamma}{4}\sin 4\psi - \frac{\beta}{4}\sin 4\psi - \frac{\gamma\beta}{8}\cos 4\psi\sin 4\psi\right]\right\}\exp\left[\frac{-\left(1+\frac{\gamma\beta}{2}\right)\psi''}{\omega_c\tau^0}\right]$$
$$\exp\left\{\frac{1}{\omega_c\tau^0}\left[\frac{\gamma}{4}\sin 4(\psi-\psi'') + \frac{\beta}{4}\sin 4(\psi-\psi'') + \frac{\gamma\beta}{8}\cos 4(\psi-\psi'')\sin 4(\psi-\psi'')\right]\right\} \quad (5.20)$$

Notice that:

$$\frac{v_z(\psi)}{\omega_c(\psi)}\exp\left\{\frac{1}{\omega_c\tau^0}\left[-\frac{\gamma}{4}\sin 4\psi - \frac{\beta}{4}\sin 4\psi - \frac{\gamma\beta}{8}\cos 4\psi\sin 4\psi\right]\right\} \quad (5.21)$$

is periodic in ψ and similarly:

$$\frac{v_z(\psi-\psi'')}{\omega_c(\psi-\psi'')}\exp\left\{\frac{1}{\omega_c\tau^0}\left[\frac{\gamma}{4}\sin 4(\psi-\psi'') + \frac{\beta}{4}\sin 4(\psi-\psi'') + \frac{\gamma\beta}{8}\cos 4(\psi-\psi'')\sin 4(\psi-\psi'')\right]\right\} \quad (5.22)$$

is periodic in $\psi - \psi''$. Therefore they can be expressed as a Fourier series:

$$\text{Equation } 5.21 = \sum_{m=0}^{\infty} a_m\cos m\psi + b_m\sin m\psi \quad (5.23)$$

$$\text{Equation } 5.22 = \sum_{n=0}^{\infty} c_n\cos n(\psi-\psi'') + d_n\sin n(\psi-\psi'') \quad (5.24)$$

So equation 5.17 becomes:

$$\sigma_{zz} = \frac{e^3}{4\pi^3\hbar^2}\int_{\frac{-\pi}{d}}^{\frac{\pi}{d}}\partial k_z B\cos\theta\int_0^{2\pi}\partial\psi\int_0^{\infty}\partial\psi''\left[\sum_{m=0}^{\infty} a_m\cos m\psi + b_m\sin m\psi\right]$$
$$\left[\sum_{n=0}^{\infty} c_n\cos n(\psi-\psi'') + d_n\sin n(\psi-\psi'')\right]\exp\left[\frac{-(1+\frac{\gamma\beta}{2})\psi''}{\omega_c\tau^0}\right] \quad (5.25)$$

Remembering that $\cos(A-B)=\cos A\cos B+\sin A\sin B$ and $\sin(A-B)=\sin A\cos B-\cos A\sin B$, the last two terms of equation 5.25 can be written as:

$$\sum_{n=0}^{\infty} c_n\left[\cos n\psi\cos n\psi''+\sin n\psi\sin n\psi''\right]\exp\left\{\frac{\psi''}{Q}\right\}+d_n\left[\sin n\psi\cos n\psi''-\cos n\psi\sin n\psi''\right]\exp\left\{\frac{-\psi''}{Q}\right\} \tag{5.26}$$

where

$$Q=\frac{\omega_c\tau^0}{1+\frac{\gamma\beta}{2}} \tag{5.27}$$

The order of the integral (over ψ'') and sum signs can be swopped since:

$$\int_0^{\infty}\Sigma k_n=\int_0^{\infty}k_1+k_2+k_3=\int_0^{\infty}k_1+\int_0^{\infty}k_2+\int_0^{\infty}k_3=\Sigma_n\int_0^{\infty}k_n \tag{5.28}$$

Now using the Laplace transforms or a table of integrals [100]:

$$\int_n^{\infty}\cos n\psi''\exp\left\{\frac{-\psi''}{Q}\right\}\partial\psi''=\frac{\frac{1}{Q}}{\left(\frac{1}{Q}\right)^2+n^2}=\frac{Q}{1+Q^2n^2} \tag{5.29}$$

and:

$$\int_n^{\infty}\sin n\psi''\exp\left\{\frac{-\psi''}{Q}\right\}\partial\psi''=\frac{n}{\left(\frac{1}{Q}\right)^2+n^2}=\frac{nQ^2}{1+Q^2n^2} \tag{5.30}$$

equation 5.25 can be written as:

$$\sigma_{zz}=\frac{e^3}{4\pi^3\hbar^2}\int_{\frac{-\pi}{d}}^{\frac{\pi}{d}}\partial k_z B\cos\theta\int_0^{2\pi}\partial\psi\left[\sum_{m=0}^{\infty}a_m\cos m\psi+b_m\sin m\psi\right]\left[\sum_{n=0}^{\infty}c_n\left[\frac{Q\cos n\psi}{1+Q^2n^2}+\frac{nQ^2\sin n\psi}{1+Q^2n^2}\right]+d_n\left[\frac{Q\sin n\psi}{1+Q^2n^2}-\frac{nQ^2\cos n\psi}{1+Q^2n^2}\right]\right] \tag{5.31}$$

Using:

$$\int_0^{2\pi}\cos m\psi\cos n\psi=\pi\delta_{mn} \tag{5.32}$$

$$\int_0^{2\pi}\sin n\psi\sin m\psi=\pi\delta_{mn} \tag{5.33}$$

$$\int_0^{2\pi}\sin n\psi\cos m\psi=0 \tag{5.34}$$

but noting that for $m=n=0$:

$$\int_0^{2\pi}\cos m\psi\cos n\psi=2\pi \tag{5.35}$$

and:

$$\int_0^{2\pi}\sin n\psi\sin m\psi=0 \tag{5.36}$$

Equation 5.31 becomes:

$$\sigma_{zz} = \frac{e^3}{4\pi^3\hbar^2}\int_{-\frac{\pi}{d}}^{\frac{\pi}{d}} \partial k_z B\cos\theta \left(2a_0c_0 + \sum_{n=1}^{\infty}\left[\frac{a_nc_n\pi Q}{1+Q^2n^2} - \frac{a_nd_n\pi nQ^2}{1+Q^2n^2} + \frac{b_nc_n\pi nQ^2}{1+Q^2n^2} + \frac{b_nd_n\pi Q}{1+Q^2n^2}\right]\right) \tag{5.37}$$

$$\sigma_{zz} = \frac{e^3B\cos\theta\pi Q}{4\pi^3\hbar^2}\int_{-\frac{\pi}{d}}^{\frac{\pi}{d}} \partial k_z 2a_0c_0 + \sum_{n=1}^{\infty}\left[\frac{a_nc_n + b_nd_n}{1+Q^2n^2} - \frac{\left[a_nd_n - b_nc_n\right]nQ}{1+Q^2n^2}\right] \tag{5.38}$$

Finally:

$$\sigma_{zz} = \frac{e^3B\cos\theta}{2\pi^2\hbar^2}\frac{\omega_c\tau^0}{\left(1+\frac{\gamma\beta}{2}\right)}\int_{-\frac{\pi}{d}}^{\frac{\pi}{d}} \partial k_z a_0c_0 + \frac{1}{2}\sum_{n=1}^{\infty}\left[\frac{a_cc_n + b_nd_n}{1+Q^2n^2} - \frac{\left[a_nd_n - b_nc_n\right]nQ}{1+Q^2n^2}\right] \tag{5.39}$$

5.1.1 Simplifications in the Isotropic τ and ω Case

Where no anisotropy is considered in the Fermi velocity or scattering rate, equation 5.18 simplifies to:

$$G(\psi) = \int \frac{1}{\omega_c\tau^0}d\psi = \frac{\psi}{\omega_c\tau^0} \tag{5.40}$$

and equation 5.19 becomes:

$$e^{-G(\psi)}e^{G(\psi-\psi'')} = \exp\left\{\frac{1}{\omega_c\tau^0}\left[-\psi+\psi-\psi''\right]\right\} = \exp\left\{\frac{-\psi''}{\omega_c\tau^0}\right\} \tag{5.41}$$

This means that the two periodic components (equations 5.21 and 5.22) are now just:

$$v_i(\psi) \text{ and } v_j(\psi-\psi'') \tag{5.42}$$

5.2 Application to $Tl_2Ba_2CuO_{6+\delta}$

5.2.1 Symmetry Consideration

Reflecting the cylindrical nature of the geometry of the Fermi surface of Tl2201 the local Fermi wavevector can be expanded in cylindrical harmonics [101]:

$$k_F(\psi,\kappa) = \sum_{m,n\geq 0} k_{mn}\left\{\begin{array}{c}\cos\\ \sin\end{array}\right\}n\kappa \times \left\{\begin{array}{c}\cos\\ \sin\end{array}\right\}m\psi \tag{5.43}$$

where $\kappa = ck_z/2$ and k_z runs over the first Brillouin zone from $k_z = 2\pi/c$ (so $\kappa = c2\pi/2c = \pi$) to $k_z = -2\pi/c$ (so $\kappa = -\pi$) and c is the c-axis lattice parameter (23.13 Å).

Considering the tetragonal crystal symmetry and the Brillouin zone stacking arrangement (see figure 3.3) some of these terms can be ruled out. Note that the hole Fermi surface cylinder is centred on the (π,π) point or the X-line. Firstly, inversion symmetry in the k_z direction (i.e. $\kappa \rightarrow -\kappa$)

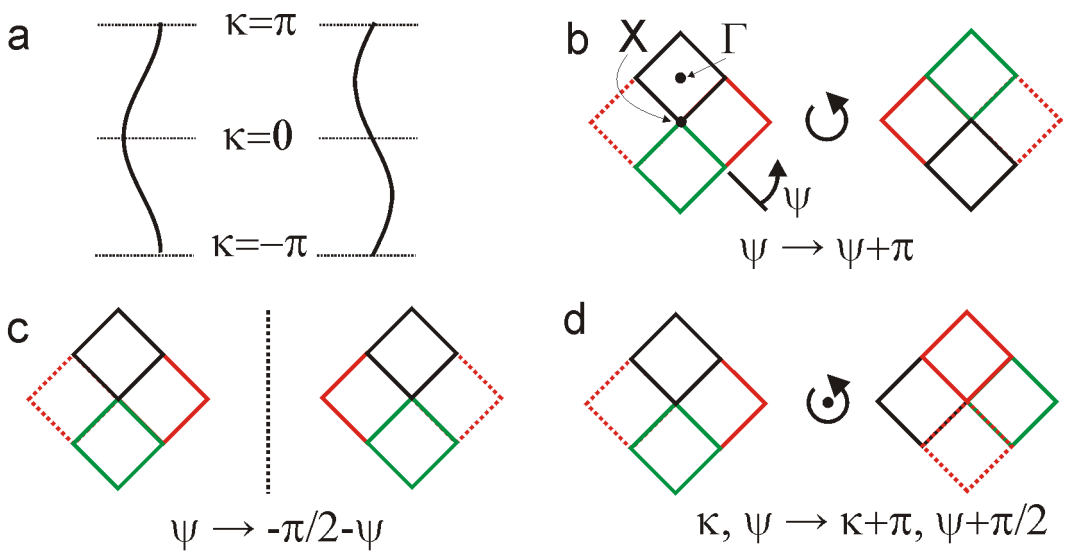

Figure 5.2: (a) Left panel shows $\cos\nu\kappa$ terms which obey the $\kappa \to -\kappa$ symmetry and right panel shows $\sin n\kappa$ terms which do not (b) the two-fold symmetry $\psi \to \psi + \pi$ (c) the mirror symmetry $\psi \to -\pi/2 - \psi$ and (d) the screw symmetry involving a translation in the k_z direction and a rotation $\kappa, \psi \to \kappa + \pi, \psi + \pi/2$.

requires that the only terms containing κ be cosines — see figure 5.2a. Secondly, there is two fold rotational symmetry about the X line i.e. $\psi \to \psi + \pi$ as shown in figure 5.2b which requires all m to be even since $\cos(m\psi) \to \cos(m\psi + m\pi)$ or $\sin(m\psi) \to \sin(m\psi + m\pi)$. Thirdly, there is a mirror symmetry (figure 5.2c) in the plane about a line connecting the X-line and the Γ-line i.e. $\psi \to -\pi/2 - \psi$ which requires that all of the cosine terms have $m \bmod 4 = 0$ and all the sine terms have $m \bmod 4 = 2$ since $\cos(4\psi) = \cos 4(-\pi/2 - \psi)$ whereas $\cos(2\psi) = -\cos 2(-\pi/2 - \psi)$ and the reverse for the sine terms. Finally, there is a screw symmetry (figure 5.2d) involving a rotation by $\pi/2$ and then a translation by π in the z direction i.e. $\kappa, \psi \to \kappa + \pi, \psi + \pi/2$. This requires that all the cosine terms be accompanied by n that are even and the sine terms be accompanied by n that are odd e.g. $\cos(\kappa)\sin(2\psi) = \cos(\kappa + \pi)\sin 2(\pi/2 + \psi)$ but $\cos(2\kappa)\sin(2\psi) = -\cos 2(\kappa + \pi)\sin 2(\pi/2 + \psi)$. Equation 5.43 can now be simplified to:

$$k_F(\psi,\kappa) = \sum_{\substack{m,n=0 \\ m \bmod 4 = 0 \\ n \text{ even}}} k_{mn}\cos(n\kappa)\cos(m\psi) + \sum_{\substack{m,n=0 \\ m \bmod 4 = 2 \\ n \text{ odd}}} k_{mn}\cos(n\kappa)\sin(m\psi) \quad (5.44)$$

k_F is then expanded to the lowest order necessary to fit the data. The n subscript is the layer index so we assume only inlayer ($n = 0$) and nearest layer ($n = 1$) terms are dominant. Therefore:

$$k_F(\psi,\kappa) = k_{00} + k_{40}\cos(4\psi) + k_{21}\cos(\kappa)\sin(2\psi) + k_{61}\cos(\kappa)\sin(6\psi) + k_{101}\cos(\kappa)\sin(10\psi) \quad (5.45)$$

or:

$$k_F(\psi,\kappa) = k_{00}\left(1+\frac{k_{40}}{k_{00}}\cos(4\psi)\right) + k_{21}\cos(\kappa)\left(\sin(2\psi)+\frac{k_{61}}{k_{21}}\sin(6\psi)+\frac{k_{101}}{k_{21}}\sin(10\psi)\right) \quad (5.46)$$

5.2.2 Velocity in the z Direction

The Fermi velocity in the z direction needs to be inserted in equations 5.21 and 5.22. This can be parameterised by taking the energy dispersion for the Fermi surface where the interplane component has a barrel shape modulation as:

$$\varepsilon = \frac{\hbar^2}{2m}\left[k_F^2(\psi) - 2t_\perp\left[k_{21}\sin(2\psi)+k_{61}\sin(6\psi)+k_{101}\sin(10\psi)\right]\cos(\kappa)\right] \quad (5.47)$$

where $k_F(\psi) = k_{00} + k_{40}\cos(4\psi)$. The velocity in the z direction is then given by:

$$v_z(\psi) = \frac{1}{\hbar}\frac{d\varepsilon}{dk_z} = \frac{ct_\perp}{\hbar}\left[k_{21}\sin(2\psi)+k_{61}\sin(6\psi)+k_{101}\sin(10\psi)\right]\sin(\kappa) \quad (5.48)$$

The one remaining integral in equation 5.39 is over dk_z and the only k_z term is in the velocity. The integration needs to be performed over the closed orbits on the Fermi surface in the plane perpendicular to the magnetic field. The exact position of these depends on the orientation of the magnetic field with respect to the k_z direction given by θ in figure 2.9 and its in-plane orientation (due to the 4-fold distortion imposed on the Fermi surface by the k_{40} term) given by ϕ. The extent of this orbit in the k_z direction is shown in figure 2.9 to be $k_F(\psi)\cos\phi\tan\theta$ and so $k_z = k_0 - k_F(\psi)\cos\phi\tan\theta$ which is substituted into equation 5.48 (remembering that $\kappa = k_z c/2$).

5.2.3 Velocity In-plane

With the assumed ψ dependencies of $1/\omega_c(\psi) = (1+\beta\cos 4\psi)/\omega_c$ and $k_F(\psi) = k_{00} + k_{40}\cos(4\psi)$ the ψ dependence of the inplane Fermi velocity $v_F(\psi)$ can be investigated. Taking:

$$\omega_c(\psi) = eB\cos\theta\frac{k_F(\psi)v_F(\psi)}{\hbar k_F(\psi)^2} \quad (5.49)$$

The ψ dependence of $v_F(\psi)$ can now be shown to be:

$$v_F(\psi) \propto \frac{\omega_c(\psi)k_F(\psi)}{\cos(\zeta(\psi))} \quad (5.50)$$

where $\zeta(\psi)$ is the angle between k_F and v_F given by equation 5.88. Considering the saddle point near the M point in the Brillouin zone it would be expected that the velocity in this direction would be lower since $v \propto \partial\varepsilon/\partial\mathbf{k}$ — see left of figure 5.3. For comparison, the right of figure 5.3 shows energy contours calculated from photoemission experiments by Eschrig *et al.*. As a result, the signs and

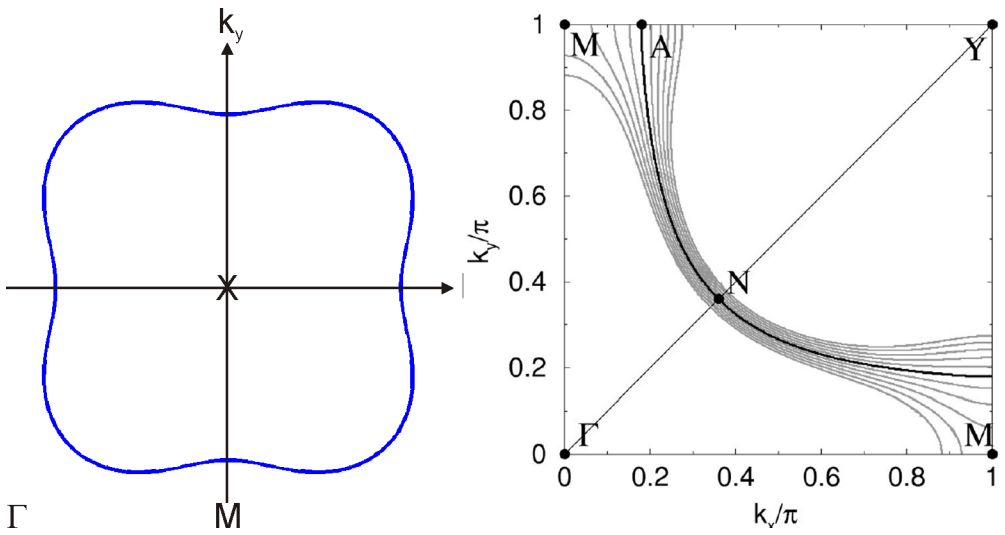

Figure 5.3: Left panel shows the magnitude of in-plane velocity with anisotropy which is consistent with the saddle point in the bandstructure at the M point. Right panel shows the Fermi surface as a black curve and equal energy contours in grey for $Bi_2Sr_2CaCu_2O_{8+x}$. Calculated from tight binding fit to photoemission data. Figure from [102].

magnitudes of k_{40} and β will be linked. If k_{40} is positive, only a negative β with a larger magnitude than k_{40} gives a consistent form for the velocity. If k_{40} is negative, then any negative β or a positive β smaller in magnitude than k_{40} gives the same form.

5.3 ADMR Examples

If the Fermi surface is considered as a simple cylinder as shown in figure 5.4a the parameterisation of the Fermi surface given in equation 5.46 contains only the k_{00} term and there is no angle dependence in the magnetoresistance.

A barrel shaped warping of the Fermi surface can be added with a $\cos(\kappa)$ modulation to $k_F(\psi, \kappa)$ as shown in figure 5.4b. There is now a z-axis dispersion of $k_F(\psi)$ which can be seen in the two dimensional projection of the Fermi surface. As can be seen from the figure, if there is no anisotropy in τ only θ dependence is present in $\Delta\rho_{zz}/\rho_{zz}$. Looking at the bottom right of figure 5.4b where anisotropy is permitted in τ, a ϕ or azimuthal angle dependence in $\Delta\rho_{zz}/\rho_{zz}$ appears.

As described in §5.2.1, terms are added which respect the crystal symmetry. Figure 5.5a shows the addition of a $k_{40}\cos(4\psi)$ in plane modulation which makes the Fermi surface slightly square. Regardless of whether anisotropy is permitted there is now θ and ϕ dependence in the ADMR data.

If a $\sin(2\psi)$ modulation term is now added to the interplane barrel warping as shown in figure 5.5b then the Fermi surface develops lines in the interplane direction along which there is no interplane warping. In the ADMR data a local peak is now observable around $\theta = 0$. Again there is θ and ϕ dependence regardless of the inclusion of anisotropy.

An additional $\sin(6\psi)$ modulation to the interplane warping can be added which provides a first approximation of a θ and ϕ dependent ADMR simulation which fits experimental data — see figure 5.6a.

Finally one further term, a $\sin(10\psi)$ interplane modulation, can be added to give an extremely accurate simulation of the data — see figure 5.6b. Notice that there are now eight (rather than four) lines in the interplane direction along which the interplane warping disappears but these only occur if $k_{101}/k_{21} = k_{61}/k_{21} - 1$.

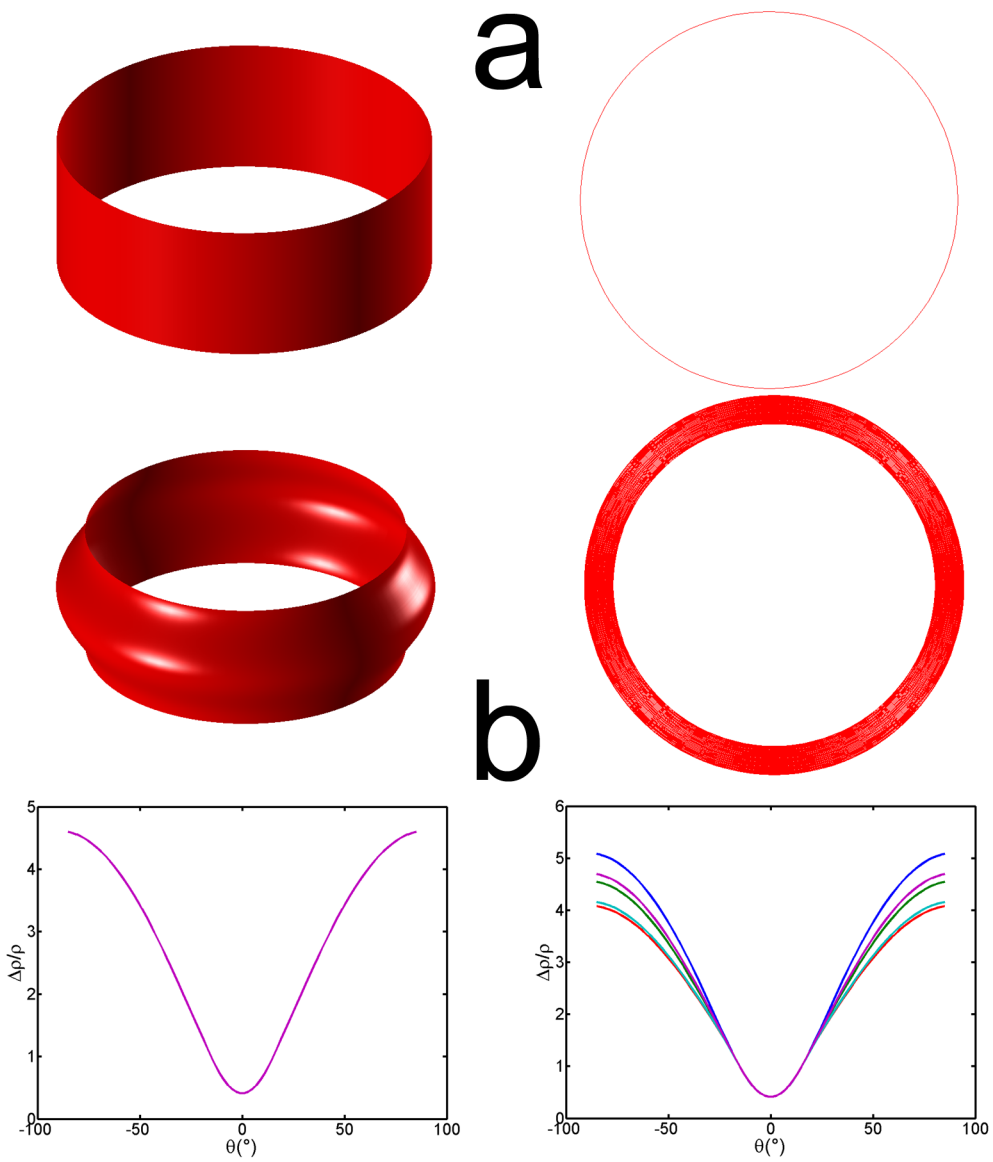

Figure 5.4: Panels around a show $k_F(\psi,\kappa) = k_{00}$. Left panel shows 3D Fermi surface. Right panel shows 2D projection of the 3D Fermi surface. Panels around b show $k_F(\psi,\kappa) = k_{00} + k_{21}\cos(\kappa)$. Top left panel shows 3D Fermi surface. Top right panel shows 2D projection of the 3D Fermi surface. Bottom left panel shows ADMR simulation with isotropic τ and v_F. Bottom right panel shows ADMR simulation with anisotropic τ and v_F. All plots with 5 ϕ angles at 13.3° increments, $k_{00} = 0.729\,\text{Å}^{-1}$, $\omega_c\tau = 0.46$, $\gamma = 0.29$, $\beta = 0$ and all asymmetries $= 0$. Created using the code in sections 10.7.4, 10.7.5 and 10.7.8.

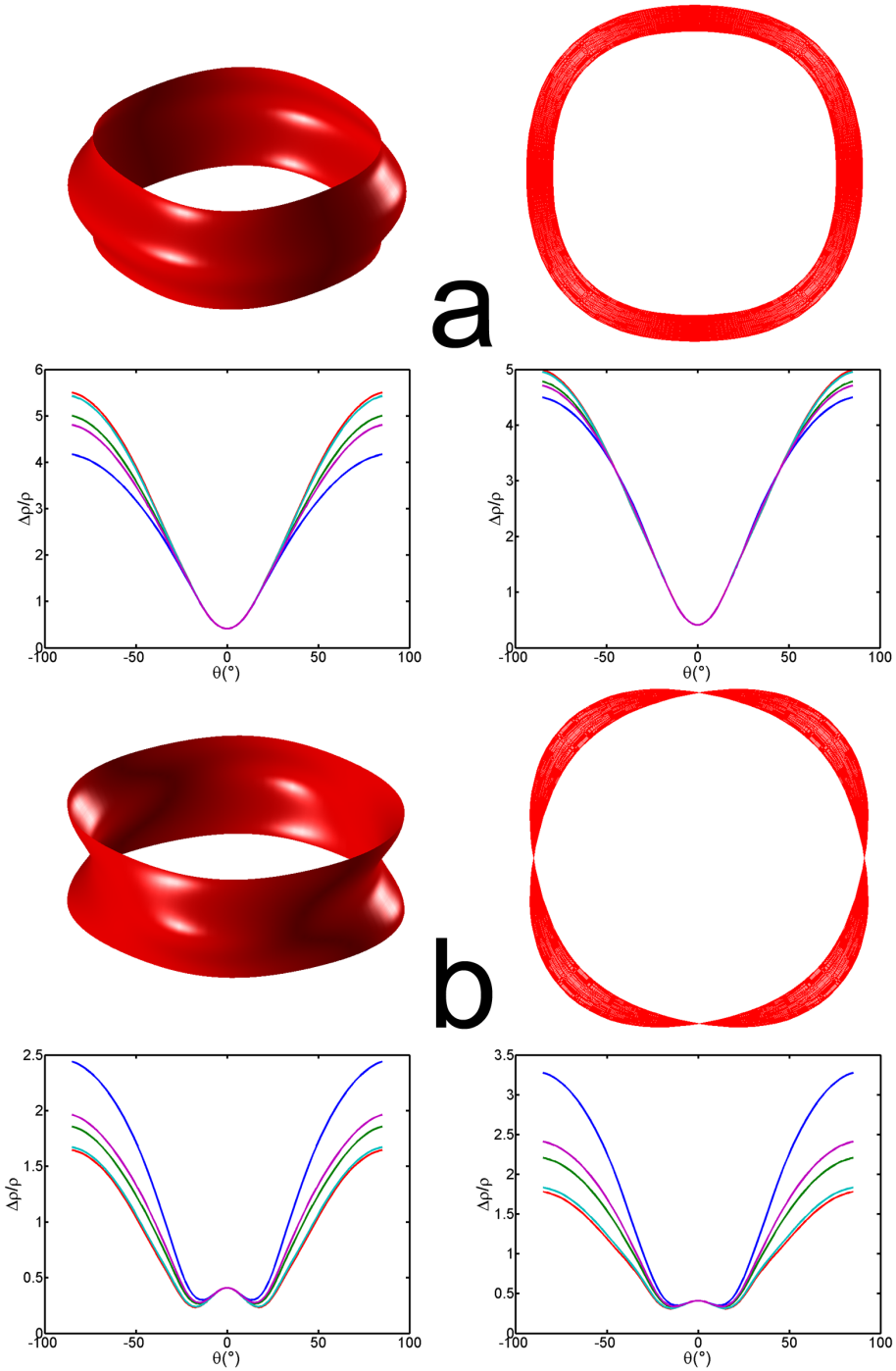

Figure 5.5: Panels around a show $k_F(\psi,\kappa) = k_{00}(1 + k_{40}/k_{00}\cos(4\psi)) + k_{21}\cos(\kappa)$. Top left panel shows 3D Fermi surface. Top right panel shows 2D projection of the 3D Fermi surface. Bottom left panel shows ADMR simulation with isotropic τ and v_F. Bottom right panel shows ADMR simulation with anisotropic τ and v_F. Panels around b show $k_F(\psi,\kappa) = k_{00}(1 + k_{40}/k_{00}\cos(4\psi)) + k_{21}\sin(2\psi)\cos(\kappa)$. Top left panel shows 3D Fermi surface. Top right panel shows 2D projection of the 3D Fermi surface. Bottom left panel shows ADMR simulation with isotropic τ and v_F. Bottom right panel shows ADMR simulation with anisotropic τ and v_F. All plots with 5 ϕ angles at 13.3° increments, $k_{00} = 0.729\,\text{Å}^{-1}$, $k_{40}/k_{00} = -0.03$, $\omega_c\tau = 0.46$, $\gamma = 0.29$, $\beta = 0$ and all asymmetries $= 0$. Created using the code in sections 10.7.4, 10.7.5 and 10.7.8.

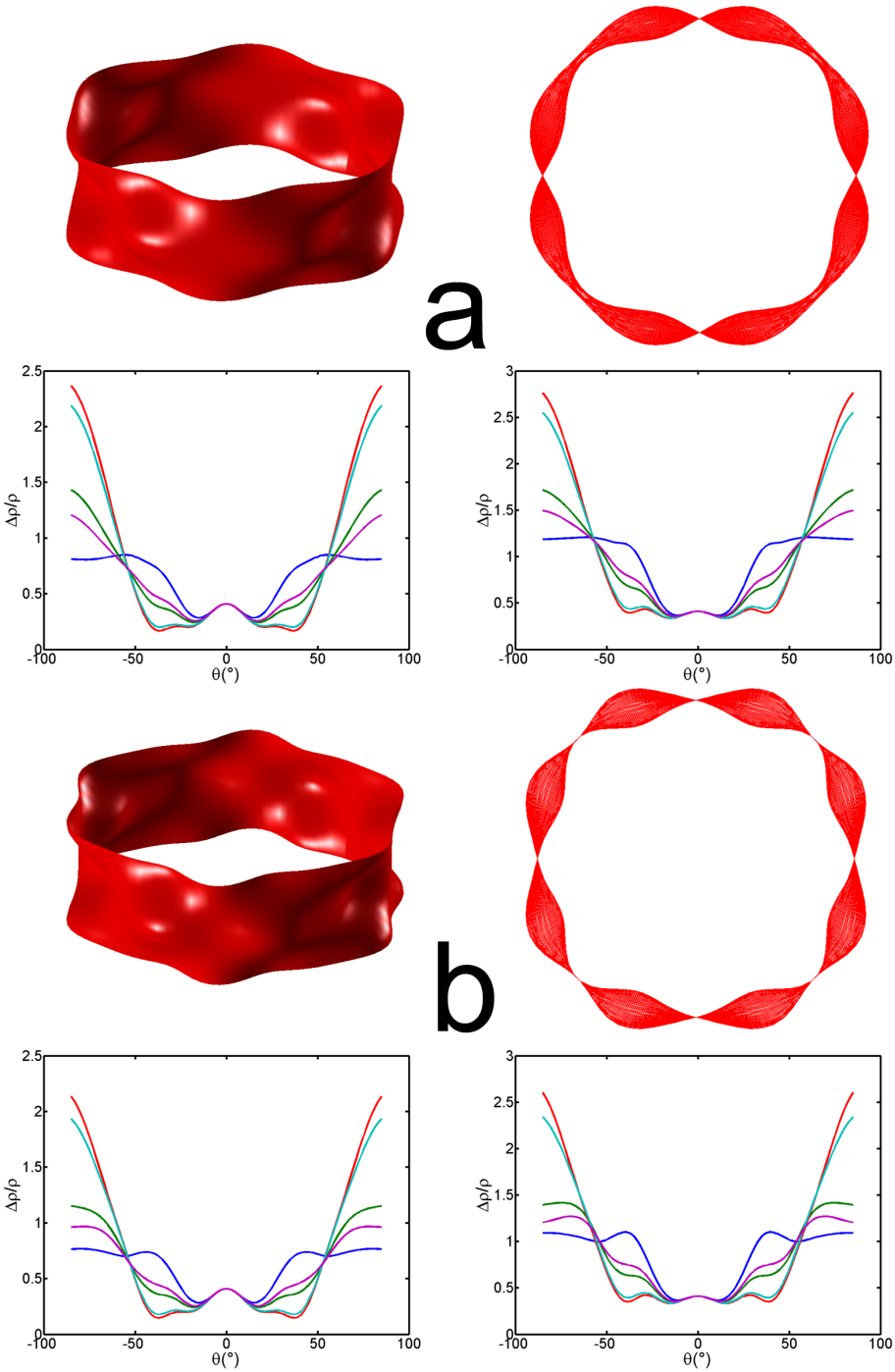

Figure 5.6: Panels around a show $k_F(\psi,\kappa) = k_{00}(1 + k_{40}/k_{00}\cos(4\psi)) + k_{21}\left[\sin(2\psi) + k_{61}/k_{21}\sin(6\psi)\right]\cos(\kappa)$. Top left panel shows 3D Fermi surface. Top right panel shows 2D projection of the 3D Fermi surface. Bottom left panels shows ADMR simulation with isotropic τ and v_F. Bottom right panel shows ADMR simulation with anisotropic τ and v_F. Panels around b show $k_F(\psi,\kappa) = k_{00}(1 + k_{40}/k_{00}\cos(4\psi)) +$
$k_{21}\left[\sin(2\psi) + k_{61}/k_{21}\sin(6\psi) + k_{101}/k_{21}\sin(10\psi)\right]\cos(\kappa)$. Top left panel shows 3D Fermi surface. Top right panel shows 2D projection of the 3D Fermi surface. Bottom left panel shows ADMR simulation with isotropic τ and v_F. Bottom right panel shows ADMR simulation with anisotropic τ and v_F. All plots with 5 ϕ angles at 13.3° increments, $k_{00} = 0.729\,\text{Å}^{-1}$, $k_{40}/k_{00} = -0.03$, $\omega_c\tau = 0.46$, $\gamma = 0.29$, $k_{61}/k_{21} = 0.7$, $k_{101}/k_{21} = -0.3$, $\beta = 0$ and all asymmetries $= 0$. Created using the code in sections 10.7.4, 10.7.5 and 10.7.8.

5.4 Matlab Computer Simulation Program

A number of factors which need to be accounted for when attempting to fit the ADMR data are discussed here. An example of the *Matlab* code is given in §10.7.8

5.4.1 Normalisation of Experimental Data and Simulated Data

Generally it is most instructive to plot $\Delta\rho/\rho$. For the experimental data at fixed temperature, T, this is straight-forward

$$\frac{\rho^{\exp}(\theta) - \rho(B=0)}{\rho(B=0)} \tag{5.51}$$

where $\rho(B=0)$ is the zero field resistivity value at temperature T and any θ dependence implies there is a magnetic field present. Below T_c this can be estimated by fitting $\rho = A + BT + CT^2$.

To normalise the simulated data is more complex. If the experiment and simulation agree then

$$\frac{\Delta\rho^{\mathrm{sim}}}{\rho^{\mathrm{sim}}(B=0)} = \frac{\Delta\rho^{\exp}}{\rho^{\exp}(B=0)} \tag{5.52}$$

It is not straightforward to get an absolute magnitude of $\rho^{\mathrm{sim}}(B=0)$ so equation 5.52 is defined to be true at one point i.e. $\theta=0$ and then $\rho^{\mathrm{sim}}(B=0)$ calculated

$$\frac{\rho^{\mathrm{sim}}(\theta=0) - \rho^{\mathrm{sim}}(B=0)}{\rho^{\mathrm{sim}}(B=0)} = \frac{\rho^{\exp}(\theta=0) - \rho^{\exp}(B=0)}{\rho^{\exp}(B=0)} \tag{5.53}$$

$$\frac{\rho^{\mathrm{sim}}(\theta=0)}{\rho^{\mathrm{sim}}(B=0)} - 1 = \frac{\rho^{\exp}(\theta=0) - \rho^{\exp}(B=0)}{\rho^{\exp}(B=0)} \tag{5.54}$$

$$\frac{\rho^{\mathrm{sim}}(\theta=0)}{\rho^{\mathrm{sim}}(B=0)} = \frac{\rho^{\exp}(\theta=0) - \rho^{\exp}(B=0) + \rho^{\exp}(B=0)}{\rho^{\exp}(B=0)} \tag{5.55}$$

$$\frac{\rho^{\mathrm{sim}}(\theta=0)}{\rho^{\mathrm{sim}}(B=0)} = \frac{\rho^{\exp}(\theta=0)}{\rho^{\exp}(B=0)} \tag{5.56}$$

$$\rho^{\mathrm{sim}}(B=0) = \frac{\rho^{\mathrm{sim}}(\theta=0)\rho^{\exp}(B=0)}{\rho^{\exp}(\theta=0)} = \rho^{\mathrm{sim}}(\theta=0) \times \chi \tag{5.57}$$

where χ is the normalisation factor inserted into the fitting program. The raw simulated data $\rho^{\mathrm{sim}}(\theta)$, is then modified as follows for comparison with the experimental data.

$$\frac{\rho^{\mathrm{sim}}(\theta) - \rho^{\mathrm{sim}}(\theta=0)\chi}{\rho^{\mathrm{sim}}(\theta=0)\chi} \tag{5.58}$$

5.4.2 Estimation of the Magnitude of k_{21}

From fitting the experimental data although it is possible to obtain accurate values for all the other parameters it is not possible to get a magnitude for k_{21}. However, this can be estimated from a

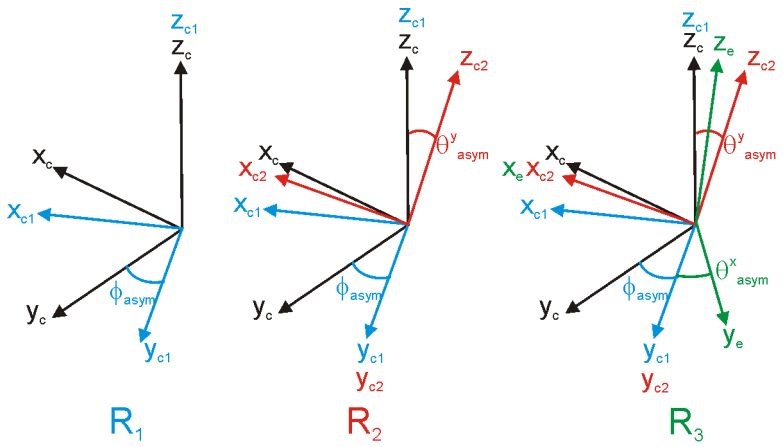

Figure 5.7: Misalignment of experimental rotation axes (e) and the crystallographic rotation axes (c). Shows the three rotations (R_1, R_2, R_3) necessary to convert angles measured with respect to the experimental axes into angles measured with respect to the crystallographic axes.

simplification of the equation given in note 17 on page 689 of [101].

$$\frac{\rho_c}{\rho_{ab}} = \frac{8}{c^2} \frac{1}{k_{21}^2 \left(1 + k_{61}^2/k_{21}^2 + k_{101}^2/k_{21}^2\right)} \tag{5.59}$$

For an anisotropy ratio (ρ_c/ρ_{ab}) of 1000 [77] this gives $k_{21} = 0.0031\,\text{Å}^{-1}$.

5.4.3 Sample Asymmetry Consideration

Very frequently the crystallographic axes of the sample do not exactly coincide with the probe rotation axes meaning that asymmetry is introduced into the ADMR data. In some cases this asymmetry is small (less than approximately 3 degrees) so that it can be neglected and a very good fit still achieved, but in other cases it needs to be accounted for in the simulation. Asymmetry has been considered previously by a number of authors [38], [103], [104]. Here the derivation given in [104] is expanded upon.

A given angular position in an ADMR data set can be defined with respect to either the sample crystallographic axes (θ_{crys} and ϕ_{crys}) or the experimental platform rotation axes (θ and ϕ). It is shown here how to convert an angle (θ,ϕ) from the experimental axes into the sample axes. See figure 5.7. The three rotation matrices are labelled as R_1, R_2 and R_3:

$$\begin{bmatrix} \cos\phi_{\text{crys}} \sin\theta_{\text{crys}} \\ \sin\phi_{\text{crys}} \sin\theta_{\text{crys}} \\ \cos\theta_{\text{crys}} \end{bmatrix} = R_1 R_2 R_3 \begin{bmatrix} \cos\phi \sin\theta \\ \sin\phi \sin\theta \\ \cos\theta \end{bmatrix} \tag{5.60}$$

where:

$$R_3 = \begin{bmatrix} 1 & 0 & 0 \\ 0 & \cos\theta^x_{\text{asym}} & \sin\theta^x_{\text{asym}} \\ 0 & -\sin\theta^x_{\text{asym}} & \cos\theta^x_{\text{asym}} \end{bmatrix} \tag{5.61}$$

$$R_2 = \begin{bmatrix} \cos\theta^y_{\text{asym}} & 0 & \sin\theta^y_{\text{asym}} \\ 0 & 1 & 0 \\ -\sin\theta^y_{\text{asym}} & 0 & \cos\theta^y_{\text{asym}} \end{bmatrix} \tag{5.62}$$

$$R_1 = \begin{bmatrix} \cos\phi_{\text{asym}} & \sin\phi_{\text{asym}} & 0 \\ -\sin\phi_{\text{asym}} & \cos\phi_{\text{asym}} & 0 \\ 0 & 0 & 1 \end{bmatrix} \tag{5.63}$$

Substituting 5.61, 5.62 and 5.63 into 5.60 gives:

$$\begin{aligned} \cos\phi_{\text{crys}}\sin\theta_{\text{crys}} = \\ \cos\phi_{\text{asym}}\left[\cos\theta^y_{\text{asym}}\cos\phi\sin\theta + \sin\theta^y_{\text{asym}}\left[-\sin\theta^x_{\text{asym}}\sin\phi\sin\theta + \cos\theta^x_{\text{asym}}\cos\theta\right]\right] \\ + \sin\phi_{\text{asym}}\left[\cos\theta^x_{\text{asym}}\sin\phi\sin\theta + \sin\theta^x_{\text{asym}}\cos\theta\right] \end{aligned} \tag{5.64}$$

$$\begin{aligned} \sin\phi_{\text{crys}}\sin\theta_{\text{crys}} = \\ -\sin\phi_{\text{asym}}\left[\cos\theta^y_{\text{asym}}\cos\phi\sin\theta + \sin\theta^y_{\text{asym}}\left[-\sin\theta^x_{\text{asym}}\sin\phi\sin\theta + \cos\theta^x_{\text{asym}}\cos\theta\right]\right] \\ + \cos\phi_{\text{asym}}\left[\cos\theta^x_{\text{asym}}\sin\phi\sin\theta + \sin\theta^x_{\text{asym}}\cos\theta\right] \end{aligned} \tag{5.65}$$

$$\cos\theta_{\text{crys}} = -\sin\theta^y_{\text{asym}}\cos\phi\sin\theta + \cos\theta^y_{\text{asym}}\left[-\sin\theta^x_{\text{asym}}\sin\phi\sin\theta + \cos\theta^x_{\text{asym}}\cos\theta\right] \tag{5.66}$$

So

$$\theta_{\text{crys}} = \arccos\left[\text{Right Hand Side Equation 5.66}\right] \tag{5.67}$$

$$\phi_{\text{crys}} = \arctan\left[\frac{\text{Right Hand Side Equation 5.65}}{\text{Right Hand Side Equation 5.64}}\right] \tag{5.68}$$

When samples are misaligned ADMR data become highly asymmetric about $\theta = 0°$. The position of the minimum which usually occurs at $\theta = 0°$ varies with the azimuthal orientation and no longer definitely indicates $B \| c$. The magnitude of magnetoresistance at the minimum also becomes dependent on the azimuthal orientation. These effects are illustrated in simulations in figure 5.8.

The probe on which these measurements were taken does not have a way to monitor the absolute θ angle of the samples. Instead, the parameter recorded is a step number, which is often reset to zero due to computer crashes. As a result of this and backlash it is almost impossible to accurately align ADMR traces in θ when there is asymmetry. The most robust approach is to simply align all the

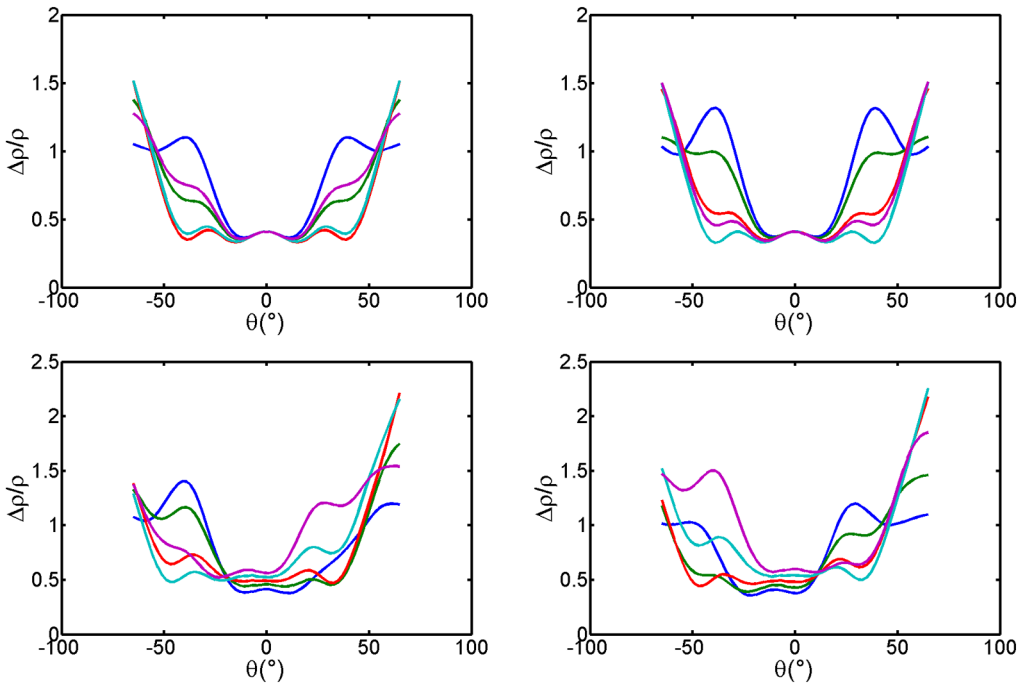

Figure 5.8: Effect of sample asymmetry on ADMR. All plots with 5 ϕ angles at 13.3° increments, $k_{00} = 0.729\,\text{Å}^{-1}$, $k_{40}/k_{00} = -0.03$, $\omega_c\tau = 0.46$, $\gamma = 0.29$, $k_{61}/k_{21} = 0.7$, $k_{101}/k_{21} = -0.3$, $\beta = 0$ and all other asymmetries = 0. Top left panel is with no asymmetry. Top right panel is with $\phi_{\text{asym}} = 10°$. Bottom left panel is with $\theta^x_{\text{asym}} = 10°$. Bottom right panel is with $\theta^y_{\text{asym}} = 10°$.

minima in θ manually and then account for this in the fitting program by considering what happens when $\theta_{\text{crys}} = \pi/2$. Equation 5.67 can be simplified and rearranged to give (note $\pi/2$ is subtracted to convert the absolute angle into an angle shift θ_{centre}):

$$\theta_{\text{centre}} = \arctan\left[\frac{\cos\theta^y_{\text{asym}}\cos\theta^x_{\text{asym}}}{\sin\theta^y_{\text{asym}}\cos\phi + \cos\theta^y_{\text{asym}}\sin\theta^x_{\text{asym}}\sin\phi}\right] - \frac{\pi}{2} \tag{5.69}$$

This θ_{centre} can be added to simulated data in order for it to align with the modified experimental data. The change in magnitude of the magnetoresistance is accounted for by having a different χ factor in the normalisation.

5.4.4 Minimisation Routine

The *Matlab* ADMR simulation script was modified to allow experimental data to be fitted by varying a number of parameters. The process of obtaining the best fit is basically one of minimising a function which is the sum of the square differences between each experimental point and a simulated point at the same angle. Efficient methods of function minimisation have long been an area of research in computer science resulting in numerous algorithms such one developed by Levenberg-Marquardt or the Nelder-Mead [105] simplex method which is used here. *Matlab* implements this using its *fminsearch* routine in the optimisation toolbox. The routine was modified to give an estimate of the errors on the parameters by calculating the covariance matrix, see §10.7.7.

As a demonstration consider a function with two parameters so the simplex is a triangle. The function to be minimised, f, is first evaluated at each of the three vertices of the triangle and the vertices ordered B(est), G(ood), W(orst) with increasing values of f. From W to B and W to G the value of the function decreases so it's feasible that f is smaller at values away from W so the triangle is reflected about the line joining B and G giving a new vertex R. The point M is defined as the point halfway between B and G (see figure 5.9a).

Consider the case where $f(R) < f(G)$. If $f(B) < f(R)$ then W is replaced with R, otherwise the simplex is extended. The line joining M and R is extended to point E. Now, if $f(E) < f(B)$ then W is replaced with E, otherwise W is replaced with R (see figure 5.9b). The process now repeats by calculating a new R point until the function falls below a pre-set tolerance or is evaluated a limiting number of times.

The alternative situation is $f(R) > f(G)$. If $f(R) < f(W)$ then W is replaced with R, otherwise the simplex is contracted. The points C_1 and C_2 are calculated (see figure 5.9c) and the point with the smaller function value is called C. If $f(C) < f(W)$ then W is replaced with C, otherwise the point S is calculated as halfway between B and W and the simplex is shrunk to BMS (see figure 5.9d). This process repeats until a predefined convergence criterion is reached such as f becoming less than a certain value, failing to change between successive iterations or a maximum number of iterations

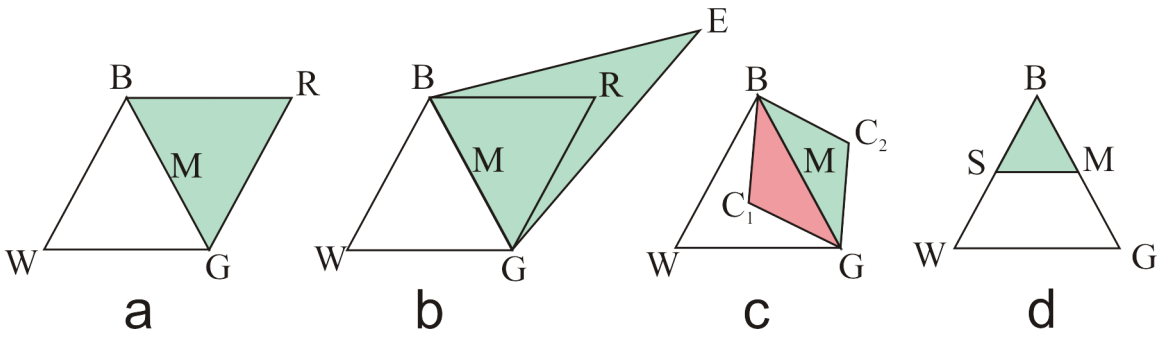

Figure 5.9: The different triangles involved in a two parameter version of the Nelder-Mead function minimisation algorithm.

is reached.

5.5 Inplane Resistivity and Hall Effect Derivation for Quasi-2D Cylindrical Fermi Surface

The inplane zero field resistivity can be calculated using only parameters for which values are available from fitting ADMR data. The required equations are shown in [36] but are derived in full here. Equation 2.21 gives

$$\sigma_{xx} = \frac{1}{4\pi^3} \int e^2 v_x v_r \tau \left(-\frac{\delta f^0_{\mathbf{k}}}{\delta \varepsilon} \right) d^3k \tag{5.70}$$

For a quasi 2D cylinder $d^3k = dk_r dS$ where v_r and k_r are radial and dS is a surface:

$$v_r = \frac{1}{\hbar} \frac{d\varepsilon}{d\mathbf{k}} \text{ so } dk_r = \frac{d\varepsilon}{\hbar v_r} = \frac{d\varepsilon}{\hbar v_F \cos\zeta} \tag{5.71}$$

where ζ is the angle between v_F and v_r. If $dS = dk_z k_F d\psi$:

$$d^3k = \frac{dS}{\hbar} \frac{d\varepsilon}{v_F \cos\zeta} = \frac{dk_z d\psi k_F d\varepsilon}{\hbar v_F \cos\zeta} \tag{5.72}$$

If the z dependence is neglected and $c = 23.13\,\text{Å}$:

$$\int d^3k = \frac{4\pi}{c} \frac{k_F}{\hbar v_F \cos\zeta} \int_0^{2\pi} d\psi \int d\varepsilon \tag{5.73}$$

So:

$$\sigma_{xx} = \frac{1}{4\pi^3} e^2 v_x v_x \tau \left(-\frac{\delta f^0_{\mathbf{k}}}{\delta \varepsilon} \right) \frac{4\pi}{c} \frac{k_F}{\hbar v_F \cos\zeta} \int_0^{2\pi} d\psi \int d\varepsilon \tag{5.74}$$

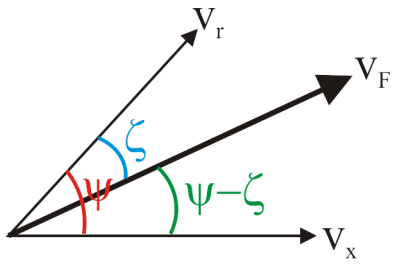

Figure 5.10: Geometry of velocity components, showing definitions of ψ and ζ angles.

Noting $\int -\delta f^0_{\mathbf{k}}/\delta\varepsilon \cdot d\varepsilon$ is 1 at the Fermi surface and 0 elsewhere:

$$\sigma_{xx} = \frac{1}{4\pi^3}\frac{4\pi}{c}\frac{e^2}{\hbar}\int_0^{2\pi}\frac{k_F v_x^2 \tau}{v_F \cos\zeta}d\psi \tag{5.75}$$

Also, $v_x = v_F\cos(\psi-\zeta)$ where ψ is the angle between v_x and v_r and $(\psi-\zeta)$ is the angle between v_x and v_F — see figure 5.10:

$$\sigma_{xx} = \frac{1}{4\pi^3}\frac{4\pi}{c}\frac{e^2}{\hbar}\int_0^{2\pi}\frac{k_F v_F \tau \cos^2(\psi-\zeta)}{\cos\zeta}d\psi \tag{5.76}$$

Explicitly noting any ψ dependencies and $\omega_c = eBk_F v_F/\hbar k_F^2$ this can be re-expressed as:

$$\sigma_{xx} = \frac{4e}{\pi^2 cB}\int_0^{\frac{\pi}{2}}\frac{\omega_c\tau(\psi)k_F(\psi)^2\cos^2(\psi-\zeta)}{\cos\zeta}d\psi \tag{5.77}$$

A simple comparison with the Drude result can be made by assuming a circular inplane cross section for the Fermi surface so that $\gamma = 0$ and therefore $\int_0^{2\pi}\cos^2\psi d\psi = \pi$:

$$\sigma_{ij} = \frac{1}{4\pi^3}\frac{4\pi^2}{c}\frac{e^2}{\hbar}k_F v_F \tau \tag{5.78}$$

Taking the carrier density factor from earlier out of equation 5.78 and using $v_F = \hbar k_F/m$ gives exactly the Drude result for the conductivity.

The Hall effect, $\sigma^{(1)}_{xy}$, can also be calculated in a similar way but taking account of the magnetic field. The Jones-Zener expansion of the relaxation time approximation (equation 5.1) is used:

$$g_k^{(n)} = -\left(\frac{e\tau}{\hbar}\left[\mathbf{v}_r\times\mathbf{B}\right]\frac{\delta}{\delta k}\right)^n\left(e\tau\mathbf{E}\cdot\mathbf{v}_r\left(-\frac{\delta f_k^0}{\delta\varepsilon}\right)\right) \tag{5.79}$$

so substituting into equation 2.20 with $n = 1$ gives:

$$\sigma^{(1)}_{ij} = \frac{1}{4\pi^3}\int ev_i\left(-\frac{e\tau}{\hbar}\left[\mathbf{v}_r\times\mathbf{B}\right]\frac{\delta}{\delta\mathbf{k}}\right)\left(\tau e v_j\left(-\frac{\delta f^0_{\mathbf{k}}}{\delta\varepsilon}\right)\right)d^3k \tag{5.80}$$

Using $\delta\mathbf{k}=k_F\delta\psi$:

$$[\mathbf{v}_r \times \mathbf{B}]\,\frac{\delta}{\delta\mathbf{k}} = \frac{v_F\cos\zeta B}{k_F}\frac{\delta}{\delta\psi} \tag{5.81}$$

and noting that from equation 2.54 σ_{xy} is required:

$$\sigma_{xy}^{(1)} = \frac{1}{4\pi^3}\int ev_x\left(-\frac{e\tau}{\hbar}\frac{v_F\cos\zeta B}{k_F}\right)\frac{\delta}{\delta\psi}\left(\tau ev_y\left(-\frac{\delta f_{\mathbf{k}}^0}{\delta\varepsilon}\right)\right)d^3k \tag{5.82}$$

Using:

$$\int -\frac{\delta f_{\mathbf{k}}^0}{\delta\varepsilon}d^3k = \frac{4\pi}{c}\int_0^{2\pi}\frac{k_F(\psi)}{\hbar v_F\cos\zeta}d\psi \tag{5.83}$$

$$\sigma_{xy}^{(1)} = \frac{1}{4\pi^3}ev_x\left(-\frac{e\tau}{\hbar}\frac{v_F\cos\zeta B}{k_F}\right)\frac{\delta}{\delta\psi}\left(\tau ev_y\frac{4\pi}{c}\int_0^{2\pi}\frac{k_F}{\hbar v_F\cos\zeta}d\psi\right) \tag{5.84}$$

$$= -\frac{1}{4\pi^3}\frac{4\pi}{c}\frac{e^3B}{\hbar^2}\int_0^{2\pi}v_x\tau\frac{\delta}{\delta\psi}\tau v_y d\psi \tag{5.85}$$

Noting that $v_x=v_F\cos(\psi-\zeta)$ and $v_y=v_F\sin(\psi-\zeta)$ as used in equation 5.76 and due to the crystal symmetry $\int_0^{2\pi}=4\int_0^{\frac{\pi}{2}}$:

$$\sigma_{xy}^{(1)} = -\frac{1}{\pi^3}\frac{4\pi}{c}\frac{e^3B}{\hbar^2}\int_0^{\frac{\pi}{2}}v_F\tau\cos(\psi-\zeta)\frac{\delta}{\delta\psi}v_F\tau\sin(\psi-\zeta)d\psi \tag{5.86}$$

Again a substitution can be made for v_F and noting explicitly the ψ dependence:

$$\sigma_{xy}^{(1)} = -\frac{1}{\pi^3}\frac{4\pi}{c}\frac{e}{B}\int_0^{\frac{\pi}{2}}k_F(\psi)\omega_c\tau(\psi)\cos(\psi-\zeta)\frac{\delta}{\delta\psi}k_F(\psi)\omega_c\tau(\psi)\sin(\psi-\zeta)d\psi \tag{5.87}$$

A program was written in *Delphi* (see §10.8.1) to simulate the inplane resistivity and Hall effect using the equations derived above. Values for k_{00} and k_{40}/k_{00} are taken from the ADMR fit. Since v_F is always perpendicular to the Fermi surface the $\zeta(\psi)$ angle is given geometrically as:

$$\zeta(\psi) = \tan^{-1}\left[\frac{\delta}{\delta\psi}\ln k_F(\psi)\right] \tag{5.88}$$

In order to calculate a temperature dependence of ρ_{ab} or R_H the temperature dependence of $\omega_c\tau$ is required. This is calculated by performing a fit of $\omega_c\tau$ and γ parameters from the ADMR analysis as a function of temperature — see §6.2.5.

5.6 Wien2K

The problem of computationally modelling the behaviour of electrons in a crystal from first principles and calculating the band structure and Fermi surface of a material initially appears very complex as a many body Schrodinger equation needs to be solved with 10^{23} interacting electrons and nuclei. In

the general case this problem is nearly intractable. However, progress can be made by making some relevant approximations which simplify the Hamiltonian. The Born-Oppenheimer approximation is applied which treats the nuclei as fixed and separates the vibrational, translational, and rotational motions. Using the Kohn-Sham equations, the Kohn-Sham Hamiltonian can be expressed in the form:

$$\hat{H}_{\mathrm{KS}} = \hat{T}[\rho] + \hat{V}_H[\rho] + \hat{V}_{\mathrm{xc}}[\rho] + \hat{V}_{\mathrm{ext}}[\rho] \tag{5.89}$$

where $\hat{T}$ is the kinetic energy term, $\hat{V}_H$ is the Hartree term, $\hat{V}_{\mathrm{xc}}$ is the exchange correlation term and $\hat{V}_{\mathrm{ext}}$ is the external potential term. These all depend on the electron density function $\rho(r)$ and so are called functionals. Applying the Schrodinger equation gives:

$$\hat{H}_{\mathrm{KS}}\psi_i = \varepsilon_i\psi_i \tag{5.90}$$

The electron density function can be expressed:

$$\rho_n(r) = \sum \psi_i(r)^*\psi_i(r) \tag{5.91}$$

This is now formulated as a self consistent problem where an initial $\rho_0(r)$ is guessed. The Hamiltonian is calculated (equation 5.89) and the eigenvalue problem solved (equation 5.90). Using the resulting wavefunctions a new $\rho_1(r)$ is constructed (equation 5.91). If $\rho_1(r) \neq \rho_0(r)$ then the input density can be slightly modified and the process repeated. Approximations also need to be made about the form of the wavefunctions ψ. In the Linear Augmented Plane Wave (LAPW) approximation there are non-overlapping spheres centred on each atom in which the most suitable form for the wavefunction basis sets are radial functions multiplied by spherical harmonics; due to its shape this is sometimes referred to as a 'muffin tin'. The rest of the space around the spheres is best represented by simpler plane-wave functions.

Wien2K [106] is a computational package which allows these calculations to be performed in a relatively straightforward way for many materials. It consists of a number of Unix programs which perform the steps described above which are linked together in a simple script.

1. *LAPW0* — Generates the potentials from the density functions.
2. *LAPW1* — Calculates the valence bands' energy values and eigenvectors.
3. *LAPW2* — Calculates the new valence densities from the eigenvectors.
4. *LCORE* — Computes the same procedure as *LAPW1* and *LAPW2* but for the core densities.
5. *MIXER* — The mixer combines the newly calculated densities and compares the value to the original. If convergence is reached the program stops. If not, the new density is input back into *LAPW0* and the process repeats.

Each of these programs takes inputs in the form of text files and also writes output to text files. Initially a number of text files need to be generated to setup the calculation. To simplify creating these files and running a calculation, *Wien2K* provides a interface which can be operated from a web browser called *w2web*. The calculation is performed for a finite number of points in the **k**-space of the Brillouin zone of the material on a '**k**-mesh'. More points means a finer mesh and more accurate results but takes longer. Typical calculations will involve between 1,000 and 100,000 **k**-points in the whole Brillouin zone. This is reduced automatically by only considering points within a small wedge of the Brillouin zone which can be repeated to represent the whole zone by symmetry arguments. The calculation can take anything from a few seconds to a few weeks to perform and scales roughly linearly in the number of **k**-points and as the number of atoms in the unit cell to the power of three. The calculation terminates at the convergence precision specified. A good description of the actual use of *Wien2K* and *w2web* is provided in the *Wien2K* user manual [107].

For calculations on $Tl_2Ba_2CuO_{6+\delta}$ performed here the symmetrised positions of the atoms in the unit cell in table 3.1 were used. After the calculation is complete either the Fermi surface or the band structure can be plotted. The Fermi surface can be plotted with a accompanying program called *xcrysden* or with *Matlab* using some programs written by Edward Yelland. The files required by *Matlab* are *case.energy*, *case.klist*, *case.output2*, *case.outputkgen*, *case.scf2* and *case.struct*. The band structure is calculated and plotted with *Matlab* or *Wien2K* using the *w2web* interface along a path in reciprocal space specified in a *case.klist_band* file. This can be generated very easily in *xcrysden* by clicking points in the Brillouin zone. Note that *xcrysden* uses the primitive unit cell while selecting the **k**-path but converts this into the conventional unit cell format required for *Wien2K* when the *case.klist_band* file is output.

5.6.1 Virtual Crystal Approximation

A first approximation to get a more accurate bandstructure is to perform a rigid band shift by simply moving the Fermi level a small amount to see how the Fermi surface changes. A potentially more accurate calculation of the band structure and Fermi surface of $Tl_2Ba_2CuO_{6+\delta}$ is achieved by considering the doping of an additional δ oxygen atoms into the structure. The problem which now needs to be solved is how to actually perform this in the *Wien2K* program. For example if $\delta = 0.1$ additional oxygen atoms then the unit cell could be expanded to 10 times the size and all the atom locations specified individually along with an additional oxygen atom in one cell. This works in theory, but the speed of *Wien2K* calculations scales approximately as the number of atoms cubed, which suggests that this would take around 50,000 times longer than the simple calculation with $\delta = 0$.

The doping with additional oxygen atoms can be simulated in a computationally efficient way by changing the nuclear charge and number of electrons associated with the Tl atoms; this is called the

virtual crystal approximation (VCA). With $\delta = 0.1$ the share of this on each Tl atom is 0.1 since there are 0.1 oxygen atoms (with valence -2) for two Tl atoms. Using the *w2web* interface for *Wien2K* the calculation is set up as normal with *StructGen*. The buttons on the '*initialize calc*' page are clicked until just before the '*prepare input files*' button. The *case.struct* file is then manually edited to change the charge on the Tl atom from 81 to 80.90.

```
Tl          NPT=  781  R0=0.00000500 RMT=    1.8700   Z: 80.90
```

Then in the *case.inst* file the number of electrons is altered for charge neutrality on the Tl atom. The last electron normally has an occupancy of 1, but here is changed to 0.9.

```
Tl
Xe 6
4, 3,3.0 N
4, 3,3.0 N
4,-4,4.0 N
4,-4,4.0 N
5, 2,2.0 N
5, 2,2.0 N
5,-3,3.0 N
5,-3,3.0 N
6,-1,1.0 N
6,-1,1.0 N
6, 1,0.9 N
6, 1,0.0 N
```

Back on the initialisation page the '*prepare input files*' button is now pressed. Lastly the *case.in2* file is edited to alter the number of electrons in a unit cell above the energy which separates the core and valence states. With 2 Tl atoms per formula unit this means that there are $2 \times 0.1 = 0.2$ less electrons so 131 becomes 130.8. The calculation is then continued as normal.

```
TOT             (TOT,FOR,QTL,EFG,FERMI)
     -11.0     130.8 0.50 0.05                EMIN, NE, ESEPERMIN, ESEPER0
```

5.7 dHvA and SdH Analysis

This section describes how experimental quantum oscillations data can be analysed to give the oscillation frequency and the quasiparticle effective mass. For example the data shown in figure 5.11 is electrical resistance data obtained from a pulsed magnetic field. The first stage is to spilt the data into up and down sweeps and to trim off the lower field data where no oscillations occur.

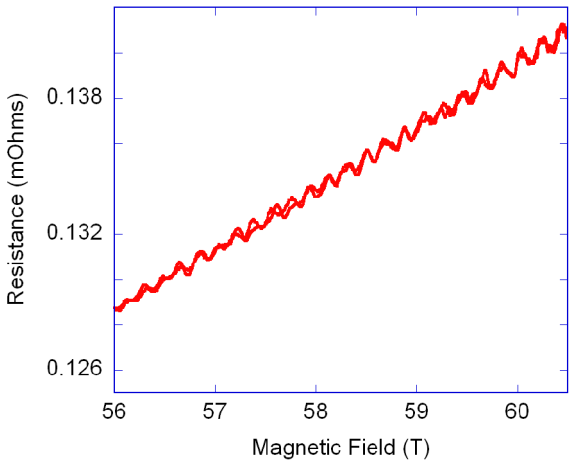

Figure 5.11: Example of electrical resistance data showing SdH oscillations.

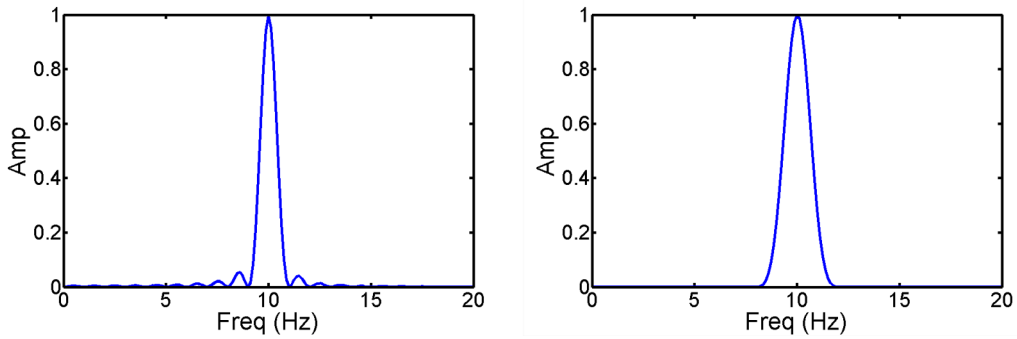

Figure 5.12: Fast Fourier transform of a sine wave with frequency 10 Hz. Left panel shows leakage with no windowing function present. Right panel shows leakage reduced with a windowing function.

Usually the down sweep data will be examined as this sweep is slower. SdH data is converted into $\Delta\rho/\rho_0$ using an extrapolated ρ_0 value as the sample is superconducting at very low fields. Next, a background polynomial needs to be fitted and subtracted to either the data plotted as a function of B or $1/B$. A fast Fourier transform (FFT) is then taken of the resulting oscillation amplitude against $1/B$ in order to find the frequency of the oscillations. However, before taking the fast Fourier transform some important points must be considered. Firstly, if the trimmed oscillation data does not contain an integer number of periods in $1/B$ then leakage will occur in the Fourier transform spectrum potentially obscuring some frequencies or adding spurious ones. This can be minimised by multiplying the original data by a window function which drops to zero at the limits of the trimmed data. For example see figure 5.12 where a 'Hann' window function has been applied to a simple sine wave with frequency 10 Hz where N is the number of data points and n is an integer between 0 and N.

$$H(n) = 0.5\left(1 - \cos\left(\frac{2\pi n}{N-1}\right)\right) \tag{5.92}$$

Secondly, the fast Fourier transform must be performed on $N = 2^k$ points where k is an integer. The oscillation frequency will show up as a peak in the fast Fourier transform spectrum. The amplitude is also noted. Using the Onsager equation (2.67) the frequency can be related to a cross-sectional area of the Fermi surface. The code written to implement this on experimental data is shown in §10.7.11.

If SdH data can be taken at a number of different constant temperatures, the Lifshitz-Kosevich formula (see §2.10) may be applied to give a value for the effective mass, m^*, of the quasiparticles. As a first approach the data at each temperature can be fitted to equation 2.70. The field dependence of R_T can be neglected and $\omega_c\tau/B$, F and ϕ fixed to the values found at the lowest temperature so that any changes in the FFT amplitude represents changes in R_T at the average magnetic field. A fit of the equation given above for R_T to the FFT amplitude verses T yields the quasiparticle effective mass (see code in §10.7.12). A more accurate method involves fitting the data at all temperatures to equation 2.70 simultaneously.

Chapter 6

$Tl_2Ba_2CuO_{6+\delta}$ T_c=15-40K ADMR

This chapter reports new ADMR measurements on $Tl_2Ba_2CuO_{6+\delta}$ over an expanded temperature range (4.2 K – 110 K) and also shows the first temperature dependence for samples with $T_c > 20$ K. Furthermore, these new data have been taken at up to five different azimuthal angles (the angle between the field and the CuO bond), adding robustness to the analysis procedure originally used in previous work [26], [37]. The scattering rate is again found to consist of an isotropic component with a quadratic temperature dependence and an anisotropic component with a linear temperature dependence (at least below 50 K). Using this large quantity of new data the temperature and doping dependence of the scattering rate components are unveiled. The work is also extended to cover samples with different impurities and to discuss relevant experimental work on the same material by other groups.

Importantly, the parameters obtained from this analysis for the size of the Fermi surface agree with those found by ARPES [25] and the SdH and dHvA work reported in [27] and the next chapter. Also, the parameters provide all that is necessary to calculate the temperature dependence of the zero field in-plane resistivity and the Hall coefficient which agree well with experiment. With further recent evidence from work on overdoped LSCO [39], this now well established linear component of the scattering rate seems to be correlated with the emergence of superconductivity from the overdoped side of the phase diagram. Although the origin of this linear component is yet to be determined, its identification provides a new handle on the mystery of high temperature superconductors.

6.1 Experimental Data

Data were taken over the course of two separate weeks of magnet time in April 2006 and April 2008. For three 'low T_c' samples there are high quality data covering up to five azimuthal angles at temperatures between 4.2 K and 110 K: tl300c1 with $T_c = 20$ K; tl320c3 with $T_c = 17$ K; and tl320c5 with $T_c = 15$ K. For two 'higher T_c' samples there are data covering five azimuthal angles at temperatures

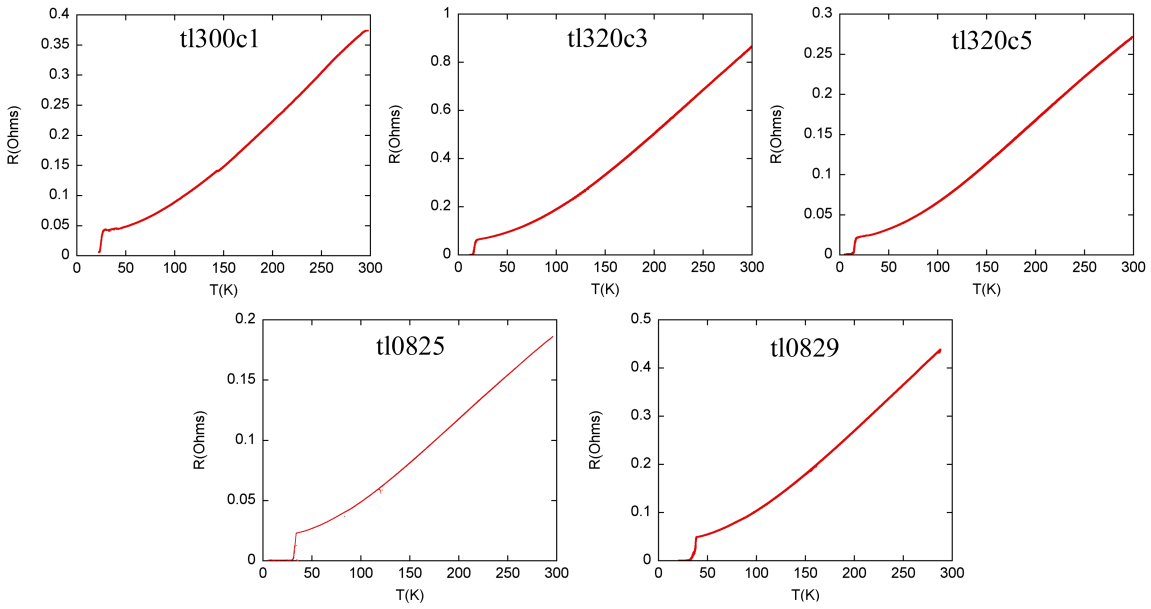

Figure 6.1: Zero field c-axis resistivity measurements for samples tl300c1, tl320c3, tl320c5, tl0825 and tl0829.

between 15 K and 70 K: tl0825 with $T_c = 33$ K and tl0829 with $T_c = 38$ K. Zero field c-axis resistance measurements for these samples are shown in figure 6.1. Samples tl300c1, tl320c3 and tl320c5 had electrical contacts attached with 6838 silver epoxy but Epotec silver epoxy was used for samples tl0825 and tl0829. ADMR data are shown in figures 6.7 – 6.11.

6.2 Analysis

Data were analysed using the methods and ideas laid out in chapter 5. Starting with the simplest case of isotropic τ and v_F the lowest temperature data were fitted. Keeping an isotropic τ and v_F is then shown to fail to fit the data at higher temperatures without substantial and unexpected changes to the Fermi surface. The inclusion of anisotropy in τ and v_F is shown to be necessary to restore the quality of the fit.

The k_{00} parameter was set to the value given by the hole counting procedure in equation 3.8 as it reduces the number of free parameters. However, it can be included in the fit and minimises to a value very close to the calculated value and that measured by ARPES and quantum oscillations.

6.2.1 Isotropic τ and ω_c

As a starting point, let us assume an isotropic τ and ω_c. The fitting procedure begins by evaluating σ_{zz} for a given polar angle θ_{crys} and azimuthal angle ϕ_{crys} using equation 5.39. This is then inverted to give ρ_{zz}. Taking sample tl320c3 as an example, the 4.2 K experimental data are shown on the

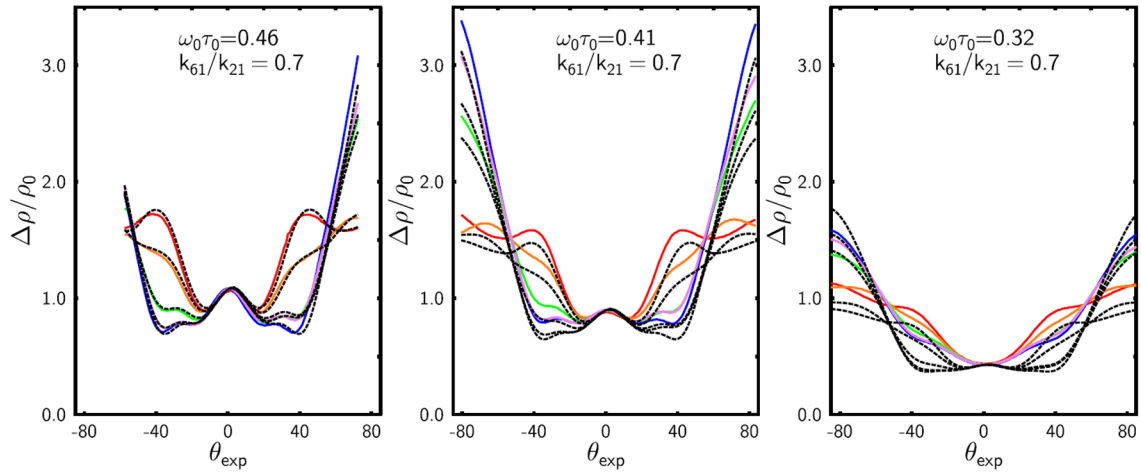

Figure 6.2: ADMR data for sample tl320c3 at 45 T normalised to the zero field c-axis resistivity. Solid coloured lines are experimental data and black dashed lines are best least squares fits. Red $\phi = 8°$, orange $\phi = 18°$, green $\phi = 32°$, blue $\phi = 45°$ and purple $\phi = 55°$. Left panel at 4.2 K, centre panel at 14 K and right panel at 50 K. All fits with isotropic τ and ω_c. Figure from [104].

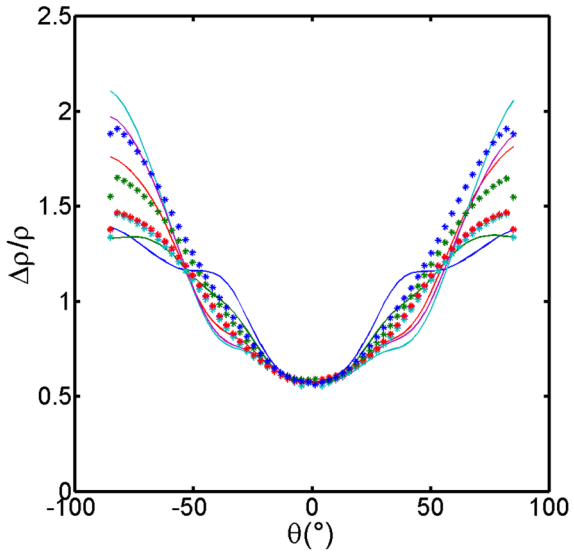

Figure 6.3: ADMR data for sample tl320c3 at 45 T normalised to the zero field c-axis resistivity. Solid lines are experimental data and asterisks are best least squares fits. Dark blue $\phi = 8°$, green $\phi = 18°$, red $\phi = 32°$, light blue $\phi = 45°$ and purple $\phi = 55°$. $T = 40$ K data with all Fermi surface parameters free.

left in figure 6.2. The coloured lines are normalised ADMR data, with each colour representing a different azimuthal angle at which a polar ADMR sweep was taken. The best least squares fits are shown as black dashed lines. The 4.2 K data show a good fit to the simulated data, suggesting that both τ and ω_c are isotropic at low temperatures. Moving to the higher temperature data, there is no expectation of any dramatic change to the Fermi surface so the **k**-parameters should be approximately the same as for the 4.2 K sample. Allowing only $\omega_c\tau$ to change as the temperature increases means the quality of the fits rapidly deteriorate — see centre and right of figure 6.2. In fact if all the parameters are freed and a fit to higher temperature data is performed this results in an improved fit (see figure 6.3) but still with significant differences from the experimental data. The best parameters were $\omega_c\tau = 0.170 \pm 0.006$, $k_{00} = 1.052 \pm 0.015\,\text{Å}^{-1}$, $k_{40}/k_{00} = 0.017 \pm 0.006$ and $k_{61}/k_{21} = 0.573 \pm 0.065$ which represents a significant topological change to the Fermi surface at 40 K compared to 4.2 K including a 20 % increase in the Fermi surface cross-sectional area. This is highly unlikely as the magnitude of $R_H(T)$, which in conventional metals is directly linked to the number of carriers in the system, changes by only a very small amount over this temperature range.

In response to the failing of this isotropic picture and considering recent suggestions of anisotropy discussed earlier, anisotropy in $\tau(\psi)$ and $\omega_c(\psi)$ is incorporated into the formalism.

6.2.2 Anisotropic $\omega_c(\psi)$

Respecting the in-plane four-fold symmetry of the crystal structure the simplest form which allows the inclusion of anisotropy in $\omega_c(\psi)$ is given by:

$$\frac{1}{\omega_c(\psi)} = \frac{1 + \beta\cos 4\psi}{\omega_c} \tag{6.1}$$

Through equation 5.49 the form for $\omega_c(\psi)$ is consistent with the expectation that the velocity will be lower in the (π,0) directions due to the presence of a van Hove singularity in the energy contours — see §5.2.3. The top row of figure 6.4 shows the effect of keeping k_{61}/k_{21} constant and allowing both $\omega_c\tau$ and β, the magnitude of the anisotropy in $\omega_c(\psi)$, to be temperature dependent. While the fits are closer to the real data than in the corresponding isotropic case, there is still a clear problem with the higher-temperature fits. If k_{61}/k_{21} is also allowed to vary with temperature the fits become reasonable at all temperatures, as shown in the bottom row of figure 6.4. The changes in k_{61}/k_{21} and β required to satisfactorily fit the data are significant ($\sim$20 % change in k_{61}/k_{21} and an order of magnitude increase in β) and, if correct, would imply pronounced Fermi surface reconstruction with increasing temperature. The magnitude of reconstruction required has never been reported in the cuprates, and in fact photoemission studies [108] have reported only very small changes with temperature in overdoped $Bi_2Sr_2CuO_6$. In order to proceed further anisotropy in τ will be considered. This will be shown to provide an excellent fit to the experimental data and,

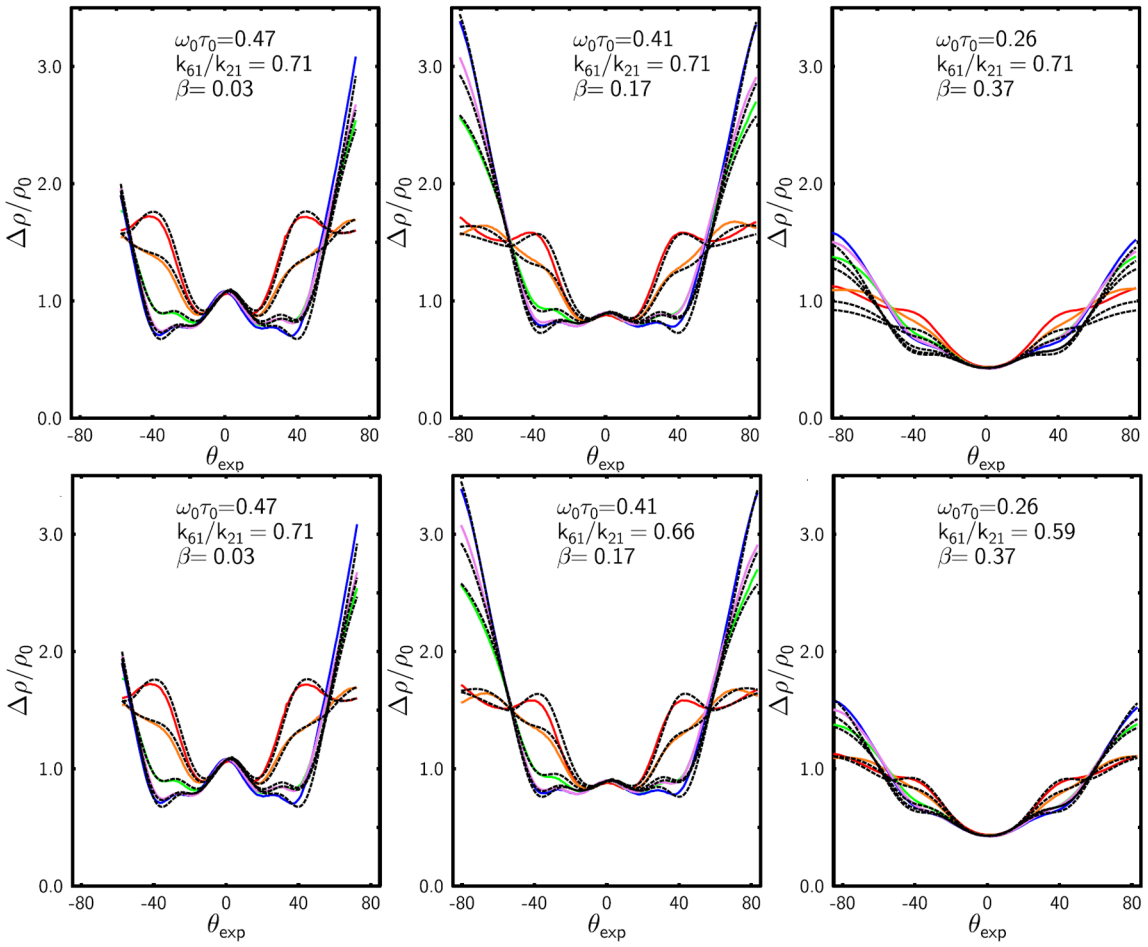

Figure 6.4: ADMR data for sample tl320c3 at 45 T normalised to the zero field c-axis resistivity. Solid coloured lines are experimental data and black dashed lines are best least squares fits. Red $\phi = 8°$, orange $\phi = 18°$, green $\phi = 32°$, blue $\phi = 45°$ and purple $\phi = 55°$. Top row shows fits with fixed Fermi surface parameters, but a temperature dependent $\omega_c\tau$ and β. Left panel at 4.2 K, centre panel at 14 K and right panel at 50 K. Bottom row shows fits with $\omega_c\tau$, β and k_{61}/k_{21} free. Left panel at 4.2 K, centre panel at 14 K and right panel at 50 K. Figure from [104].

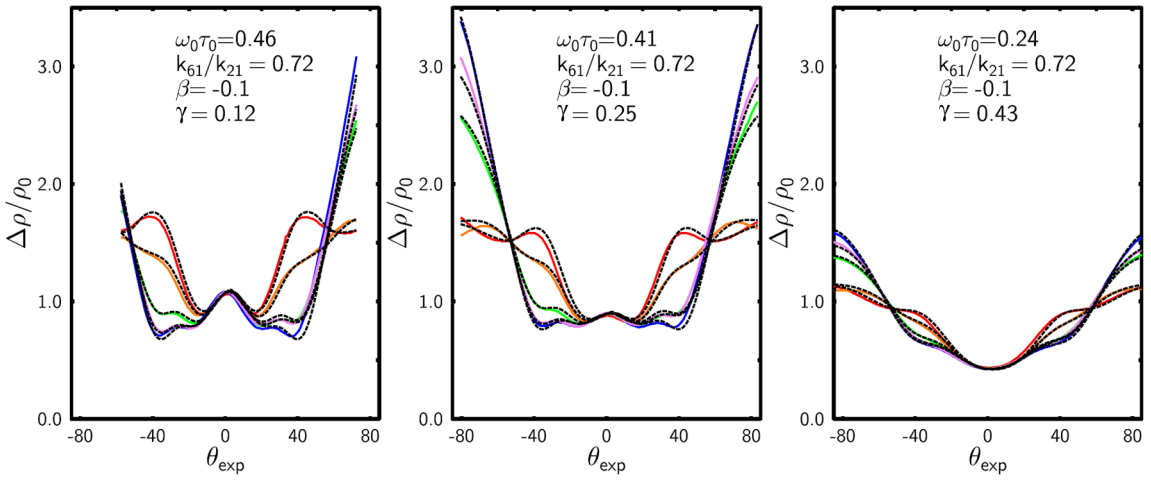

Figure 6.5: ADMR data for sample tl320c3 at 45 T normalised to the zero field c-axis resistivity. Solid coloured lines are experimental data and black dashed lines are best least squares fits. Red $\phi = 8°$, orange $\phi = 18°$, green $\phi = 32°$, blue $\phi = 45°$ and purple $\phi = 55°$. Fits with fixed β and Fermi surface parameters, but a temperature dependent $\omega_c\tau$ and γ. Left panel at 4.2 K, centre panel at 14 K and right panel at 50 K. Figure from [104].

importantly, avoid the physical difficulties discussed here.

6.2.3 Anisotropic $\omega_c(\psi)$ and $\tau(\psi)$

Again, respecting the in-plane four-fold symmetry of the crystal structure the simplest form which allows the addition of anisotropy in $\tau(\psi)$ is given by:

$$\frac{1}{\omega_c(\psi)\tau(\psi)} = \frac{1+\beta\cos 4\psi}{\omega_c}\frac{1+\gamma\cos 4\psi}{\tau} \tag{6.2}$$

The form for $\tau(\psi)$ is consistent with that suggested by Sandeman & Schofield [109] and Ioffe & Millis [35]. Figure 6.5 shows the excellent fits achieved by using an anisotropic τ with a temperature dependent magnitude. In contrast to previous schemes, the quality of the fits are comparable at all temperatures, without the need for any variation in β or k_{61}/k_{21}. Hence, by introducing a T-dependent anisotropy into the scattering rate, there is no longer any need to invoke Fermi surface reconstruction to account for the evolution of the ADMR data.

6.2.4 Final Fits

Inspecting equations 5.21 and 5.22 it can be seen that γ and β compensate for each other to within a factor of $\pm\gamma\beta/4$ meaning it is not possible to accurately quote absolute values for each parameter. The quality of the fits are parameterised by the sum of the square differences between the data and the fitted curve, and denoted by $\Sigma\delta^2$. Taking the 4.2K data for tl320c3 we systematically set β to a

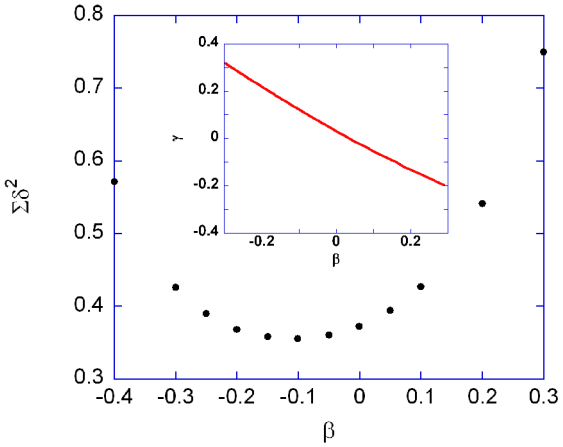

Figure 6.6: The quality of the fit parameterised by the sum $\Sigma\delta^2$ as a function of β which is set at fixed values between -0.4 and 0.3. $\Sigma\delta^2$ has a broad minimum indicating that a good fit can be achieved for a broad range of β. Figure adapted from [104].

fixed value then proceed to fit $\omega_c\tau$, γ, k_{61} and k_{101} as usual, noting the value for $\Sigma\delta^2$. A graph of $\Sigma\delta^2$ against β (figure 6.6) shows a broad flat region over which $\Sigma\delta^2$ is minimised so it is not possible to pinpoint the exact value of β within the range $-0.2<\beta<0$. The compensation effect can be clearly seen in the 4.2 K data where the value of $\gamma+\beta$ is pinned to nearly zero (see inset to figure 6.6). Thus for the initial low temperature fits for each sample (and the subsequent higher temperature fits) a value of $\beta=0$ was settled upon to remove the over parameterisation effects. Note that $v_F(\psi)$ still retains anisotropy (in the correct form due to the saddle point in the the bandstructure) as a result of the $k_F(\psi)$ and $\zeta(\psi)$ terms in equation 5.50.

Keeping all the Fermi surface k-parameters fixed for each sample at their 4.2 K values and only allowing $\omega_c\tau$ and γ to vary, the anisotropic scattering rate was applied to fit the data for all temperatures measured. The best fits are achieved with k_{101} free as shown in figures 6.7, 6.8, 6.9, 6.10 and 6.11. Note that allowing k_{101}/k_{21} and k_{61}/k_{21} to vary independently does not break the crystal symmetry as they are both terms allowed by equation 5.44.

The temperature dependencies of $1/\omega_c\tau$ and γ, tabulated in the figure captions, are graphed in figure 6.12. Good consistency is found amongst all the samples, especially tl300c1, tl320c3 and tl320c5 which have very similar T_c values. For these samples γ is found to increase from a value close to zero, tending towards a constant value of around 0.4 at the highest temperatures. For samples with high T_c values γ appears not to tend to zero in the low temperature limit, implying that significant anisotropy in the scattering rate remains. This may provide a vital clue to the origin of the anisotropic scattering.

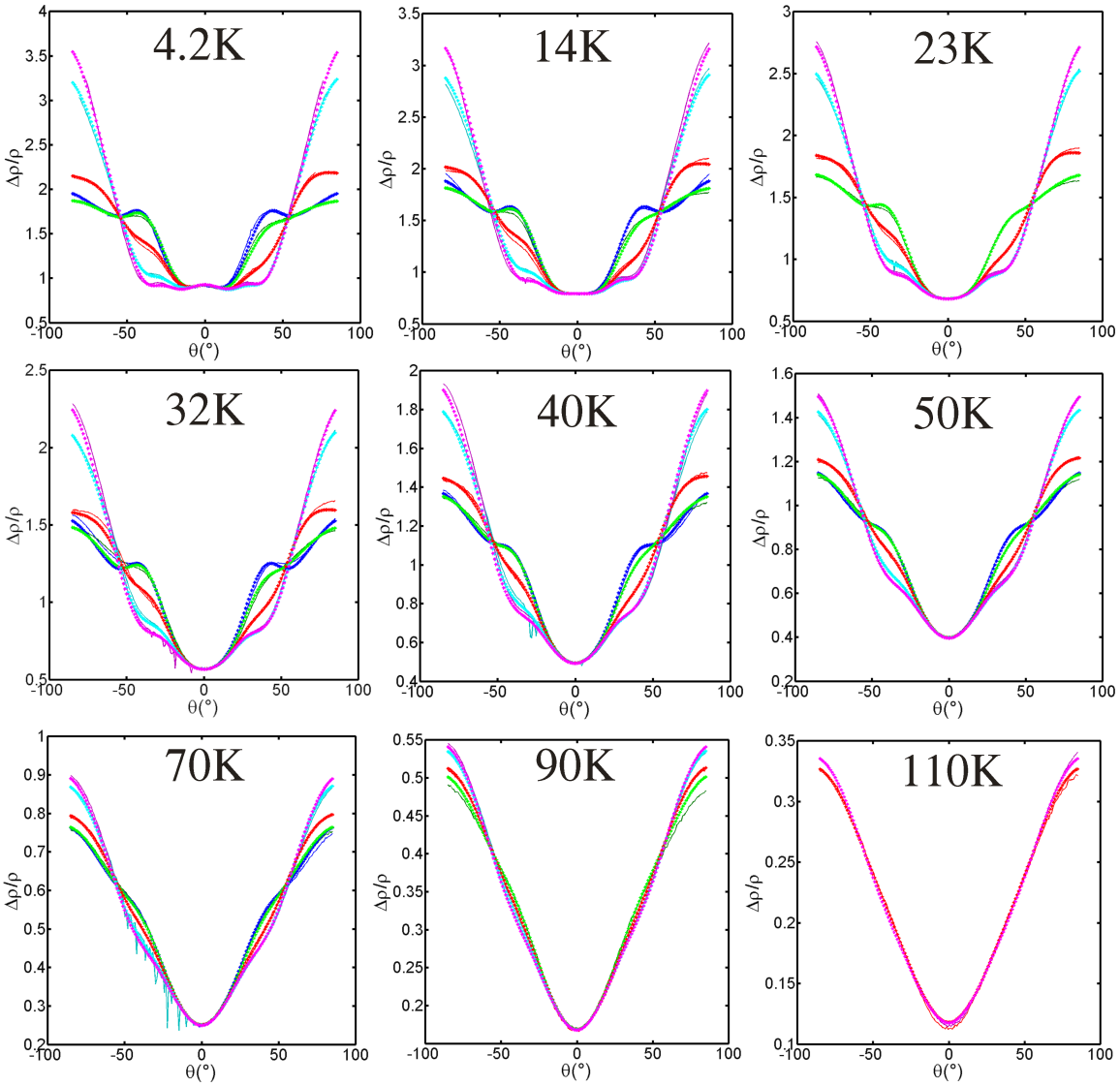

Figure 6.7: ADMR data for sample tl300c1 with $T_c = 20\,\mathrm{K}$ at 45 T normalised to the zero field c-axis resistivity. Solid lines are experimental data and asterisks are best least squares fits. Dark blue $\phi = -2°$, green $\phi = 8°$, red $\phi = 21°$, light blue $\phi = 34°$ and purple $\phi = 44°$. Fit to data with anisotropic τ. Parameters are $k_{00} = 0.728\,\mathrm{Å}^{-1}$, $k_{40}/k_{00} = -0.033 \pm 0.002$, $k_{61}/k_{21} = 0.646 \pm 0.012$ and $k_{101}/k_{21} = -0.306 \pm 0.009$ with $\omega_c\tau$ and γ given in the table.

Temperature	$\omega_c\tau$	γ	Temperature	$\omega_c\tau$	γ
4.2 K	0.360 ± 0.004	0.080 ± 0.005	50 K	0.212 ± 0.002	0.325 ± 0.017
14 K	0.331 ± 0.005	0.180 ± 0.014	70 K	0.159 ± 0.004	0.364 ± 0.012
23 K	0.300 ± 0.004	0.232 ± 0.011	90 K	0.119 ± 0.002	0.388 ± 0.015
32 K	0.270 ± 0.002	0.270 ± 0.009	110 K	0.091 ± 0.009	0.369 ± 0.015
40 K	0.242 ± 0.003	0.298 ± 0.004			

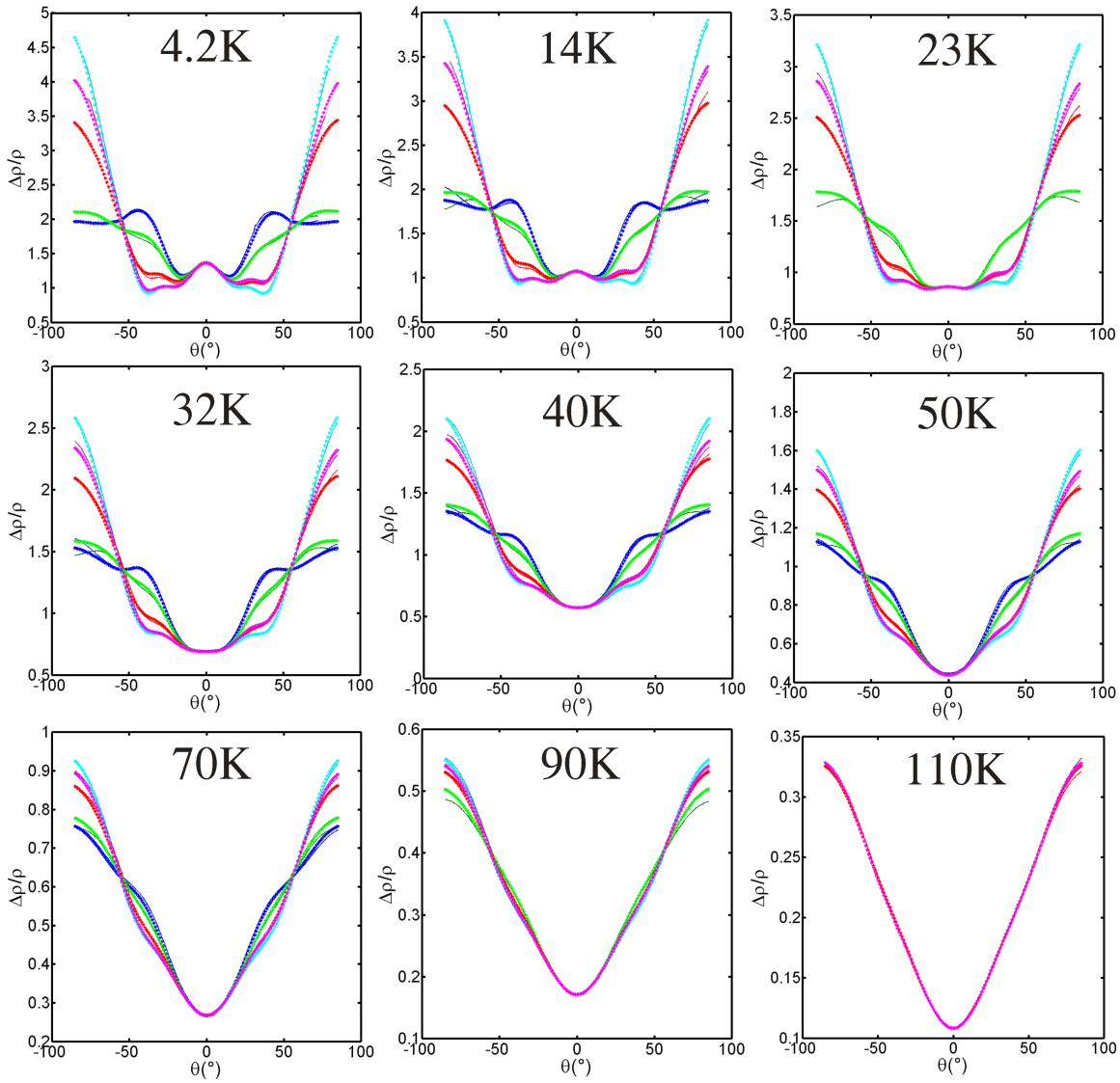

Figure 6.8: ADMR data for sample tl320c3 with $T_c = 17\,\mathrm{K}$ at 45 T normalised to the zero field c-axis resistivity. Solid lines are experimental data and asterisks are best least squares fits. Dark blue $\phi = 8°$, green $\phi = 18°$, red $\phi = 32°$, light blue $\phi = 45°$ and purple $\phi = 55°$. Fit to data with anisotropic τ. Parameters are $k_{00} = 0.729\,\mathrm{Å}^{-1}$, $k_{40}/k_{00} = -0.034 \pm 0.003$, $k_{61}/k_{21} = 0.698 \pm 0.019$ and $k_{101}/k_{21} = -0.258 \pm 0.014$ with $\omega_c\tau$ and γ given in the table.

Temperature	$\omega_c\tau$	γ	Temperature	$\omega_c\tau$	γ
4.2 K	0.452 ± 0.008	-0.015 ± 0.003	50 K	0.240 ± 0.004	0.305 ± 0.021
14 K	0.404 ± 0.004	0.109 ± 0.012	70 K	0.176 ± 0.008	0.354 ± 0.017
23 K	0.359 ± 0.006	0.178 ± 0.018	90 K	0.132 ± 0.009	0.382 ± 0.013
32 K	0.315 ± 0.005	0.238 ± 0.012	110 K	0.100 ± 0.007	0.418 ± 0.016
40 K	0.279 ± 0.006	0.265 ± 0.011			

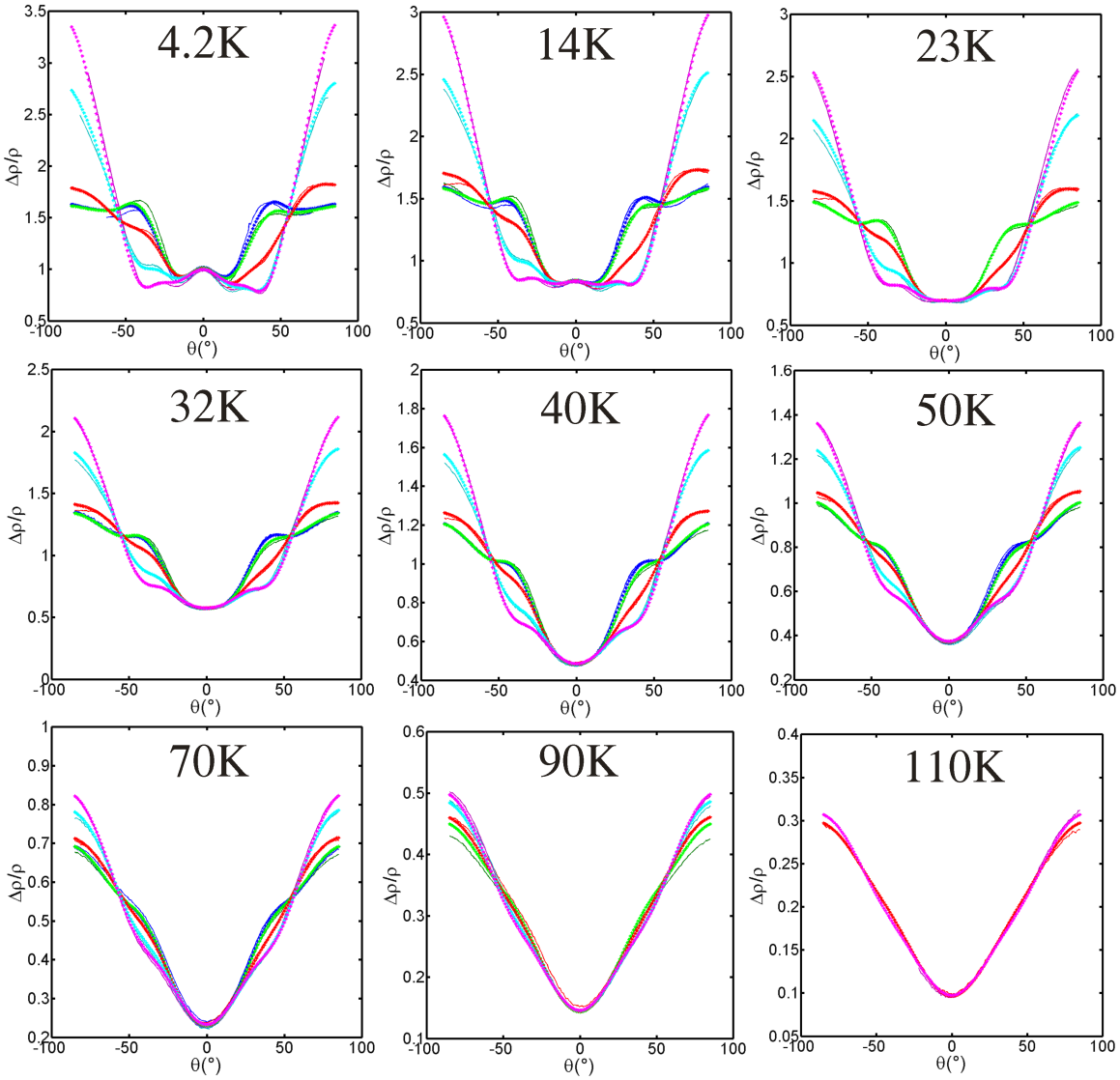

Figure 6.9: ADMR data for sample tl320c5 with $T_c = 15\,\mathrm{K}$ at 45 T normalised to the zero field c-axis resistivity. Solid lines are experimental data and asterisks are best least squares fits. Dark blue $\phi = -3°$, green $\phi = 7°$, red $\phi = 20°$, light blue $\phi = 33°$ and purple $\phi = 43°$. Fit to data with anisotropic τ. Parameters are $k_{00} = 0.730\,\mathrm{Å}^{-1}$, $k_{40}/k_{00} = -0.032 \pm 0.003$, $k_{61}/k_{21} = 0.711 \pm 0.021$ and $k_{101}/k_{21} = -0.249 \pm 0.011$ with $\omega_c\tau$ and γ given in the table.

Temperature	$\omega_c\tau$	γ	Temperature	$\omega_c\tau$	γ
4.2 K	0.389 ± 0.003	-0.018 ± 0.012	50 K	0.226 ± 0.002	0.312 ± 0.008
14 K	0.357 ± 0.007	0.100 ± 0.010	70 K	0.169 ± 0.004	0.378 ± 0.012
23 K	0.321 ± 0.003	0.187 ± 0.012	90 K	0.130 ± 0.004	0.383 ± 0.011
32 K	0.289 ± 0.001	0.240 ± 0.014	110 K	0.098 ± 0.005	0.425 ± 0.019
40 K	0.259 ± 0.003	0.280 ± 0.011			

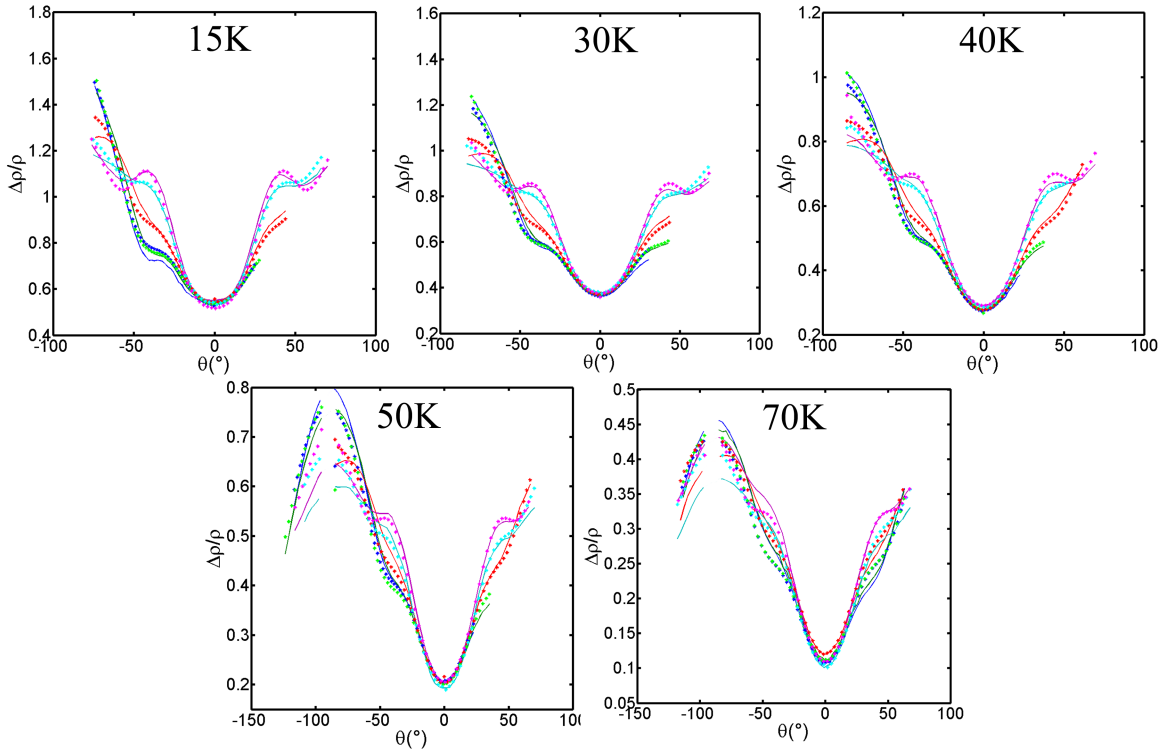

Figure 6.10: ADMR data for sample tl0825 with $T_c = 33\,\mathrm{K}$ at 45 T normalised to the zero field c-axis resistivity. Solid lines are experimental data and asterisks are best least squares fits. Dark blue $\phi \approx 53°$, green $\phi \approx 40°$, red $\phi \approx 27°$, light blue $\phi \approx 13°$ and purple $\phi \approx 0°$. Fit to data with anisotropic τ. Parameters are $k_{00} = 0.726\,\mathrm{Å}^{-1}$, $k_{40}/k_{00} = -0.030 \pm 0.002$, $k_{61}/k_{21} = 0.594 \pm 0.022$ and $k_{101}/k_{21} = -0.471 \pm 0.018$ with $\omega_c\tau$ and γ given in the table. Note that the poorer fit for the 70 K data is most probably due to experimental temperature control issues.

Temperature	$\omega_c\tau$	γ	Temperature	$\omega_c\tau$	γ
15 K	0.269 ± 0.005	0.294 ± 0.015	50 K	0.180 ± 0.003	0.416 ± 0.018
30 K	0.236 ± 0.004	0.332 ± 0.011	70 K	0.143 ± 0.003	0.465 ± 0.023
40 K	0.210 ± 0.003	0.370 ± 0.012			

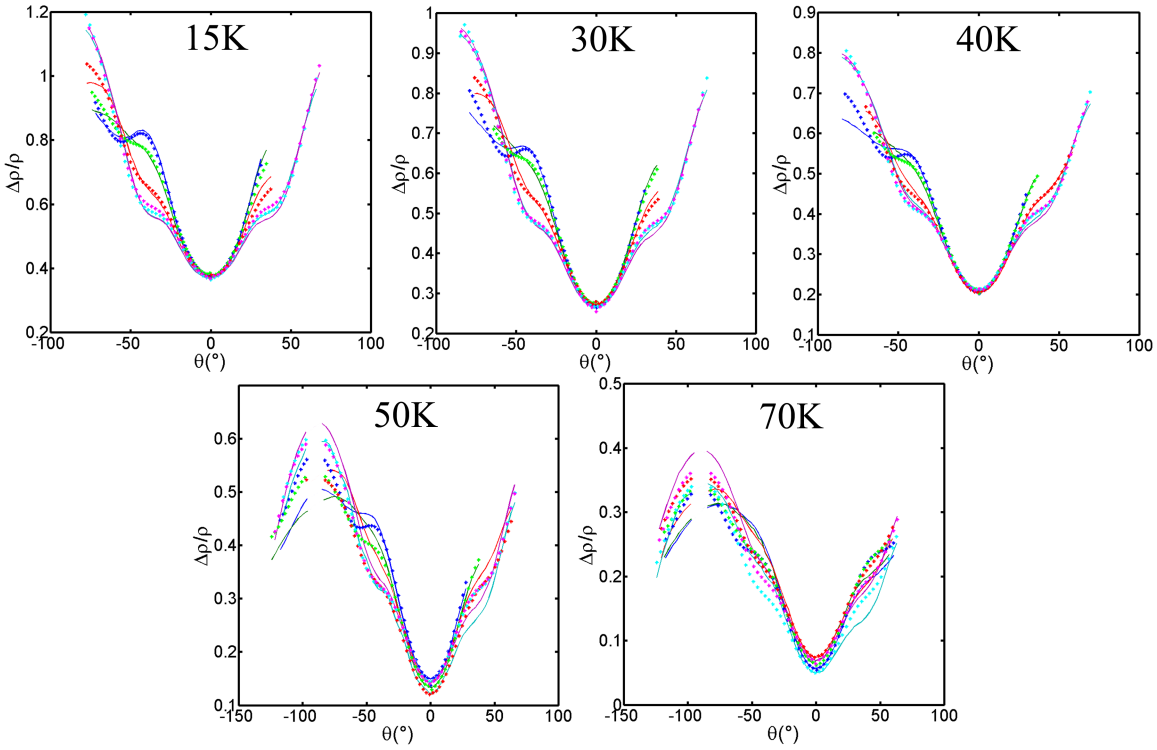

Figure 6.11: ADMR data for sample tl0829 with $T_c = 38\,\mathrm{K}$ at 45 T normalised to the zero field c-axis resistivity. Solid lines are experimental data and asterisks are best least squares fits. Dark blue $\phi \approx 0°$, green $\phi \approx 13°$, red $\phi \approx 27°$, light blue $\phi \approx 40°$ and purple $\phi \approx 53°$. Fit to data with anisotropic τ. Parameters are $k_{00} = 0.724\,\mathrm{Å}^{-1}$, $k_{40}/k_{00} = -0.030 \pm 0.002$, $k_{61}/k_{21} = 0.703 \pm 0.037$ and $k_{101}/k_{21} = -0.381 \pm 0.037$ with $\omega_c\tau$ and γ given in the table. Note that the poorer fit for the 70 K data is most probably due to experimental temperature control issues.

Temperature	$\omega_c\tau$	γ	Temperature	$\omega_c\tau$	γ
15 K	0.227 ± 0.005	0.372 ± 0.023	50 K	0.155 ± 0.004	0.525 ± 0.027
30 K	0.201 ± 0.002	0.436 ± 0.008	70 K	0.128 ± 0.004	0.505 ± 0.029
40 K	0.183 ± 0.002	0.462 ± 0.010			

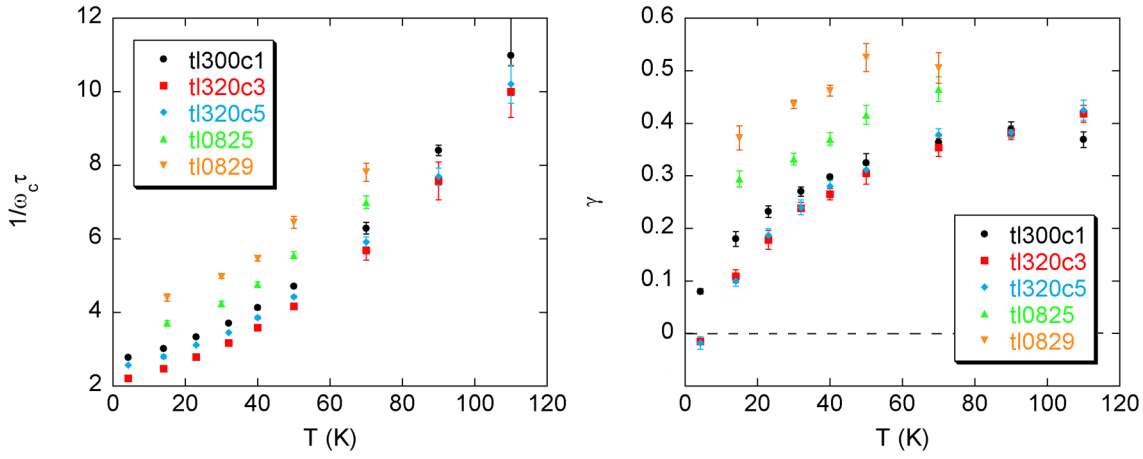

Figure 6.12: Temperature dependence of $1/\omega_c\tau$ and γ.

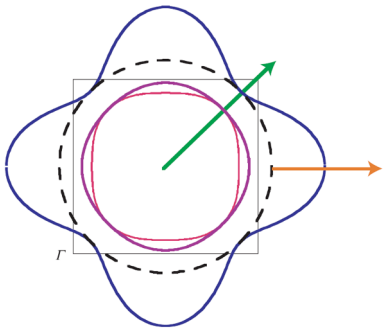

Figure 6.13: Red curve is schematic 2D projection of the FS of overdoped Tl2201. Purple curve is schematic representation of the d-wave superconducting gap. Blue curve is geometry of $1/\omega_c\tau(\psi)$. Black dashed line is isotropic part of $1/\omega_c\tau(\psi)$. Green arrow indicates the 'nodal' direction along which the isotopic component is the sole contributor. Orange arrow indicates the 'anti-nodal' direction along which the anisotropic component is maximum. Figure from [37].

6.2.5 Isotropic and Anisotropic Components of the Scattering Rate

Using $\cos 2X = 2\cos^2 X - 1$, equation 6.2 can be rewritten giving a component $(1 - \gamma/\omega_c\tau)$ which is isotropic around the Fermi surface and another component $(2\gamma/\omega_c\tau)$ which is anisotropic around the Fermi surface with a minimum of zero along the direction of the nodes of the superconducting gap — see figure 6.13:

$$\frac{1 + \alpha\cos 4\psi}{\omega_c\tau} = \frac{1-\alpha}{\omega_c\tau} + \frac{2\alpha}{\omega_c\tau}\cos^2 2\psi \tag{6.3}$$

This simple rearrangement of the anisotropic scattering rate into two components allows the temperature and doping dependencies of each of to be examined.

6.2.6 Temperature and Doping Dependence of the Scattering Rate Components

Figure 6.14 shows the temperature dependence of the isotropic and anisotropic components of the scattering rate using the parameters in the tables in figures 6.7 – 6.11. The isotropic component fits well to a $A + BT^2$ dependence implying a combination of impurity and fermion-fermion scattering. Whereas, following previous work at temperatures less than 55 K [37], the anisotropic component is fitted to $C + DT$. At higher temperatures there are less features in the ADMR data making the parameters less reliable as indicated by the larger error bars. As a result in figure 6.14 the T-linear and T^2 fits are only performed on data taken at 70 K and below. It can be seen in figures 6.14 and 6.17 that the error bars are small and the fit very good at the lower temperatures. At higher temperatures the error bars are larger in all cases. The magnitude of the isotropic component seems to be independent of the sample doping (T_c) whereas the magnitude of the anisotropic component increases with decreasing doping (increasing T_c) — see figures 6.16 and 6.17.

The anisotropic component for the three lower T_c samples shows the points systematically devi-

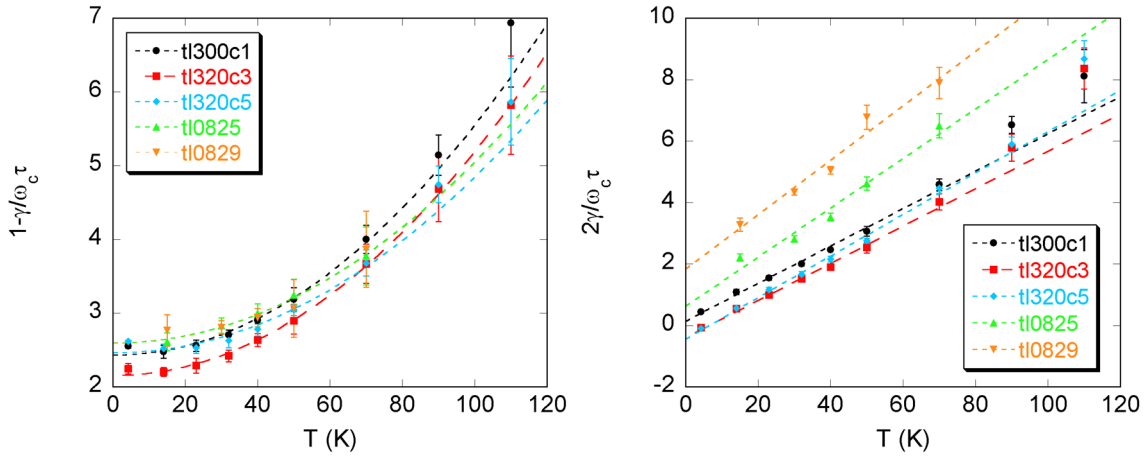

Figure 6.14: Temperature dependence of the isotropic $(1-\gamma/\omega_c\tau)$ and anisotropic $(2\gamma/\omega_c\tau)$ components of the scattering rate for each sample. For the isotropic component the dashed line is a least squares fit to $A+BT^2$ for $T\leq 70\,\mathrm{K}$. For the anisotropic component the dashed line is a least squares fit to $C+DT$ for $T\leq 70\,\mathrm{K}$. For tl300c1 $A=2.43$, $B=0.000313$, $C=0.135$, $D=0.0611$; tl320c3 $A=2.16$, $B=0.000304$, $C=-0.388$, $D=0.0607$; tl320c5 $A=2.46$, $B=0.000238$, $C=-0.435$, $D=0.0675$; tl0825 $A=2.60$, $B=0.000246$, $C=0.639$, $D=0.0804$; tl0829 $A=2.60$, $B=0.000242$, $C=1.85$, $D=0.0883$.

ating upwards from the fit. This suggests the temperature dependence of the anisotropic component could have an additional T^2 term [110] which would not have been picked up in previous work due to its negligible effect in the temperature range studied [37]. However this systematic trend cannot be confirmed or ruled out in the higher T_c samples as there is no reliable data above 70 K. Figure 6.15 shows a good fit for data up to 110 K of the isotropic component to a $A+BT^2$ and the anisotropic component to a $C+DT+ET^2$ form for the lower T_c samples. As the sample is hole doped with interstitial oxygen atoms, an increasing T_c implies a reduction in doping and also in the disorder created by the extra atoms. Thus the lower T_c samples, where this additional scattering component is observed, are more disordered than the higher T_c samples. Therefore it is possible that the additional T^2 term in the anisotropic scattering component may be linked to sample disorder i.e. the T^2 anisotropy decreases as the sample doping is decreased and the Fermi surface moves away from the saddle point.

Figure 6.16 shows the temperature and doping (T_c) dependence of the isotropic and anisotropic components of the scattering rate. The magnitude of the isotropic component increases linearly with both increasing temperature and increasing (decreasing) T_c (hole doping) from around zero at 4.2 K for a sample with $T_c=15\,\mathrm{K}$ to around 8 at 70 K for a sample with $T_c=38\,\mathrm{K}$. Slices through this graph showing the doping dependence at fixed temperature are shown in figure 6.17. Although at present, it seems to have no significance, it is interesting to note that at 40 K the magnitude of the anisotropic component extrapolates to zero for a sample with $T_c=0\,\mathrm{K}$. The graphs show a strong correlation between T_c and the magnitude of the anisotropic component of the scattering rate,

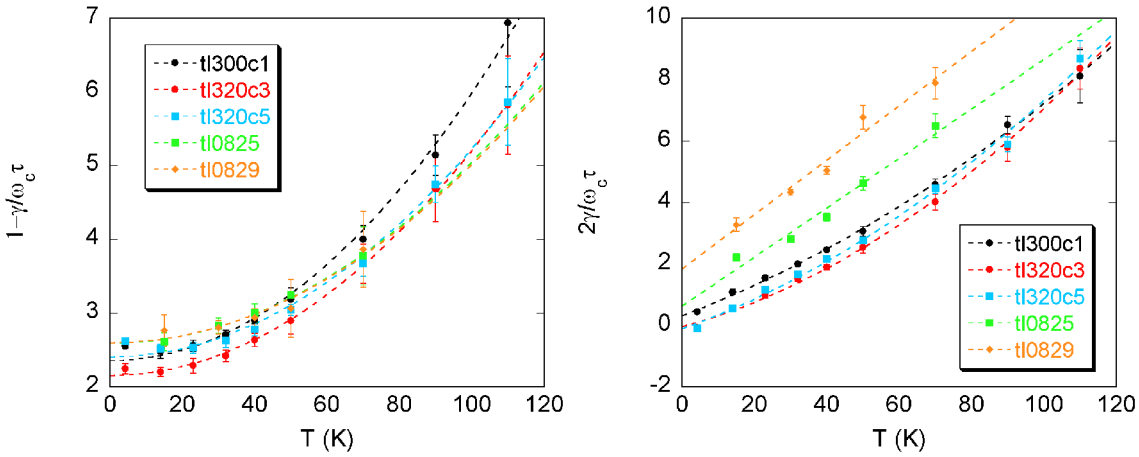

Figure 6.15: Temperature dependence of the isotropic $(1-\gamma/\omega_c\tau)$ and anisotropic $(2\gamma/\omega_c\tau)$ components of the scattering rate for each sample. For the isotropic component the dashed line is a least squares fit to $A+BT^2$ for all data. For the anisotropic component the dashed line is a least squares fit to $C+DT+ET^2$ for all tl300c1, tl320c3 and tl320c5 and to $C+DT$ for tl0825 and tl0829. For tl300c1 $A=2.36$, $B=0.000363$, $C=0.324$, $D=0.0445$, $E=0.000246$; tl320c3 $A=2.16$, $B=0.000305$, $C=-0.0338$, $D=0.0317$, $E=0.000393$; tl320c5 $A=2.41$, $B=0.000282$, $C=-0.0994$, $D=0.0415$, $E=0.000329$; tl0825 $A=2.60$, $B=0.000246$, $C=0.639$, $D=0.0804$; tl0829 $A=2.60$, $B=0.000242$, $C=1.85$, $D=0.0883$.

whilst the isotropic component remains constant. This emphasises the fact that regardless of the specific details of the temperature dependencies of the scattering rate components, the presence of anisotropic scattering is a key component of the cuprates.

6.3 AMRO on Different $Tl_2Ba_2CuO_{6+\delta}$ Samples

ADMR were also measured on three samples grown by Walter Hardy (University of British Columbia, Canada) at a single azimuthal angle: tc14k1 with $T_c=17\,\mathrm{K}$; tc33k4 with $T_c=30\,\mathrm{K}$ and tc38k1 with $T_c=39\,\mathrm{K}$. The data were taken between 4.2 K and 90 K and analysed in the same way as the data already presented. Zero field c-axis resistance measurements for these samples are shown in figure 6.18. Electrical contacts were attached to these samples with 6838 silver epoxy. High quality ADMR fits are shown in figures 6.19, 6.20 and 6.21. It should be noted that even though there is only a single azimuthal angle, robust conclusions can be drawn from this quantity of data [37].

In the same way as before the anisotropic scattering rate is split into isotropic and anisotropic components in figure 6.22. The isotropic component shows a very good fit to a $A+BT^2$ form as before with approximately the same magnitudes. The anisotropic component, however, shows much more T^2 dependence which onsets at a much lower temperature and so is fitted to a $C+DT+ET^2$ form. In contrast to the other set of samples where the T^2 term only became relevant above 70 K, here is it required from the lowest temperatures in samples across the doping range. This potentially

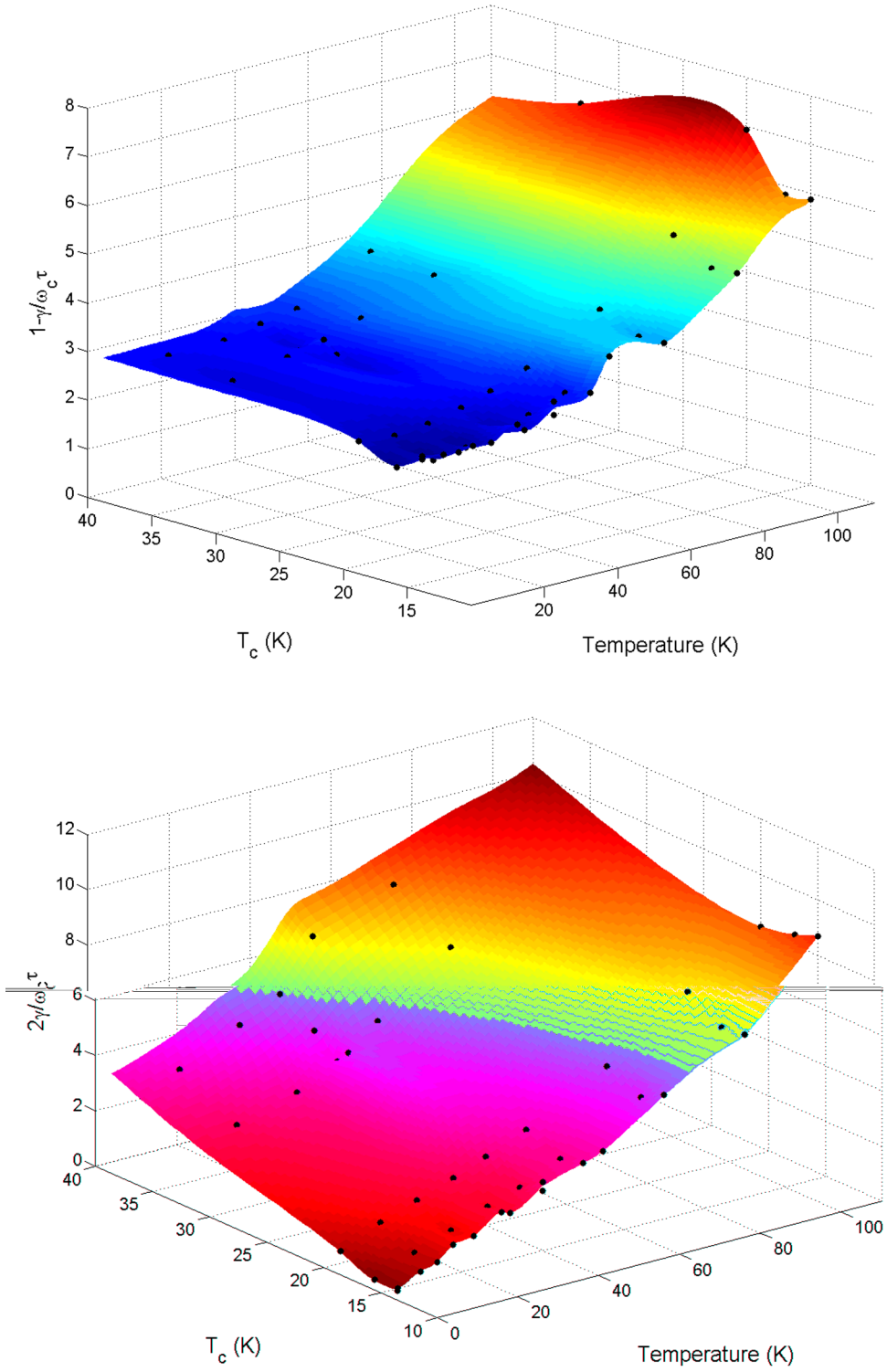

Figure 6.16: Top panel shows the temperature and doping (T_c) dependence of the isotropic component of the scattering rate. Bottom panel shows the temperature and doping (T_c) dependence of the anisotropic component of the scattering rate. Coloured surface is a fit to the data points from samples above (black dots). Additional data points taken from previous publications [37] and [111].

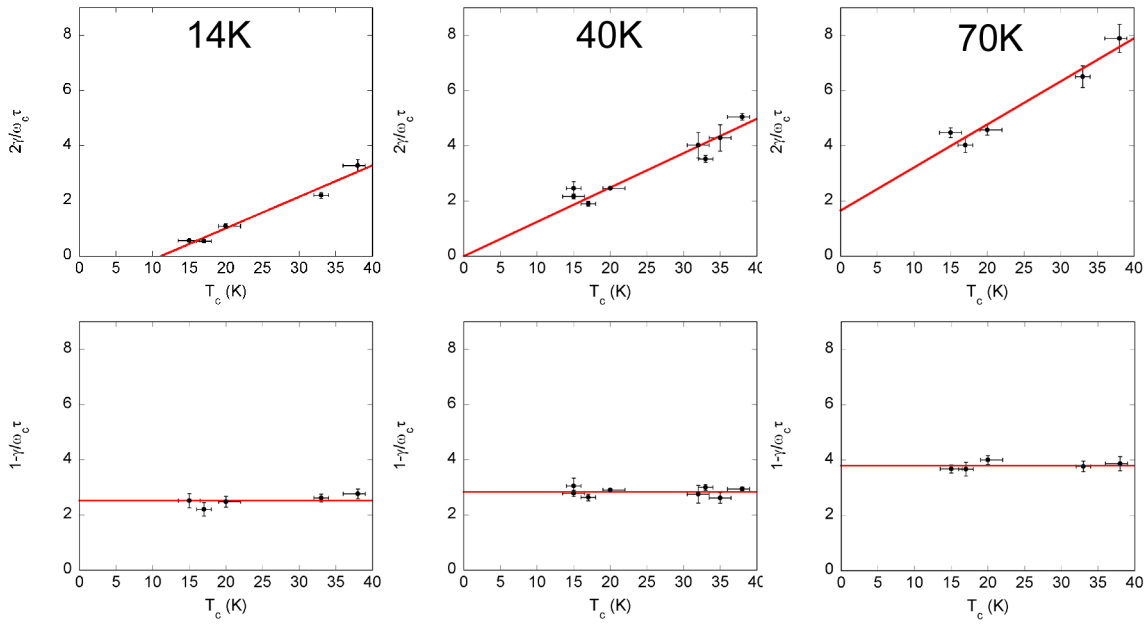

Figure 6.17: Selected slices through the 3D graph (figure 6.16) at constant temperature. Additional data points taken from previous publications [37] and [111]. Top panels show anisotropic components and bottom panels show isotropic components of the scattering rate.

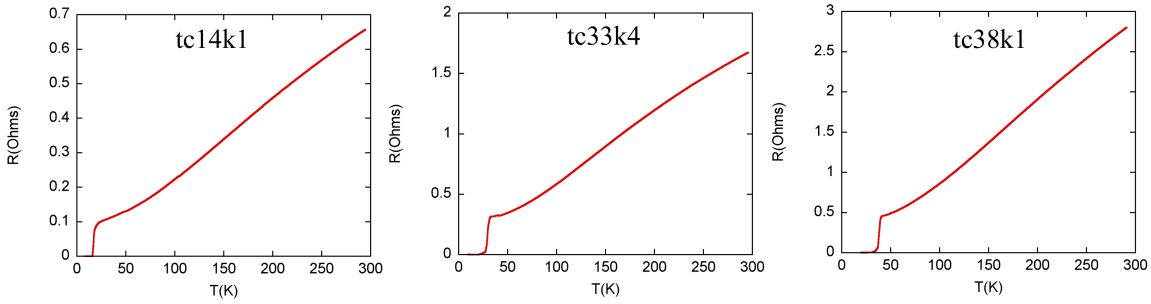

Figure 6.18: Zero field c-axis resistivity measurements for samples tc14k1, tc33k4 and tc38k1.

provides further evidence to support the idea raised earlier that the appearance of an additional T^2 term in the anisotropic component is due to increased sample disorder. From the consideration of zero field residual resistivity ratios as well as fitted $\omega_c\tau$ values, it is clear that these samples are more disordered than the samples used previously.

A further difference, potentially due to sample quality, is that the magnitude of the anisotropic component at $T = 0\,\mathrm{K}$ is significantly higher than for the previous samples where the lower T_c samples had $2\gamma/\omega_c\tau \to 0$ as $T \to 0\,\mathrm{K}$. In these samples there is significant anisotropic scattering at $T = 0\,\mathrm{K}$.

Seeing broadly similar results on this alternative set of samples gives us further confidence that the observation of ADMR and interpretation of the anisotropic scattering rate is intrinsic to this material and not an artifact of the sample growth technique or impurities.

6.4 X-ray Orientation Results

The relative ϕ angles for each data set (where ϕ is the angle between the CuO bond and the plane of rotation of the magnetic field) for samples tl300c1, tl320c3 and tl320c5 are known because the ϕ rotation was recorded during the experiment. The first rotation was 10° followed by two rotations of 13° and finally one of 10°. Taking tl300c1 as an initial example. The image in the top left of figure 6.23 shows a visual spectrum image of part of the sample (Note that the sample has broken and also that in the images in the top row the sample is viewed from the opposite side when compared with the images in the bottom left and centre). The images from the diffractometer in the centre and right of the top row of the figure show the reciprocal space directions corresponding to the face perpendiculars. Also obtained from the diffractometer are the lattice constants $a = 3.858\,\text{Å}$, $b = 3.866\,\text{Å}$ and $c = 23.12\,\text{Å}$ along with the units cell angles $\alpha = 90.01°$, $\beta = 89.95°$ and $\gamma = 89.87°$. The bottom left image of figure 6.23 shows the position of the sample on the probe at the end of the experiment; that is the alignment of the sample for the purple traces in figure 6.7. The field orientation is from left to right along the length of the block in the top right of the image. The bottom middle shows an enlarged image of the sample in the same alignment as the bottom left. The bottom right shows a reversed image of the sample to correspond with the images in the top row of the figure along with the face perpendiculars. It shows the orientation of the field for the purple ADMR trace is almost exactly along the $[-1-10]$ direction of the sample. Specifically this gives an angle of $\phi = 44°$ between the CuO bond and the field. The angles of the other traces are calculated by subtracting the relevant amounts of 10° and 13°. For the field in-plane (i.e. $\theta = 90°$) $\phi = 45°$ corresponds to a maximum in the magnetoresistance. This corresponds with the data in [26] and [77] as well as data on tl320c3 and tl320c5 giving confidence that the determination of orientation of ϕ is correct. This conclusion about the sample orientation is backed up with similar work on the two other samples (tl320c3 and tl320c5) as shown in figures 6.24 and 6.25.

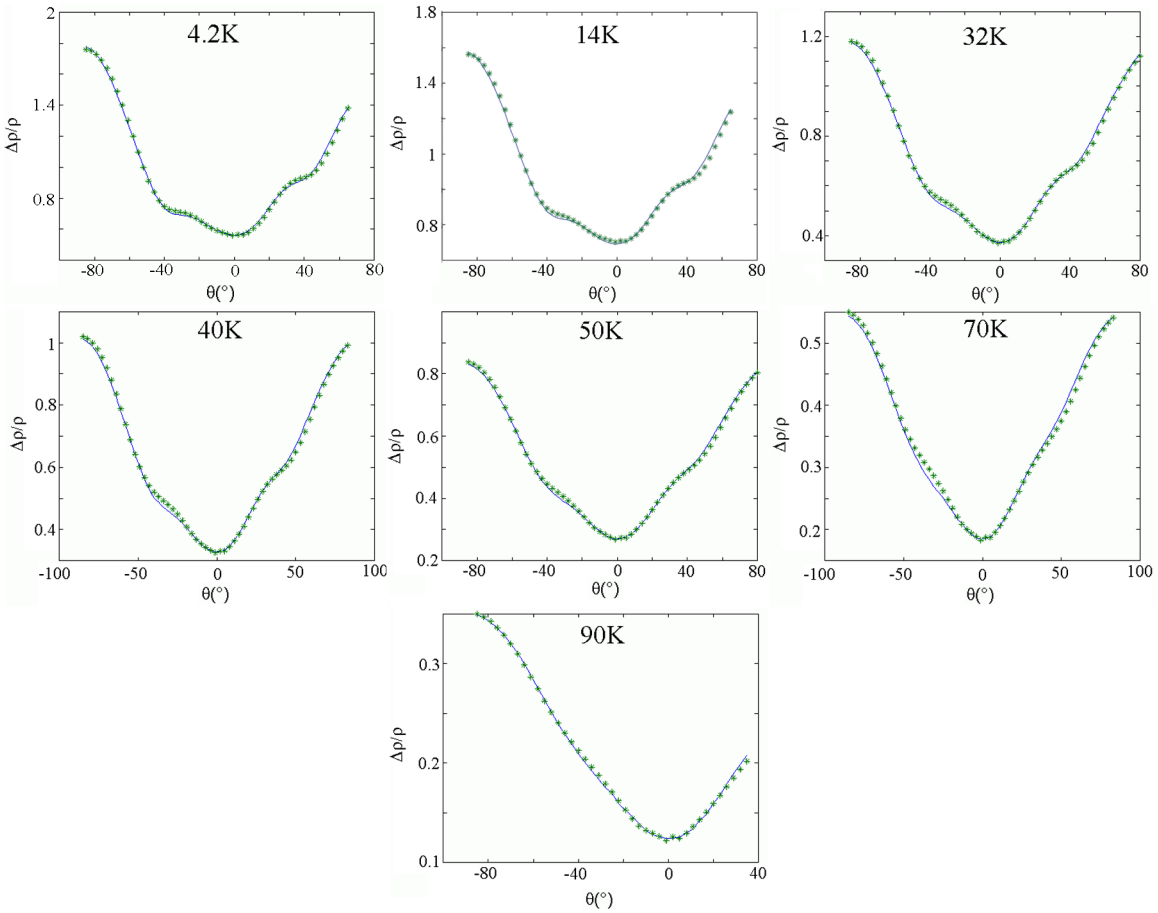

Figure 6.19: ADMR data for sample tc14k1 with $T_c = 17\,\mathrm{K}$ at 45 T normalised to the zero field c-axis resistivity. Solid lines are experimental data and asterisks are best least squares fits. Fit to data with anisotropic τ. Parameters are $k_{00} = 0.728\,\mathrm{Å}^{-1}$, $k_{40}/k_{00} = -0.03$, $k_{61}/k_{21} = 0.627 \pm 0.045$ and $k_{101}/k_{21} = -0.373 \pm 0.045$ with $\omega_c\tau$ and γ given in the table.

Temperature	$\omega_c\tau$	γ	Temperature	$\omega_c\tau$	γ
4.2 K	0.292 ± 0.008	0.225 ± 0.025	50 K	0.185 ± 0.002	0.306 ± 0.011
14 K	0.272 ± 0.003	0.251 ± 0.011	70 K	0.142 ± 0.002	0.354 ± 0.023
32 K	0.228 ± 0.002	0.281 ± 0.010	90 K	0.111 ± 0.001	0.354 ± 0.013
40 K	0.207 ± 0.002	0.295 ± 0.013			

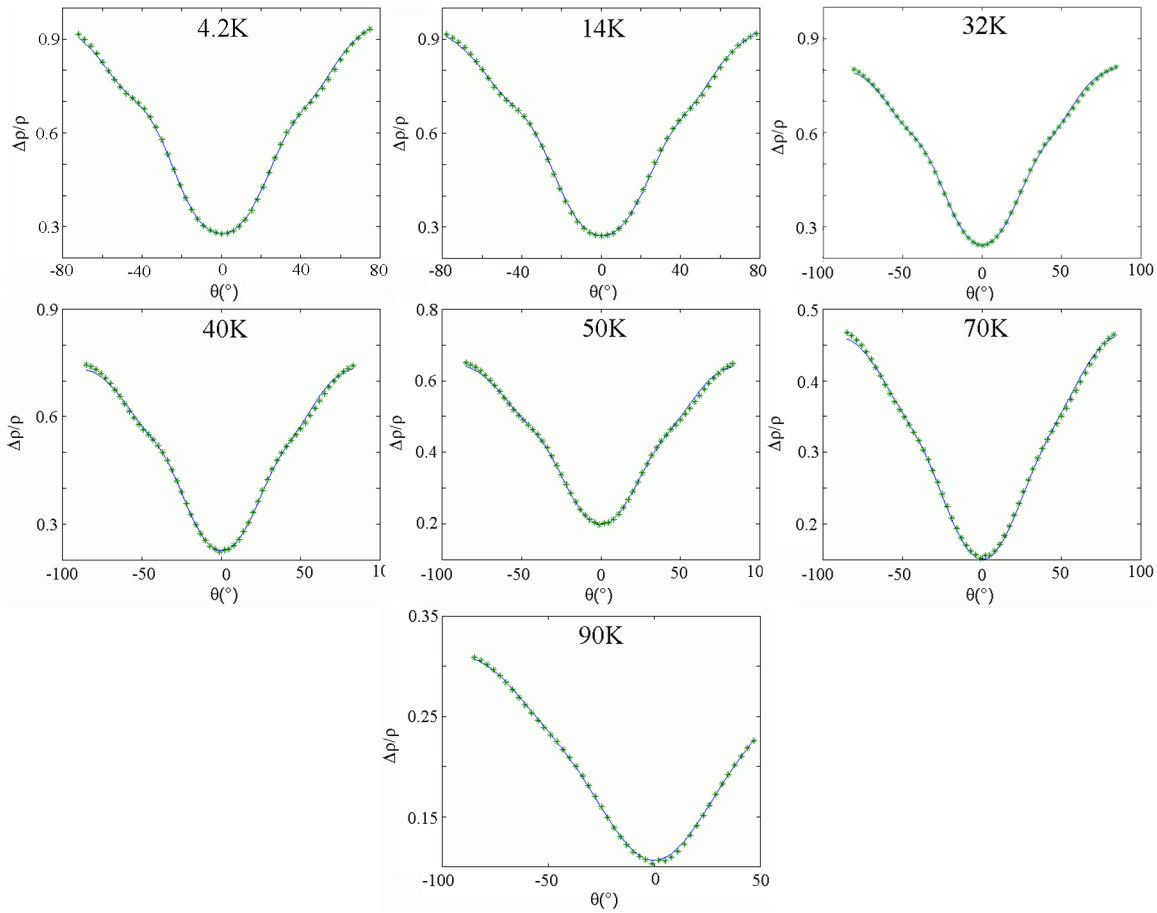

Figure 6.20: ADMR data for sample tc33k4 with $T_c = 30\,\mathrm{K}$ at 45 T normalised to the zero field c-axis resistivity. Solid lines are experimental data and asterisks are best least squares fits. Fit to data with anisotropic τ. Parameters are $k_{00} = 0.726\,\text{Å}^{-1}$, $k_{40}/k_{00} = -0.03$, $k_{61}/k_{21} = 0.715 \pm 0.029$ and $k_{101}/k_{21} = -0.285 \pm 0.029$ with $\omega_c\tau$ and γ given in the table.

Temperature	$\omega_c\tau$	γ	Temperature	$\omega_c\tau$	γ
4.2 K	0.255 ± 0.009	0.361 ± 0.013	50 K	0.161 ± 0.002	0.456 ± 0.013
14 K	0.245 ± 0.004	0.365 ± 0.009	70 K	0.126 ± 0.002	0.463 ± 0.012
32 K	0.198 ± 0.003	0.423 ± 0.013	90 K	0.096 ± 0.004	0.519 ± 0.038
40 K	0.180 ± 0.003	0.443 ± 0.014			

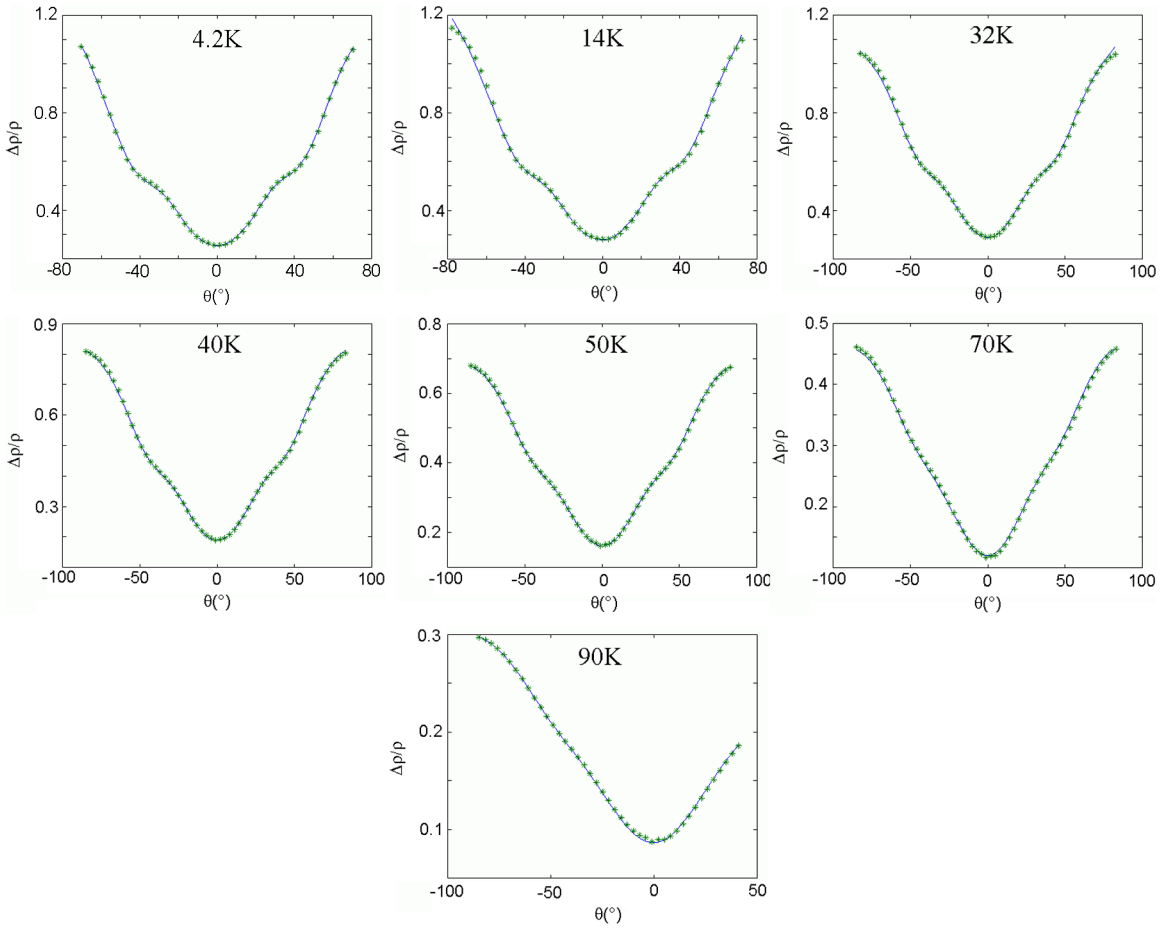

Figure 6.21: ADMR data for sample tc38k1 with $T_c = 39\,\mathrm{K}$ at 45 T normalised to the zero field c-axis resistivity. Solid lines are experimental data and asterisks are best least squares fits. Fit to data with anisotropic τ. Parameters are $k_{00} = 0.724\,\mathrm{\AA}^{-1}$, $k_{40}/k_{00} = -0.03$, $k_{61}/k_{21} = 0.731 \pm 0.024$ and $k_{101}/k_{21} = -0.269 \pm 0.024$ with $\omega_c\tau$ and γ given in the table.

Temperature	$\omega_c\tau$	γ	Temperature	$\omega_c\tau$	γ
4.2 K	0.273 ± 0.004	0.383 ± 0.011	50 K	0.175 ± 0.001	0.424 ± 0.005
14 K	0.267 ± 0.003	0.377 ± 0.007	70 K	0.132 ± 0.001	0.475 ± 0.011
32 K	0.223 ± 0.002	0.391 ± 0.008	90 K	0.100 ± 0.001	0.485 ± 0.002
40 K	0.200 ± 0.001	0.405 ± 0.005			

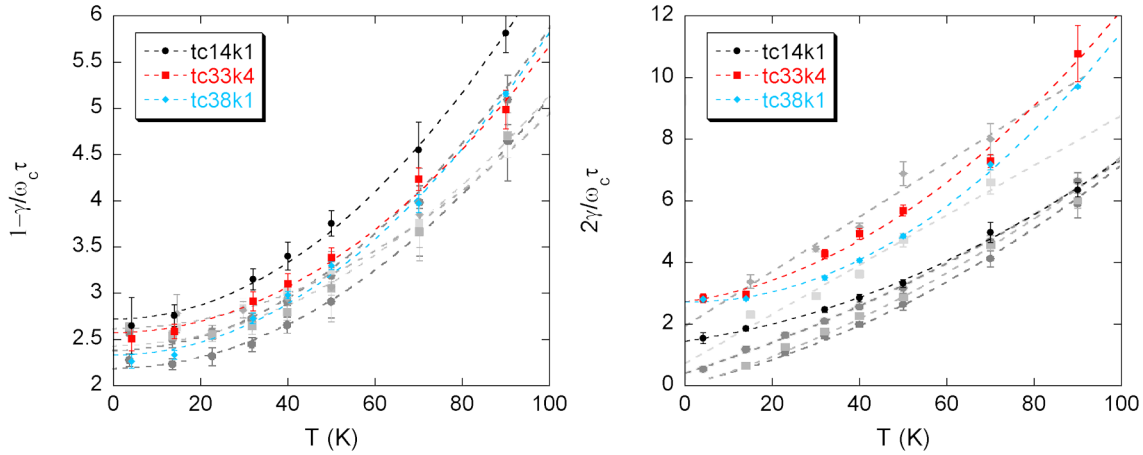

Figure 6.22: Temperature dependence of the isotropic $(1-\gamma/\omega_c\tau)$ and anisotropic $(2\gamma/\omega_c\tau)$ components of the scattering rate for each sample. For the isotropic component the dashed line is a least squares fit to $A+BT^2$. For the anisotropic component the dashed line is a least squares fit to $C+DT+ET^2$. For tc14k1 $A=2.72$, $B=0.000383$, $C=1.45$, $D=0.0197$, $E=0.000397$; tc33k4 $A=2.57$, $B=0.000310$, $C=2.72$, $D=0.0201$, $E=0.000745$; tc38k1 $A=2.33$, $B=0.000349$, $C=2.71$, $D=-0.00118$, $E=0.000888$. Also shown for comparison in greyscale are the data from figure 6.15 for tl300c1, tl320c3, tl320c5, tl0825 and tl0829.

6.5 Comparison With Other Experiments on $Tl_2Ba_2CuO_{6+\delta}$

6.5.1 Quasiparticle Anisotropy Reversal Implied by ARPES

Plat*é et al.* [25] use ARPES to study the same material but despite seeing a superconducting gap consistent with $d_{x^2-y^2}$ symmetry, their ARPES line shapes show an unexpected momentum dependence. They see quasiparticle peaks which are sharp in the (superconducting gap) antinodal direction (i.e. $(\pi,0)$ or $\phi=0°$) and broad in the nodal direction (i.e. (π,π) or $\phi=45°$). The sharp quasiparticle peaks suggest a smaller amount of scattering compared with the broad peaks which suggest more scattering. Further, as doping is increased (on the overdoped side of the phase diagram) they observe a trend of the nodal quasiparticles broadening and the antinodal quasiparticles sharpening.

This is opposite to the findings in underdoped and optimally doped cuprates [112] where quasiparticles are sharp near (π,π) and broad near $(\pi,0)$ in the normal state. When in the superconducting state the quasiparticles gain coherence everywhere but ARPES derived scattering rates are still anisotropic with a minimum at (π,π) i.e. $\phi=45°$, as found in this work. As the doping is increased up to optimal doping the antinodal quasiparticles sharpen up, although they remain broader than the nodal ones.

The results of Plat*é et al.* contrast with those of this work where it is found that the anisotropic scattering rate has a minimum along (π,π) such that there is no reversal observed across optimal doping. Furthermore, in this work the nodal scattering rate is found to be approximately constant over the range from $T_c=0\,\mathrm{K}$ up to $40\,\mathrm{K}$. The antinodal scattering rate is found to decrease with

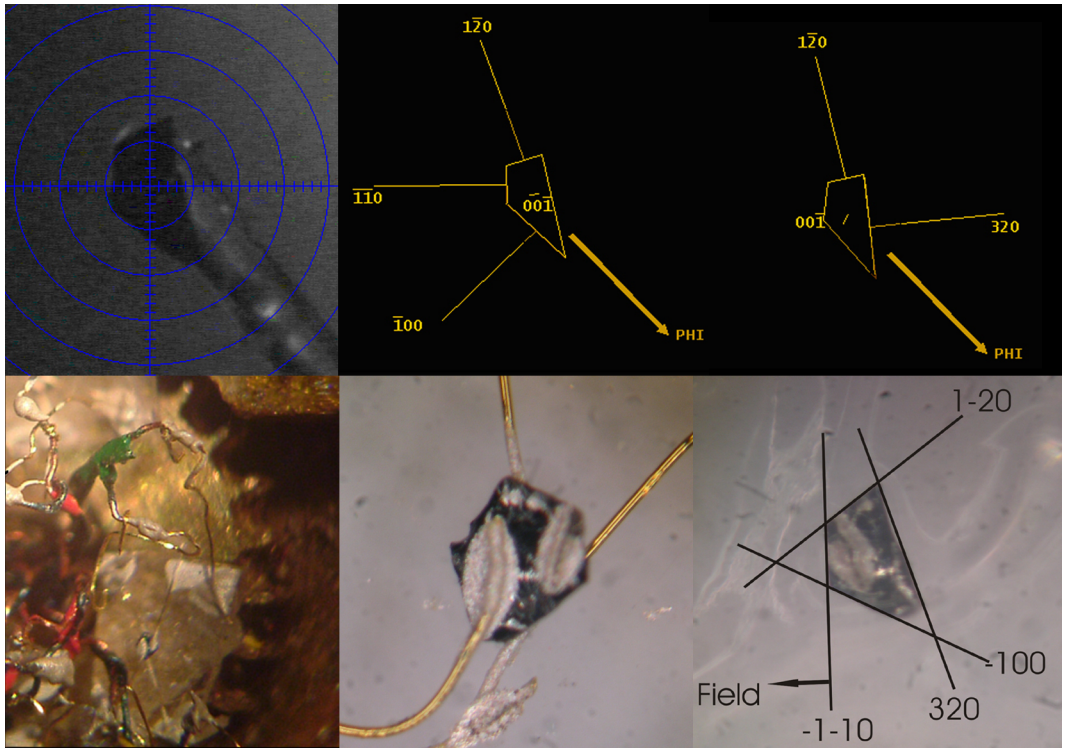

Figure 6.23: Sample tl300c1 X-ray alignment. Top left panel shows a visible spectrum image from the X-ray diffractometer of the sample. Top middle and right panels show the reciprocal space indices of the face perpendiculars corresponding to the image in the top left. Bottom left panel shows a photograph of the sample on the probe at the end of the experiment. Direction of the field for the last ADMR trace is from left to right along block in the top right of the image. Bottom middle panel shows a close up photo of the sample. Bottom right panel shows a reversed photo of the sample to correspond with the top row of images with reciprocal space indices of face perpendiculars.

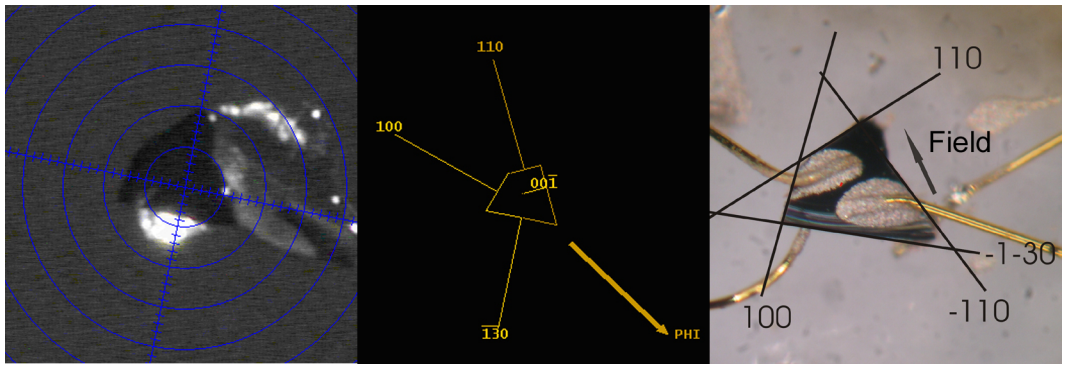

Figure 6.24: Sample tl320c3 X-ray alignment. Left panel shows a visible spectrum image from the X-ray diffractometer of the sample. Middle panel shows the reciprocal space indices of the face perpendiculars corresponding to the image on the left. Right panel shows a photo of sample with reciprocal space indices of the face perpendiculars. $a = 3.860$ Å, $b = 3.871$ Å, $c = 23.23$ Å, $\alpha = 89.898°$, $\beta = 89.825°$ and $\gamma = 90.107°$.

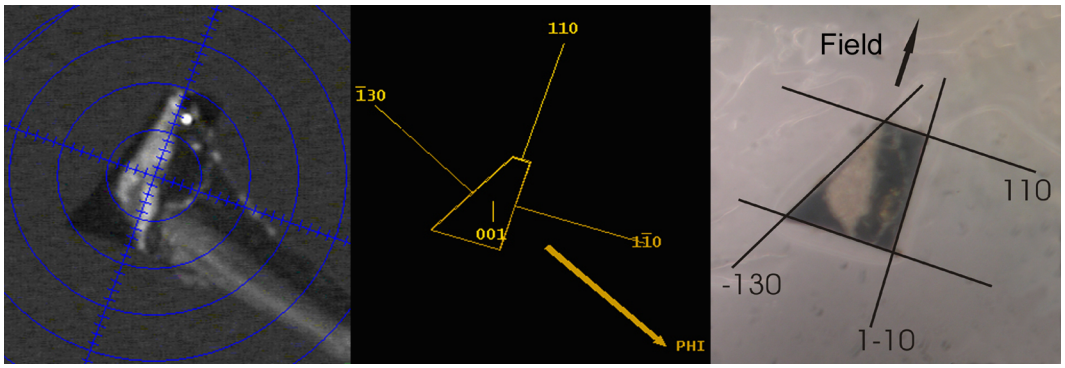

Figure 6.25: Sample tl320c5 X-ray alignment. Left panel shows a visible spectrum image from the X-ray diffractometer of the sample. Middle panel shows the reciprocal space indices of the face perpendiculars corresponding to the image on the left. Right panel shows a photo of the sample with the reciprocal space indices of the face perpendiculars. $a = 3.90$ Å, $b = 3.95$ Å, $c = 23.5$ Å, $\alpha = 87°$, $\beta = 92°$ and $\gamma = 92°$.

overdoping (i.e. with lower T_c).

These differences may be due to ARPES-specific mechanisms such as instrumental resolution broadening, elastic forward scattering, residual k_z dispersion or surface effects due to cleaving the crystal. Elastic forward scattering can be caused by out-of-plane impurities such as substitution of copper onto thallium sites or oxygen doping atoms. Above T_c, in the normal state, its contribution to the scattering is larger in the antinodal direction (as the Fermi velocity is smaller) than in the nodal direction. Below T_c, due to the opening of the superconducting gap, it is strongly suppressed in the antinodal direction, but not in the nodal direction. Comparing the magnitude of the scattering rates observed by ARPES ([25]) and this ADMR work ($\hbar/\tau = \hbar eB/(\omega_c \tau m^*) \approx 3$ meV where B = 45 T, $\omega_c \tau = 0.45$ and $m* = 4.1 m_e$ [27]) shows that the ARPES measurement is an order of magnitude larger. This suggests that significant forward scattering is picked up in the ARPES measurement, but this scattering has much less of an effect on a transport measurement as it is not a direct **k**-state probe. Given that ADMR is a bulk probe, it is possible that the anomalously large line widths seen in ARPES most probably arise from additional scattering at the (cleaved) surface. The k_z dispersion vanishes along both the nodal and antinodal directions, so it is not obvious how this could relate to the quasiparticle anisotropy. It should also be noted that the results in Platé *et al.* are taken below T_c in the the superconducting state, whereas this work is performed in the field induced normal state and the true normal state. The data presented here (both above and below the sample T_c) are fully consistent with the scattering rate being anisotropic and maximal along (π,0).

It is speculated by Platé *et al.* in [25] that, if really present, the quasiparticle anisotropy reversal they see across optimal doping might be the signature a quantum critical point within the superconducting dome. It has been suggested a QCP occurs at a critical doping level where the pseudogap energy scale, T^*, vanishes [113].

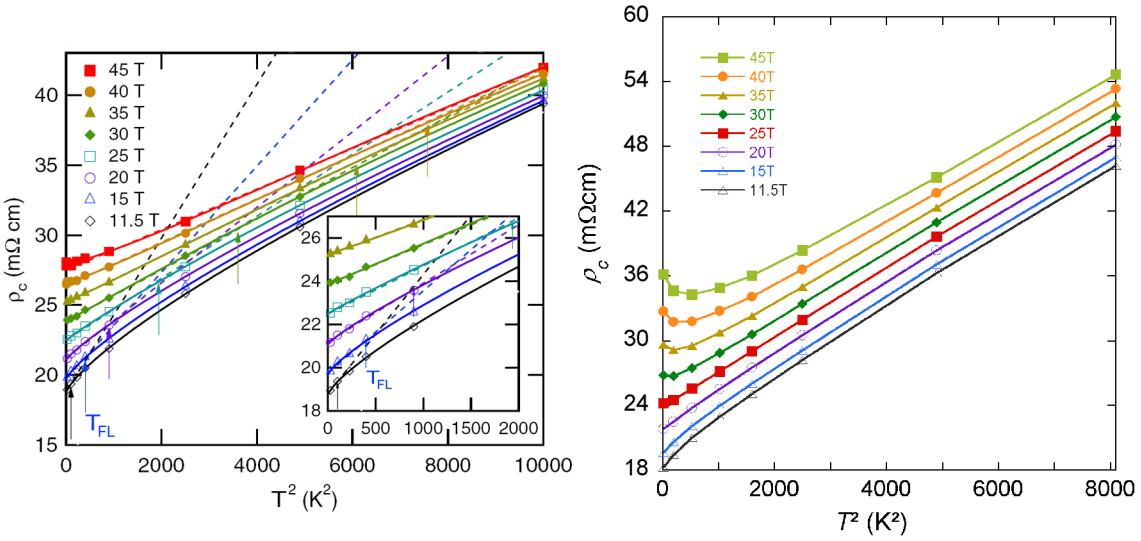

Figure 6.26: Left panel shows a figure from the Shibauchi paper [114] showing ρ_c fitted to a AT^2 dependence (dashed lines) at low temperatures. Arrows indicate 'deviation' from T^2 behaviour. Right panel shows a simulation of the graph from the Shibauchi paper using parameters from ADMR analysis for sample tl320c5.

6.5.2 A Possible Field Induced 'Quantum Critical Point'

Shibauchi *et al.* [114] report on a boundary between a Fermi liquid and non-Fermi liquid state, ending in a potential field induced quantum critical point. This would seem to bear some similarities to the quantum criticality observed in heavy-Fermion compounds, suggesting common underlying physics between these materials and the cuprates. Their investigation was performed by measuring high field c-axis magnetoresistivity data in $Tl_2Ba_2CuO_{6+\delta}$; exactly the same as the data measured for the above work, but at a range of fields and only at $\theta = 0°$. Figure 6.26 left is from their paper and identifies an apparent field dependent deviation at $T_{\rm FL}$ of the resistivity from a T^2 fit at low temperatures. However, no evidence of this is observed in data taken for this thesis. The results presented earlier in this chapter offer an alternative explanation based on cyclotron effects.

The earlier graphs of tl320c5 (which has $T_c = 15\,\mathrm{K}$ — the same as the sample reported in [114]) in figure 6.9 show an upturn around $\theta = 0°$ at low temperatures which arises because of the presence of a two fold term (k_{21}) in the Fermi surface modulation (see figure 5.5). Figure 6.26 right reproduces Shibauchi's figure for tl320c5 showing the actual data points at 45 T and scaled, simulated data ($\omega_c\tau(B) = \omega_c\tau(45T) \times B/45$ — which was found to give an accurate fit [37]) at lower fields. The upturn seen in figure 6.26 down to 30 T appears when the sample is clean enough and $\omega_c\tau$ and the magnetic field are high enough. At a particular intermediate field (25 T in this example), ρ_c appears to follow a T^2 dependence over a wide temperature range similar to the 45 T data in [114]. However, neither the upturn in ρ_c vs T^2 nor the T^2 crossover regime have any physical meaning. It appears that Shibauchi *et al.* have simply measured a sample of exactly the correct quality to observe their

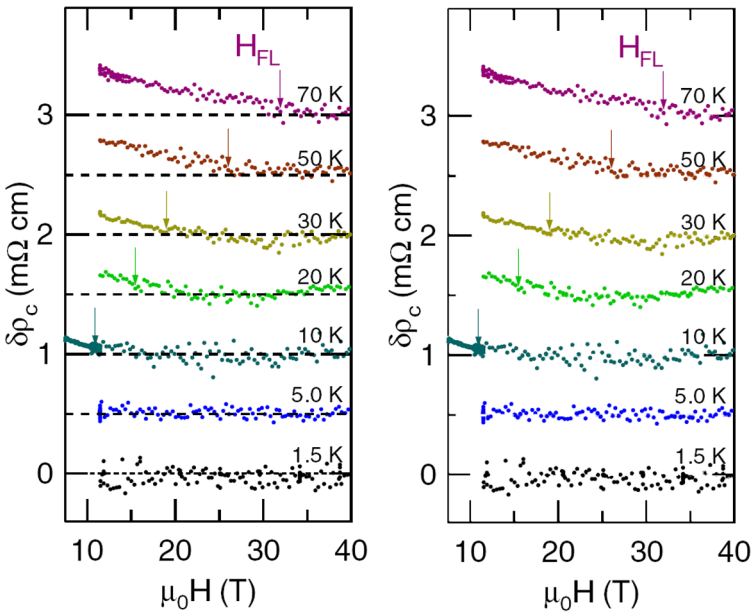

Figure 6.27: Left panel shows a figure from the Shibauchi paper [114] showing $\delta\rho_c$ obtained by subtracting the H-linear part from $\rho_c(H)$ at fixed temperature. Each curve is shifted vertically for clarity. $H_{\rm FL}(T)$, marked by arrows, are the deviation points from H-linear magnetoresistance. Right panel shows the same figure as on the left with the horizontal dashed lines removed illuminating the potential dubious positioning of the $H_{\rm FL}(T)$ arrows.

results and draw their conclusion of a field-induced quantum critical point. With lower quality samples the primary difference is the reduced $\omega_c\tau$ value at a given field strength. Figure 6.26 clearly shows that at $T = 0\,\mathrm{K}$ a reduction in the $\omega_c\tau$ value as the field decreases removes the upturn and the 25 T data becomes linear and comparable to Shibauchi's 45 T data. A further, direct indicator of the high quality of the samples used in this thesis comes from the first observation of Shubnikov-de Haas (SdH) oscillations reported in the next chapter using samples from the same batch.

As well as finding a $T_{\rm FL}$, Shibauchi *et al.* find a corresponding $H_{\rm FL}$ by examining the difference, $\delta\rho_c(H)$, between ρ_c and the H-linear part of ρ_c at fixed temperature. Looking at figure 4b in [114] and reproduced here in figure 6.27 left, it is potentially possible that there is some systematic deviation from a H-linear magnetoresistance indicated by the $H_{\rm FL}$ arrows. However, when the dashed horizontal 'guides to the eye' are removed as shown in figure 6.27 right, the determination of $H_{\rm FL}$ does not seem reliable or even possible from the presented data. Further, Shibauchi *et al.* argue that the field dependent $T_{\rm FL}$ and temperature dependent $H_{\rm FL}$ they observe can only be the result of the system being driven towards a quantum critical point. This is very similar to field induced quantum critical point found in $CeCoIn_5$ [115], which is probably related to spin correlations. Further evidence that quantum criticality is not the cause of these effects are given by Phillips using a percolative network model for dopant atoms [116].

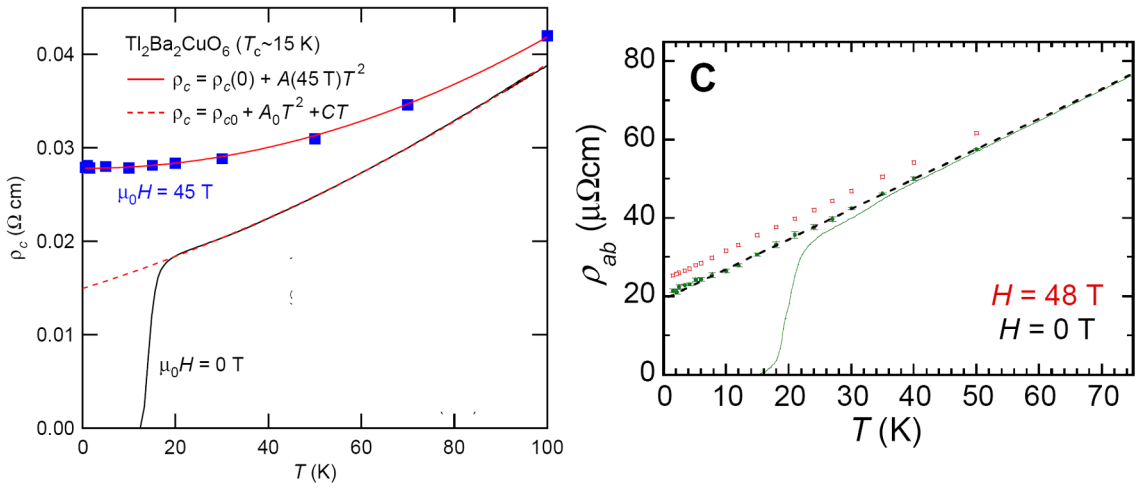

Figure 6.28: Left panel shows the temperature dependence of c-axis resistivity of $Tl_2Ba_2CuO_{6+\delta}$. Figure from [114]. Right panel shows the temperature dependence of the in-plane resistivity of LSCO. Figure from [39].

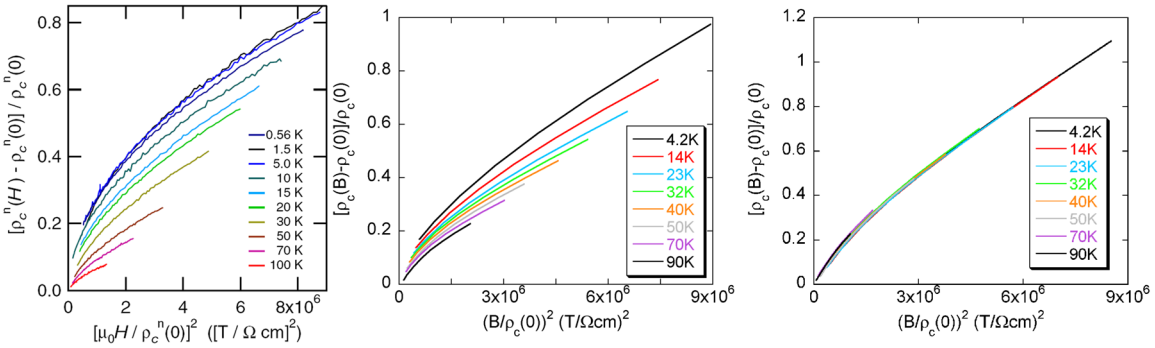

Figure 6.29: Left panel shows the Kohler plot of normal state magnetoresistance from [117]. Centre panel shows a simulation of the Kohler plot using anisotropic $\omega_c\tau$. Right panel shows a simulation of the Kohler plot with isotropic $\omega_c\tau$.

In the case of the in-plane resistivity of LSCO, the application of a magnetic field of 48 T is shown to have no effect on the temperature dependence of the resistivity [39], see figure right of figure 6.28. This is in contrast to what is observed in the c-axis resistivity of $Tl_2Ba_2CuO_{6+\delta}$ (see left of figure 6.28), which data presented in this thesis suggests is due to a systematically varying ADMR which gives the impression of a T^2 $\rho_c(T)$ but can be explained using a temperature dependent anisotropic scattering rate.

Shibauchi *et al.* observe a violation of Kohler's rule as shown in [114], [117] and reproduced on the left in figure 6.29. They argue that this proves that the critical scaling they observe is intrinsic and not simply governed by $\omega_c\tau$. This is not necessarily correct. Kohler's rule is obeyed only if $\omega_c\tau$ is isotropic or its basal plane anisotropy is constant with temperature. The right of figure 6.29 shows a Kohler plot simulation using measured and scaled parameters with an isotropic $\omega_c\tau$. This shows no

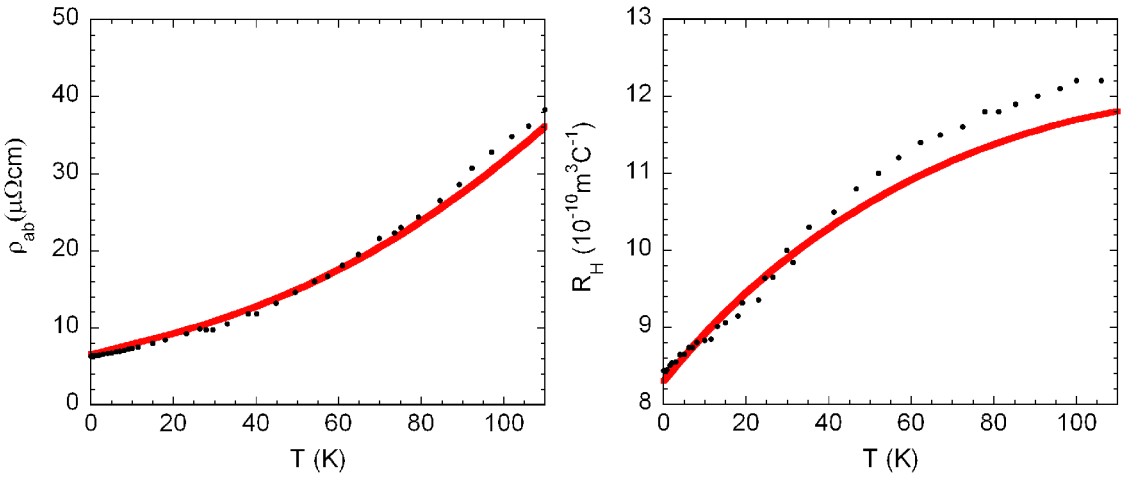

Figure 6.30: Temperature dependence of the in-plane resistivity (left panel) and in-plane Hall coefficient (right panel) for $Tl_2Ba_2CuO_{6+\delta}$ with $T_c = 15\,\mathrm{K}$. The black circles are experimental data from reference [19] and the red solid lines are simulations for tl320c5 using the Fermi surface parameters and the temperature dependence of the scattering rate given above.

violation of Kohler's rule, as expected. The centre of figure 6.29 shows a Kohler plot simulation with an anisotropic $\omega_c\tau$ where the anisotropy is temperature dependent and the magnitude is obtained from ADMR measurements. This shows a violation of Kohler's rule in good agreement with that measured by Shibauchi and shows that contrary to their assertion, the effect they see *can* be entirely explained by cyclotron effects and their work is not evidence of a quantum critical point.

6.6 Transport Coefficients Simulation

Using the parameters from the above ADMR fits (specifically k_{00}, k_{40} and the temperature dependence of $2\gamma/\omega_c\tau$ and $1-\gamma/\omega_c\tau$) we have all that is needed in principle to calculate the various coefficients of the in-plane conductivity tensor using the method described in §5.5. One way to include the anticipated return to isotropic scattering at high temperature is to add, in parallel, a maximum scattering rate $\Gamma_{\max} = \langle v_F(\psi)\rangle/a$ where a is the in-plane lattice spacing and $\Gamma(\psi)$ is the anisotropic scattering rate from the above fits:

$$\frac{1}{\Gamma_{\text{effective}}(\psi)} = \frac{1}{\Gamma(\psi)} + \frac{1}{\Gamma_{\max}(\psi)} \tag{6.4}$$

This was suggested by Hussey [36] and was shown to both qualitatively and quantitatively account for the temperature dependence of the in-plane resistivity and Hall effect in a number of overdoped cuprates. It is simply the application of the Mott-Ioffe-Regel limit [118] i.e. the mean free path ℓ can never become shorter than the interatomic spacing a, since at that point the concept of carrier velocity is lost and all coherent quasiparticle motion vanishes. This suggests that there is a

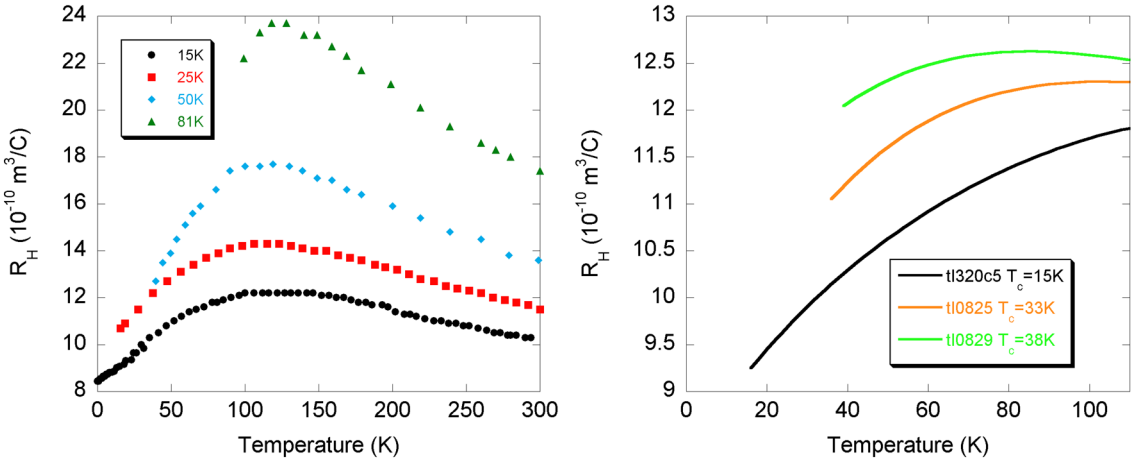

Figure 6.31: Temperature dependence of the in-plane Hall coefficient. Left panel shows experimental data — $T_c = 15\,\mathrm{K}$ [19], $T_c = 25\,\mathrm{K}$ [77], $T_c = 50\,\mathrm{K}$ [84] and $T_c = 81\,\mathrm{K}$ [76]. Right panel shows simulations using ADMR parameters for samples tl320c5 ($T_c = 15\,\mathrm{K}$), tl0825 ($T_c = 33\,\mathrm{K}$) and tl0829 ($T_c = 38\,\mathrm{K}$).

maximum scattering rate modeled by $\Gamma_{\max}$. By adding this to the observed anisotropic scattering rate in parallel, $\Gamma_{\text{effective}}$ saturates at different points on the Fermi surface at different temperatures.

Simulations of both ρ_{ab} and R_H for tl320c5 ($T_c = 15\,\mathrm{K}$) are shown in figure 6.30 as solid red lines alongside experimental data for a $T_c = 15\,\mathrm{K}$ crystal as black circles taken from reference [19]. The strong linear form of ρ_{ab} up to 110 K is reproduced well by this parameterisation ($3\,\mu\Omega$cm was subtracted from the simulated value, but it is not unreasonable to expect different crystals to have different residual resistivities). Comparison with figure 6.14 suggests that the temperature dependence of ρ_{ab} is largely determined by the linear anisotropic scattering component. Further, as the doping is decreased, figure 6.14 also shows that the strength of the anisotropic scattering increases in line with the strengthening T-linear component observed in ρ_{ab} (see figure 3.9). The calculated value of R_H at $T = 0\,\mathrm{K}$ is found to be in excellent agreement with the experimental value confirming that the isotropic-ℓ approximation is valid and $R_H(0)$ can be estimated directly from the size of the Fermi surface in overdoped $Tl_2Ba_2CuO_{6+\delta}$. The good fit of the temperature dependence of R_H shows that the change in anisotropy in $1/\omega_c\tau$ as a function of angle and temperature can account for the observed rise in R_H. Good fits are also found between samples tl300c1 ($T_c = 20\,\mathrm{K}$) and tl320c3 ($T_c = 17\,\mathrm{K}$) and the sample experimental data. These fits provide a good consistency check that the parameters extracted from the ADMR analysis are reasonable.

Simulations on the right of figure 6.31 for tl0825 and tl0829, which have higher T_c values, show $R_H(T)$ increases as a function of increasing T_c. This is in qualitative agreement with what is found experimentally and shown on the left in figure 6.31. However, the discrepancies which begin to appear as T_c increases from 15 K possibly arise from the emergence of vertex corrections [119]. To lowest order the c-axis conductivity is related to the convolution of two in-plane spectral functions

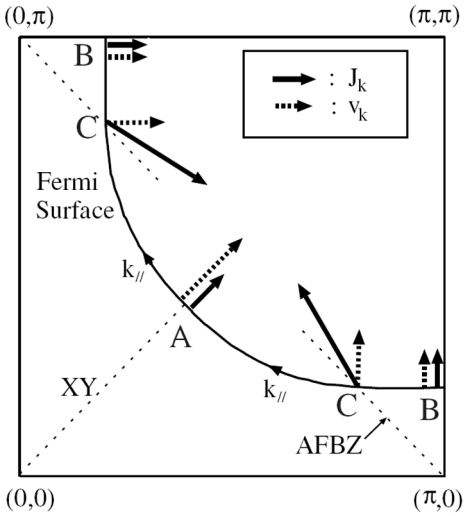

Figure 6.32: Schematic behaviour of the total current $\mathbf{J}_k$ and the quasiparticle velocity $\mathbf{v}_k$ on the Fermi surface. Figure from [119].

so that it may be calculated without the need for vertex corrections [109]. This means that vertex corrections may only effect in-plane transport and not ADMR which is an out of plane effect. In fact, Kontani [120] has recently pointed out that current vertex corrections may play a significant role in determining the transport properties. In the relaxation time approximation used here these currents, arising because of the interactions between quasiparticles, are ignored. Using the fluctuation-exchange (FLEX) model, Kontani has showed that (for LSCO) a T-linear ρ_{ab} and a Hall effect with a $1/T$ dependence (in agreement with experiment) arise naturally from the variations in the $\mathbf{k}$-dependence of the total current $\mathbf{J}_k$ and velocity $\mathbf{v}_k$ around the Fermi surface due to the current vertex corrections, see figure 6.32.

6.7 Discussion

The ADMR data can be fitted extremely accurately using the anisotropic scattering rate across the full range of θ, ϕ, temperature up to 110 K and T_c up to 38 K. The simulations of the Hall effect and in-plane resistivity provide strong evidence that the previously anomalous transport properties of $Tl_2Ba_2CuO_{6+\delta}$ are, to a large degree, explained by the temperature dependent anisotropy in the scattering rate. This is especially true at higher doping, although perhaps less so at lower doping where vertex corrections or, as we shall see in chapter 8, the pseudogap may play an increasingly important role. At $T_c = 15$ K the anisotropic scattering rate reproduces accurately the in-plane transport properties. As these are found to evolve gradually and smoothly as doping is decreased, it is likely that the anisotropic scattering rate found here exists across the entire overdoped side of the phase diagram. Fruchter *et al.* [121] recently showed that the Hall effect in $Bi_2Sr_2CuO_{6+\delta}$ can be

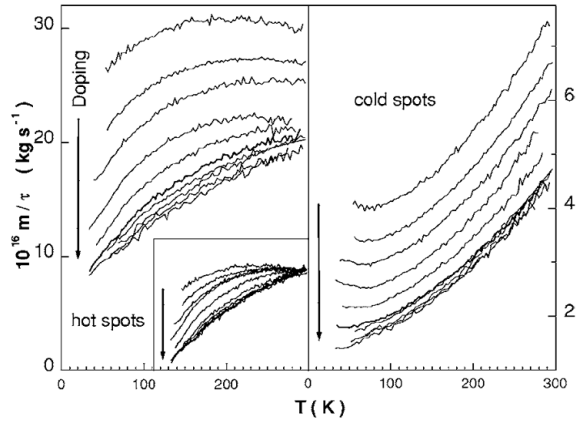

Figure 6.33: Scattering time for $Bi_2Sr_2CuO_{6+\delta}$ obtained from analysis of Hall effect data using an anisotropic mean-free-path model. Left panel is along (π,0) and right panel is along (π,π). Figure from [121].

explained by a combination of a large T-independent scattering rate and an anisotropic temperature dependent one. This allowed a scattering time along the (π,0) and (π,π) directions to be extracted — see figure 6.33. Interestingly, the temperature dependence along (π,π) was found to be quadratic and along (π,0) it was found to be linear below 100 K and saturating at higher temperatures — in agreement with what is found in this work.

The inconsistency between the magnitudes of the scattering rate found by ARPES and ADMR is probably routed in the two probes measuring different scattering rates. Recent theoretical work has helped clarify the meaning of the relaxation rate determined by ADMR measurements. Smith *et al.* [122] suggest that although ADMR is a transport measurement the fact that electrons are bound in tight electron orbits and can be transferred from one orbit to another via small angle scattering suggests that scattering processes (which play no role in zero-field transport) might be significant. They find that at $\theta = 0°$ (i.e. field parallel to the current and perpendicular to the layers) the effective scattering rate is the transport relaxation rate, while at $\theta = 90°$ the relevant quantity is the total quasiparticle scattering rate. At intermediate θ the scattering rate depends on the in-layer momentum dependence of the scattering cross section. This suggests that an improved fit for ADMR data might be achieved by allowing the scattering rate to depend on θ. Notably, if the scattering is by atomic scale defects there should only be up to a factor of unity difference between the $\theta = 0°$ and $\theta = 90°$ scattering rates. If the dominant scattering mechanism is of electronic origin then the two scattering rates are approximately equal. Although if the scattering is from extended defects or long wavelength phonons there will be a large difference in the scattering rates. Given that in the ADMR data above there seems little need for a θ dependent scattering rate this might point the way to the source of the anisotropic scattering.

Finite temperature effects, i.e. the broadening of the Fermi distribution function at high temper-

ature, are not included in the above analysis. Their effect has recently been considered by Brinkman *et al.* [123] where they find that the T-linear anisotropic term in the scattering rate is robust up to 110 K. Finite temperature effects, however, may affect the form of the scattering rate components at higher temperatures.

The correlation between T_c and the magnitude of the anisotropic scattering revealed in figures 6.16 and 6.17 is also backed up by recent measurements on LSCO [39]. Here the resistivity fits well to $\rho_{ab}(T) = \alpha_0 + \alpha_1 T + \alpha_2 T^2$. α_1, the T-linear contribution, is found to scale with T_c and notably to persist down to a temperature of the order 1 K. It rises from zero as doping is decreased from the superconducting/non-superconducting boundary. The T^2 coefficient, α_2, remains approximately constant as a function of doping. Although in line with what is found in this work, the study in reference [39] covers a larger doping region. Furthermore, the separation of $\rho_{ab}(T)$ into two temperature dependent terms which sum in 'series' in reference [39] is in agreement with the separation of the anisotropic scattering rate into two additive components. As these have contrasting temperature and doping dependencies, this suggests that there are two independent quasiparticle scattering processes which coexist everywhere on the Fermi surface (except perhaps, along the zone diagonals where the anisotropic component vanishes).

With the observation of a quadratic energy/ω (as well as a quadratic T) dependence of the scattering rate in ARPES measurements on overdoped cuprates [124] it is possible to attribute the T^2 term to conventional Fermi liquid electron-electron scattering. What remains now is to identify the origin of the T linear scattering. Together, the additive components in $1/\tau$ and the T-linear component present along the nodes (which vanishes as superconductivity vanishes, persists to very low temperatures and seems to be present across the entire overdoped side of the phase diagram) places strong constraints on any theoretical model. A number of models have been proposed which will be briefly reviewed below, although they have some of the relevant features, none are able to satisfactorily explain all the experimental observations.

Recently Dell'Anna *et al.* [125] showed that a d-wave Pomeranchuk instability in a two dimensional metal has a transport decay rate with a linear temperature dependence everywhere on the Fermi surface (except at the zone diagonals). A Pomeranchuk instability is a topological deformation of the Fermi surface, although they have never been observed they are often suggested as mechanisms for some correlated electron phenomena. When this predicted linear component is combined with impurity scattering and conventional isotropic electron-electron scattering this gives a form of the scattering rate which is identical to what is observed in $Tl_2Ba_2CuO_{6+\delta}$. As yet it is not clear whether a Pomeranchuk instability can explain the observed doping dependence of the magnitude of the scattering rate, but since it is a small angle effect it appears that it can't create pairing (and therefore superconductivity).

Similar to $Tl_2Ba_2CuO_{6+\delta}$ and the other cuprates, an anomalous Hall coefficient and T-linear

resistivity have been observed in the heavy fermion superconductor $CeCoIn_5$. Comparisons are often drawn between the cuprates and heavy fermion compounds despite their very low T_c values. They have similar phase diagrams and transport properties but do not suffer from the disorder introduced by doping as this tuning parameter is replaced by pressure. An anisotropic form for the scattering rate with separate T and T^2 dependent components is suggested by Nakajima *et al.* [126] and agrees well with experimental data. This anisotropic scattering rate is attributed to scattering by antiferromagnetic spin fluctuations and may prove relevant to $Tl_2Ba_2CuO_{6+\delta}$ as the origin of the T-linear anisotropic scattering. Notably, it has been observed that the appearance of spin fluctuations on the overdoped side of the phase diagram is correlated with the onset of superconductivity [127].

A T-linear anisotropic scattering term and its angle dependence (of the same form as found in this work) have recently been observed in the frequency dependent scattering rate in LSCO [40]. The linearity in both the temperature and frequency scales is suggestive of a marginal Fermi liquid [128], which has been shown able to support (up to a factor of two) anisotropy in the scattering rate [129]. Whilst sufficient to explain the observed scattering rate anisotropy in the $T_c \approx 20\,\mathrm{K}$ samples, it does not account for the larger anisotropy observed in the higher T_c samples.

A T-linear scattering rate has been predicted by Alexandrov [130] in a two dimensional fermion-boson mixture as a result of fermion scattering from fluctuations in the density distribution of charge $2e$ bosons. The linearity arises because the screening radius squared for Coulomb repulsion between free fermions and more localized bosons is proportional to the temperature above a boson condensation temperature. Thus the scattering rate should be linear in T above this condensation temperature, although the boson density needs to be small to be consistent with the observed large Fermi surface.

It has been suggested by Anderson [131], that the microscopic origin of the T-linear resistivity is associated with the Gutzwiller projection operator and the observed scattering rate anisotropy is due to the anisotropy in the Fermi velocity. An electron is thought of as decaying into two parts — a density wave and the electron. While these parts are separate one is scattered ordinarily and so can't combine back into the original electron. If there is no ordinary scattering the electron just recoheres after a finite time dependent upon the density of states. The density of states is proportional to the inverse of the Fermi velocity so the orientation is correct, although it is not yet clear if the scattering magnitude also agrees with experimental work.

Mishonov has derived an analytical formula for the Fermi surface of $Tl_2Ba_2CuO_{6+\delta}$ using the LCAO approximation spanned over the Cu4s, Cu3$d_{x^2-y^2}$, O2p_x and O2p_y states [73]. This is in good agreement with the shape suggested by the above ADMR measurements. By considering the same states, specifically hybridisation between the Cu4s and Cu3$d_{x^2-y^2}$ mediated by the O2p orbitals, an electron pairing interaction is predicted [132]. This is found to explain a number of experimental observations on the cuprates and the d-wave form for the superconducting gap. Due to

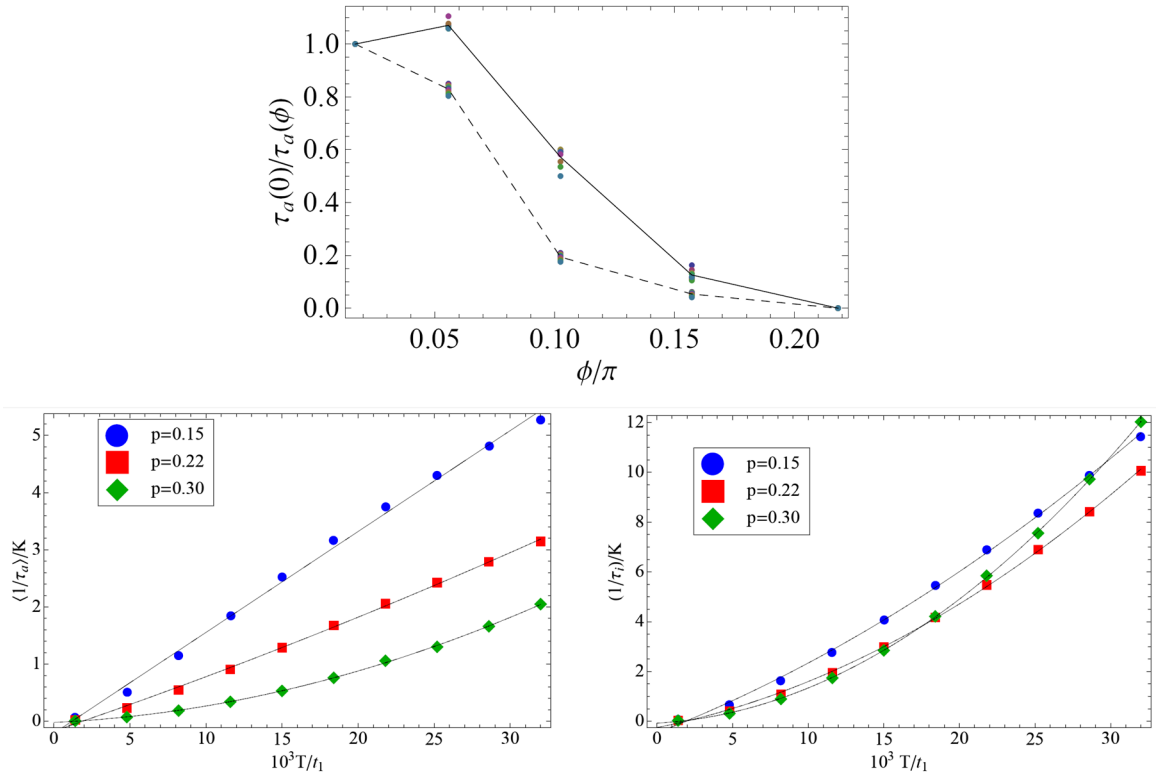

Figure 6.34: Top panel shows the angle dependence of the anisotropic component of the scattering rate where ϕ is the angle around the Fermi surface from (π,0). Dashed line is $p = 0.15$ and solid line is $p = 0.30$. Bottom panels show the temperature dependence of the anisotropic (left) and isotropic (right) components of the scattering rate at different hole dopings. Figure from [134].

the location of the Cu and O atoms in the CuO_2 plane, there is very little hybridisation along the zone diagonals leading to a minimum in back scattering in this direction. Considering the layered nature of $Tl_2Ba_2CuO_{6+\delta}$, Mishonov explains the observed linear temperature dependence of the resistivity as resulting from the scattering of charge carriers by fluctuations of electric charge between the layers [133]. It remains unclear at present, whether these predictions can be successfully combined to give a T-linear anisotropic scattering rate in agreement with experiments.

Finally, Ossadnik *et al.* [134] have used functional renormalisation group calculations in the two-dimensional Hubbard model to analyse the quasi-particle scattering rates. By suppressing the pairing divergence they find a rising anisotropic scattering vertex which gives a linear contribution to the anisotropic scattering rate. Significantly, this has the same angle, temperature and doping dependence and vanishes as superconductivity disappears, consistent with experimental observations above — see figure 6.34. They note that their linear contribution to the anisotropic scattering rate is due to strong scattering processes at large momentum transfer which arise in their calculations as a precursor to the Mott insulating behaviour at half filling.

When the origin of the T-linear anisotropic scattering rate is confirmed it will inevitably provide

a key piece in the puzzle of explaining the mechanism of high temperature superconductivity in the cuprates. Further work may be necessary on $Tl_2Ba_2CuO_{6+\delta}$ samples with higher T_c values and at even higher temperatures, but this may not be possible until advances in magnet technology permit even higher persistent fields to be reached.

Chapter 7

Quantum Oscillations in $Tl_2Ba_2CuO_{6+\delta}$

As shown earlier in §3.2, bandstructure calculations for overdoped $Tl_2Ba_2CuO_{6+\delta}$ predict a large two-dimensional cylindrical shaped Fermi surface. The analysis of the ADMR measurements described in chapter 6 yield a Fermi surface in broad agreement with the bandstructure results. Despite this, ADMR are the result of a semi-classical effect and therefore cannot give any definitive conclusions about the quantum mechanical nature of the electronic ground state. Similarly, quasiparticle like peaks have been seen in the ARPES derived energy density curves around the full Fermi surface of overdoped copper oxides including $Tl_2Ba_2CuO_{6+\delta}$ [25],[135]. However, their widths near the zone boundaries are often too broad (up to 0.1 eV) to be considered as conclusive evidence for long-lived fermionic quasiparticle states.

The observation of quantum oscillations in the magnetoresistance (the Shubnikov–de Haas (SdH) effect) and/or magnetisation (the de Haas–van Alphen (dHvA) effect) are a much more powerful, definitive signature of coherent quasiparticles. The quantisation condition that underlies this effect requires the quasiparticle wavefunction to remain coherent throughout an entire orbit of the Fermi surface. Recently, small Fermi surface pockets were discovered in the underdoped yttrium based copper oxides $YBa_2Cu_3O_{6.5}$ and $YBa_2Cu_4O_8$ through a series of quantum oscillation experiments [30],[31],[32],[136]. In contrast, ARPES measurements performed on other underdoped copper oxides suggest that the large underlying Fermi surface disintegrates into a set of disconnected Fermi arcs, centred on the zone diagonal, whose width diminishes with decreasing doping and temperature [137].

This chapter describes the recent observation of both the SdH and dHvA effects in overdoped $Tl_2Ba_2CuO_{6+\delta}$[27].

7.1 Experimental Procedure

The ADMR measurements in the previous chapter imply the existence of a Fermi surface cylinder in Tl2201 with an average Fermi wavevector k_F of 7.24 nm^{-1} (a factor of six larger than that of

the pocket first discovered in the yttrium-based copper oxides). Section 2.10 describes how the amplitude of the quantum oscillations is suppressed by impurity scattering as $\exp(-\pi k_F/eB\ell)$. At the combination of B and ℓ (respectively 35 T and 165 Å) at which dHvA oscillations from the small Fermi surface first become visible in $YBa_2Cu_3O_{6.5}$ [136], the signal from a correspondingly large sheet would be damped by a further ten orders of magnitude. So for any experiment on overdoped copper oxides to be viable, it is essential to work at the highest magnetic fields, with optimized signal-to-noise ratio, on single crystals of the highest quality available.

The Tl2201 crystals used in this experiment were grown and annealed as described in chapter 4. Around 20 crystals were screened for purity by measuring their zero field interlayer resistivity $\rho_\perp(T)$ via the standard 4 contact AC technique described in chapter 4 and compared with many others whose $\rho_\perp(T)$ had already been measured. Only four crystals with sufficiently large residual resistivity ratios (≈ 20) were selected for the high field magnetoresistance measurements carried out in a standard ^{4}He cryostat at the LNCMP pulsed field facility in Toulouse using the same contact configuration. For the torque measurements, small pieces of the same crystals were attached to sensitive piezoresistive cantilevers and mounted in a dilution refrigerator in a second magnet cell at LNCMP.

7.2 Data

High quality resistivity data were taken at five different temperatures with $B \parallel c$. The full up and down sweep at $2.8\,\mathrm{K} \pm 0.1\,\mathrm{K}$ is shown in figure 7.1. $\rho_\perp(B)$ rises rapidly above the irreversibility field, passes through a small plateau, then grows quasi quadratically with field up to 60 T. The inset shows a magnified view of the high field region of the down sweep. Small but well defined oscillations are clearly resolved in the raw data, with an amplitude that grows with increasing field strength. The maximum amplitude of the oscillations is only 0.5 mΩ.

Five sets of torque measurements were taken all at the lowest temperature achievable ($0.7\,\mathrm{K} \pm 0.2\,\mathrm{K}$) and are shown averaged in figure 7.1. Below $B = 14\,\mathrm{T}$, the torque shows hysteretic behaviour due to flux trapping and expulsion in the superconducting mixed state. Again, well defined oscillations are clearly resolved in the expanded region shown in the inset. The value of T_c for both crystals is 10 K (defined by their zero resistive state), compared with the maximal T_c in Tl2201 of 93 K. The torque crystal showed a very small kink in the zero field $\rho_\perp$ data around 20 K, suggesting that some fraction of the crystal, presumably the surface layer, had a higher T_c value.

7.3 Analysis and Discussion

SdH data for three of the five temperatures are shown in figures 7.2, 7.3 and 7.4. The top left panel of each figure shows the full field sweep. The top right panel shows the data trimmed to between

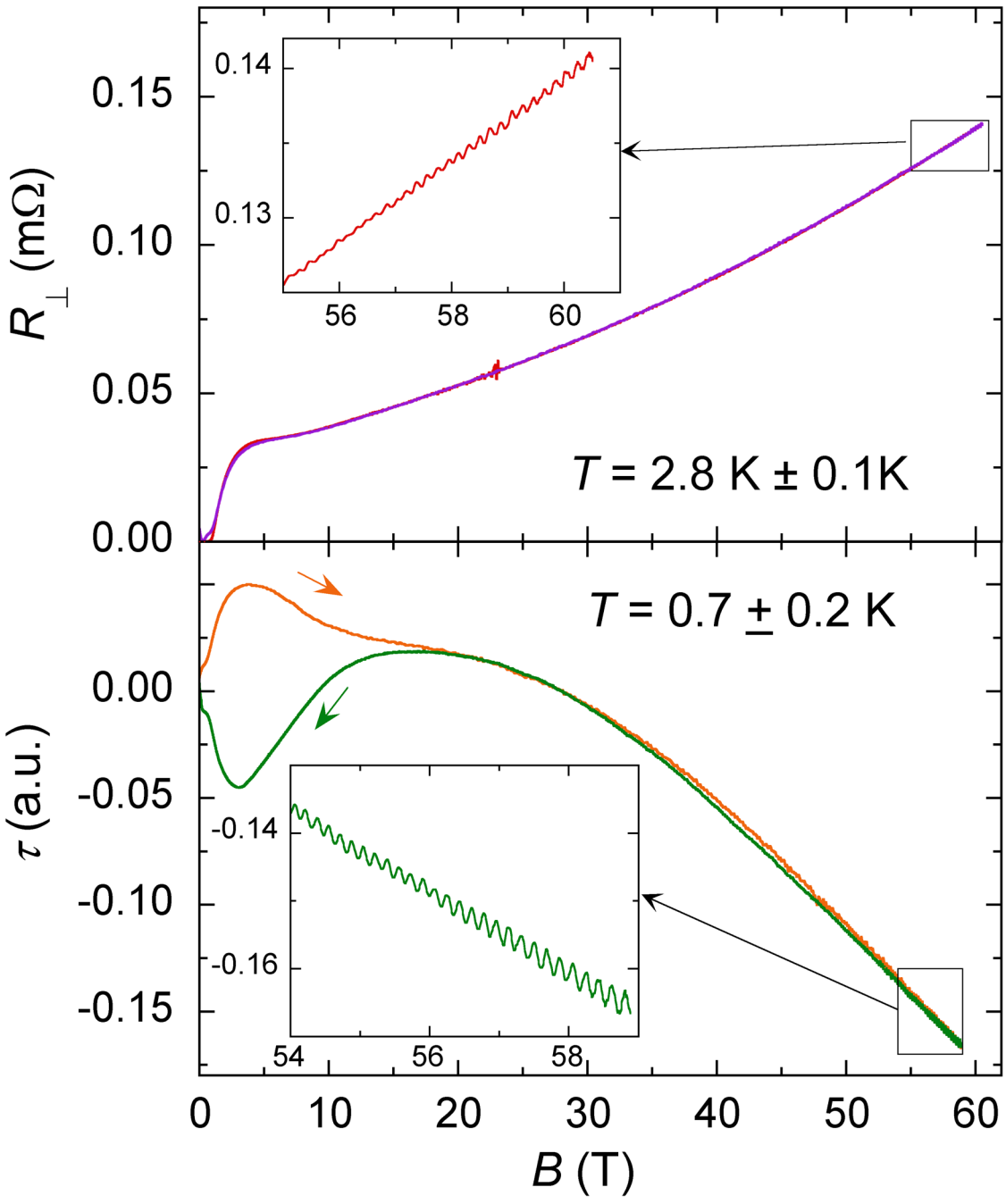

Figure 7.1: Top panel shows raw interlayer resistance $R_\perp$ data with $B \parallel c$ at 2.8 K. Bottom panel shows averaged magnetic torque data (from five sweeps) with B close to the c-axis at 0.7 K. Figure from [27].

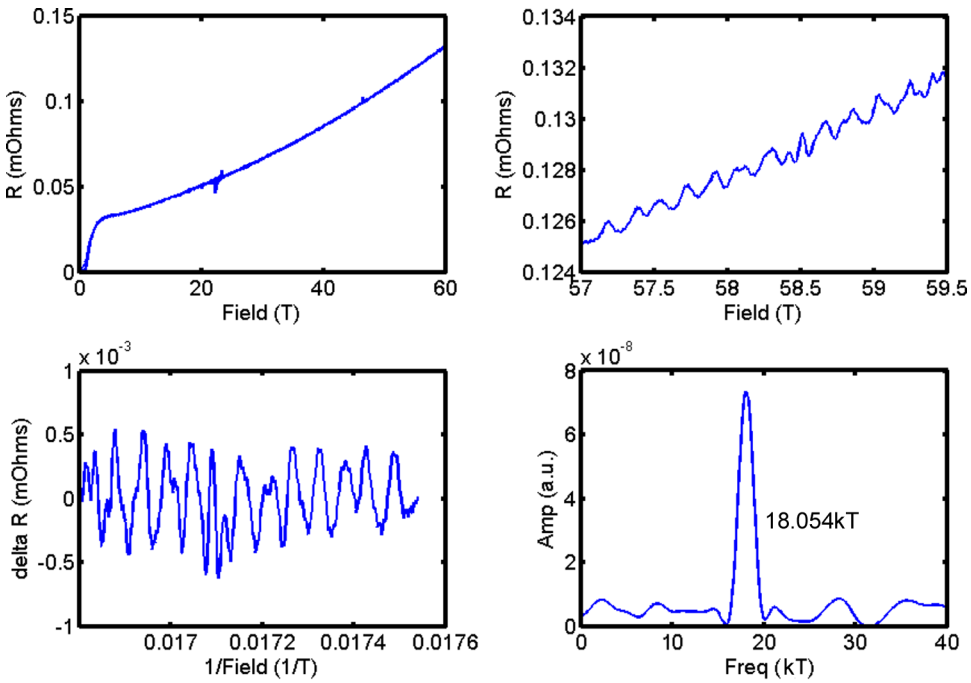

Figure 7.2: Top Left panel shows raw $R_\perp$ data at 2.9 K. Top right panel shows down sweep $R_\perp$ data between 57 T and 59.5 T. Bottom left panel shows down sweep $R_\perp$ data between 57 T and 59.5 T with monotonic background subtracted, plotted against inverse field. Bottom right panel shows Fast Fourier transform of data in previous panel showing sharp SdH frequency of 18.054 kT.

57 T and 59.5 T with clearly observable oscillations. The bottom right figure shows a monotonic background subtracted from the data and is plotted against $1/B$ to illustrate the periodic nature of the oscillations. Finally, the bottom right figure shows the fast Fourier transform of the oscillations from the previous panel. Due to the poor coupling between the sample and the thermometer in the ^{4}He cryostat it was not initially easy to determine the temperature of the sample. In order to do this accurately the same sample was returned to Bristol and placed into the 'Yellow Magnet' (see §4.10.2) where the sample temperature is known much more accurately as it is placed next to a thermometer. Field sweeps were performed for a large number of fixed temperatures less than 7.5 K and H_{c2} was measured (see figure 3.13). The resulting graph of H_{c2} verses temperature (see figure 7.5) was used to accurately calculate the temperature of the data with quantum oscillations by comparing H_{c2} values.

Torque data averaged from five sweeps is shown in figure 7.6 and shows clear oscillations down to 50 T. The fact that these oscillations are visible in both the resistivity and magnetisation well above the upper critical field confirms them as quantum oscillations. The temperature of the measurements are subject to an uncertainty of ≈ 150 mK due to the weak thermal link inside the dilution refrigerator and the high currents needed to observe the oscillations. Via the Onsager relation (equation 2.67) the frequency found of 18100 ± 50 T can be related to an area of $172.8 \pm 0.5\,\mathrm{nm}^{-2}$ and an average k_F of

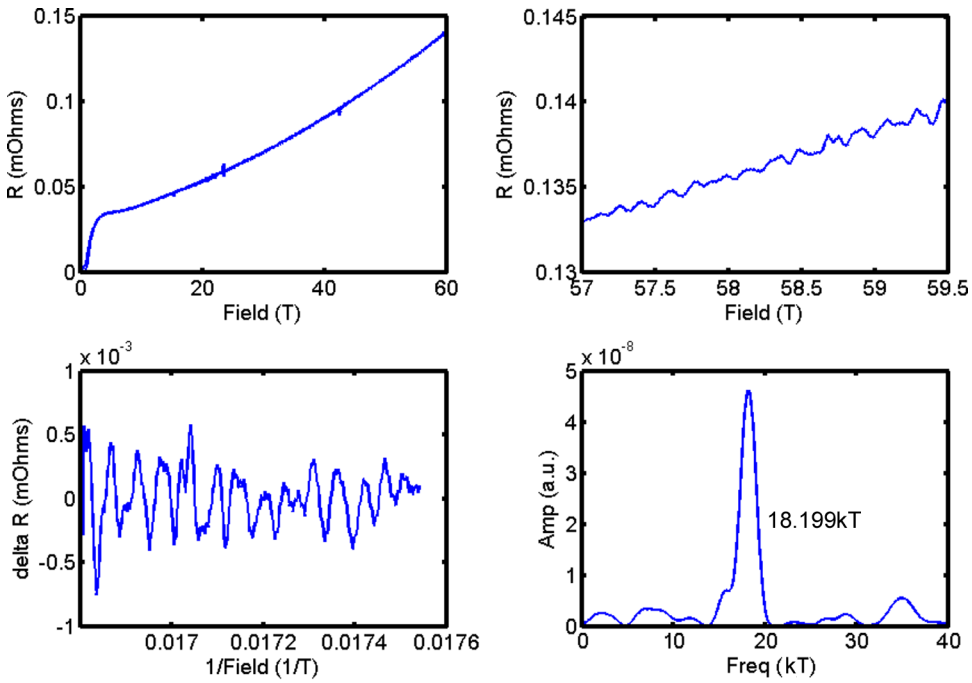

Figure 7.3: Top left panel shows raw $R_\perp$ data at 3.8 K. Top right panel shows down sweep $R_\perp$ data between 57 T and 59.5 T. Bottom left panel shows down sweep $R_\perp$ data between 57 T and 59.5 T with monotonic background subtracted, plotted against inverse field. Bottom right panel shows Fast Fourier transform of data in previous panel showing sharp SdH frequency of 18.199 kT.

$7.42 \pm 0.05\,\mathrm{nm}^{-1}$. The Fermi surface area and k_F deduced by ADMR in the previous chapter, ARPES [25] and bandstructure calculations (§3.2) are in close agreement with the values found here. The magnitude of the scattering rate is found to be between that measured by ARPES (≈ 35 meV [25]) and ADMR (≈ 3 meV) — $\hbar/\tau = \hbar^2 k_F/m^*\ell = 4.3$ meV (dHvA) where $k_F = 7.42\,\mathrm{nm}^{-1}$, $m^* = 4.1\,m_e$ and $\ell = 320$ Å [27]). This good overall consistency between these different measurements suggests that the Fermi surface is composed entirely of the single quasi two dimensional sheet that is observed in both the ADMR and quantum oscillations work presented here.

The temperature dependence of the Shubnikov–de Haas amplitude is shown in figure 7.6. Fitting this with the standard Lifshitz–Kosevich theory (see §2.10), a cyclotron effective mass of $m^* = 4.1 \pm 1.0\,m_e$ is obtained, where m_e is the free electron mass. Given that for a two-dimensional Fermi surface, the electronic specific heat (Sommerfeld coefficient) is

$$\gamma_{el} = \frac{\pi N_A k_B^2 a^2}{3\hbar^2} m^* \tag{7.1}$$

where k_B is the Boltzmann constant, N_A is Avogadro's number and $a = 3.86$ Åis the in-plane lattice constant, an m^* of $4.1 \pm 1.0\,m_e$ corresponds to $\gamma_{el} \approx 6.0 \pm 1.0\,\mathrm{mJmol}^{-1}\mathrm{K}^{-2}$, in excellent agreement with that measured directly for overdoped polycrystalline $Tl_2Ba_2CuO_{6+\delta}$ ($7 \pm 2\,\mathrm{mJmol}^{-1}\mathrm{K}^{-2}$) [138].

Bandstructure calculations predict that the bare band mass in stoichiometric $Tl_2Ba_2CuO_{6+\delta}$ is

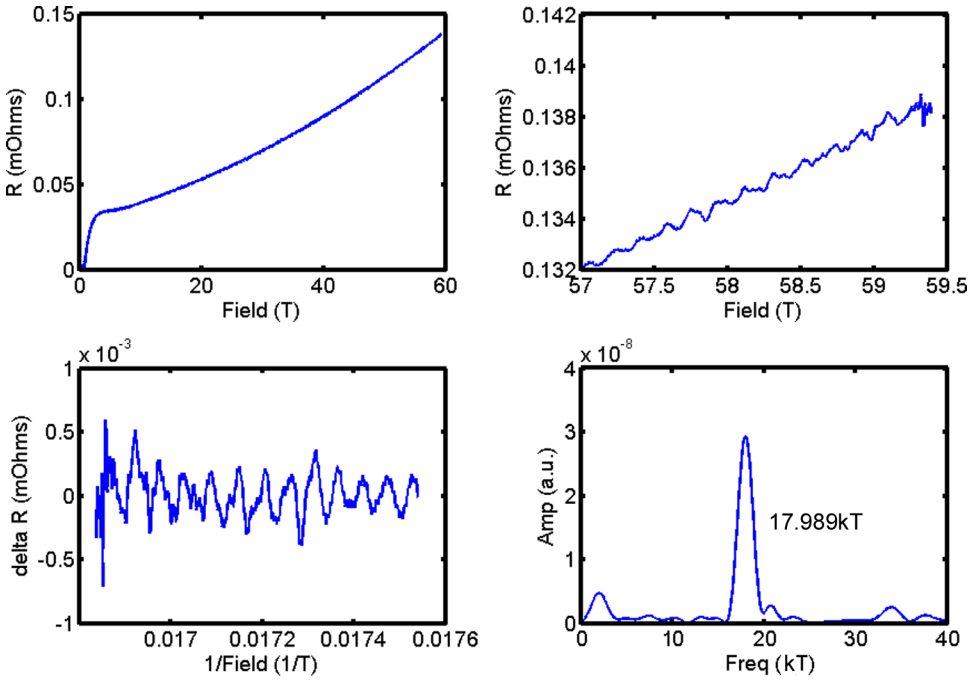

Figure 7.4: Top left panel shows raw $R_\perp$ data at 4.5 K. Top right panel shows down sweep $R_\perp$ data between 57 T and 59.5 T. Bottom left panel shows down sweep $R_\perp$ data between 57 T and 59.5 T with monotonic background subtracted, plotted against inverse field. Bottom right panel shows Fast Fourier transform of data in previous panel showing sharp SdH frequency of 17.989 kT.

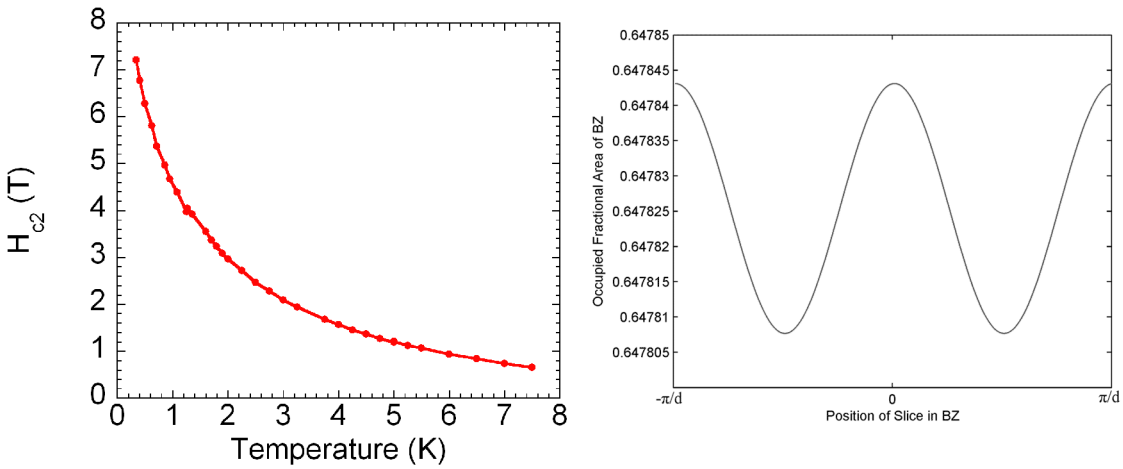

Figure 7.5: Left panel shows a graph of H_{c2} against temperature for the sample used for SdH measurements. Right panel shows the variation of area of ab-plane slice of Fermi surface with position down c-axis of Brillouin zone.

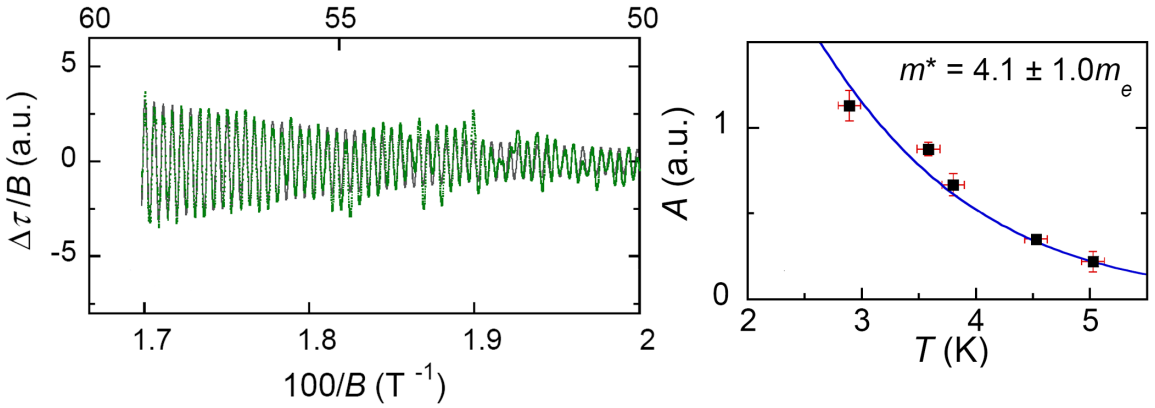

Figure 7.6: Left panel shows the oscillatory component of the torque data shown in figure 7.1 plotted as green dots against $1/B$ after a monotonic background has been subtracted. The black line is a fit to the Lifshitz–Kosevich formula described in §2.10. Right panel shows the temperature dependence of SdH amplitude. Solid line is fit to Lifshitz–Kosevich formula described in §2.10. Figures from [27].

$1.2\,m_e$ [72]. The difference between the measured and calculated masses implies strong electron correlation driven renormalisation effects. Despite the strong electron-electron interactions, observation of quantum oscillations implies that quasiparticles exist at all points on the Fermi surface of overdoped $Tl_2Ba_2CuO_{6+\delta}$. This observation of quantum oscillations in overdoped cuprates together with the reported oscillations in underdoped cuprates suggests that coherent quasiparticle states might exist across the whole doping range — at least at some points on the Fermi surface. These quantum oscillations also suggest that Fermi liquid theory can be applied on the overdoped side of the phase diagram and backs up the application of the Boltzman transport equation in the ADMR analysis.

According to the ADMR work of the previous chapter and [37], both on similar overdoped $Tl_2Ba_2CuO_{6+\delta}$ samples, the scattering rate contains two temperature dependent components; a dominant isotropic component, which varies quadratically with temperature and is characteristic of fermionic quasiparticle scattering, and an anisotropic component, maximal near the Brillouin zone boundaries and varying linearly with temperature down to very low temperatures. Thus, in this work, quantum oscillations have been observed in a metal for which a purely quadratic temperature dependence of the electrical resistivity at low temperatures (a key signature of a Landau Fermi liquid) is absent. The fact that quasiparticles arise, despite there being a T-linear contribution to the scattering rate, is in agreement with theoretical predictions [139],[140].

At first it might appear that these quantum oscillation results, taken at a very high magnetic field, only suggest that the pseudogap is closed at high field — i.e. it is field induced. It should be noted however that the Fermi surface parameters are consistent with transport [19], specific heat [138] and ARPES [25] data all taken at $B = 0\,\mathrm{T}$.

It will be interesting to see in the future how this well defined large barrel shaped Fermi surface in the overdoped regime evolves as doping is decreased towards the underdoped side of the phase

diagram. This will resolve whether the carrier density changes smoothly as doping decreases or if there is Fermi surface reconstruction along some critical line in the phase diagram caused by a competing order such as antiferromagnetism [141] or stripes [142]. On the underdoped side ARPES suggests there are disconnected Fermi arcs, whereas dHvA suggests a collection of small pockets so it seems that combined ARPES and dHvA measurements on the same underdoped compound are essential.

7.3.1 Beat Frequency Investigation

Given the three dimensional warping of the Fermi surface implied from ADMR measurements it is interesting to consider how the area of *ab*-plane slices of the Fermi Surface changes through the Brillouin zone. Clearly for a simple barrel shaped Fermi surface there will be a difference in area between an *ab*-plane slice at $k_z = 0$ and $k_z = \pi/d$ but for the three dimensional warping suggested by ADMR the magnitude and character of the variation is not immediately obvious. Using *Matlab* and a representative parameter set ($k_{00} = 0.739\,\text{Å}^{-1}$, $k_{40}/k_{00} = -0.03$, $k_{61}/k_{21} = 0.68$, $k_{101}/k_{21} = -0.25$ and $\rho_c/\rho_{ab} = 1000$) the area of a slice can be calculated — see Figure 7.5 and §10.7.6. In the case of dHvA or SdH measurements a difference in area corresponds to different frequencies being visible which may show up as a beat frequency. (Simply by having two frequencies, f_1 and f_2, a beat would be observed at a frequency of $|f_1 - f_2|$.) Using the Onsager relation the change in area can be converted into a beat frequency of approximately 1 T which will be unresolvable in main signal of 18.1 kT.

Chapter 8

$Tl_2Ba_2CuO_{6+\delta}$ T_c=45K ADMR

This chapter reports detailed measurements on the temperature and angle dependence of ADMR measurements on two $Tl_2Ba_2CuO_{6+\delta}$ samples with $T_c = 45\,\mathrm{K}$. In contrast with data in chapter 6 it is found that these data do not fit the model used previously. A number of alternative forms for the anisotropy are investigated but fail to improve the fit to the experimental data. By considering the existence of the pseudogap removing certain states, it has been possible to analyse data at specific azimuthal angles for the first time.

8.1 Experimental Data

These data were taken concurrently with that for samples tl0825 ($T_c = 33\,\mathrm{K}$) and tl0829 ($T_c = 38\,\mathrm{K}$) during April 2008. They cover five azimuthal angles at temperatures between 15 K and 70 K for samples tl0803 and tl0807 both with $T_c = 45\,\mathrm{K}$. Zero field c-axis resistance measurements for these samples are shown in figure 8.1. Electrical contacts were attached with 6838 silver epoxy. Figures 8.2 and 8.3 show the experimental ADMR data as solid lines. These data are noticeably different to any other AMDR data shown in chapter 6 — even from the tl0829 sample. At the lowest temperature the previous data fan out over different azimuthal angles at around $\pm 40°$. In the $T_c = 45\,\mathrm{K}$ samples the spread of data across the range of azimuthal angles at fixed θ is significantly less and of a different shape. Further differences are noticeable at $\theta = \pm 90°$ where the previous data showed significant ϕ dependence at all temperatures, the $T_c = 45\,\mathrm{K}$ data show this ϕ dependence has (almost) vanished. The magnitude of $\Delta\rho/\rho$ at $\theta = 90°$ is also increased for the $T_c = 45\,\mathrm{K}$ samples compared to tl0825 and tl0829. This is all neatly summarised in figure 8.4 where b/a is the normalised spread of the data at $\theta = 75°$ across the range of ϕ angles and c/a is the spread at $\theta = 40°$ [143]. Figure 8.4 demonstrates that there is a clear trend with increasing T_c of the ϕ dependence of the ADMR decreasing. These new data are in agreement with that previously reported on a single sample measured at two temperatures [38].

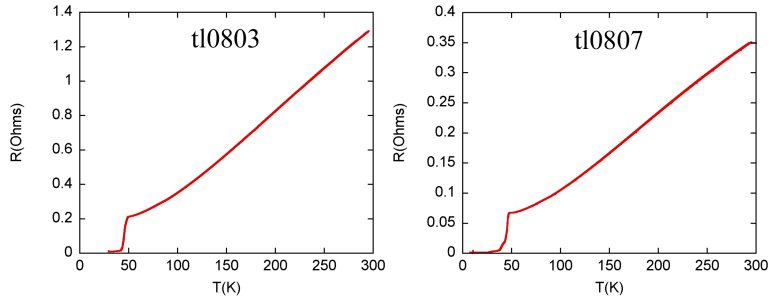

Figure 8.1: Zero field c-axis resistivity measurements for samples tl0803 and tl0807.

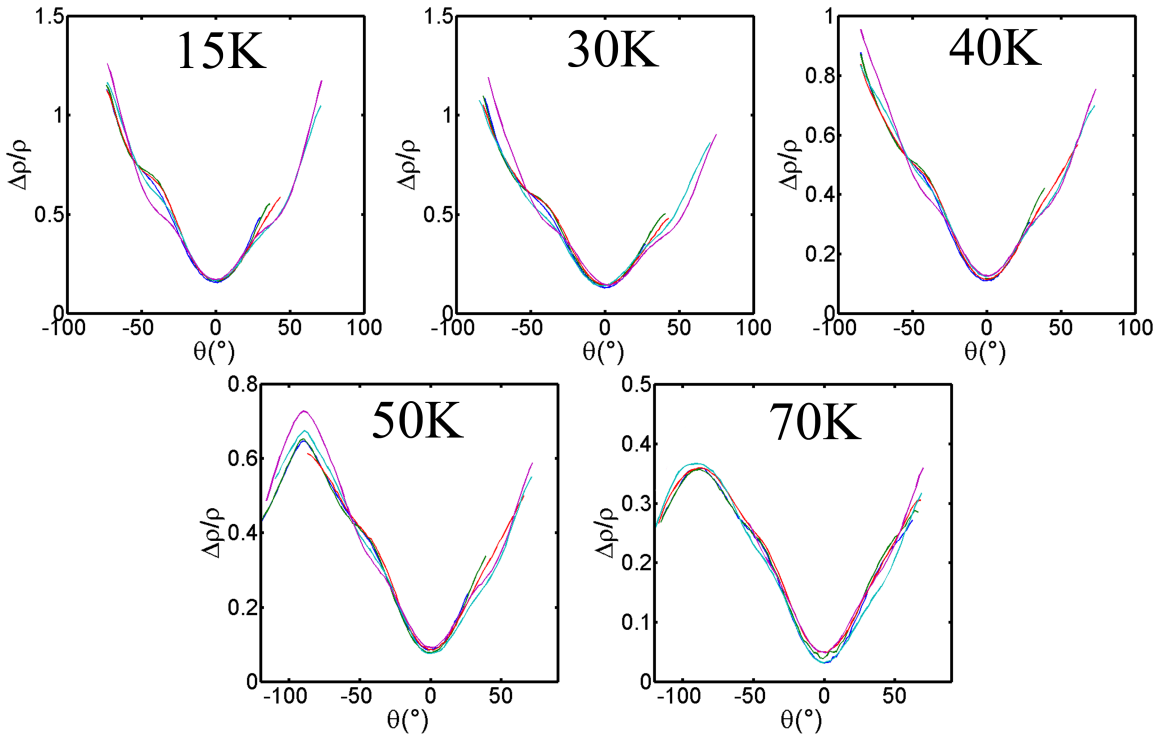

Figure 8.2: ADMR data for sample tl0803 with $T_c = 45\,\mathrm{K}$ at 45 T normalised to the zero field c-axis resistivity. Dark blue $\phi \approx 17°$, green $\phi \approx 4°$, red $\phi \approx 9°$, light blue $\phi \approx 23°$ and purple $\phi \approx 36°$.

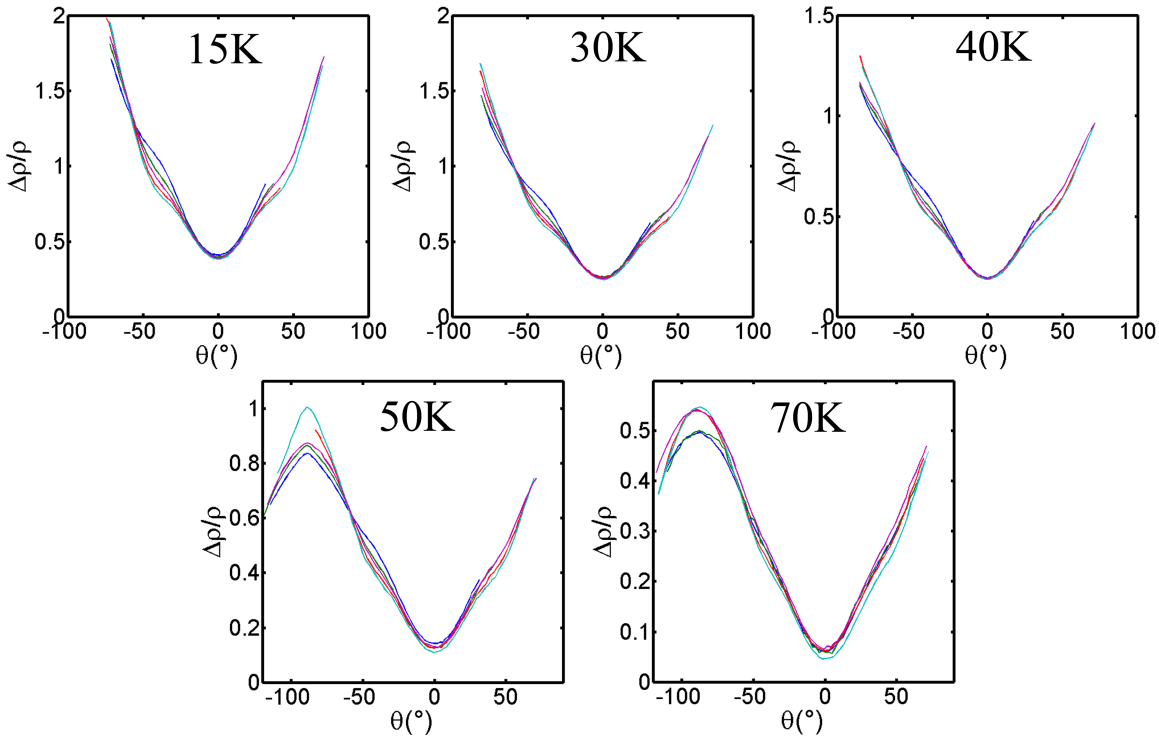

Figure 8.3: ADMR data for sample tl0807 with $T_c = 45\,\mathrm{K}$ at 45 T normalised to the zero field c-axis resistivity. Dark blue $\phi \approx 11°$, green $\phi \approx 24°$, red $\phi \approx 37°$, light blue $\phi \approx 40°$ and purple $\phi \approx 27°$.

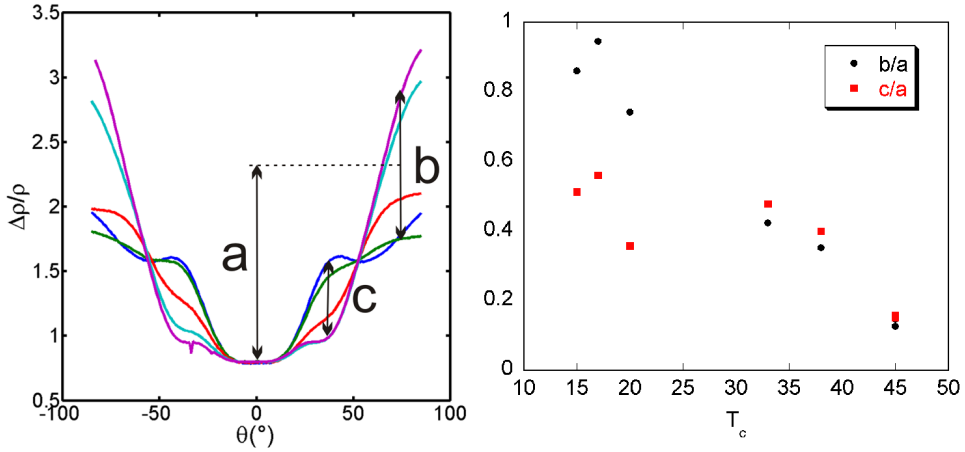

Figure 8.4: Left panel shows the definitions of 'a', 'b' and 'c'. 'a' is measured between the value of $\Delta\rho/\rho$ at $\theta = 0°$ and the midpoint of the spread in $\Delta\rho/\rho$ at $\theta = 75°$; 'b' is the spread in $\Delta\rho/\rho$ at $\theta = 75°$ and 'c' is the spread in $\Delta\rho/\rho$ at $\theta = 40°$. Right panel shows the doping dependence of the (normalised) spread of the data at 14/15 K. $\theta = 75°$ (b/a) in black circles and at $\theta = 40°$ (c/a) in red squares.

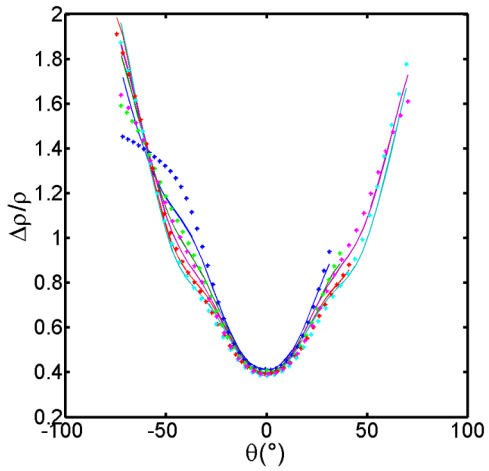

Figure 8.5: ADMR data for sample tl0807 with $T_c = 45\,\mathrm{K}$ at 45 T normalised to the zero field c-axis resistivity. Solid lines are experimental data and asterisks are a least squares fits. Dark blue $\phi \approx 11°$, green $\phi \approx 24°$, red $\phi \approx 37°$, light blue $\phi \approx 40°$ and purple $\phi \approx 27°$. Fit parameters were $\omega_c\tau = 0.273 \pm 0.009$, $\gamma = 0.337 \pm 0.030$, $k_{61}/k_{21} = 0.493 \pm 0.051$, $k_{101}/k_{21} = -0.148 \pm 0.065$, $k_{40}/k_{00} = -0.052 \pm 0.005$ and $k_{00} = 0.723\,\mathrm{Å}^{-1}$.

8.2 Analysis and Discussion

The model described in chapter 5 and successfully used to model data in chapter 6 fails to provide a satisfactory fit to these data with parameters consistent with those found on samples with a lower T_c. An initial fit is shown in figure 8.5. The parameters are reasonable (see figure caption), but the quality of the fit is quite poor especially at higher angles. This suggests that the $T_c = 45\,\mathrm{K}$ data cannot be described merely by a smooth gradual change in the parameters from the $T_c = 38\,\mathrm{K}$ data in the same way as the $T_c = 38\,\mathrm{K}$ data are from the $T_c = 33\,\mathrm{K}$ data or the $T_c = 20\,\mathrm{K}$ data. It is suggestive of some kind of change in the material whose effect on ADMR turns on quite abruptly at a doping level corresponding to between $T_c = 38\,\mathrm{K}$ and $T_c = 45\,\mathrm{K}$. A few possibilities for a physical explanation for the change in the data will now be discussed.

It is possible that a different form for the anisotropy is necessary. Various parameterisations of $\tau(\psi)$ were tested including a 45° rotation of the four-fold anisotropy used previously i.e. $1/\tau(\psi) = (1 + \gamma \sin 4\psi)/\tau^0$. This produced a very poor fit to the data suggesting an anisotropy reversal is not the cause. Recent functional renormalisation group calculations [134] are consistent with a different shape for $\tau(\psi)$. This still has the scattering maxima along (π,0) but has a sharper ψ dependence and was simply parameterised by two straight lines of variable gradient. This also failed to fit the data well. The failure of the previous model and of simple changes to the form of $\tau(\psi)$ to come close to fitting the data suggests that further changes to the fitting parameterisation are necessary.

Kartsovnik *et al.* [144] recently saw a similar collapse of the azimuthal (ϕ) dependence of ADMR data near $\theta = 90°$ in an organic material — see figure 8.6. They attribute this to a crossover

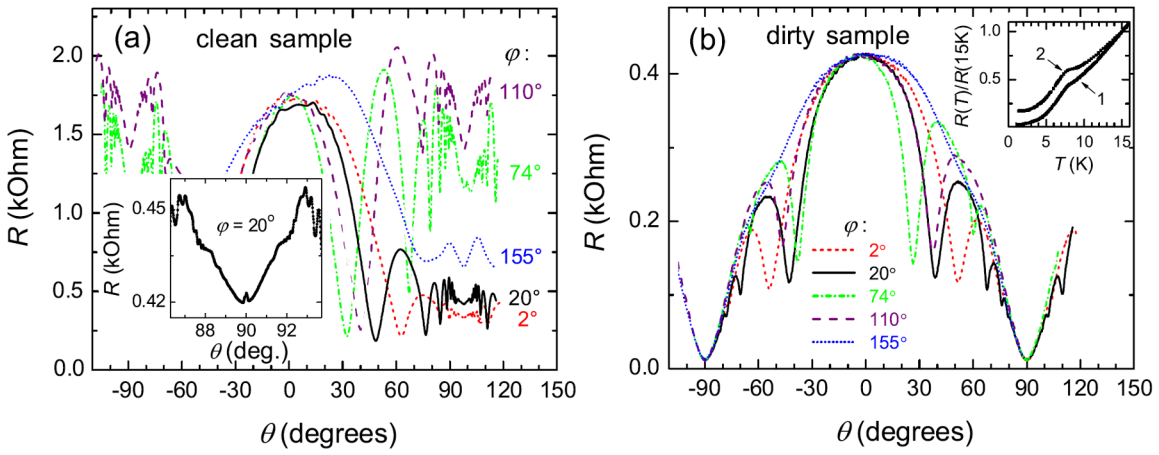

Figure 8.6: c-axis resistance of $\alpha-(\mathrm{BEDT-TTF})_2\mathrm{KHg(SCN)}_4$ as a function of polar angle θ and various azimuthal angles (ψ). The 'clean' sample on the left shows a marked azimuthal angle dependence near $\theta = 90°$, but this collapses in the 'dirty' sample on the right. Figure from [144].

between coherent and weakly incoherent interlayer transport regimes. In the coherent regime the magnetoresistance is highly sensitive to both the polar and azimuthal directions of the magnetic field. In the weakly incoherent regime the magnetoresistance does not depend on the azimuthal orientation in fields strongly inclined towards the layers (i.e. $\theta \sim 90°$) and can be scaled simply as a function of the out-of-plane field component. Incoherent c-axis transport occurs when the scattering rate, τ, is larger than the interlayer hopping rate $\hbar/t_\perp$. The fact that the magnetoresistance in $Tl_2Ba_2CuO_{6+\delta}$ continues to increase as $\theta \to 90°$ gives evidence against a similarity with Kartsovnik's data (where the magnetoresistance decreases as $\theta \to 90°$) as the out-of-plane magnetic field component tends to zero as $\theta \to 90°$. Furthermore, work by Kennett *et al.* [145] suggest that ADMR in $Tl_2Ba_2CuO_{6+\delta}$ should be unaffected by a crossover from a coherent to a weakly incoherent regime.

It is possible that the pseudogap may be playing a significant role in driving the changes observed in the data between $T_c = 38\,\mathrm{K}$ and $T_c = 45\,\mathrm{K}$. It was suggested earlier that the pseudogap may open at a finite doping level which in $Tl_2Ba_2CuO_{6+\delta}$ could lie somewhere between $T_c = 38\,\mathrm{K}$ and $T_c = 45\,\mathrm{K}$ which corresponds to $p = 0.245$ and $p = 0.239$ (using equation 1.1). The pseudogap has d-wave symmetry and so has a greater influence along the antinodal (π,0) directions than the nodal (π,π) directions. It reduces the density of states at the Fermi level and probably gives rise to the Fermi arcs seen in underdoped cuprates. As a starting point let us look at the qualitative effect of the pseudogap on ADMR. It is difficult to include the idea of Fermi arcs directly in the analysis described in chapter 5 by reducing the limits of the ψ integration as this leads to algebraic complications which dramatically increases the computer calculation time. It seems the best way to simulate the pseudogap is with a multiplicative factor which reduces the contribution from certain portions of the Fermi surface. If $\chi(\psi)$ is a simple ψ dependent factor [146] which simulates the effect

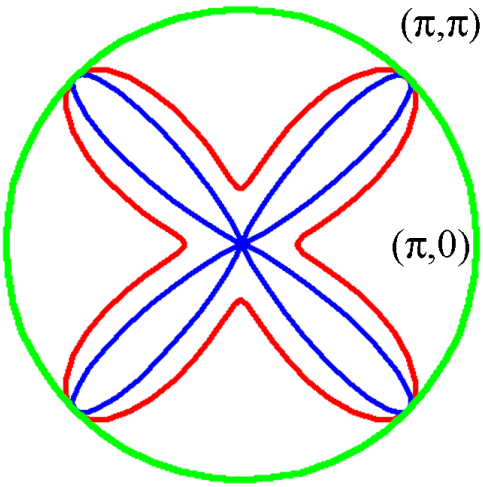

Figure 8.7: Diagram showing the variation of $\chi(\psi)$ around the Fermi surface. The green line corresponds to $\Delta/k_BT=0$, the red line to $\Delta/k_BT=2$ and the blue line to $\Delta/k_BT=8$.

of the pseudogap it can be added into equation 5.39 for σ_{zz}:

$$\chi(\psi) = \frac{2}{\exp\left\{\left[\frac{\Delta}{k_BT}\right]^2 \cos^2 2\psi\right\} + 1} \tag{8.1}$$

The ψ dependence of χ is illustrated in figure 8.7. If $\Delta/(k_BT) = 0$ then $\chi(\psi) = 1$ and there is no suppression of states. Performing a series of simulations shown in figure 8.8 as a function of $\Delta/(k_BT)$ shows that as $\Delta/(k_BT)$ is increased corresponding to the opening of the pseudogap the ϕ dependence of the ADMR at $\theta=90°$ lessens. This qualitatively reproduces what is seen in the experimental data, although a full quantitative fit fails to accurately reproduce the data regardless of whether this $\chi(\psi)$ suppression is allowed at all ψ as shown in the left of figure 8.9 or across only a limited range of ψ as shown in the right of figure 8.9.

Looking at figure 8.5, although the overall fit is poor, it appears that the ADMR traces at $\phi\approx37°$ (red) and $\phi\approx40°$ (light blue) show quite a good fit to the data. These are the ϕ angles which in underdoped cuprates correspond to the region of the Fermi arcs. Thus it is possible that at ϕ around 45° the effect of the pseudogap is minimal and the data may be fitted using the original parameterisation. The angle dependent contribution to the magnetoresistance is selected by the ϕ angle of the magnetic field. So for $\phi\approx45°$ the states along (π,π) are selected, but when the field is along $\phi\approx0°$ and the pseudogap has gapped out the states along (π,0) the ADMR traces are modified only at these angles. In the absence of any states along (π,0) it is possible that the states at (π,π) may contribute to the ADMR at $\phi\approx0°$. This is consistent with the experimental data in figure 8.3 and a comparison with data in chapter 6. For tl0803 and tl0807 a reduction of ϕ dependence is observed, with ADMR traces at $\phi\approx0°$ looking more like those at $\phi\approx45°$.

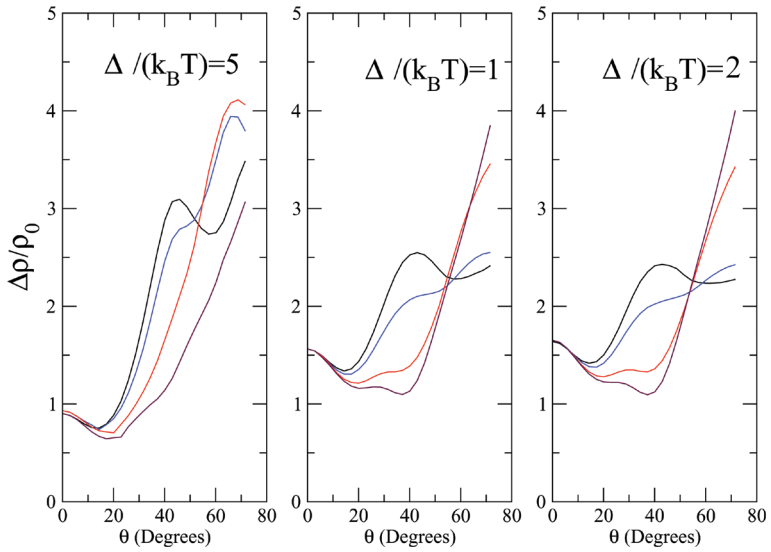

Figure 8.8: Simulation of the effect of a simple parameterisation of the pseudogap on ADMR. $\Delta/(k_BT)$ is the magnitude of the gap. Figure from [146].

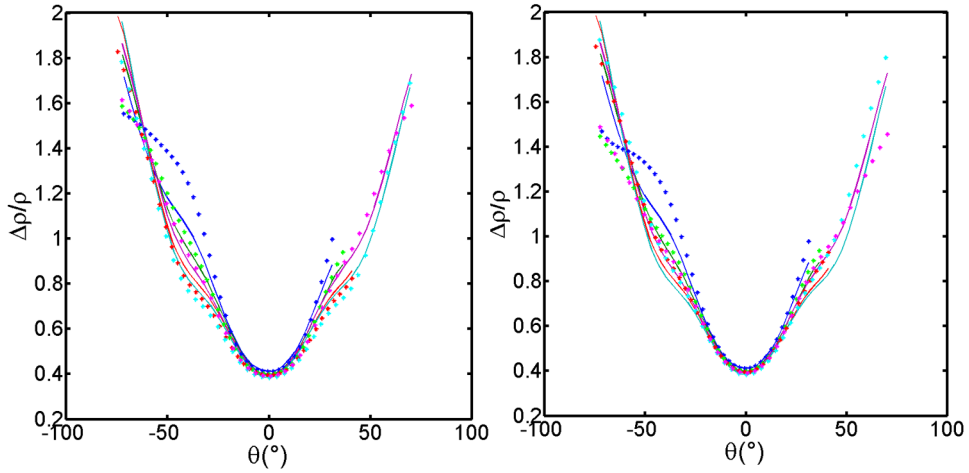

Figure 8.9: ADMR data for sample tl0807 with $T_c = 45\,\mathrm{K}$ at 45 T normalised to the zero field c-axis resistivity. Solid lines are experimental data and asterisks are a least squares fits. Dark blue $\phi \approx 11°$, green $\phi \approx 24°$, red $\phi \approx 37°$, light blue $\phi \approx 40°$ and purple $\phi \approx 27°$. Left panel is using the pseudogap parameterised by the $\chi(\psi)$ function. Fit parameters were $\omega_c\tau = 0.302 \pm 0.008$, $\gamma = 0.391 \pm 0.023$, $k_{61}/k_{21} = 0.588 \pm 0.023$, $k_{101}/k_{21} = -0.044 \pm 0.018$, $\Delta/k_BT = 0.000 \pm 0.002$, $k_{40}/k_{00} = -0.03$ and $k_{00} = 0.723\,\mathrm{Å}^{-1}$. Right panel is using pseudogap parameterised by $\chi(\psi)$ function only for data at $\theta > 70°$. Fit parameters were $\omega_c\tau = 0.239 \pm 0.021$, $\gamma = 0.341 \pm 0.053$, $k_{61}/k_{21} = 1.24 \pm 0.110$, $k_{101}/k_{21} = 0.235 \pm 0.110$, $\Delta/k_BT = 6.07 \pm 0.70$, $k_{40}/k_{00} = -0.03$ and $k_{00} = 0.723\,\mathrm{Å}^{-1}$.

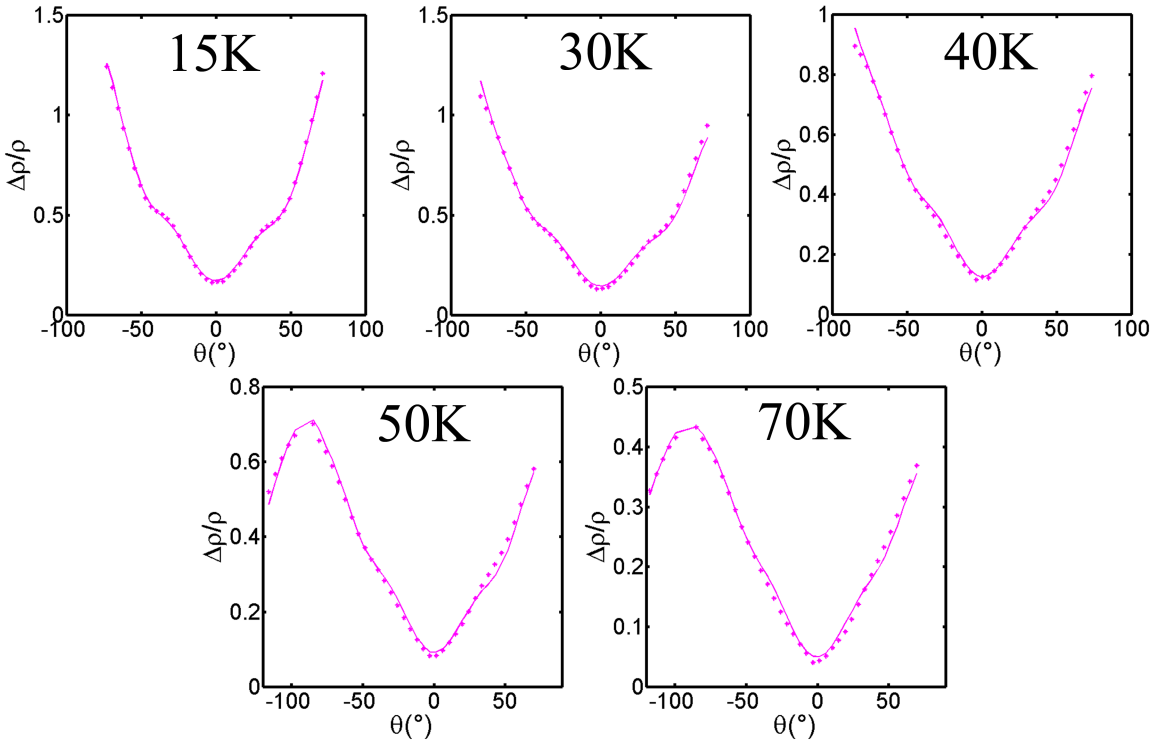

Figure 8.10: ADMR data for sample tl0803 with $T_c = 45\,\mathrm{K}$ at 45 T normalised to the zero field c-axis resistivity. Solid lines are experimental data and asterisks are best least squares fits. Purple $\phi \approx 36°$. Fit parameters were $k_{61}/k_{21} = 0.437 \pm 0.095$, $k_{101}/k_{21} = -0.347 \pm 0.048$, $k_{40}/k_{00} = -0.03$ and $k_{00} = 0.723\,\mathrm{Å}^{-1}$ with $\omega_c\tau$ and γ given in the table.

Temperature	$\omega_c\tau$	γ	Temperature	$\omega_c\tau$	γ
15 K	0.322 ± 0.004	0.294 ± 0.012	50 K	0.177 ± 0.004	0.346 ± 0.025
30 K	0.262 ± 0.006	0.282 ± 0.028	70 K	0.137 ± 0.001	0.319 ± 0.003
40 K	0.217 ± 0.005	0.273 ± 0.034			

Fits were performed on only the ADMR traces nearest to $\phi = 45°$. A good agreement between the experimental data and the fits is found as shown in figures 8.10 and 8.11. These fits were actually performed using the full Fermi surface, with no attempt to account for the pseudogap, although when this was included Δ/k_BT minimised to zero, indicating that its inclusion for this data was unnecessary. Simulations of the in-plane transport properties such as the Hall coefficient fail to reproduce either a quantitative fit or a qualitative fit consistent with the trend shown in chapter 6. As pointed out earlier this may be the result of an in-plane measurement (such as R_H or ρ_{ab}) and an out-of-plane measurement (such as ADMR) being affected by vertex corrections in different ways. Alternatively it could be related to the interlayer coherence or the pseudogap.

Figure 8.12 shows the scattering rate split into isotropic and anisotropic components, as previously. The isotropic component is found to have a magnitude and temperature dependence which is consistent with that found earlier for the lower T_c samples. The anisotropic component which was

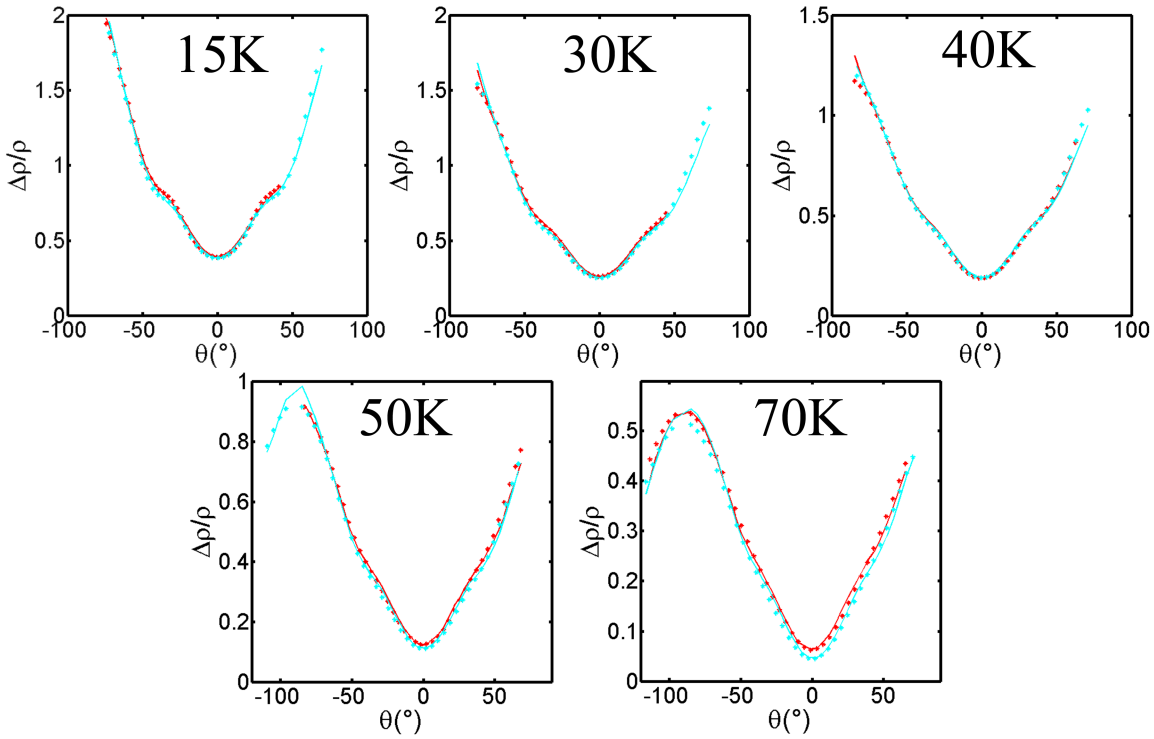

Figure 8.11: ADMR data for sample tl0807 with $T_c = 45\,\mathrm{K}$ at 45 T normalised to the zero field c-axis resistivity. Solid lines are experimental data and asterisks are best least squares fits. Red $\phi \approx 37°$ and light blue $\phi \approx 40°$. Fit parameters were $k_{61}/k_{21} = 0.550 \pm 0.022$, $k_{101}/k_{21} = -0.202 \pm 0.057$, $k_{40}/k_{00} = -0.03$ and $k_{00} = 0.723\,\mathrm{Å}^{-1}$ with $\omega_c\tau$ and γ given in the table.

Temperature	$\omega_c\tau$	γ	Temperature	$\omega_c\tau$	γ
15 K	0.316 ± 0.007	0.473 ± 0.022	50 K	0.201 ± 0.003	0.310 ± 0.016
30 K	0.271 ± 0.004	0.383 ± 0.016	70 K	0.152 ± 0.002	0.282 ± 0.022
40 K	0.234 ± 0.004	0.333 ± 0.018			

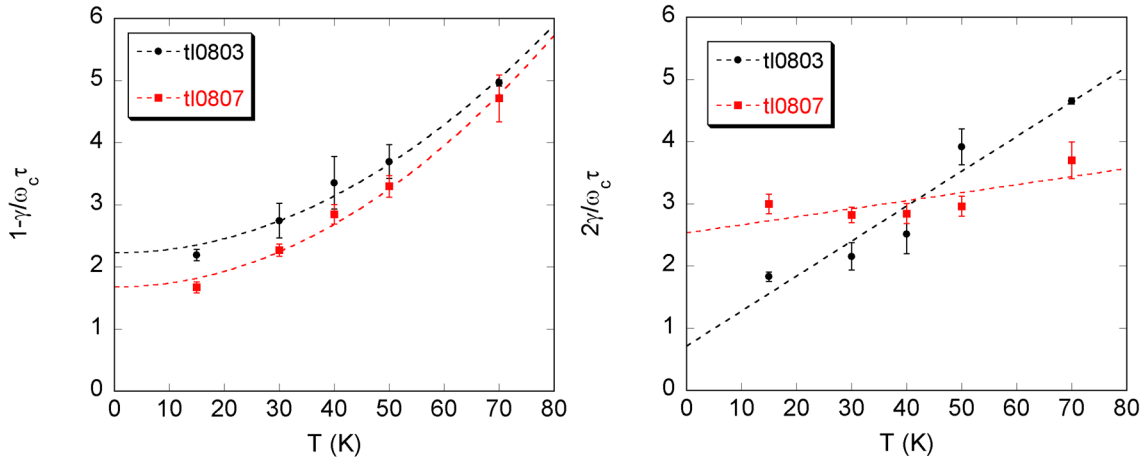

Figure 8.12: Temperature dependence of the isotropic $(1-\gamma/\omega_c\tau)$ and anisotropic $(2\gamma/\omega_c\tau)$ components of the scattering rate for each sample. For the isotropic component the dashed line is a least squares fit to $A+BT^2$. For the anisotropic component the dashed line is a least squares fit to $C+DT$. For tl0803 A = 2.23, B = 0.000574, C = 0.715, D = 0.0560; tl0807 A = 1.67, B = 0.000634, C = 2.54, D = 0.0129.

previously found to be T-linear still retains this temperature dependence but its magnitude is different. Although starting from approximately the same magnitude at $T=0\,\mathrm{K}$, it has a much weaker temperature dependence than would be expected from the trend observed for the higher T_c samples in figure 6.15. This may be consistent with the effect of the pseudogap reducing the states available in the regions where the anisotropic scattering is present and therefore reducing its magnitude.

The success of this fitting gives some indication of the form of the pseudogap on the overdoped side of the phase diagram. Firstly, this suggests that the pseudogap exists at the doping corresponding to $T_c=45\,\mathrm{K}$. Secondly, the abruptness with which it seems to begin to affect the data could be evidence for the pseudogap turning on at some specific doping level which is not commensurate with the onset of superconductivity. An alternative suggestion is that the pseudogap vanishes as superconductivity vanishes on the overdoped side although this may be inconsistent with Hall effect and specific heat measurements. This means that the gap is present at all doping levels including those studied in chapter 6, but may not have had any effect on ADMR data as the high magnetic field caused magnetic breakdown i.e. the quasiparticles are able to tunnel across the gap. Falicov and Sievert [147] give an equation for the gap size a quasiparticle can tunnel across:

$$\Delta \sim \sqrt{\frac{\varepsilon_F \hbar e B}{m^*}} \tag{8.2}$$

where ε is the Fermi energy, B is the magnetic field and m^* is the quasiparticle effective mass. Using appropriate values for $\varepsilon_F=0.2438\,\mathrm{eV}$ [25], $m^*=4.1\,m_e$ [27] and $B=45\,\mathrm{T}$ gives an approximate gap that can be bridged by tunneling to be $\Delta\sim 18\,\mathrm{meV}$. Using a much lower field of 5 T, which would

be more consistent with a field highly angled to the plane ($\approx 85°$) in a lower T_c sample where the pseudogap seems to have no effect on the data gives $\Delta \sim 6\,\mathrm{meV}$. This agrees remarkably well with the size of the pseudogap suggested by Hüfner [9].

It should also be noted that the probability of an electron to bridge the gap can be given by:

$$P \propto \exp\left\{-\frac{B_0}{B_c}\right\} \tag{8.3}$$

where B_0 is a parameter which depends on the gap and B_c is the component of the magnetic field perpendicular to the gap. Converting into $\omega_c\tau$ gives:

$$P \propto \exp\left\{-\frac{\omega_0\tau}{\omega_c\tau}\right\} \tag{8.4}$$

where $\omega_0\tau$ is independent of the magnetic field. This implies that the probability of bridging the gap is maximum when the field is parallel to the c-axis ($\theta = 0°$) as $\omega_c\tau = \omega_c^0\tau\cos\theta$ and is minimum when the field is in the ab plane ($\theta = 90°$). This is consistent with the data for tl0803 and tl0807 which shows significant changes around $\theta = 90°$ (for $\phi \approx 0°$) but very little change around $\theta = 0°$ compared with data on any of the lower T_c samples in chapter 6. Even if these ideas are not relevant due to the form of the pseudogap, they may help to explain the fact ADMR is still observable at $\phi = 45°$ as the quasiparticles will bridge the gapped sections of the Fermi surface.

Further ADMR experimental work could test this magnetic breakdown idea by measuring ADMR on a $T_c = 38\,\mathrm{K}$ sample but at a lower magnetic field thus reducing the size of the gap that can be bridged. If the above conjecture is true then this new data could show the same features seen here in samples tl0803 and tl0807, hopefully before the ADMR features disappear due to the lower field.

Chapter 9

Conclusions

This thesis reports on ADMR measurements on the cuprate superconductor $Tl_2Ba_2CuO_{6+\delta}$ across a significantly expanded temperature, azimuthal angle and doping range than in previous work. Using the Boltzmann transport equation, considering the specific form of the 3D warping of the Fermi surface and the inclusion of an anisotropic scattering rate allows the experimental data to be successfully modeled. Considering samples with $T_c \lessapprox 40\,\mathrm{K}$ the anisotropic scattering rate extracted from this modeling can be split into two components. One which is isotropic around the Fermi surface with a quadratic temperature dependence and negligible doping dependence and another which is anisotropic around the Fermi surface with zeros along the (π,π) directions and maxima along the (π,0) directions. This is found to have a linear temperature dependence (below 70 K) and a linear doping dependence. Examining the highest temperature ADMR data for the lowest T_c samples a new T^2 term is uncovered in the anisotropic component of the scattering rate which may be due to sample disorder. The parameters extracted from this analysis are able to reproduce the zero field in-plane resistivity and the Hall effect, demonstrating that the parameters are reasonable.

ADMR data was taken on samples from a different crystal grower and was analysed in the same way confirming this effect is intrinsic to $Tl_2Ba_2CuO_{6+\delta}$. Careful crystal alignment measurements indicate there is no evidence in this work to support the quasiparticle lifetime anisotropy reversal across optimal doping implied by ARPES measurements [25]. The size of the Fermi surface implied by the modeling is in good agreement with that determined by bandstructure calculations and ARPES measurements. A recent suggestion of evidence for a field induced quantum critical point in $Tl_2Ba_2CuO_{6+\delta}$ is ruled out as the results are shown to be due to the specific sample quality and a temperature dependent anisotropic scattering rate.

Quantum oscillations in both the magnetisation and the electrical resistance were observed for the first time in an overdoped cuprate. The implied cross-sectional area of the orbit corresponds extremely well that found from the ADMR analysis and other work. From the temperature dependence of the oscillations the quasiparticle effective mass is found to be $4.1 \pm 1.0\, m_e$, which is in agreement

with that calculated from specific heat measurements.

Finally ADMR measurements were reported on $Tl_2Ba_2CuO_{6+\delta}$ samples with $T_c = 45\,\mathrm{K}$. The data here shows marked differences compared with data from lower T_c samples, even that of the $T_c = 38\,\mathrm{K}$ sample. The failure of the original model to fit the data has led to the inclusion of the effects of the pseudogap. This has allowed some of the data to be modeled for the first time giving an insight into the form of the pseudogap on the overdoped side of the phase diagram, suggesting it may turn on at a doping level not commensurate with the disappearance of superconductivity.

Further ideas and analysis work may be necessary for a full understanding of the $T_c = 45\,\mathrm{K}$ data, ADMR data for these samples at $\mathrm{T} \leq 15\,\mathrm{K}$ may be helpful for this. As suggested earlier, the magnetic breakdown scenario as explanation for the $T_c = 45\,\mathrm{K}$ data maybe tested by measuring ADMR on the $T_c = 38\,\mathrm{K}$ sample at a lower magnetic field. Further experimental work could focus on what happens as the doping is gradually increased giving samples with $T_c \leq 15\,\mathrm{K}$ and into the non-superconducting region of the phase diagram. This may confirm in $Tl_2Ba_2CuO_{6+\delta}$ whether the emergence of the T-linear anisotropic scattering rate is coupled to emergence of superconductivity. As we learn more about the $T_c = 45\,\mathrm{K}$ data, it maybe useful to measure ADMR on samples with even higher T_c. Although to discern any features in data on such samples may require higher magnetic fields and improved sample quality. Further work on quantum oscillation experiments could extend the work to a doping dependence or a polar angle dependence, both of which would give an insight into the evolution of shape of the Fermi surface.

From this work it is clear that a T-linear anisotropic scattering rate is key to developing a deeper understanding of the cuprates. However, as yet, no consensus has emerged about its origin. Suggestions have included a Pomeranchuk instability [125], antiferromagnetic spin fluctuations [126], a marginal Fermi liquid [128], boson density fluctuations [130], a combination of the Fermi velocity anisotropy and the Gutzwiller projection operator [131], orbital hybridisation coupled with charge fluctuations [133] & [132] and strong scattering at large $\mathbf{Q}$ arising due to the proximity to the Mott insulating state [134]. Once this is determined, we may well come to an understanding of the origin of the pairing mechanism and superconductivity in the cuprates which, despite intense research, has remained a mystery for the last 23 years.

Chapter 10

Appendix

10.1 Conductivity Tensor Derivation

10.1.1 Zero Field Conductivity for a Spherical Fermi Surface

Using $v_x = v_F \sin\theta\cos\phi$, $v_y = v_F \sin\theta\sin\phi$ and $v_z = v_F\cos\theta$ and equation 2.23:

$$\begin{aligned}
\sigma_{xx} &= \frac{1}{4\pi^3}\frac{e^2\tau}{\hbar}\int_0^{\pi}\int_0^{2\pi}\frac{(v_F\sin\theta\cos\phi)^2}{v_F}k_F^2\sin\theta\partial\theta\partial\phi && (10.1)\\
&= \frac{1}{4\pi^3}\frac{e^2\tau}{\hbar}v_F k_F^2\int_0^{\pi}\sin^3\theta\partial\theta\int_0^{2\pi}\cos^2\phi\partial\phi && (10.2)\\
&= \frac{1}{4\pi^3}\frac{e^2\tau}{\hbar}\frac{\hbar k_F}{m^*}k_F^2\times\frac{4}{3}\times\pi = \frac{e^2\tau k_F^3}{3\pi^2 m^*} && (10.3)
\end{aligned}$$

Now since this is for an isotropic sphere the same result should be obtained for σ_{yy} and σ_{zz} and this is the case:

$$\begin{aligned}
\sigma_{yy} &= \frac{1}{4\pi^3}\frac{e^2\tau}{\hbar}\int_0^{\pi}\int_0^{2\pi}\frac{(v_F\sin\theta\sin\phi)^2}{v_F}k_F^2\sin\theta\partial\theta\partial\phi && (10.4)\\
&= \frac{1}{4\pi^3}\frac{e^2\tau}{\hbar}v_F k_F^2\int_0^{\pi}\sin^3\theta\partial\theta\int_0^{2\pi}\sin^2\phi\partial\phi && (10.5)\\
&= \frac{1}{4\pi^3}\frac{e^2\tau}{\hbar}\frac{\hbar k_F}{m^*}k_F^2\times\frac{4}{3}\times\pi = \frac{e^2\tau k_F^3}{3\pi^2 m^*} && (10.6)
\end{aligned}$$

and:

$$\begin{aligned}
\sigma_{zz} &= \frac{1}{4\pi^3}\frac{e^2\tau}{\hbar}\int_0^{\pi}\int_0^{2\pi}\frac{(v_F\cos\theta)^2}{v_F}k_F^2\sin\theta\partial\theta\partial\phi && (10.7)\\
&= \frac{1}{4\pi^3}\frac{e^2\tau}{\hbar}v_F k_F^2\int_0^{\pi}\cos^2\theta\sin\theta\partial\theta\int_0^{2\pi}\partial\phi && (10.8)\\
&= \frac{1}{4\pi^3}\frac{e^2\tau}{\hbar}\frac{\hbar k_F}{m^*}k_F^2\times\frac{2}{3}\times 2\pi = \frac{e^2\tau k_F^3}{3\pi^2 m^*} && (10.9)
\end{aligned}$$

10.1.2 Zero Field Conductivity for a Barrel Shaped Fermi Surface

This is given by:

$$\sigma_{zz} = \frac{1}{4\pi^3}\int_0^{2\pi}\int_{-\frac{2\pi}{c}}^{\frac{2\pi}{c}} e^2 v_z v_z \tau \frac{k_F}{\hbar v_F}\partial\phi\partial k_z \tag{10.10}$$

$$= \frac{1}{4\pi^3}\frac{e^2\tau k_F}{\hbar v_F}\left(\frac{ct_\perp}{\hbar}\right)^2\int_0^{2\pi}\partial\phi\int_{-\frac{2\pi}{c}}^{\frac{2\pi}{c}}\sin^2\left(\frac{k_z c}{2}\right)\partial k_z \tag{10.11}$$

$$= \frac{e^2\tau m^* c^2 t_\perp^2}{4\pi^3\hbar^4}\times 2\pi\times\frac{2\pi}{c} = \frac{e^2\tau m^* c t_\perp^2}{\pi\hbar^4} \tag{10.12}$$

As expected from symmetry σ_{xx} and σ_{yy} are the same where σ_{xx} is given by:

$$\sigma_{xx} = \frac{1}{4\pi^3}\int_0^{2\pi}\int_{-\frac{2\pi}{c}}^{\frac{2\pi}{c}} e^2 v_x v_x \tau \frac{k_F}{\hbar v_F}\partial\phi\partial z \tag{10.13}$$

$$= \frac{1}{4\pi^3}\frac{e^2\tau k_F v_F^2}{\hbar v_F}\int_{-\frac{2\pi}{c}}^{\frac{2\pi}{c}}\partial z\int_0^{2\pi}\cos^2\phi\partial\phi \tag{10.14}$$

$$= \frac{e^2\tau k_F^2}{4\pi^3 m^*}\times\frac{4\pi}{c}\times\pi = \frac{e^2\tau k_F^2}{\pi m^* c} \tag{10.15}$$

Using the carrier density for this system shown in the text, means that σ_{xx} and σ_{yy} reduce to the Drude result.

10.1.3 Conductivity Tensor for a Spherical Fermi Surface in a Magnetic Field

With the magnetic field along the cartesian z axis, substituting $v_x = v_F\sin\theta\cos\phi$ for v_i and v_j gives:

$$\sigma_{xx} = \frac{e^2}{4\pi^3\hbar^2}\int_0^\pi k_F\sin\theta\partial\theta\int_0^{2\pi}\partial\phi\int_0^\infty\partial\phi'\frac{\hbar^2k_F^2}{m^{*2}}\sin^2\theta\cos\phi\cos(\phi-\phi')\frac{m^*}{\omega_c}e^{-\frac{\phi'}{\omega_c\tau}} \tag{10.16}$$

where $\partial k_B = \partial k_z = m^*/\hbar\partial v_z = k_F\sin\theta\partial\theta$. Rearranging and expanding $\cos(\phi-\phi')$ as $\cos\phi\cos\phi' + \sin\phi\sin\phi'$ gives:

$$\sigma_{xx} = \frac{e^2k_F^3}{4\pi^3m^*}\int_0^\pi\sin^3\theta\partial\theta\int_0^{2\pi}\partial\phi\cos\phi\int_0^\infty\partial\phi'\left(\frac{\cos\phi\cos\phi'}{\omega_c}+\frac{\sin\phi\sin\phi'}{\omega_c}\right)e^{-\frac{\phi'}{\omega_c\tau}} \tag{10.17}$$

Noticing that the last integral is the Laplace integral of sin and cos:

$$\int_0^\infty\frac{\cos\phi'}{\omega_c}e^{-\frac{\phi'}{\omega_c\tau}}\partial\phi' = \frac{\tau}{1+(\omega_c\tau)^2} \tag{10.18}$$

$$\int_0^\infty\frac{\sin\phi'}{\omega_c}e^{-\frac{\phi'}{\omega_c\tau}}\partial\phi' = \frac{\omega_c\tau^2}{1+(\omega_c\tau)^2} \tag{10.19}$$

this can be written as:

$$\sigma_{xx} = \frac{e^2 k_F^3}{4\pi^3 m^*} \frac{4}{3} \int_0^{2\pi} \partial\phi\tau \cos\phi \left(\frac{\cos\phi + \sin\phi\omega_c\tau}{1+\omega_c^2\tau^2} \right) \tag{10.20}$$

$$\sigma_{xx} = \frac{e^2\tau k_F^3}{3\pi^2 m^*} \frac{1}{1+(\omega_c\tau)^2} = \frac{\sigma_0}{1+(\omega_c\tau)^2} \tag{10.21}$$

Following the same method for σ_{yy} gives:

$$\sigma_{yy} = \frac{e^2 k_F^3}{4\pi^3 m^*} \int_0^{\pi} \sin^3\theta\partial\theta \int_0^{2\pi} \partial\phi \sin\phi \int_0^{\infty} \partial\phi' \left(\frac{\sin\phi\cos\phi'}{\omega_c} - \frac{\cos\phi\sin\phi'}{\omega_c} \right) e^{-\frac{\phi'}{\omega_c\tau}} \tag{10.22}$$

$$\sigma_{yy} = \frac{e^2 k_F^3}{4\pi^3 m^*} \frac{4}{3} \int_0^{2\pi} \partial\phi\tau \sin\phi \left(\frac{\sin\phi - \cos\phi\omega_c\tau}{1+\omega_c^2\tau^2} \right) \tag{10.23}$$

$$\sigma_{yy} = \frac{e^2\tau k_F^3}{3\pi^2 m^*} \frac{1}{1+(\omega_c\tau)^2} = \frac{\sigma_0}{1+(\omega_c\tau)^2} \tag{10.24}$$

and for σ_{zz} gives:

$$\sigma_{zz} = \frac{e^2 k_F^3}{4\pi^3 m^*} \int_0^{\pi} \sin\theta\cos^2\theta\partial\theta \int_0^{2\pi} \partial\phi \int_0^{\infty} \partial\phi' \frac{1}{\omega_c} e^{-\frac{\phi'}{\omega_c\tau}} \tag{10.25}$$

$$\sigma_{zz} = \frac{e^2 k_F^3}{4\pi^3 m^*} \times \frac{2}{3} \times 2\pi \times \frac{\omega_c\tau}{\omega_c} = \frac{e^2\tau k_F^3}{3\pi^2 m^*} = \sigma_0 \tag{10.26}$$

The σ_{xz}, σ_{yz}, σ_{zx} and σ_{zy} terms are all zero as the θ integral is $\int_0^{\pi} \sin^2\theta\cos\theta\partial\theta = 0$. The remaining two terms are σ_{xy} and σ_{yx} where:

$$\sigma_{xy} = \frac{e^2 k_F^3}{4\pi^3 m^*} \int_0^{\pi} \sin^3\theta\partial\theta \int_0^{2\pi} \partial\phi \cos\phi \int_0^{\infty} \partial\phi' \left(\frac{\sin\phi\cos\phi'}{\omega_c} - \frac{\cos\phi\sin\phi'}{\omega_c} \right) e^{-\frac{\phi'}{\omega_c\tau}} \tag{10.27}$$

$$\sigma_{xy} = \frac{e^2 k_F^3}{4\pi^3 m^*} \frac{4}{3} \int_0^{2\pi} \partial\phi\tau \cos\phi \left(\frac{\sin\phi - \cos\phi\omega_c\tau}{1+\omega_c^2\tau^2} \right) \tag{10.28}$$

$$\sigma_{xy} = \frac{e^2 k_F^3}{4\pi^3 m^*} \times \frac{4}{3} \times \frac{\pi\omega_c\tau^2}{1+\omega_c^2\tau^2} = -\frac{\sigma_0\omega_c\tau}{1+\omega_c^2\tau^2} \tag{10.29}$$

and:

$$\sigma_{yx} = \frac{\sigma_0\omega_c\tau}{1+\omega_c^2\tau^2} = -\sigma_{xy} \tag{10.30}$$

10.1.4 Conductivity Tensor for a Barrel Shaped Fermi Surface in a Magnetic Field

If the magnetic field is parallel to the axis of the cylinder (i.e. the z axis) the Shockley-Chambers tube-integral (equation 2.43) for σ_{xx} can be written as:

$$\sigma_{xx} = \frac{e^2 k_{F\parallel}^2}{4\pi^3 m^*} \int_{-\frac{2\pi}{c}}^{\frac{2\pi}{c}} \partial k_z \int_0^{2\pi} \cos\phi\partial\phi \int_0^{\infty} \frac{\cos(\phi-\phi'')}{\omega_c} e^{-\frac{\phi''}{\omega_c\tau}} \partial\phi'' \tag{10.31}$$

Integrating in the same way as previously gives:

$$\sigma_{xx} = \frac{e^2 \tau k_{F\|}^2}{\pi m^* c} \frac{1}{1+(\omega_c \tau)^2} \tag{10.32}$$

Using the carrier density given in §2.5.3 gives:

$$\sigma_{xx} = \frac{\sigma_0}{1+(\omega_c \tau)^2} \tag{10.33}$$

As expected by symmetry:

$$\sigma_{yy} = \frac{e^2 k_{F\|}^2}{4\pi^3 m^*} \int_{-\frac{2\pi}{c}}^{\frac{2\pi}{c}} \partial k_z \int_0^{2\pi} \sin\phi \partial\phi \int_0^{\infty} \frac{\sin(\phi-\phi'')}{\omega_c} e^{-\frac{\phi''}{\omega_c \tau}} \partial\phi'' = \frac{\sigma_0}{1+(\omega_c \tau)^2} \tag{10.34}$$

The cross terms σ_{xz}, σ_{yz}, σ_{zx} and σ_{zy} are all zero since $\int_0^{2\pi} \sin\phi = 0$ and $\int_0^{2\pi} \cos\phi = 0$. The other cross terms σ_{xy} and σ_{yx} are:

$$\sigma_{xy} = \frac{e^2 k_{F\|}^2}{4\pi^3 m^*} \int_{-\frac{2\pi}{c}}^{\frac{2\pi}{c}} \partial k_z \int_0^{2\pi} \cos\phi \partial\phi \int_0^{\infty} \frac{\sin(\phi-\phi'')}{\omega_c} e^{-\frac{\phi''}{\omega_c \tau}} \partial\phi'' = -\frac{\sigma_0 \omega_c \tau}{1+(\omega_c \tau)^2} \tag{10.35}$$

and:

$$\sigma_{yx} = \frac{e^2 k_{F\|}^2}{4\pi^3 m^*} \int_{-\frac{2\pi}{c}}^{\frac{2\pi}{c}} \partial k_z \int_0^{2\pi} \cos\phi \partial\phi \int_0^{\infty} \frac{\sin(\phi-\phi'')}{\omega_c} e^{-\frac{\phi''}{\omega_c \tau}} \partial\phi'' = \frac{\sigma_0 \omega_c \tau}{1+(\omega_c \tau)^2} \tag{10.36}$$

The final term is:

$$\sigma_{zz} = \frac{e^2}{4\pi^3 \hbar} \frac{c^2 t_\perp^2}{\hbar^2} m^* \int_{-\frac{2\pi}{c}}^{\frac{2\pi}{c}} \partial k_z \sin^2\left(\frac{k_z c}{2}\right) \int_0^{2\pi} d\phi \int_0^{\infty} d\phi'' \frac{1}{\omega_c} e^{-\frac{\psi''}{\omega_c \tau}} \tag{10.37}$$

$$= \frac{e^2}{4\pi^3 \hbar} \frac{c^2 t_\perp^2}{\hbar^2} m^* \times \frac{2\pi}{c} \times 2\pi \times \tau = \frac{e^2 c t_\perp m^* \tau}{\pi \hbar^4} \tag{10.38}$$

If the magnetic field is rotated in the x-z plane:

$$B_x = B\sin\theta \tag{10.39}$$

$$B_y = 0 \tag{10.40}$$

$$B_z = B\cos\theta \tag{10.41}$$

and using equations 2.46 – 2.48:

$$\frac{\partial k_x}{\partial t} = \frac{eBk_\parallel}{m^*}\cos\theta\sin\phi \tag{10.42}$$

$$\frac{\partial k_y}{\partial t} = -\frac{eBk_\parallel}{m^*}\cos\theta\cos\phi \tag{10.43}$$

$$\frac{\partial k_z}{\partial t} = -\frac{eBk_\parallel}{m^*}\sin\theta\sin\phi \tag{10.44}$$

If the field is perpendicular to the z axis i.e. $\theta=0$ and σ_{zz} is examined first:

$$v_z(k,0) = \frac{ct_\perp}{\hbar}\sin\left(\frac{k_z c}{2}\right) \tag{10.45}$$

$$v_z(k,t) = \frac{ct_\perp}{\hbar}\sin\left(\frac{k_z c}{2}+\frac{eBk_\parallel}{m^*}t\sin\phi\right) \tag{10.46}$$

writing d^3k as before as $\partial\varepsilon_F/\hbar v_F \times \partial k_z k_F \partial\phi$ gives:

$$\sigma_{zz} = \frac{e^2}{4\pi^3}\frac{c^2t_\perp^2}{\hbar^2}\frac{1}{\hbar v_F}\int_{-\frac{2\pi}{c}}^{\frac{2\pi}{c}}\partial k_z\int_0^{2\pi}k_F\partial\phi\int_0^\infty\sin\left(\frac{k_z c}{2}\right)\sin\left(\frac{k_z c}{2}+\frac{eBk_\parallel}{m^*}t\sin\phi\right)e^{-\frac{t}{\tau}}dt \tag{10.47}$$

Expanding $\sin(A+B)$ as $\sin A\cos B+\cos A\sin B$:

$$\sigma_{zz} = \frac{e^2c^2t_\perp^2}{4\pi^3\hbar^3 v_F}\int_{-\frac{2\pi}{c}}^{\frac{2\pi}{c}}\partial k_z\int_0^{2\pi}k_F\partial\phi\int_0^\infty dt\sin\left(\frac{k_z c}{2}\right)\left[\sin\left(\frac{k_z c}{2}\right)\cos(\alpha t)+\cos\left(\frac{k_z c}{2}\right)\sin(\alpha t)\right]e^{-\frac{t}{\tau}} \tag{10.48}$$

where $\alpha = eBk_\parallel/m^* \times \sin\phi$. Using the standard integrals:

$$\int_0^\infty\cos(\alpha t)e^{-\frac{t}{\tau}}dt = \frac{\tau}{1+(\alpha\tau)^2} \tag{10.49}$$

$$\int_0^\infty\sin(\alpha t)e^{-\frac{t}{\tau}}dt = \frac{\alpha\tau^2}{1+(\alpha\tau)^2} \tag{10.50}$$

and integrating gives:

$$\sigma_{zz} = \frac{e^2c^2t_\perp^2\tau}{4\pi^3\hbar^3 v_F}\int_{-\frac{2\pi}{c}}^{\frac{2\pi}{c}}\partial k_z\int_0^{2\pi}k_F\partial\phi\sin\left(\frac{k_z c}{2}\right)\left[\frac{\sin\left(\frac{k_z c}{2}\right)+\alpha\tau\cos\left(\frac{k_z c}{2}\right)}{1+(\alpha\tau)^2}\right] \tag{10.51}$$

$$= \frac{e^2c^2t_\perp^2\tau}{4\pi^3\hbar^3 v_F}\times\frac{2\pi}{c}\times k_F\times\frac{2\pi}{\sqrt{1+\left(\frac{eBv_F\tau}{\hbar}\right)^2}} = \frac{e^2ct_\perp^2\tau m^*}{\pi\hbar^4}\frac{1}{\sqrt{1+\left(\frac{eBv_F\tau}{\hbar}\right)^2}} \tag{10.52}$$

$$= \frac{\sigma_{zz}^0}{\sqrt{1+\left(\frac{eBv_F\tau}{\hbar}\right)^2}} \tag{10.53}$$

where σ_{zz}^0 is the conductivity when no magnetic field is present. Since for B perpendicular to z $\cos\theta = 0$, σ_{xx} is given by:

$$\sigma_{xx} = \frac{e^2}{4\pi^3}\frac{1}{\hbar v_F}\frac{\hbar^2 k_F^2}{m^{*2}}\int_{-\frac{2\pi}{c}}^{\frac{2\pi}{c}}\partial k_z\int_0^{2\pi}k_F\partial\phi\int_0^{\infty}dte^{-\frac{t}{\tau}}\cos^2\phi \tag{10.54}$$

$$= \frac{e^2}{4\pi^3}\frac{1}{\hbar v_F}\frac{\hbar^2 k_F^3}{m^{*2}}\times\frac{4\pi}{c}\times\pi\times\tau = \frac{k_F^2 e^2\tau}{\pi c m^*} = \sigma_0 \tag{10.55}$$

σ_{yy} can be shown to be equal to σ_0 using $\int_0^{2\pi}\sin^2\phi = \pi$. The cross terms σ_{xy} and σ_{yx} will be zero since $\int_0^{2\pi}\sin\phi\cos\phi = 0$. The cross terms σ_{zx} and σ_{zy} will be zero since $\int_0^{2\pi}\sin\phi = \int_0^{2\pi}\cos\phi = 0$. The remaining two cross terms σ_{xz} and σ_{yz} can also be shown to be zero.

10.2 Effect on ADMR of varying $\omega_c\tau$

Figure 10.1 shows the effect on the ADMR of varying $\omega_c\tau$.

10.3 Effect on ADMR of varying k_{00}

Figure 10.2 shows the effect on the ADMR of varying k_{00}.

10.4 Measurement Noise Reduction Techniques

There are a number of possible sources of noise/error which might affect these measurements such as external electromagnetic fields, ground loops, capacitive coupling, self-inductive effects and inductive cross-talk between wires.

The total impedance of a circuit is given by the sum

$$Z = \sqrt{X^2 + Y^2} \tag{10.56}$$

$$= \sqrt{R^2 + X_C^2 + X_L^2} \tag{10.57}$$

$$= \sqrt{R^2 + \left(\frac{1}{\omega_r C}\right)^2 + (\omega_r L)^2} \tag{10.58}$$

where R is the resistance, X_C is the reactance due to the capacitive voltage component with a phase which lags the current by $\pi/2$ and X_L is the reactance due to the inductive voltage component which leads the current by $\pi/2$. This means that the Y output on the lock-in contains all the voltages of capacitive and inductive origin and is dependent on the frequency of the excitation current ω_r and the X output contains just the resistive component and is independent of frequency. Clearly the capacitive and inductive components can also be temperature dependent.

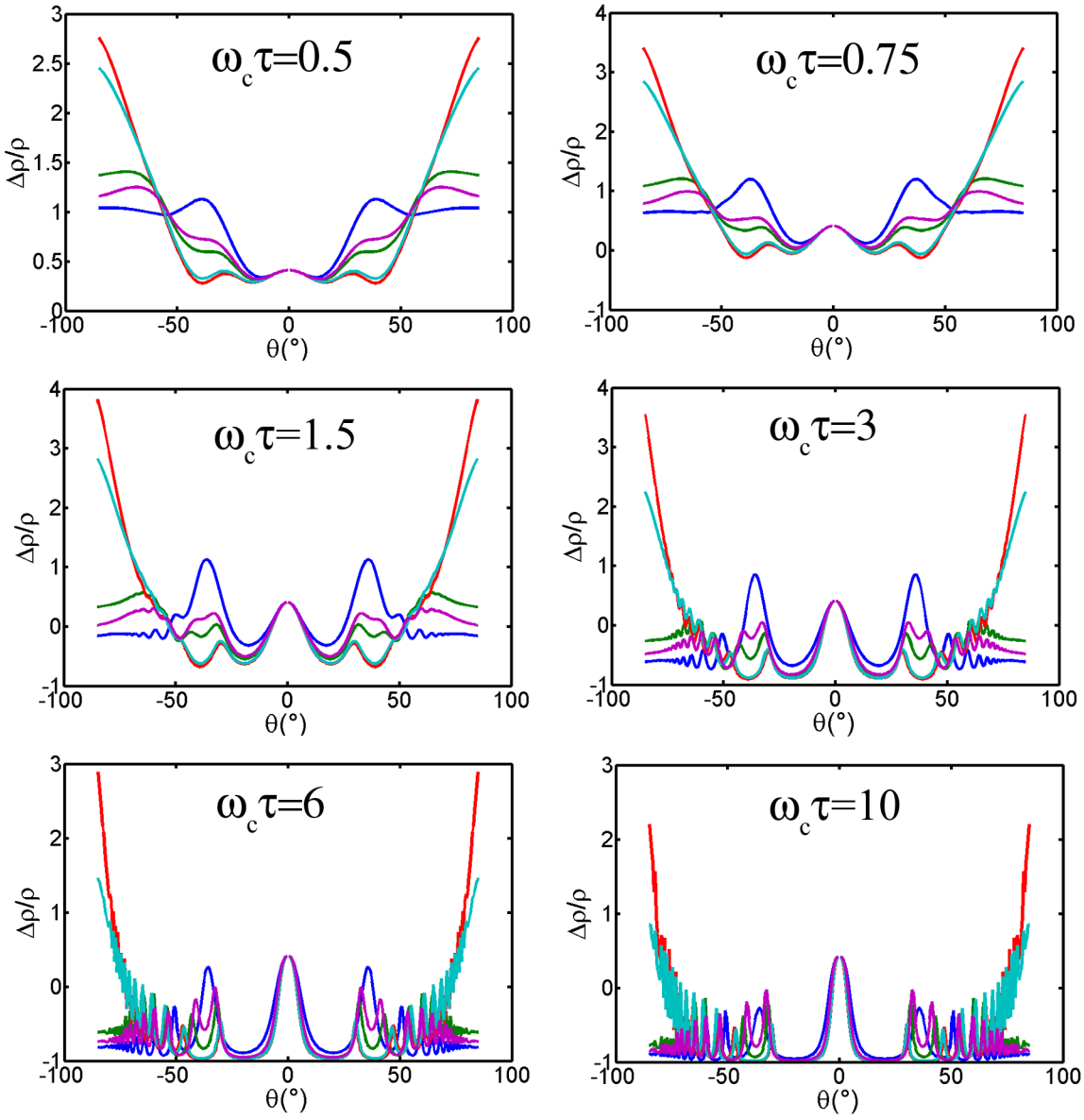

Figure 10.1: Effect on ADMR of varying $\omega_c\tau$.

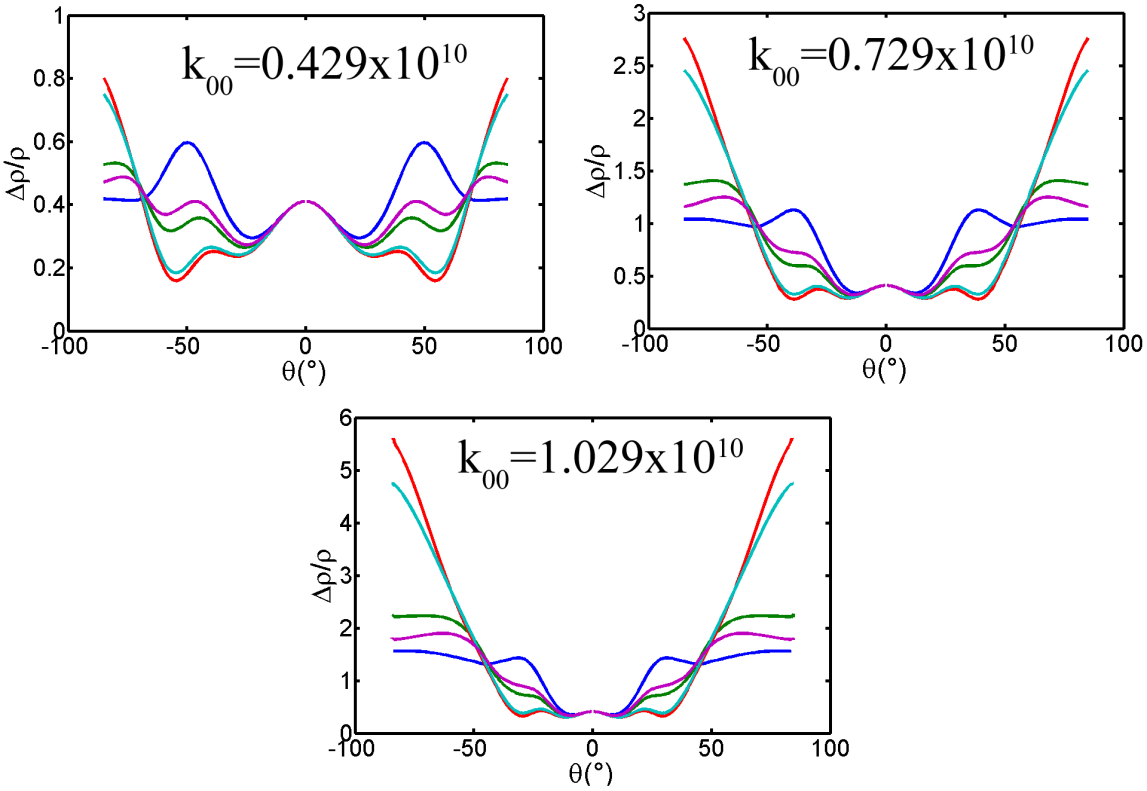

Figure 10.2: Effect on ADMR of varying k_{00}.

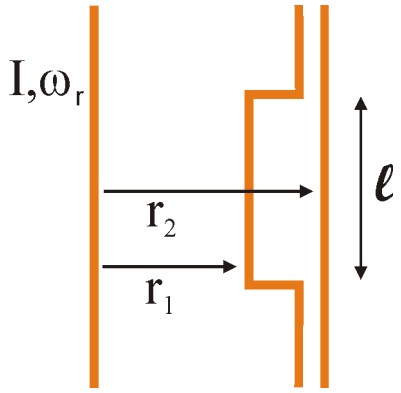

Figure 10.3: Inductive cross-talk between wires in two closed circuits carrying AC signals.

The effect of external fields can be reduced by shielding as much of the wiring as possible. This takes the form of a grounded fine woven metal braid and/or metal foil surrounding a set of wires and is built into any cables used to connect experimental probes to the breakout boxes and any cables used between instruments and the breakout boxes.

All cable shielding and grounds of equipment should be connected together to a single grounding point. Alternatively the cable shielding is sometimes broken in a certain place to isolate two true ground points from each other such as the experimental cryostat and the mains electricity ground of the instruments. If great care is not taken over this then there may be more than one grounding point in the circuit. A potential difference can arise between these points which can cause large noise currents to flow and adversely affect the quality of the measured signal significantly.

Inductive cross-talk is voltage noise resulting from the mutual inductance of two or more closed circuits with paths located near each other — i.e. the changing magnetic field created by an alternating current in one circuit induces spurious signals in a neighboring circuit according to Faradays law $V = d\Phi/dt$. Figure 10.3 shows an arrangement of wires that are subject to cross-talk. In the top wire a current I with frequency ω_r flows. The current induces a magnetic field at distance r from the wire at time t given by

$$B(r,t) = \frac{\mu_0 I \sin \omega_r t}{2\pi r} \tag{10.59}$$

The other two wires are part of a neighboring circuit and situated parallel to the first wire a distance of r_1 and r_2 away. The separation of these two wires $(r_2 - r_1)$ continues for length ℓ. Ampere's law can be used to show the magnetic flux induced through this area of the circuit is

$$\Phi = \oint_S \mathbf{B}(r,t) \cdot d\mathbf{A} \tag{10.60}$$

$$= \int_{r_1}^{r_2} \int_0^l \frac{\mu_0 I \sin \omega_r t}{2\pi r} dz dr \tag{10.61}$$

$$= \frac{l \mu_0 I \sin \omega_r t}{2\pi} \ln \frac{r_2}{r_1} \tag{10.62}$$

Using Faraday's law gives the voltage drop this causes is proportional to ω_r and $\ln r_2/r_1$

$$V = \frac{-d\Phi}{dt} \tag{10.63}$$

$$= \frac{-l\mu_0 I\omega_r \cos\omega_r t}{2\pi} \ln\frac{r_2}{r_1} \tag{10.64}$$

To minimise voltages induced in this way the frequency of the AC current is kept low and the loop area between wires is kept to a minimum by twisting both wires of a circuit together creating twisted pairs. Another important reason to keep loop areas to a minimum arises when measurements in a magnetic field are considered. Any current carrying loop of wire in a magnetic field will be subject to a torque ($T = IAB$) proportional to the current I, the loop area A and the magnetic field B. As the current is AC, this will cause the loop to vibrate and induce a voltage at the same frequency, ω_r as the current. The best way to minimise this is to securely stick/tie down all wires to the probe - usually using GE varnish.

The lock-in uses a differential amplifier whose ideal output is proportional to the voltage difference between its inputs i.e. the voltage drop across the sample $V = Gain \times (V_+ - V_-)$. A real amplifier also has an output component proportional to the actual voltages $V = Gain \times \left((V_+ - V_-) + 10^{-6}\frac{(V_+ + V_-)}{2}\right)$. This additional component is the common-mode voltage. When the voltage measured by the lock-in is very small this common-mode leak voltage can adversly affect the results. The best way to minimise this effect is to balance the resistance of each probe wire with its pair leaving only the contact resistance between the wires and the sample as the main source of resistance difference between the pairs. The contact resistance is nearly impossible to balance so it is minimised to reduce its contribution to the total resistance and minimise any common-mode voltage.

10.5 Delphi Tutorial

This section provides a brief tutorial on setting up *Delphi* to record experimental data. If an instrument doesn't have a GPIB interface a serial port connection to the computer is used. This simply involves connecting a cable from the instrument to a serial port on a computer. Frequently on modern computers these are becoming obsolete — although they can often be purchased on separate PCI cards or as a USB adapter.

Where possible instruments were connected to the computer using a GPIB interface. A Measurement Computing GPIB PCI card needs to be installed into a standard Windows PC and the drivers correctly setup. A GPIB cable is run from the back of the card on the PC to the first instrument. Up to 14 further instruments can be connected in a daisy chain with a single cable linking an instrument to the previous one. Each instrument requires a unique address which is set in the configuration

options on the instrument itself. (Addresses can be chosen regardless of where the instrument is located in the chain and also of which other address are chosen provided each is unique).

The card driver installation on the computer should have created a shortcut called *CBCONF32* in the start menu. This program is used to link the GPIB address of the instrument to a short text handle which is used to refer to the instrument in Delphi. Any other settings required can be configured using this program too, although the defaults are sufficient for most instruments.

10.5.1 The Delphi Environment

The *Delphi* program then needs to be installed on the PC. Each instrument requires specific text commands sent over the GPIB bus in order to respond with the required data. These sometimes complex commands are written out once in *Delphi* in an interface unit specific to that instrument. Each *Delphi* program that is then written uses these interface units to communicate with instruments. A standard interface unit (called *gpib*) is also required in order for the *Delphi* program to communicate with the GPIB card in the computer.

All the steps described in the last two sections need only be performed once. After this is all setup it provides a simple and rapid method to write new programs.

10.5.2 A Simple Delphi Program

As an example consider reading the X output from a SR830 lock-in amplifier. A simple interface unit would be as follows below. The unit name (*DCSTAN830*) is given at the top, then there are two main sections 'interface' and 'implementation'. The interface section contains definitions of class properties, global variables and all procedures contained in the unit. The first line of the implementation section contains a list of other units from which code is referenced rather than duplicated. The code at the very end encapsulated with a 'begin' and 'end' statement creates the class and sets a text handle which corresponds to the text handle linked to the correct GPIB address set earlier in the *CBCONF32* program. There are two procedures also in the implementation section, the first initialises the instrument and the second 'GetVolts' sends a message over the GPIB interface ('SNAP?1,2,3,4') and waits for the response to come back before interpreting it and saving it as the variable x. These messages and the form of the response are detailed for each instrument in its manual.

```
unit DCSTAN830;

interface

type  TLIA= Class
  ieeehdl:integer;
  ieeestr:String;
  x:real;
```

```
Procedure Initialise; Procedure GetVolts; end;

var LIA:array[1..4] of TLIA;

implementation

uses dieeecb,dmisc,sysutils,gpib;

Procedure TLIA.Initialise; begin
  ieeeHdl:=InitDevice(ieeeStr);
  ibclr(ieeeHdl);
  writeieee(ieeeHdl,'OUTX1');
  writeieee(ieeeHdl,'*CLS');
end;

Procedure TLIA.GetVolts; var s:string; begin
  writeieee(ieeeHdl,'SNAP?1,2,3,4');
  readieee(ieeeHdl,s);
  x:=s2r(copy(s,1,pos(',',s)-1));
end;

begin LIA[1]:=TLIA.Create; LIA[1].ieeeStr:='SR830'; end.
```

As well as the interface unit the actual program is needed — the simple one shown below sets a label on the *Delphi* form to show the lock-in X value when a button is pressed. At the top in the 'uses' section we can see that the name of the interface unit (*dcstan830*) has been added — this automatically includes the code from the file above to save it being typed out again. The 'FormCreate' function is run automatically when the program is opened and just runs the instrument initialisation procedure. The 'Button1Click' function is run when the button on the form is clicked. This first runs the 'GetVolts' procedure to get the value from the instrument and then sets the label caption to be the value returned and saved to the variable x.

```
unit Unit1;

interface

uses
  Windows, Messages, SysUtils, Variants, Classes, Graphics, Controls, Forms,
  Dialogs, StdCtrls, dcstan830, dmisc;

type
  TForm1 = class(TForm)
    Button1: TButton;
    Label1: TLabel;
    procedure Button1Click(Sender: TObject);
  private
    { Private declarations }
  public
    { Public declarations }
  end;
```

```
var
  Form1: TForm1;

implementation

{$R *.dfm}

procedure TForm1.Button1Click(Sender: TObject); begin
  lia[1].getvolts;
  label1.caption:=r2s(lia[1].x,13,-1);
end;

procedure TForm1.FormCreate(Sender: TObject); begin
  Lia[1].initialise;
end;

end.
```

This example can be extended to include all the instrument functions that are required. In practise the programs are run on a timed loop which reads the value on the instrument approximately every one second. This is plotted on a graph and saved to a file to be analysed later. To include a graph within a program *CGraph* [148] needs to be added to the list of 'uses' units at the top of the program and the command to add a point to a graph is

```
GraphName.Addpointtoplot(xvalue,yvalue,seriesnumber);
```

In order save the data to a file it needs to be assigned a handle using

```
AssignFile(handlename,filename);
```

It is then opened in append mode to add a line to the file or rewrite mode to over-write the current contents.

```
append(handlename);
```

or

```
rewrite(handlename);
```

The line is then written using

```
writeln(handlename, 'Text',_tb,VariableName);
```

where each element is separated with a comma, text is written in quote marks, variable values are written by including the variable name and a tab is written with '_tb'. The file is then closed using

```
closefile(handlename);
```

The handlename needs to be declared as a textfile and the filename as a string.

10.5.3 Remote Monitoring Code

```
procedure tform1.publish(s, filename: string);
var today : TDateTime; statusfile: textfile;
  begin
    AssignFile(statusfile, 'C:\Program Files\Apache Software Foundation\
        Apache2.2\htdocs\'+filename+'.html');
    ReWrite(statusfile);
    today := Time;
    writeln(statusfile, '<html><body>',TimeToStr(today),_tb,s,'</body></html>');
    closefile(statusfile);
  end;
```

This procedure quoted above can be included in any program and is called from within the code with

```
publish('X'+r2s(lia[1].x,1,1)+'V','expstatus');
```

which records the lock-in X output voltage in a file called *expstatus.html*.

10.6 Period of Quantum Oscillations

With the measured signal periodic in $1/B$, for a single period the start point is $1/B_0$ and the end is $1/B_1$ so the period is $1/B_0 - 1/B_1$ and the frequency is:

$$f = \frac{1}{\frac{1}{B_1} - \frac{1}{B_0}} = \frac{B_1 B_0}{B_0 - B_1} \tag{10.65}$$

So the period of the oscillation when viewed against B is:

$$P = \frac{B_1 B_0}{f} \approx \frac{B^2}{f} \tag{10.66}$$

10.7 Matlab Code

10.7.1 Yamaji AMRO Simulation

This code produces simulations of Yamaji oscillations in the magnetoresistance.

```
function fitprm = amrosimyamaji()

%set angles
psi=[0];
theta_a=0:0.5:70;
%simulations with different omega_c-tau
simulation1=amro(theta_a,psi,4);
simulation2=amro(theta_a,psi,3.5);
simulation3=amro(theta_a,psi,3);
simulation4=amro(theta_a,psi,2.5);
simulation5=amro(theta_a,psi,2);
```

```
simulation6=amro(theta_a,psi,1.5);
simulation7=amro(theta_a,psi,1);
simulation8=amro(theta_a,psi,0.5);
%plot graph
h=plot(theta_a,simulation1,'red-',theta_a,simulation2,'blue-',theta_a,simulation3,'green-',
    theta_a,simulation4,'black-',theta_a,simulation5,'red-',theta_a,simulation6,'blue-',
    theta_a,simulation7,'green-',theta_a,simulation8,'black-');
xlabel('\theta()','FontSize',35);
ylabel('\Delta\rho/\rho','FontSize',35);
set(gca,'LineWidth',4);
set(h,'LineWidth',4);
set(gca,'FontSize',30);
%plot(tan(theta_a/180*pi),simulation,'-');
fitprm = 1;

%Function to calculate rho
function rho = amro(theta_a,psi,wct0)
k00=0.725; %diameter of Fermi surface
d=23.2e-10;%lattice dimension
amro=zeros(length(psi),length(theta_a));
rho=zeros(length(psi),length(theta_a));
theta_a=theta_a.*pi./180;
psi=psi.*pi./180;
%calculate sigma at each phi and theta
for i = 1:length(psi)
    for j=1:length(theta_a)
        amro(i,j)=quadl(@sigzz,-2*pi/d,2*pi/d,[],[],theta_a(j),psi(i),wct0,k00);
    end
    rho_norm=1/quadl(@sigzz,-2*pi/d,2*pi/d,[],[],0,0,wct0,k00);
    rho(i,:) = ((1./amro(i,:))-rho_norm)/rho_norm;
end
%Function to calculate sigma_zz
function s = sigzz(k0,theta,psi,wct0,k00)
N=10;%size of integration and FFT
c=23.2e-10;
k00=k00*1e10;
wct=wct0*cos(theta);
fx=zeros(1,length(k0));
for j = 1:length(k0)
    phi=0:2*pi/(2^N-1):2*pi;
    kf=k00;
    tp1=1;
    kz=k0(j)-kf.*cos(phi)*tan(theta);
    vi=tp1.*sin(kz*c*0.5);
    vj=tp1.*sin(kz*c*0.5);
    an=real(fft(vi,2^N));
    bn=-1.0*imag(fft(vi,2^N));
    cn=real(fft(vj,2^N));
    dn=-1.0*imag(fft(vj,2^N));
    freq = 0:1/(max(phi)-min(phi)):(length(an)-1)/(max(phi)-min(phi));
    szz=an(1)*cn(1);
    for k = 2:length(freq)*0.5
        factor=1.0/(1+(wct*(k-1))^2);
        szz=szz+2.0*factor*(an(k)*cn(k)+bn(k)*dn(k)-wct*(k-1)*(an(k)*dn(k)-bn(k)*cn(k)))+eps;
```

```
    end
    fx(j) = szz+eps;
end s=fx*wct0/45/(length(freq)*0.5)*5.0724e-10;
```

10.7.2 Bandstructure Plot

This reads in *case.spaghetti_ene* file output by *Wien2K* after it has calculated the bandstructure. There are header lines dispersed through the file indicating the start of each band, these are noted and stripped out. The fourth and fifth columns are the **k** and energy coordinated respectively and for each band are written into separate columns in an array. The bandstructure is then plotted and various graphical details altered to make the plots which appear in this work.

```
%Load File
clear;
fid = fopen('tl2201vca0.06_1000\tl2201vca0.06_1000.spaghetti_ene');

k=0; while k<12036
    dataline=fgetl(fid);
    newband=strfind(dataline, 'band');
    k=k+1;
    if newband
        [a bandnum]=strread(dataline, '%s %d');
        i=1;
    else
        [kx ky kz x y]=strread(dataline, '%f %f %f %f %f');
        xarray(i,bandnum)=x;
        yarray(i,bandnum)=y;
        i=i+1;
    end;
end;
    h=plot(5.*xarray,yarray,'b .');
    axis equal;
    ylim('manual');
    ylim([-5 5]);
    xlim('manual');
    xlim([0 8]);
    set(h,'LineWidth',1);
    ylabel('Energy (eV)','FontSize',25);
    set(gca,'FontSize',20);
    set(gca,'xtick',[0 2.215 4.335 4.435 7.435 8]);
    set(gca,'XTickLabel',{'';'M';'';'';'';'Z'});
    text('Interpreter','latex','String','$$\Gamma$$','Position',[0 -5.35],'FontSize',22);
    text('Interpreter','latex','String','P','Position',[4.0 -5.35],'FontSize',22);
    text('Interpreter','latex','String','X','Position',[4.4 -5.35],'FontSize',22);
    text('Interpreter','latex','String','$$\Gamma$$','Position',[7.25 -5.35],'FontSize',22);
    set(gca,'ytick',[-5 -2.5 0 2.5 5]);
    line([0 0],[-5 5],'LineWidth',2,'Color','k');
    line([2.215 2.215],[-5 5],'LineWidth',2,'Color','k');
    line([4.335 4.335],[-5 5],'LineWidth',2,'Color','k');
    line([4.435 4.435],[-5 5],'LineWidth',2,'Color','k');
    line([7.435 7.435],[-5 5],'LineWidth',2,'Color','k');
    line([8 8],[-5 5],'LineWidth',2,'Color','k');
```

```
    line([0 8],[0 0],'LineWidth',2,'Color','k','LineStyle','--');
```

10.7.3 Mishonov LCAO Fermi Surface Plot

Plots the $Tl_2Ba_2CuO_{6+\delta}$ Fermi surface from the LCAO model derived by Mishonov [73].

```
clear;
e=1.89; %fermi Level
es=6.5; %Cu 4s level epsilon_s
ed=0; %Cu 3d level epsilon_d
ep=-0.9; %O 2p level epsilon_p
tss=0.14; %Fitted interlayer Cu 4s-Cu 4s hopping
tpd=1.6; %Cu 3d-O 2p sigma hopping amplitude
tpp=0; %oxygen-oxygen transfer integral
tsp=2.3; %Cu 4s-) 2p hopping amplitude
ees=e-es; %var epsilon_s Equation 10
eed=e-ed; %var epsilon_d Equation 10
eep=e-ep; %var epsilon_p Equation 10

%Equation 10
A=16*(4.*tpd.^2.*tsp.*2+2.*tsp.^2.*tpp.*eed-2.*tpd.^2.*tpp.*ees-tpp.^2.*eed.*ees);
B=-4.*eep.*(tsp.^2.*eed+tpd.^2.*ees); C=eed.*eep.^2.*ees;
K=-tss.*tpp.*(eed.*tpp+2.*tpd.^2); L=-eep.*tss.*tpd.^2;
M=eed.*eep.^2.*tss;

%Equation 19
ap=16.*(2.*tsp.^2.*tpp-2.*tpd.^2.*tpp-tpp.^2.*(eed+ees));
bp=-4.*(tsp.^2.*eed+tpd.^2.*ees+eep.*(tsp.^2+tpd.^2));
cp=(ees+eed).*eep.^2+2.*eed.*ees.*eep;

n=100;

xd=(-B+sqrt(B.^2-A.*C))/A; %Equation 22
pd=2.*asin(sqrt(xd)); %Equation 22

%calculate filling factor Equation 21
deltap=(pi-pd)/n; surface=0; for i=0:n
    px=pd+i.*deltap;
    X=(sin(px/2)).^2;
    Y=-(B.*X+C)/(A.*X+B); %Equation 15
    py=2.*asin(sqrt(Y));
    surface=surface+(px-py);
end;
filling=8.*surface.*deltap/((2.*pi).^2);
disp('Filling');
disp(filling);

k=1;

%draw Fermi Surface
for pz=0:pi/15:pi
    cz=cos(pz); %equation 5
    for px=pd:deltap:(2.*pi-pd)
        sx=sin(px/2);
```

```
        cx=abs(cos(px/2));
        X=sx.^2; %equation 5
        Y=-(B.*X+C)/(A.*X+B); %Equation 15
        if (0<Y) && (Y<1)
            py=2.*asin(sqrt(Y)); %equation 15
            sy=sin(py/2); %equation 5
            cy=abs(cos(py/2)); %equation 5
            den=ap.*(X.*Y)+bp.*(X+Y)+cp; %equation 17
            vx=-(A.*Y+B).*sin(px)/(2.*den); %equation 17
            vy=-(A.*X+B).*sin(py)/(2.*den); %equation 17
            v2=vx.^2+vy.^2; %equation 16
            tau2=tsp.^2-ees.*tpp/2; %equation 12
            psi1=-ep.*eep.^2+4.*eep.*tsp.^2.*(X+Y)-32.*tpp.*tau2.*X.*Y;
            psi2=-4.*eep.*tsp.*tpd.*(X-Y);
            psi3=-(ees.*eep-8.*tau2.*Y).*tpd.*sx;
            psi4=(ees.*eep-8.*tau2.*X).*tpd.*sy;
            norm=psi1.^2+psi2.^2+psi3.^2+psi4.^2; %equation 12
            pert=-8.*tss.*cx.*cy.*cz.*psi2.^2/norm; %equation 13
            dpx=pert.*vx/v2;
            dpy=pert.*vy/v2;
            pxp=px+dpx;
            pyp=py+dpy; %equation 20
            plotdata(k,1)=pxp;
            plotdata(k,2)=pyp;
            plotdata(k+1,1)=pyp;
            plotdata(k+1,2)=pxp;
            py=2.*pi-py;
            pyp=2.*pi-pyp;
            plotdata(k+2,1)=pxp;
            plotdata(k+2,2)=pyp;
            plotdata(k+3,1)=pyp;
            plotdata(k+3,2)=pxp;
            k=k+4;
        end
    end
end

plot(plotdata(:,1)/(2*pi),plotdata(:,2)/(2*pi),'.');
axis([0 1 0 1]);
axis equal;
```

10.7.4 3D Fermi Surface Plot

Plots a 3D representation of the Fermi surface of $Tl_2Ba_2CuO_{6+\delta}$ using the parameterisation used in ADMR fits.

```
%3D Fermi Surface Plotting Script
clear;
a=3.86e-10; %lattice parameter
c=23.2e-10; %lattice parameter
k21=-3e8; %enhanced to make noticable
k61=0.7; k101=-0.3; k04=-0.03; k00=0.729e10;
nphi=100; %number of phi steps
```

```
nz=100; %number of z steps

j=1;
for z=-nz:1:nz %loop over z
    i=1;
    for phi=1:1:nphi+1 %loop over phi
        %kf=k00;
        %kf=k00-2*k21*cos(c*(z*pi/c/nz));
        %kf=k00*(1+k04*cos(4*phi*2*pi/nphi))-2*k21*cos(c*(z*pi/c/nz));
        %kf=k00*(1+k04*cos(4*phi*2*pi/nphi))-2*k21*(sin(2*phi*2*pi/nphi))
            *cos(c*(z*pi/c/nz));
        %kf=k00*(1+k04*cos(4*phi*2*pi/nphi))-2*k21*(sin(2*phi*2*pi/nphi)
            +k61*sin(6*phi*2*pi/nphi))*cos(c*(z*pi/c/nz));
        kf=k00*(1+k04*cos(4*phi*2*pi/nphi))-2*k21*(sin(2*phi*2*pi/nphi)
            +k61*sin(6*phi*2*pi/nphi)+k101*sin(10*phi*2*pi/nphi))
            *cos(c*(z*pi/c/nz));
        kx(i,j)=kf*cos(phi*2*pi/nphi); %array of kx points
        ky(i,j)=kf*sin(phi*2*pi/nphi); %array of ky points
        kz(i,j)=z*pi/c/nz; %array of kz points
        i=i+1;
    end
    j=j+1;
end

normxy=2*pi/a/2; %normalisation for kx ky
normz=pi/c; %normalisation for kz

surf(kx/normxy,ky/normxy,kz/normz,'FaceColor','red','EdgeColor','none',
    'SpecularStrength',1);
lighting gouraud;
material shiny;
light('Position',[1 0 0],'Style','infinite');
light('Position',[-1 0 0],'Style','infinite');
set(gca,'DataAspectRatio',[1 1 3]);
axis off;
grid off;
```

10.7.5 2D Fermi Surface Projection Plot

Plots a 2D projection of the Fermi surface of $Tl_2Ba_2CuO_{6+\delta}$ using the parameterisation used in ADMR fits.

```
%2D Fermi Surface Projection Plotting Script
clear;
a=3.86e-10; %lattice parameter
c=23.2e-10; %lattice parameter
k21=-3e8; % (guess to make noticable)
k61=0.7; k101=-0.1;
k04=-0.03; %usually 0.03 in fits
k00=0.729e10;
nphi=100; %number of phi steps
nz=100; %number of z steps
```

```
i=1;
for z=-nz:1:nz %loop over z
    for phi=1:1:nphi+1 %loop over phi
        %kf=k00;
        %kf=k00-2*k21*cos(c*(z*pi/c/nz));
        %kf=k00*(1+k04*cos(4*phi*2*pi/nphi))-2*k21*cos(c*(z*pi/c/nz));
        %kf=k00*(1+k04*cos(4*phi*2*pi/nphi))-2*k21*(sin(2*phi*2*pi/nphi))
            *cos(c*(z*pi/c/nz));
        %kf=k00*(1+k04*cos(4*phi*2*pi/nphi))-2*k21*(sin(2*phi*2*pi/nphi)
            +k61*sin(6*phi*2*pi/nphi))*cos(c*(z*pi/c/nz));
        kf=k00*(1+k04*cos(4*phi*2*pi/nphi))-2*k21*(sin(2*phi*2*pi/nphi)
            +k61*sin(6*phi*2*pi/nphi)+k101*sin(10*phi*2*pi/nphi))
            *cos(c*(z*pi/c/nz));
        kx(i)=kf*cos(phi*2*pi/nphi); %array of kx points
        ky(i)=kf*sin(phi*2*pi/nphi); %array of ky points
        i=i+1;
    end
end

normxy=2*pi/a/2; %normalisation for kx ky
normz=pi/c; %normalisation for kz

plot(kx./normxy,ky./normxy,'red-');
PlotBoxAspectRatio=[1 1 1];
pbaspect('manual');
axis off;
grid off;
```

10.7.6 Area of Slice of Fermi Surface

This calculates the area of a cross-section slice of the Fermi surface which can be related to the dHvA or SdH area.

```
clear;
a=3.86e-10;
c=23.1331e-10;
d=c/2;
k61=0.68;
k101=-0.25;
k04=-0.03;
k00=0.739e10;
nphi=1000; %number of phi steps
nz=100; %number of z steps
normxy=2*pi/a/2; %normalisation for kx ky
normz=pi/d; %normalisation for kz

anisotropy=1000;
k21=sqrt(8./(anisotropy.*c.*c.*(1+k61.*k61+k101.*k101)));

for z=-nz:1:nz %loop over z
    i=1;
    for phi=1:1:nphi+1 %loop over phi
```

```
        kf=k00*(1+k04*cos(4*phi*2*pi/nphi))-2*k21*(sin(2*phi*2*pi/nphi)
         +k61*sin(6*phi*2*pi/nphi)+k101*sin(10*phi*2*pi/nphi))*cos(d*(z*pi/d/nz));
        kx(i)=kf*cos(phi*2*pi/nphi); %array of kx points
        ky(i)=kf*sin(phi*2*pi/nphi); %array of ky points
        i=i+1;
    end
    intarea=-cumtrapz(kx./normxy,ky./normxy);
    area(z+101)=intarea(1,end)/4; %gives area as fraction since
    %normalised BZ goes from -1..1 in x and y i.e. 2*2=4
end

plot(area); xlabel('Position of Slice in BZ');
ylabel('Occupied Fractional Area of BZ');
```

10.7.7 Modification to fminsearch for Covariance Matrix

The *Matlab* function *fminsearch* was modified to calculate and return the covariance matrix — i.e. the errors on the fit parameters using the method outlined in the appendix of [105]. The declaration at the top was modified to include an additional parameter N which is passed in the function call which gives the total number of data points and also to return the error vector.

```
function [x,errorvector,fval,exitflag,output] = fminsearchmf(funfcn,x,N,options,varargin)
```

This additional code was added after line 382 in the code for *fminsearch* and is based on the appendix of [105].

```
    %calculate covariance matrix
    %qmatrix
    temp=size(v);
    numberofparams=temp(1,1);
    for i=1:numberofparams
        qmatrix(i,:)=v(i,:)-v(i,1);
    end
    qmatrix(:,1)=[];
    %bmatrix
    for i=1:numberofparams
        for j=1:numberofparams
            if i==j
                yi=fv(1,i+1);
                y0=fv(1,1);
                p0i=(v(:,1)+v(:,i+1))./2;
                y0i=funfcn(p0i,varargin{:});
                bmatrix(i,i)=2*(yi+y0-2*y0i);
                a(i)=2*y0i-(yi+3*y0)/2;
            else
                pij=(v(:,i+1)+v(:,j+1))./2;
                yij=funfcn(pij,varargin{:});
                yi=fv(1,i+1);
                y0=fv(1,1);
                p0i=(v(:,1)+v(:,i+1))./2;
                p0j=(v(:,1)+v(:,j+1))./2;
                y0i=funfcn(p0i,varargin{:});
```

```
                y0j=funfcn(p0j,varargin{:});
                bmatrix(i,j)=2*(yij+y0-y0i-y0j);
                a(i)=2*y0i-(yi+3*y0)/2;
            end
        end
    end
    covarmatrix=qmatrix*inv(bmatrix)*qmatrix';
    ymin=y0-a*inv(bmatrix)*a';
    normalisefactor=2*ymin/(N-numberofparams);
    covarmatrix=covarmatrix.*normalisefactor;
    %get standard deviation
    for i=1:numberofparams
        errorvector(i)=sqrt(covarmatrix(i,i));
    end
    %end covariance matrix calculation
```

10.7.8 ADMR Data Fitting Code

This is the main code used to fit the ADMR experimental data to simulations.

```
function fitprm = amrosimasym(angle)
loaddata('data\tl320c3-14K.txt')
dataFiles=['file1.dat';'file2.dat';'file3.dat';'file4.dat';'file5.dat'];
params = [0.4 0.01];

psi=[1 2 3 4 5]*13.333;

options=optimset('Display','iter'); %set options for fminsearch

points = 191; %variable step to allow different theta range on different phi
minth=[]; maxth=[];
for q = 1:size(dataFiles,1) %loop over all data files
    data=load(dataFiles(q,:));
    mindatatheta=min(data(:,1));
    if mindatatheta < -95
        mintheta=mindatatheta;
        maxtheta=min(max(data(:,1)),85);
        range=maxtheta-mintheta-10; %don't use -85 to -95 part
        theta_a(q,:)=[mintheta:range/(points-1):-95,-85:range/(points-1):maxtheta];
    else
        mintheta=max(min(data(:,1)),-angle);
        maxtheta=min(max(data(:,1)),angle);
        range=maxtheta-mintheta;
        theta_a(q,:)=[mintheta:range/(points-1):maxtheta];
    end
end

for i = 1:length(psi)
    dataName=dataFiles(i,:);
    s=dataimport(theta_a(i,:),i,dataName);
    expData(i,:)=s;
end

%fminsearch fit - uses Nelder and Mead downhill simplex method - uses only function
```

```
    evaluations and not derivatives
numberofdatapoints=points*length(psi);
[estimates,errorvector]=fminsearchmf(@amrofit,params,numberofdatapoints,options,
    theta_a,psi,expData);
disp('Estimates');
disp(num2str(estimates));
simulation=amro(theta_a,psi,estimates(1),estimates(2));
%plot graph
plot(theta_a(1,:),expData(1,:),'-',theta_a(2,:),expData(2,:),'-',theta_a(3,:),
    expData(3,:),'-',theta_a(4,:),expData(4,:),'-',theta_a(5,:),expData(5,:),'-',
    theta_a(1,:),simulation(1,:),'*',theta_a(2,:),simulation(2,:),'*',
    theta_a(3,:),simulation(3,:),'*',theta_a(4,:),simulation(4,:),'*',
    theta_a(5,:),simulation(5,:),'*');
fitprm = 1;

%imports already normalised data from file for each psi
function s = dataimport(theta_a,i,dataName) amroData = load(dataName);

s =interp1(amroData(:,1),amroData(:,2),theta_a,'spline');

%least squares fit of amro data (expData)
function sse = amrofit(params,theta,psi,expData) disp(params);
wct0=params(1);
gamma=params(2);
fitData = amro(theta,psi,wct0,gamma); errorVector=fitData - expData;
sse=sum(sum(errorVector.^2));%Double sum to sum over the entire Matrix

function rho = amro(theta_a,psi,wct0,gamma)
k00=0.729;
k04=-0.03;
k61ok21=0.7;
k101ok21=k61ok21-1;
beta=0;
psi_AS=0;
theta_AS=0;
theta_AS2=0;
phiOffset=0;

c=23.2e-10;%lattice dimension
d=c;
theta_XAS=theta_AS*pi/180;
theta_YAS=theta_AS2*pi/180;
psi_AS=psi_AS*pi/180;
theta_a=theta_a.*pi./180;
psi=psi.*pi./180;
theta_a_original=theta_a;
psi=psi+(phiOffset*13.333);
phiOffset=phiOffset*pi/180;

for i = 1:length(psi)

    if (theta_XAS==0 && theta_YAS==0) || (theta_YAS==0 && psi(i)==0)
        theta_center=0;
    else
```

```
        theta_center=atan((cos(theta_YAS).*cos(theta_XAS))./(sin(theta_YAS).
            *cos(psi(i))+cos(theta_YAS).*sin(theta_XAS).*sin(psi(i))))-pi/2;
    end

    theta_a=theta_a_original(i,:)+theta_center;
    asym1=cos(psi_AS).*(cos(theta_YAS).*cos(psi(i)).*sin(theta_a)+
        sin(theta_YAS).*(-sin(theta_XAS).*sin(psi(i)).*sin(theta_a)+
        cos(theta_XAS).*cos(theta_a)))+sin(psi_AS).*(cos(theta_XAS).*
        sin(psi(i)).*sin(theta_a)+sin(theta_XAS).*cos(theta_a));
    asym2=-sin(psi_AS).*(cos(theta_YAS).*cos(psi(i)).*sin(theta_a)+
        sin(theta_YAS).*(-sin(theta_XAS).*sin(psi(i)).*sin(theta_a)+
        cos(theta_XAS).*cos(theta_a)))+cos(psi_AS).*(cos(theta_XAS).*
        sin(psi(i)).*sin(theta_a)+sin(theta_XAS).*cos(theta_a));
    asym3=-sin(theta_YAS).*cos(psi(i)).*sin(theta_a)+cos(theta_YAS).*
        (-sin(theta_XAS).*sin(psi(i)).*sin(theta_a)+cos(theta_XAS).*
        cos(theta_a));
    theta_crystal=acos(asym3);
    psi_crystal=atan(asym2./asym1);
    for j=1:length(theta_a)
    amro(i,j)=quadl(@sigzz,-2*pi/d,2*pi/d,[],[],theta_crystal(j),psi_crystal(j),
        wct0,k00,k04,k61ok21,k101ok21,gamma,beta);
    end

    normal_factor=0.001704/0.003527; %tl320c3_14K

    asym1n=cos(psi_AS).*(cos(theta_YAS).*cos(psi(i)).*sin(theta_center)+
        sin(theta_YAS).*(-sin(theta_XAS).*sin(psi(i)).*sin(theta_center)+
        cos(theta_XAS).*cos(theta_center)))+sin(psi_AS).*(cos(theta_XAS).*
        sin(psi(i)).*sin(theta_center)+sin(theta_XAS).*cos(theta_center));
    asym2n=-sin(psi_AS).*(cos(theta_YAS).*cos(psi(i)).*sin(theta_center)+
        sin(theta_YAS).*(-sin(theta_XAS).*sin(psi(i)).*sin(theta_center)+
        cos(theta_XAS).*cos(theta_center)))+cos(psi_AS).*(cos(theta_XAS).*
        sin(psi(i)).*sin(theta_center)+sin(theta_XAS).*cos(theta_center));
    asym3n=-sin(theta_YAS).*cos(psi(i)).*sin(theta_center)+cos(theta_YAS).*
        (-sin(theta_XAS).*sin(psi(i)).*sin(theta_center)+cos(theta_XAS).*
        cos(theta_center));

    theta_normal=acos(asym3n);

    if theta_AS==0 && theta_AS2==0 && psi_AS==0
        psi_normal=psi(i);
    else
        psi_normal=atan(asym2n./asym1n);
    end
    rho_norm=normal_factor./quadl(@sigzz,-2*pi/d,2*pi/d,[],[],theta_normal,
        psi_normal,wct0,k00,k04,k61ok21,k101ok21,gamma,beta);
    rho(i,:) = ((1./amro(i,:))-rho_norm)/rho_norm;

end

function s = sigzz(k0,theta,psi,wct0,k00,k04,k61ok21,k101ok21,gamma,beta)
N=10;%size of integration and FFT
c=23.2e-10;
k00=k00*1e10;
```

```
wct=wct0*cos(theta)/(1+beta*gamma/2);
wct00=wct0*cos(theta); fx=zeros(1,length(k0));
for j = 1:length(k0)
    phi=0:2*pi/(2^N-1):2*pi;%phase variable
    kf=k00*(1+k04*cos(4*(phi+psi)));
    tp1=sin(2*(phi+psi))+k61ok21*sin(6*(phi+psi))+k101ok21*sin(10*(phi+psi));
    kz=k0(j)-kf.*cos(phi)*tan(theta);
    kzj=kz;
    vi=tp1.*sin(kz*c*0.5).*exp(-1.0/wct00*((gamma+beta).*sin(4*(phi+psi))/4+
        gamma*beta.*sin(4*(phi+psi)).*cos(4*(phi+psi))/8)).*
        (1+beta*cos(4*(phi+psi)));%velocity in zth direction
    vj=tp1.*sin(kzj*c*0.5).*exp(1.0/wct00*((gamma+beta).*sin(4*(phi+psi))/4+
        gamma*beta.*sin(4*(phi+psi)).*cos(4*(phi+psi))/8)).*
        (1+beta*cos(4*(phi+psi)));%velocity in zth direction at an earlie
    an=real(fft(vi,2^N));%cosine coeff of vi
    bn=-1.0*imag(fft(vi,2^N));%sine coeff of vi
    cn=real(fft(vj,2^N));%cos coeff of vj
    dn=-1.0*imag(fft(vj,2^N));%sine coeff of vj
    freq = 0:1/(max(phi)-min(phi)):(length(an)-1)/(max(phi)-min(phi));
    szz=an(1)*cn(1);
    for k = 2:length(freq)*0.5
        factor=1.0/(1+(wct*(k-1))^2);
        szz=szz+2.0*factor*(an(k)*cn(k)+bn(k)*dn(k)-wct*(k-1)*
            (an(k)*dn(k)-bn(k)*cn(k)))+eps;
    end
    fx(j) = szz+eps;
end
s=fx*wct0/45/(length(freq)*0.5);
```

10.7.9 Shibauchi Simulation Code

This code produces the simulation of the magnetoresistivity versus temperature graph shown in figure 6.26.

```
function fitprm = amrosim()
field=[11.5 15 20 25 30 35 40 45];
temp=[4.2 14 23 32 40 50 70 90];
wct0=[0.39824 0.36387 0.32756 0.29355 0.26402 0.23030 0.17339 0.13370]; %tl320c5 151206
gamma=[-0.02556 0.09398 0.18205 0.23372 0.27586 0.30787 0.37265 0.37993]; %tl320c5 151206
rho=amro(field,temp,wct0,gamma);
plot(temp.*temp,rho,'-*');
fitprm = 1;

function rho= amro(field,temp,wct0,gamma)
k00=0.729; %tl320c5 151206
k04=-0.03354; %tl320c5 151206
k61ok21=0.67576; %tl320c5 151206

k101ok21=k61ok21-1; beta=0; c=23.2e-10; d=c;

for i = 1:length(field)
    for j=1:length(temp)
        amro(j,i)=quadl(@sigzz,-2*pi/d,2*pi/d,[],[],0,0,wct0(j)*field(i)/45,
```

```
            k00,k04,k61ok21,k101ok21,gamma(j),beta,field(i));
    end
end
    rho=1./amro;

function s = sigzz(k0,theta,psi,wct0,k00,k04,k61ok21,k101ok21,gamma,beta,field)
N=10;
c=23.2e-10;
k00=k00*1e10;
wct=wct0*cos(theta)/(1+beta*gamma/2);
wct00=wct0*cos(theta);
fx=zeros(1,length(k0));
for j = 1:length(k0)
    phi=0:2*pi/(2^N-1):2*pi;
    kf=k00*(1+k04*cos(4*(phi+psi)));
    tp1=sin(2*(phi+psi))+k61ok21*sin(6*(phi+psi))+k101ok21*sin(10*(phi+psi));
    kz=k0(j)-kf.*cos(phi)*tan(theta);
    vi=tp1.*sin(kz*c*0.5).*exp(-1.0/wct00*((gamma+beta).*sin(4*(phi+psi))
        /4+gamma*beta.*sin(4*(phi+psi)).*cos(4*(phi+psi))/8))
        .*(1+beta*cos(4*(phi+psi)));%velocity in zth direction
    vj=tp1.*sin(kz*c*0.5).*exp(1.0/wct00*((gamma+beta).*sin(4*(phi+psi))
        /4+gamma*beta.*sin(4*(phi+psi)).*cos(4*(phi+psi))/8))
        .*(1+beta*cos(4*(phi+psi)));%velocity in zth direction at an earlier time
    an=real(fft(vi,2^N));%cosine coeff of vi
    bn=-1.0*imag(fft(vi,2^N));%sine coeff of vi
    cn=real(fft(vj,2^N));%cos coeff of vj
    dn=-1.0*imag(fft(vj,2^N));%sine coeff of vj
    freq = 0:1/(max(phi)-min(phi)):(length(an)-1)/(max(phi)-min(phi));
    szz=an(1)*cn(1);
    for k = 2:length(freq)*0.5
        factor=1.0/(1+(wct*(k-1))^2);
        szz=szz+2.0*factor*(an(k)*cn(k)+bn(k)*dn(k)-wct*(k-1)*(an(k)*dn(k)-bn(k)*cn(k)));
    end
    fx(j) = szz;
end
s=fx*wct0/field/(1+beta*gamma/2)/(length(freq)*0.5);
```

This code produces the Kohler plot in figure 6.29.

```
function fitprm = amrosim()
field=[11.5 15 20 25 30 35 40 45];
temp=[4.2 14 23 32 40 50 70 90];
wct0=[0.39824 0.36387 0.32756 0.29355 0.26402 0.23030 0.17339 0.13370]; %tl320c5 151206
%wct0=1.*[0.30824 0.28387 0.26756 0.24355 0.22402 0.20030 0.18339 0.15370]; %tl320c5 151206
gamma=[-0.02556 0.09398 0.18205 0.23372 0.27586 0.30787 0.37265 0.37993]; %tl320c5 151206

power=2; [rho, rho_norm]=amro(field,temp,wct0,gamma,1);

offset=0;
output(:,1)=(field./rho_norm(1)).^power;
output(:,2)=rho(1,:)+offset;
output(:,3)=(field./rho_norm(2)).^power;
output(:,4)=rho(2,:)+offset;
output(:,5)=(field./rho_norm(3)).^power;
output(:,6)=rho(3,:)+offset;
```

```
output(:,7)=(field./rho_norm(4)).^power;
output(:,8)=rho(4,:)+offset;
output(:,9)=(field./rho_norm(5)).^power;
output(:,10)=rho(5,:)+offset;
output(:,11)=(field./rho_norm(6)).^power;
output(:,12)=rho(6,:)+offset;
output(:,13)=(field./rho_norm(7)).^power;
output(:,14)=rho(7,:)+offset;
output(:,15)=(field./rho_norm(8)).^power;
output(:,16)=rho(8,:)+offset;
save('shibauchikohler.dat','output','-ASCII','-tabs');

plot((field./rho_norm(1)).^power,rho(1,:)+offset,(field./rho_norm(2)).^power,rho(2,:)
    +offset,(field./rho_norm(3)).^power,rho(3,:)+offset,(field./rho_norm(4)).^power,rho(4,:)
    +offset,(field./rho_norm(5)).^power,rho(5,:)+offset,(field./rho_norm(6)).^power,rho(6,:)
    +offset,(field./rho_norm(7)).^power,rho(7,:)+offset,(field./rho_norm(8)).^power,rho(8,:)+offset);

fitprm = 1;

function [rho, rho_norm] = amro(field,temp,wct0,gamma,power)
k00=0.729; %tl320c5 151206
k04=-0.03354; %tl320c5 151206
k61ok21=0.67576; %tl320c5 151206

k101ok21=k61ok21-1; beta=0; c=23.2e-10; d=c;

normal_factor=1.*[0.501452081 0.545185185 0.589364844 0.624615384 0.673023255 0.727352297 0.810538116
0.872287662];
%normal_factor=1.*[0.511452081 0.572185185 0.614364844 0.656615384 0.693023255 0.737352297 0.77238116 0.828287662];
for j=1:length(temp)
    rho_norm(j,1)=normal_factor(j)/quadl(@sigzz,-2*pi/d,2*pi/d,[],[],0,0,wct0(j),
        k00,k04,k61ok21,k101ok21,gamma(j),beta,45);
end

for i = 1:length(field)
    for j=1:length(temp)
        amro(j,i)=quadl(@sigzz,-2*pi/d,2*pi/d,[],[],0,0,wct0(j)*field(i)/45,
            k00,k04,k61ok21,k101ok21,gamma(j),beta,field(i));
    end
rho(:,i)=((1./amro(:,i)).^power-rho_norm(:,1).^power)./rho_norm(:,1).^power; end

function s = sigzz(k0,theta,psi,wct0,k00,k04,k61ok21,k101ok21,gamma,beta,field) N=8; c=23.2e-10; k00=k00*1e10;
wct=wct0*cos(theta)/(1+beta*gamma/2); wct00=wct0*cos(theta); fx=zeros(1,length(k0)); for j = 1:length(k0)
    phi=0:2*pi/(2^N-1):2*pi;
    kf=k00*(1+k04*cos(4*(phi+psi)));
    tp1=sin(2*(phi+psi))+k61ok21*sin(6*(phi+psi))+k101ok21*sin(10*(phi+psi));
    kz=k0(j)-kf.*cos(phi)*tan(theta);
    vi=tp1.*sin(kz*c*0.5).*exp(-1.0/wct00*((gamma+beta).*sin(4*(phi+psi))/4
        +gamma*beta.*sin(4*(phi+psi)).*cos(4*(phi+psi))/8))
        .*(1+beta*cos(4*(phi+psi)));%velocity in zth direction
    vj=tp1.*sin(kz*c*0.5).*exp(1.0/wct00*((gamma+beta).*sin(4*(phi+psi))/4
        +gamma*beta.*sin(4*(phi+psi)).*cos(4*(phi+psi))/8))
        .*(1+beta*cos(4*(phi+psi)));%velocity in zth direction at an earlier time
    an=real(fft(vi,2^N));%cosine coeff of vi
```

```
    bn=-1.0*imag(fft(vi,2^N));%sine coeff of vi
    cn=real(fft(vj,2^N));%cos coeff of vj
    dn=-1.0*imag(fft(vj,2^N));%sine coeff of vj
    freq = 0:1/(max(phi)-min(phi)):(length(an)-1)/(max(phi)-min(phi));
    szz=an(1)*cn(1);
    for k = 2:length(freq)*0.5
        factor=1.0/(1+(wct*(k-1))^2);
        szz=szz+2.0*factor*(an(k)*cn(k)+bn(k)*dn(k)-wct*(k-1)*(an(k)*dn(k)-bn(k)*cn(k)));
    end
    fx(j) = szz;
end
s=fx*wct0/field/(1+beta*gamma/2)/(length(freq)*0.5);
```

10.7.10 FFT Leakage

This code shows the effect of leakage when performing a FFT and how this can minimised by using a 'Hann' window function as shown in figure 5.12.

```
clear;
data=0:1/511:1;
for i=1:length(data)
y(i)=sin(data(i)*(1*pi*20))*0.5*(1-cos(2*pi*i/(512)));
%y(i)=sin(data(i)*(1*pi*20));
end
x=fft(y,2^12);
fftdata(:,2)=x.*conj(x)/2^14;
for i=1:2^(12-1)+1
    fftdata(i,1)=512/(1)*(i-1)/2^12;
end for i=1:2048
    cfftdata(i,1)=fftdata(i,1);
    cfftdata(i,2)=fftdata(i,2);
end
h=plot(cfftdata(:,1),cfftdata(:,2));
xlim([0 20]);
xlabel('Freq (Hz)','FontSize',35);
ylabel('Amp','FontSize',35);
set(gca,'LineWidth',4);
set(h,'LineWidth',4);
set(gca,'FontSize',30);
```

10.7.11 dHvA and SdH Analysis Code

This code finds the frequency of oscillations in dHvA and SdH data.

```
function sdhfftresult=sdhfft(filename,temperature,fieldcolumn,resistancecolumn,direction,
minfield,maxfield,bgorder,bgfield,window,n,fftminfield,fftmaxfield,savedata);

%'filename'         datafile name and extension containing raw data with no header lines
%temperature        temp at which data taken
%fieldcolumn        column number that contains field
%resistancecolumn   column number that contains resistance
%'direction'        either 'up' sweep or 'down' sweep
%minfield           minimum field to consider oscillations start
```

```
%maxfield           maximum field to consider oscillations end
%bgorder            order of background to subtract
%bgfield            fit background to 'B' or 'invB'
%window             fft window function 'hanning' 'parzen' 'welch' or none
%n                  order of fft must be great than 9
%fftminfield        min frequency to plot
%fftmaxfield        max frequency to plot
%savedata           'save' or 'nosave' saves plotted data to .dat file

%load raw datafile
loaddata=load(filename);
%get field and resistance
data(:,1)=loaddata(:,fieldcolumn);
data(:,2)=loaddata(:,resistancecolumn);
%plot graph
figure; subplot(2,2,1);
plot(data(:,1),data(:,2),'-');
xlabel('Field');
ylabel('R');

%trim data
j=1; for i =1:size(data,1)
    if ((data(i,1) > minfield) & (data(i,1) < maxfield))
        cdata(j,1)=data(i,1);
        cdata(j,2)=data(i,2);
        j=j+1;
    end
end
%plot trimmed data
subplot(2,2,2);
plot(cdata(:,1),cdata(:,2),'-');
xlabel('Field');
ylabel('R');

%split up and down sweep
j=1;k=1; for i=1:(size(cdata,1)-1)
    deriv=(cdata(i+1,1)-cdata(i,1));
    if deriv > 0
        tudata(j,1)=cdata(i,1);
        tudata(j,2)=cdata(i,2);
        j=j+1;
    end
    if deriv < 0
        tddata(k,1)=cdata(i,1);
        tddata(k,2)=cdata(i,2);
        k=k+1;
    end
end

if strcmp(lower(direction),'up')
    tdata=tudata;
end if strcmp(lower(direction),'down')
    tdata=tddata;
end
```

```
%fit background polynomial to B
if strcmp(lower(bgfield),'b')
    bgfit=polyfit(tdata(:,1),tdata(:,2),bgorder);
    sdata(:,1)=1./tdata(:,1);
    sdata(:,2)=tdata(:,2);
    bgfit=bgfit(end:-1:1); %reverse vector
    %subtract background
    for i=1:length(bgfit)
        for j=1:length(sdata)
            sdata(j,2)=sdata(j,2)-bgfit(i)*tdata(j,1)^(i-1);
        end
    end
end
%fit background polynomical to 1/B
if strcmp(lower(bgfield),'invb')
    bgfit=polyfit(1./tdata(:,1),tdata(:,2),bgorder);
    sdata(:,1)=1./tdata(:,1);
    sdata(:,2)=tdata(:,2);
    bgfit=bgfit(end:-1:1); %reverse vector
    %subtract background
    for i=1:length(bgfit)
        for j=1:length(sdata)
            sdata(j,2)=sdata(j,2)-bgfit(i)*1/(tdata(j,1)^(i-1));
        end
    end
end

%plot trimed data with bg subtracted
subplot(2,2,3); plot(sdata(:,1),sdata(:,2)); xlabel('1/Field'); ylabel('delta R');

%window function
spoints=length(sdata(:,2)); for i=1:spoints
    if strcmp(lower(window),'hanning')
        sdata(i,2)=sdata(i,2)*0.5*(1-cos(2*pi*i/(spoints)));
    end
    if strcmp(lower(window),'welch')
        sdata(i,2)=sdata(i,2)*(1-sqrt((i-0.5*(spoints))/(0.5*(spoints))));
    end
    if strcmp(lower(window),'parzen')
        sdata(i,2)=sdata(i,2)*(1-abs((i-0.5*(spoints))/(0.5*(spoints))));
    end
    if strcmp(lower(window),'none')
        sdata(i,2)=sdata(i,2);
    end
end
%fft to get frequency
%regular array of 2^n datapoints
maxsdata=max(sdata(:,1));
minsdata=min(sdata(:,1));
for i=1:512
    fxdata(i,1)=minsdata+i*(maxsdata-minsdata)/(512);
end
fydata = interp1(sdata(:,1),sdata(:,2),fxdata(:,1),'spline');
```

```
%do fft
x=fft(fydata,2^n);
fftdata(:,2)=x.*conj(x)/2^n;
for i=1:2^(n-1)+1
    fftdata(i,1)=512/(maxsdata-minsdata)*(i-1)/2^n;
end

j=1; for i =1:size(fftdata,1)
   if ((fftdata(i,1) > fftminfield) & (fftdata(i,1) < fftmaxfield))
       cfftdata(j,1)=fftdata(i,1);
       cfftdata(j,2)=fftdata(i,2);
       j=j+1;
   end
end

subplot(2,2,4);
plot(cfftdata(:,1),cfftdata(:,2));
xlabel('Freq');
ylabel('Amp');

[C,I]=max(cfftdata(:,2));
%find peak max
maxf=cfftdata(I,1);
maxa=cfftdata(I,2);
disp('Peak Max at'); disp(maxf);
%find halfwidth
halfheight=maxa/2;
for i=1:length(cfftdata(:,1))
    if cfftdata(i,2) > halfheight
        %look for points above halfheight
        hwx=cfftdata(i,1);
    end
end
halfwidth=hwx-maxf;
disp('+/-');
disp(halfwidth);
disp('T');

disp('Amplitude');
disp(cfftdata(I,2));

if strcmp(lower(savedata),'save')
save([filename(1:end-4),'_graph1.dat'],'data','-ASCII','-tabs');
save([filename(1:end-4),'_graph2.dat'],'cdata','-ASCII','-tabs');
save([filename(1:end-4),'_graph3.dat'],'sdata','-ASCII','-tabs');
save([filename(1:end-4),'_graph4.dat'],'cfftdata','-ASCII','-tabs');
end;

%return results
sdhfftresult(1)=maxf;
sdhfftresult(2)=halfwidth;
sdhfftresult(3)=maxa;
sdhfftresult(4)=temperature;
```

10.7.12 Mass Plot Code

This code plots the temperature dependence of the FFT amplitude and fits the Lifshitz-Kosevich formula to find the quasiparticle effective mass.

```
function sdh=sdhanalysis();
options=optimset('Display','off'); %set options for fminsearch
startfield=57;
endfield=59.5;

fit1=sdhfft('TL450C4_1p5K-03_20us.dat',2.9,2,3,'down',startfield,endfield,1,'B','hanning',14,0,40000,'nosave');
fit2=sdhfft('TL450C4_1p5K-10_20mus.dat',3.6,2,3,'down',startfield,endfield,1,'B','hanning',14,0,40000,'nosave');
fit3=sdhfft('TL450C4_2K-08.dat',3.8,2,3,'down',startfield,endfield,1,'B','hanning',14,0,40000,'nosave');
fit4=sdhfft('TL450C4_2p2K-09.dat',4.5,2,3,'down',startfield,endfield,1,'B','hanning',14,0,40000,'nosave');
fit5=sdhfft('TL450C4_3K-06.dat',5,2,3,'down',startfield,endfield,1,'B','hanning',14,0,40000,'nosave');

fits = cat(1,fit1,fit2,fit3,fit4,fit5);
%fit temp vs amp
params(1)=0.000001; params(2)=2; %starting parameters
numberofdatapoints=length(fits(:,1));

[estimates errors]=fminsearchmf(@fit,params,numberofdatapoints,options,fits(:,4),fits(:,3));
disp(estimates)
disp('Effective Mass');
field=(startfield+endfield)/2;
me=estimates(2)*1.055e-34*1.6e-19*field/2/pi/pi/1.38e-23/9.11e-31;
disp(me);

figure; massfits(:,1)=0.1:0.05:5;
massfits(:,2)=estimates(1)*estimates(2).*massfits(:,1)./sinh(estimates(2)*massfits(:,1));
plot(fits(:,4),fits(:,3),'*',massfits(:,1),massfits(:,2),'-');
xlabel('Temp');
ylabel('Amp');
save('massplotdata.dat','fits','-ASCII','-tabs');
save('massplotfit.dat','massfits','-ASCII','-tabs');

function errorVector=fit(params,x,expData)
fitData=params(1)*params(2).*x./sinh(params(2)*x);
errorVector=sum((fitData-expData).^2);
```

10.8 Delphi Code

10.8.1 Hall Effect and ρ_{ab} Simulation Program Code

This calculates the Hall effect and in-plane resistivity using only parameters taken from ADMR fits using the method shown in [36].

```
unit Unit1;

interface

uses
```

```
  Windows, Messages, SysUtils, Variants, Classes, Graphics, Controls, Forms,
  Dialogs, StdCtrls, dmisc, math, ExtCtrls, CGraph, ComCtrls, dintegration,
  drealfft, heapsort;

type
  TForm1 = class(TForm)
    rhograph: TCGraph;
    hallgraph: TCGraph;
    procedure FormCreate(Sender: TObject);
    procedure main;
    procedure findphi;
    procedure findkxyvxy;
    procedure findkf;
    procedure findvf;
    procedure findphidash;
    procedure findgamma;
    function findsxx0(t:integer):real;
    function findsxy1(t:integer):real;
    procedure findwct(t:integer);
    procedure plot;
  private
    { Private declarations }
  public
    { Public declarations }
  end;
var
  Form1: TForm1;
  a,pi,c,conv: real;
  n,tmax: integer; //number of points around the Fermi Surface used in evalutaion
  m: integer;
  pa: array[0..20000,0..13] of real;
  //pa array  column 1  phi
  //          column 2  kx
  //          column 3  ky
  //          column 4  kf
  //          column 5  vx
  //          column 6  vy
  //          column 7  vf
  //          column 8  phi dash
  //          column 9  gamma
  //          column 10 wct
  //          column 11 sigma xx0 parts
  //          column 12 sigma xy1 parts
  sxx0a: array[1..300,1..2] of real;
  sxy1a: array[1..300,1..2] of real;
  rho: array[0..1000,0..8] of real;
  //needs function definition here to work with qromb integration function
  function sxx0(phi:real):real;
  function sxy1(phi:real):real;

implementation

{$R *.dfm}
//---------------------------------------------------------------------------
```

```
procedure TForm1.FormCreate(Sender: TObject);
  begin
    pi:=3.141592654; //pi
    m:=1000; //number of points
    a:=3.8608e-10; //lattice parameter
    conv:=pi/180;
    c:=23.2e-10; //c axis lattice parameter
    tmax:=300;
    main;
end;
//---------------------------------------------------------------------------
procedure tform1.main; var t: integer;
  begin
    findphi;
    findkf;
    findkxyvxy;
    findvf;
    findgamma;
    findphidash;
    for t:=1 to tmax do sxx0a[t,1]:=findsxx0(t); //find T dep of sigma xx0
    for t:=1 to tmax do sxy1a[t,1]:=findsxy1(t); //find T dep of sigma xy1
    plot;
  end;
//---------------------------------------------------------------------------
procedure tform1.findphi;
var i: integer;
  begin
    for i:=0 to m do pa[i,1]:=i*pi/(2*m);
    pa[m+1,1]:=pa[m,1]+pi/(2*m);
    pa[m+2,1]:=pa[m,2]+pi/(2*m);
    n:=m;
  end;
//---------------------------------------------------------------------------
procedure tform1.findkf;
var i: integer; k00, k40: real;
  begin
    k00=0.726e10;
    k40=0.03;
    for i:=0 to m do pa[i,4]:=k00*(1-k40*cos(4*pa[i,1]));
    pa[n+1,4]:=pa[n-1,4];
    pa[n+2,4]:=pa[n-2,4];
  end;
//---------------------------------------------------------------------------
procedure tform1.findkxyvxy;
var i: integer;
  begin
    for i:=0 to m do pa[i,2]:=pa[i,4]*cos(pa[i,1]);
    for i:=0 to m do pa[i,3]:=pa[i,4]*sin(pa[i,1]);
    pa[m+1,2]:=-pa[m-1,2];
    pa[m+1,3]:=pa[m-1,3];
  end;
//---------------------------------------------------------------------------
procedure tform1.findvf;
var i: integer;
```

```
  begin
    for i:=0 to n do pa[i,7]:=sqrt(pa[i,5]*pa[i,5]+pa[i,6]*pa[i,6]);
    pa[n+1,7]:=pa[n-1,7];
  end;
//---------------------------------------------------------------------------
procedure tform1.findphidash;
//calculates phi dash the angle between vf and horizontal
var i:integer;
  begin
    for i:=1 to n+2 do pa[i,8]:=pa[i,1]-pa[i,9];
  end;
//---------------------------------------------------------------------------
procedure tform1.findgamma;
//calculates gamma the angle between vf and kf
var i:integer;
  begin
    for i:=0 to n do pa[i,9]:=arctan((ln(pa[i+1,4])-ln(pa[i,4]))
        /(pa[i+1,1]-pa[i,1]));
    pa[n+1,9]:=pa[n-1,9];
    pa[n+2,9]:=pa[n-2,9];
  end;

//---------------------------------------------------------------------------
function tform1.findsxx0(t:integer):real;
//calculates signma xx
var i:integer;
  begin
    findwct(t);
    for i:=0 to n do pa[i,11]:=pa[i,10]*power(pa[i,4],2)*power(cos(pa[i,8]),2)
        /(cos(pa[i,9]));
    result:=4*1.6e-19/(power(pi,2)*23.1332e-10)*qromb(0,pi/2,0.00000001,sxx0);
  end;
//---------------------------------------------------------------------------
function tform1.findsxy1(t:integer):real;
//calculates sigma xy
var i:integer;
  begin
    findwct(t);
    for i:=0 to n do pa[i,12]:=pa[i,10]*pa[i,4]*cos(pa[i,8])*((pa[i+1,4]
        *pa[i+1,10]*sin(pa[i+1,8])-pa[i,4]*pa[i,10]*sin(pa[i,8]))
        /(pa[i+1,1]-pa[i,1]));
    result:=-4*1.6e-19/(power(pi,2)*23.1332e-10)*qromb(0,pi/2,0.00000001,sxy1);
  end;
//---------------------------------------------------------------------------
procedure tform1.findwct(t:integer);
//wct parameterisation - usually taken from AMRO fits
var i:integer; iso, isot1, aniso, anisot: real;
  begin
    iso:=2.3869;
    isot2:=0.00027241;
    aniso:=0.33323;
    anisot:=0.060119;
    gammaideal=(iso+isot2*t*t+(aniso+anisot*t)*power(cos(i*pi/n),2));
    gammamax=2e5;
```

```
    for i:=0 to n do
    begin
        pa[i,10]:=(gammaideal+gammamax)/(gammaideal+gammamax);
    end;
    pa[n+1,10]:=pa[n-1,10];
    pa[n+2,10]:=pa[n-2,10];
  end;
//---------------------------------------------------------------------------
function sxx0(phi:real):real;
//gives sigma xx value to be used in integral
//uses liner interpolation to return a value for sigma xx for any given phi
var i, high, low: integer; fraction: real;
  begin
    i:=1;
    while phi > pa[i,1] do begin i:=i+1; end;
    low:=i-1;
    high:=i;
    fraction:=(phi-pa[low,1])/(pa[high,1]-pa[low,1]);
    result:=fraction*(pa[high,11]-pa[low,11])+pa[low,11];
  end;
//---------------------------------------------------------------------------
function sxy1(phi:real):real;
//gives sigma xy value to be used in integral
//uses liner interpolation to return a value for sigma xy for any given phi
var i, high, low: integer; fraction: real;
  begin
    i:=1;
    while phi > pa[i,1] do begin i:=i+1; end;
    low:=i-1;
    high:=i;
    fraction:=(phi-pa[low,1])/(pa[high,1]-pa[low,1]);
    result:=fraction*(pa[high,12]-pa[low,12])+pa[low,12];
  end;
//---------------------------------------------------------------------------
procedure tform1.plot;
//plots kf, vf, gamma, resistivity and Rh
var t: integer;
  begin
    for t:=1 to tmax do
      begin
        rhograph.addpointtoplot(t,1e8/sxx0a[t,1],4);
        hallgraph.addpointtoplot(t,-1e10*sxy1a[t,1]/(power(sxx0a[t,1],2)),5);
      end;
  end;
end.
```

Publications

- **Tracking anisotropic scattering in overdoped $Tl_2Ba_2CuO_{6+\delta}$ above 100 K**
  M. M. J. French, J. G. Analytis, A. Carrington, L. Balicas and N. E. Hussey, *submitted to* New J. Phys.

- **Field-induced insulator-to-metal crossover in quasi-one-dimensional $Li_{0.9}Mo_6O_{17}$**
  X. Xu, A. F. Bangura, J. G. Analytis, J. D. Fletcher, M. M. J. French, N. Shannon, N. E. Hussey, J. He, S. Zhang, D. Mandrus and R. Jin *submitted to* Phys. Rev. Lett.

- **Orbital origin of field-induced 'quantum criticality' in overdoped $Tl_2Ba_2CuO_{6+\delta}$**
  M. M. J. French and N. E. Hussey, Proc. Natl. Acad. Sci. USA 105:E58 (2008)

- **Anisotropic scattering and superconductivity in high-T_c cuprates**,
  M. M. J. French, M. Abdel-Jawad, J. G. Analytis, L. Balicas and N. E. Hussey, J. Phys. Chem. Solids **69** 3191 (2008)

- **Quantum oscillations in an overdoped high temperature superconductor**,
  B. Vignolle, A. Carrington, R. A. Cooper, M. M. J. French, A. P. Mackenzie, C. Jaudet, D. Vignolles, C. Proust and N. E. Hussey, Nature **455** 952 (2008)

- **Violation of the isotropic mean free path approximation for overdoped $La_{2-x}Sr_xCuO_4$**,
  A. Narduzzo, G. Albert, M. M. J. French, N. Mangkorntong, M. Nohara, H. Takagi and N. E. Hussey, Phys. Rev. B **77**, 220502(R) (2008)

- **Angle-dependent magnetoresistance measurements in $Tl_2Ba_2CuO_{6+\delta}$ and the need for anisotropic scattering**,
  J. G. Analytis, M. Abdel-Jawad, L. Balicas M. M. J. French and N. E. Hussey, Phys. Rev. B **76**, 104523 (2007)

- **Correlation between the superconducting transition temperature and anisotropic quasiparticle scattering in $Tl_2Ba_2CuO_{6+\delta}$**,
  M. Abdel-Jawad, J. G. Analytis, L. Balicas, A. Carrington, J. P. H. Charmant, M. M. J. French and N. E. Hussey, Phys. Rev. Lett. **99**, 107002 (2007)

Bibliography

[1] H. K. Onnes, On the sudden rate at which the resistance of mercury disappears, Comm. Phy. Lab. Univ. Leiden, p. 122 and 124 (1911)

[2] J. Bardeen, L. N. Cooper and J. R. Schrieffer, Theory of superconductivity, Phy. Rev., 108 1175 (1957)

[3] J. G. Bednorz and K. A. Muller, Possible high-T_c superconductivity in the Ba-La-Cu-O system, Z. Physik B, 64 189 (1986)

[4] A. Schilling, M. Cantoni, J. D. Guo and H. R. Ott, Superconductivity above 130 K in the Hg-Ba-Ca-Cu-O system, Nature, 363 56 (1993)

[5] C. E. Gough, M. A. Colclough, E. M. Forgan, R. G. Jordan, M. Keene, C. M. Muirhead, A. I. Rae, N. Thomas and S. Abell, J. S. Sutton, Flux quantisation in a high-T_c superconductor, Nature, 326 855 (1987)

[6] D. M. Broun, What lies beneath the dome?, Nat. Phys., 4 170 (2008)

[7] J. L. Tallon, C. Bernhard, H. Shaked, R. L. Hitterman and J. D. Jorgensen, Generic superconducting phase behavior in high-T_c cuprates: T_c variation with hole concentration in $YBa_2Cu_3O_{7-\delta}$, Phys. Rev. B, 51 12911 (1995)

[8] T. Timusk and B. Statt, The pseudogap in high-temperature superconductors: an experimental survey, Rep. Prog. Phys., 62 61 (1999)

[9] S. Hüfner, M. A. Hossain, A. Damascelli and G. A. Sawatzky, Two gaps make a hight-temperature superconductor?, Rep. Prog. Phys., 71 062501 (2008)

[10] A. J. Millis, Gaps and our understanding, Science, 314 1888 (2006)

[11] M. R. Norman, D. Pines and K. C., The pseudogap: friend or foe of high T_c?, Adv. Phys., 54 715 (2005)

[12] A. Cho, High T_c: the mystery that defies solution, Science, 314 1072 (2006)

[13] T. Valla, A. V. Fedorov, J. Lee, J. C. Davis and G. D. Gu, The ground state of the pseudogap in cuprate superconductors, Science, 314 1914 (2006)

[14] T. Sakai and Y. Takahashi, Pseudogap induced by antiferromagnetic spin correlation in high temperature superconductors, J. Phys. Soc. Japan, 70 272 (2001)

[15] V. J. Emery and S. A. Kivelson, Importance of phase fluctuations in superconductors with small superfluid density, Nature, 374 434 (1995)

[16] B. Bucher, P. Steiner, J. Karpinski, E. Kaldis and P. Wachter, Influence of the spin gap on the normal state transport in $YBa_2Cu_4O_8$, Phys. Rev. Lett., 70 2012 (1993)

[17] N. E. Hussey, K. Nozawa, H. Takagi, S. Adachi and K. Tanabe, Anisotropic resistivity of $YBa_2Cu_4O_8$: Incoherent-to-metallic crossover in the out-of-plane transport, Phys. Rev. B, 56 R11423 (1997)

[18] J. Custers, P. Gegenwart, H. Wilhelm, K. Neumaier, Y. Tokiwa, O. Trovarelli, C. Geibel, F. Steglich, C. Pepin and P. Coleman, The break-up of heavy electrons at a quantum critical point, Nature, 424 524 (2003)

[19] A. P. Mackenzie, S. R. Julian, D. C. Sinclair and C. T. Lin, Normal-state magnetotransport in superconducting $Tl_2Ba_2CuO_{6+\delta}$ to millikelvin temperatures, Phys. Rev. B, 53 5848 (1996)

[20] N. E. Hussey, Phenomenology of the normal state in-plane transport properties of high-T_c cuprates, J. Phys. Condens. Matter, 20 123201 (2008)

[21] H. Y. Hwang, B. Batlogg, H. Takagi, H. L. Kao, J. Kwo, R. J. Cava, J. J. Krajewski and W. F. J. Peck, Scaling of the temperature dependent Hall effect in $La_{2-x}Sr_xCuO_4$, Phys. Rev. Lett., 72 2636 (1994)

[22] P. W. Anderson, Hall effect in the two-dimensional Luttinger liquid, Phys. Rev. Lett., 67 2092 (1991)

[23] T. R. Chien, Z. Z. Wang and N. P. Ong, Effect of Zn impurities on the normal-state Hall angle in single-crystal $YBa_2Cu_{3-x}Zn_xO_{7-\delta}$, Phys. Rev. Lett., 67 2088 (1991)

[24] E. Pavarini, I. Dasgupta, T. Saha-Dasgupta, O. Jepsen and O. K. Anderson, Band-structure trend in hole-doped cuprates and correlation with $T_{c,\max}$, Phys. Rev. Lett., 87 047003 (2001)

[25] M. Platé, J. D. F. Mottershead, I. S. Elfimov, D. C. Peets, R. Liang, D. A. Bonn, W. N. Hardy, S. Chiuzbaian, M. Falub, M. Shi, L. Patthey and A. Damascelli, Fermi surface and quasiparticle excitations of overdoped $Tl_2Ba_2CuO_{6+\delta}$, Phys. Rev. Lett., 95 077001 (2005)

[26] N. E. Hussey, M. Abdel-Jawad, A. Carrington, A. P. Mackenzie and L. Balicas, A coherent three-dimensional Fermi surface in a high-transition-temperature superconductor, Nature, 425 814 (2003)

[27] B. Vignolle, A. Carrington, R. A. Cooper, M. M. J. French, A. P. Mackenzie, C. Jaudet, D. Vignolles, C. Proust and N. E. Hussey, Quantum oscillations in an overdoped high-T_c superconductor, Nature, 455 952 (2008)

[28] S. Sahrakorpi, H. Lin, R. S. Makiewicz and A. Bansil, Effect of hole doping on the electronic structure of Tl2201, arXiv:cond-mat/0607132 (2006)

[29] M. R. Norman, H. Ding, M. Randeria, J. C. Campuzano, T. Yokoya, T. Takeuchi, T. Takahashi, T. Mochiku, K. Kasowaki, P. Guptasarma and D. G. Hinks, Destruction of the Fermi surface in underdoped high-T_c superconductors, Nature, 392 157 (1998)

[30] N. Doiron-Leyraud, C. Proust, D. LeBoeuf, J. Levallois, J. Bonnemaison, R. Liang, D. A. Bonn, W. N. Hardy and L. Taillefer, Quantum oscillations and the Fermi surface in an underdoped high-Tc superconductor, Nature, 447 565 (2007)

[31] E. A. Yelland, J. Singleton, C. H. Mielke, N. Harrison, F. F. Balakirev, B. Dabrowski and J. R. Cooper, Quantum oscillations in the underdoped cuprate $YBa_2Cu_4O_8$, Phys. Rev. Lett., 100 047003 (2008)

[32] A. F. Bangura, J. D. Fletcher, A. Carrington, J. Levallois, M. Nardone, B. Vignolle, P. J. Heard, N. Doiron-Leyraud, D. LeBoeuf, L. Taillefer, S. Adachi, C. Proust and N. E. Hussey, Small Fermi surface pockets in underdoped high temperature superconductors: observation of Shubnikov-de Haas Oscillations in $YBa_2Cu_4O_8$, Phys. Rev. Lett., 100 047004 (2008)

[33] D. Pines, Nearly antiferromagnetic Fermi liquids: a progress report, Z. Phys. B, 103 129 (1997)

[34] R. Hlubina and T. M. Rice, Resistivity as a function of temperature for models with hot spots on the Fermi surface, Phys. Rev. B, 51 9253 (1995)

[35] L. B. Ioffe and A. J. Millis, Zone-diagonal-dominated transport in high-T_c cuprates, Phys. Rev. B, 58 11631 (1998)

[36] N. E. Hussey, The normal state scattering rate in high-T_c cuprates, Eur. Phys. J. B, 31 495 (2003)

[37] M. Abdel-Jawad, M. P. Kennett, L. Balica, A. Carrington, A. P. Mackenzie, R. H. McKenzie and N. E. Hussey, Anisotropic scattering and anomalous normal-state transport in a high-temperature superconductor, Nat. Phys., 2 821 (2006)

[38] M. Abdel-Jawad, Fermiology and anomalous transport in quasi-two-dimensional compounds, Ph.D. thesis, University of Bristol (2007)

[39] R. A. Cooper, Y. Wang, B. Vignolle, O. J. Lipscombe, S. M. Hayden, Y. Tanabe, T. Adachi, Y. Koike, M. Nohara, H. Takagi, C. Proust and N. E. Hussey, Anomalous criticality in the electrical resistivity of $La_{2-x}Sr_xCuO_4$, Science, 323 603 (2009)

[40] J. Chang, M. Shi, S. Pailhes, M. Mansson, T. Claesson, O. Tjernberg, A. Bendounan, Y. Sassa, L. Patthey, N. Momono, M. Oda, M. Ido, S. Guerrero, C. Mudry and J. Mesot, Anisotropic quasiparticle scattering rates in slightly underdoped to optimally doped high-temperature $La_{2-x}Sr_xCuO_4$ superconductors, Phys. Rev. B, 78 205103 (2008)

[41] C. Kittel, Introduction to solid state physics, John Wiley and Sons, London (1976), ISBN 0-471-49024-5

[42] N. W. Ashcroft and N. D. Mermin, Solid state physics, Thomson Learning, London (1976), ISBN 0-03-083993-9

[43] J. Singleton, Band theory and electronic properties of solids, Oxford University Press (2001), ISBN 0-19-850644-9

[44] A. J. Schofield, Non-Fermi liquids, Contemporary Physics, 40 95 (1999)

[45] D. B. Poker and C. E. Klabunde, Temperature dependence of electrical resistivity of vanadium, platinum and copper, Phys. Rev. B, 26 7012 (1982)

[46] G. Kastrinakis, A common origin for the resistivity of $Cd_2Re_2O_7$, the cuprates and Sr_2RuO_4?, Physica C, 382 443 (2002)

[47] M. N. McBrien, N. E. Hussey, P. J. Meeson, S. Horii and H. Ikuta, Metallic c-axis transport across insulating planes in $PrBa_2Cu_4O_8$, J. Phys. Soc. Jpn., 71 701 (2002)

[48] M. Lang and J. Müller, Organic superconductors, arXiv:cond-mat/0302157 (2003)

[49] C. A. Domenicali and E. L. Christenson, Effects of transition metal solutes on the electrical resistivity of copper and gold between 4 and 1200 K, J. Appl. Phys., 32 2450 (1961)

[50] K. Andres, J. E. Graebner and H. R. Ott, 4f-Virtual-bound-state formation in $CeAl_3$ at low temperatures, Phys. Rev. Lett., 35 1779 (1975)

[51] A. J. Schofield and J. R. Cooper, Quasilinear magnetoresistance in an almost two-dimensional band structure, Phys. Rev. B, 62 10779 (2000)

[52] N. P. Ong, Geometric interpretation of the weak-field Hall conductivity in two-dimensional metals with arbitrary Fermi surfaces, Phys. Rev. B., 43 193 (1991)

[53] K. Kajita, Y. Nishio, T. Takahashi, W. Sasaki, R. Kato, H. Kobayashi, A. Kobayashi and Y. Iye, A new type oscillatory phenomenon in the magnetotransport of $\theta-(BEDT-TTF)_2I_3$, Solid Sate Commun, 70 1189 (1989)

[54] K. Yamaji, On the angle dependence of the magnetoresistance in quasi-two-dimensional organic superconductors, J. Phys. Soc. Jpn., 58 1520 (1989)

[55] M. L. Boas, Mathematical methods in the physical sciences, page 525, John Wiley and Sons (1983), ISBN 0-471-04409-1

[56] W. J. de Haas and P. M. van Alphen, Proc. Netherlands Roy. Acad. Sci., 33 1106 (1930)

[57] R. S. Liu, S. D. Hughes, R. J. Angel, T. P. Hackwell, A. P. Mackenzie and P. P. Edwards, Crystal structure and cation stoichiometry of superconducting $Tl_2Ba_2CuO_{6+\delta}$ single crystals, Physica C, 198 203 (1992)

[58] J. M. Ziman, Principles of the theory of solids, Cambridge University Press, Cambridge (1965)

[59] D. Shoenberg, Magnetic oscillations in metals, Cambridge University Press (1984), ISBN 0-521-22480-2

[60] R. B. Dingle, Some magnetic properties of metals. II. The influence of collisions on the magnetic behaviour of large systems, Proc. Roy. Soc. A, 211 517 (1952)

[61] P. G. Radaelli, D. G. Hinks, A. W. Mitchell, B. A. Hunter, J. L. Wagner, B. Dabrowski, K. G. Vandervoort, H. K. Viswanathan and J. D. Jorgensen, Structural and superconducting properties of $La_{2-x}Sr_xCuO_4$ as a function of Sr content, Phys. Rev. B, 49 4163 (1994)

[62] T. Amano, M. Tange, S. Nishizaki and R. Yoshizaki, Magnetic properties of Bi2201 phase single crystals, Physica C, 408 649 (2004)

[63] X. Chen, Z. Xu, Z. Jiao and Q. Zhang, Oxidation state of Cu and superconductivity in bilayer Tl-based cuprates, Chin. Phy. Lett., 14 221 (1997)

[64] C. C. Tsuei, J. R. Kirtley, Z. F. Ren, J. H. Wang, H. Raffy and Z. Z. Li, Pure $d_{x^2-y^2}$ order-parameter symmetry in the tetragonal superconductor $Tl_2Ba_2CuO_{6+\delta}$, Nature, 387 481 (1997)

[65] H. He, P. Bourges, Y. Sidis, C. Ulrich, L. P. Regnault, S. Pailhes, N. S. Berzigiarova, N. N. Kolesnikov and B. Keimer, Magnetic resonant mode in the single-layer high-temperature superconductor $Tl_2Ba_2CuO_{6+\delta}$, Science, 295 1045 (2002)

[66] T. C. Ozawa and S. J. Kang, Balls and Sticks: easy-to-use structure visualization and animation program, J. Appl. Cryst., 37 679 (2004)

[67] J. L. Wagner, O. Chmaissem, J. D. Jorgensen, D. G. Hinks, P. G. Radaelli, B. A. Hunter and W. R. Jensen, Multiple defects in overdoped $Tl_2Ba_2CuO_{6+\delta}$: effects on structure and superconductivity, Physica C, 277 170 (1997)

[68] Y. Shimakawa, T. Kubo, T. Manako and H. Igarashi, Neutron-diffraction study of $Tl_2Ba_2CuO_{6+\delta}$ with various T_cs from 0 to 73 K, Phys. Rev. B, 42 10165 (1990)

[69] M. A. G. Aranda, D. C. Sinclair, J. P. Attfield and A. P. Mackenzie, Cation distributions and possible phase separation in $Tl_2Ba_2CuO_{6+\delta}$ from synchrotron powder x-ray diffraction, Phys. Rev. B, 51 12747 (1995)

[70] R. Sieburger and J. S. Schilling, Marked anomalies in the pressure dependence of the superconducting transition temperature in $Tl_2Ba_2CuO_{6+\delta}$ as a function of oxygen content, Physica C, 173 403 (1991)

[71] D. R. Hamann and L. F. Mattheiss, Electronic band properties of $Ba_2Tl_2CuO_6$, Phys. Rev. B, 38 5138 (1988)

[72] D. J. Singh and W. E. Pickett, Electronic characteristics of $Tl_2Ba_2CuO_{6+\delta}$, Physica C, 203 193 (1992)

[73] T. M. Mishonov and S. Savova, LCAO model for 3D Fermi surface of high-T_c cuprate $Tl_2Ba_2CuO_{6+\delta}$, arXiv:cond-mat/0504290 (2005)

[74] A. C. Carrington, Private Communication

[75] Y. Shimakawa, T. Kubo, T. Manako and H. Igarashi, Variation in T_c and carrier concentration in Tl-based superconductors, Phys. Rev. B, 40 11400 (1989)

[76] Y. Kubo, Y. Shimakawa, T. Manako and H. Igarashi, Transport and magnetic properties of $Tl_2Ba_2CuO_{6+\delta}$ showing a δ-dependent gradual transition from an 85 K superconductor to a nonsuperconducting metal, Phys. Rev. B, 43 7875 (1991)

[77] N. E. Hussey, J. R. Cooper, J. M. Wheatley, I. R. Fisher, A. Carrington, A. P. Mackenzie, C. T. Lin and O. Milat, Angular dependence of the c-axis normal state magnetoresistance in single crystal $Tl_2Ba_2CuO_{6+\delta}$, Phys. Rev. Lett., 76 122 (1996)

[78] A. W. Tyler and A. P. Mackenzie, Hall effect of single layer, tetragonal $Tl_2Ba_2CuO_{6+\delta}$ near optimal doping, Physica C, 282 1185 (1997)

[79] A. W. Tyler, Y. Ando, F. F. Balakirev, A. Passner, G. S. Boebinger, A. J. Schofield, A. P. Mackenzie and O. Laborde, High-field study of normal-state magnetotransport in $Tl_2Ba_2CuO_{6+\delta}$, Phys. Rev. B, 57 R728 (1998)

[80] J. M. Harris, Y. F. Yan, P. Matl, N. P. Ong, P. W. Anderson, T. Kimura and K. Kitazawa, Violation of Kohler's rule in the normal state magnetoresistance of $YBa_2Cu_3O_{7-x}$ and $La_{2-x}Sr_xCuO_4$, Phys. Rev. Lett., 75 1391 (1995)

[81] Majed Abdel-Jawad, Private Communication

[82] A. P. Mackenzie, S. R. Julian, G. G. Lonzarich, A. Carrington, S. D. Hughes, R. S. Liu and D. C. Sinclair, Resistive upper critical field of $Tl_2Ba_2CuO_{6+\delta}$ at low temperatures and high magnetic fields, Phys. Rev. Lett., 71 1238 (1993)

[83] A. W. Tyler, An investigation into the magnetotransport properties of layered superconducting perovskites, Ph.D. thesis, University of Cambridge (1997)

[84] T. Manako, Y. Kubo and Y. Shimakawa, Transport and structural study of $Tl_2Ba_2CuO_{6+\delta}$ single crystals prepared by KCl flux method, Phys. Rev. B, 46 11019 (1992)

[85] http://www.lentonfurnaces.com

[86] http://www.eurotherm.com

[87] Dr. Richard Brooker, Earth Sciences Department, University College London

[88] L. J. van der Pauw, A method of measuring specific resistivity and hall coefficient of disks of arbitrary shape, Philips Research Reports, 13 1 (1958)

[89] J. D. Wasscher, Note on four-point resistivity measurments on anisotropic conductors, Philips Reseach Reports, 16 301 (1961)

[90] L. J. van der Pauw, Determination of resistivity tensor and hall tensor of anisotropic conductors, Philips Research Reports, 16 187 (1961)

[91] H. C. Montgomery, Method for measuring electrical resistivity of anisotropic materials, J. Appl. Phys, 42 2971 (1971)

[92] A. W. Tyler, A. P. Mackenzie, S. NishiZaki and Y. Maeno, High-temperature resistivity of Sr_2RuO_4: Bad metallic transport in a good metal, Phys. Rev. B, 58 10107 (1998)

[93] http://www.thinksrs.com

[94] http://www.keithley.com

[95] http://www.magnet.fsu.edu

[96] http://www.lakeshore.com

[97] B. L. Brandt, D. W. Liu and L. G. Rubin, Low temperature thermometry in high magnetic fields. Cernox sensors to 32 T, Rev. Sci. Instrum., 70 104 (1999)

[98] http://www.ni.com/labview

[99] http://www.apache.org

[100] A. P. Prudnikov, Y. A. Brychkov and O. I. Marichev, Integrals and series volume 1: elementary functions, p445, Gordon and Breach Science Publishers (1988)

[101] C. Bergemann, A. P. Mackenzie, S. R. Julian, D. Forsythe and E. Ohmichi, Quasi-two-dimensional Fermi liquid properties of the unconventional superconductor Sr_2RuO_4, Adv. Phys, 52 639 (2003)

[102] M. Eschrig and M. R. Norman, Effect of the magnetic resonance on the electronic spectra of high-T_c superconductors, Phys. Rev. B, 67 144503 (2003)

[103] P. A. Goddard, S. W. Tozer, J. Singleton, A. Ardavan, A. Abate and M. Kurmoo, Superconductivity, incoherence and Anderson localization in the crystalline organic conductor $(BEDT-TTF)_3Cl_2 2H_2O$ at high pressures, J. Phys. Cond. Matt., 14 7345 (2002)

[104] J. G. Analytis, M. Abdel-Jawad, L. Balicas, M. M. J. French and N. E. Hussey, Angle-dependent magnetoresistance measurements in $Tl_2Ba_2CuO_{6+\delta}$ and the need for anisotropic scattering, Phys. Rev. B, 76 104523 (2007)

[105] J. A. Nelder and R. Mead, A simplex method for function minimisation, Computer Journal, 7 308 (1965)

[106] P. Blaha, K. Schwarz, G. K. H. Madsen, K. D. and J. Luitz, WIEN2k, An augmented plane wave + local orbitals program for calculating crystal properties, Karlheinz Schwarz, Techn. Universitat Wien, Austria (2001), ISBN 3-9501031-1-2

[107] Available from http://www.wien2k.at

[108] C. Kim, F. Ronning, A. Damascelli, D. L. Feng, Z. X. Shen, B. O. Wells, Y. J. Kim, R. J. Birgeneau, M. A. Kastner, L. L. Miller, H. Eisaki and S. Uchida, Anomalous temperature dependence in the photoemission spectral function of cuprates, Phy. Rev. B, 65 174516 (2002)

[109] K. G. Sandermann and A. J. Schofield, Model of anisotropic scattering in a quasi-two-dimensional metal, Phys. Rev. B, 63 094510 (2001)

[110] M. M. J. French, J. G. Analytis, A. Carrington, L. Balicas and N. E. Hussey, Tracking anisotropic scattering in overdoped $Tl_2Ba_2CuO_{6+\delta}$ above 100 K, submitted to New. J. Phys (2009)

[111] M. Abdel-Jawad, J. G. Analytis, L. Balica, A. Carrington, J. P. H. Charmant, M. M. J. French and N. E. Hussey, Correlation between the superconducting transition temperature and anisoptropic quasiparticle scattering in $Tl_2Ba_2CuO_{6+\delta}$, Phys. Rev. Lett., 99 107002 (2007)

[112] A. Damascelli, Z. Hussain and Z. X. Shen, Angle-resolved photoemission studies of the cuprate superconductors, Rev. Mod. Phys., 75 473 (2003)

[113] J. L. Tallon and J. W. Loram, The doping dependence of T^* — what is the real high-T_c phase diagram?, Physica C, 349 53 (2001)

[114] T. Shibauchi, L. Krusin-Elbaum, M. Hasegawa, Y. Kasahara, R. Okazaki and Y. Matsuda, Field-induced quantum critical route to a Fermi liquid in high-temperature superconductors, Proc. Natl. Acad. Sci. USA, 105 7120 (2008)

[115] J. Paglione, M. A. Tanatar, D. G. Hawthorn, E. Boaknin, R. W. Hill, F. Ronning, M. Sutherland and L. Taillefer, Field-induced quantum critical point in $CeCoIn_5$, Phys. Rev. Lett., 91 246405 (2003)

[116] J. C. Phillips, Private Communication and Self-organised networks and lattice effects in high-temperature superconductors, Phys. Rev. B., 75 214503 (2007)

[117] T. Shibauchi, L. Krusin-Elbaum and Y. Matsuda, Reply to French and Hussey: Evidence against orbital origin of field-induced quantum criticality in $Tl_2Ba_2CuO_{6+\delta}$ superconductors, Proc. Natl. Acad. Sci. USA, 105 E59 (2008)

[118] M. Gurvitch, Ioffe-Regel criterion and resistivity of metals, Phys. Rev. B, 24 7404 (1981)

[119] H. Kontani, Optical conductivity and Hall coefficient in high-T_c superconductors: significant role of current vertex corrections, J. Phys. Soc. Japan, 75 013703 (2006)

[120] H. Kontani, Anomalous transport phenomena in Fermi liquids with strong magnetic fluctuations, Rep. Prog. Phys., 71 026501 (2008)

[121] L. Fruchter, H. Raffy, F. Bouquet and Z. Z. Li, Contribution of disorder to the Hall effect in $Bi_2Sr_2CuO_{6+\delta}$, Phys. Rev. B, 75 092502 (2007)

[122] M. F. Smith and R. McKenzie, Anisotropic scattering in angular-dependent magnetoresistance osciallations of quasi-2D and quasi-1D metals: beyond the relaxation-time approximation, arXiv:cond-mat/0804.2725 (2008)

[123] B. A. W. Brinkman and M. P. Kennett, Temperature dependence of interlayer magnetoresistance in anisotropic layered metals, arXiv:cond-mat/0811.4442 (2008)

[124] A. A. Kordyuk, S. V. Borisenko, A. Koitzsch, J. Fink, M. Knupfer, B. Buchner, H. Berger, G. Margaritondo, C. T. Lin, B. Keimer, S. Ono and Y. Ando, Manifestation of the magnetic resonance mode in the nodal quasiparticle lifetime of the superconducting cuprates, Phys. Rev. Lett., 92 257006 (2004)

[125] L. Dell'Anna and W. Metzner, Electrical resistivity near Pomeranchuk instability in two dimensions, Phys. Rev. Lett., 98 136402 (2007)

[126] Y. Nakajima, K. Izawa, Y. Matsuda, K. Behnia, H. Kontani, M. Hedo, Y. Uwatoko, T. Matsumoto, H. Shishido, R. Settai and Y. Onuki, Evolution of Hall coefficient in two-dimensional heavy fermion $CeCoIn_5$, J. Phys. Soc. Japan, 75 023705 (2006)

[127] S. Wakimoto, H. Zhang, K. Yamada, I. Swainson, H. Kim and R. J. Birgeneau, Direct relation between the low-energy spin excitations and superconductivity of overdoped high-T_c superconductors, Phys. Rev. Lett., 92 217004 (2004)

[128] C. M. Varma, P. B. Littlewood and S. Schmitt-Rink, Phenomenology of the normal state of Cu-O high temperature superconductors, Phys. Rev. Lett., 63 1996 (1989)

[129] L. Zhu, V. Aji, A. Shekhter and C. M. Varma, Universality of single-particle spectra of cuprate superconductors, Phys. Rev. Lett., 100 057001 (2008)

[130] A. S. Alexandrov, Condensation of charged bosons hybridised with fermions, Physica C, 274 237 (1997)

[131] P. W. Anderson, Private Communication and The 'strange metal' is a projected Fermi liquid with edge singularities, Nat. Phys., 2 626 (2006)

[132] T. M. Mishonov, J. O. Indekeu and E. S. Penev, The $3d$ to $4s$ by $2p$ highway to superconductivity in cuprates, arXiv:cond-mat/0206350 (2002)

[133] T. M. Mishonov and M. T. Mishonov, Simple model for the linear temperature dependence of the electrical resistivity of layered cuprates, arXiv:cond-mat/0001031 (2000)

[134] M. Ossadnik, C. Honerkamp, T. M. Rice and M. Sigrist, Breakdown of Landau theory in overdoped cuprates near the onset of superconductivity, Phys. Rev. Lett., 101 256405 (2008)

[135] Z. M. Yusof, B. O. Wells, T. Valla, A. V. Fedorov, P. D. Johnson, Q. Li, K. C., S. Jian and D. G. Hinks, Quasiparticle Liquid in the Highly Overdoped $Bi_2Sr_2CaCu_2O_{8+\delta}$, Phys. Rev. Lett., 88 167006 (2002)

[136] C. Jaudet, D. Vignolles, A. Audouard, J. Levallois, D. LeBoeuf, N. Doiron-Leyraud, B. Vignolle, M. Nardone, A. Zitouni, R. Liang, D. A. Bonn, W. N. Hardy, L. Taillefer and C. Proust, de Haas-van Alphen oscillations in the underdoped high-temperature superconductor $YBa_2Cu_3O_{6.5}$, Phys. Rev. Lett., 100 187005 (2008)

[137] A. Kanigel, M. R. Norman, M. Randeria, U. Chatterjee, S. Souma, A. Kaminski, H. M. Fretwell, S. Rosenkranz, M. Shi, T. Sato, T. Takahashi, Z. Z. Li, H. Raffy, K. Kadowaki, D. Hinks, L. Ozyuzer and J. C. Campuzano, Evolution of the pseudogap from Fermi arcs to the nodal metal, Nature Phys., 2 447 (2006)

[138] J. W. Loram, K. A. Mirza, J. M. Wade, J. R. Cooper and W. Y. Liang, The electronic specific heat of cuprate superconductors, Physica C, 235 134 (1994)

[139] A. Wasserman, M. Springford and F. Han, The de Haas-van Alphen effect in a marginal Fermi liquid, J. Phys. Condens. Matter, 3 5335 (1991)

[140] A. Wasserman and M. Springford, The influence of many-body interactions on the de Haas-van Alphen effect, Adv. Phys., 45 471 (1996)

[141] J. Lin and A. J. Millis, Theory of low-temperature Hall effect in electron-doped cuprates, Phys. Rev. B, 72 214506 (2005)

[142] A. J. Millis and M. R. Norman, Antiphase stripe order as the origin of electron pockets observed in 1/8-hole-doped cuprates, Phys. Rev. B, 76 220503 (2007)

[143] Suggestion for this plot by Ross McKenzie

[144] M. V. Kartsovnik, D. Andres, S. V. Simonov, W. Biberacher, I. Sheikin, N. D. Kushch and H. Müller, Angle-dependent magnetoresistance in the weakly incoherent interlayer transport regime in a layered organic conductor, Phys. Rev. Lett., 96 166601 (2006)

[145] M. P. Kennett and R. H. McKenzie, Sensitivity of the interlayer magnetoresistance of layered metals to intralayer anisotropies, Phy. Rev. B, 76 054515 (2007)

[146] Mike Smith, Private Communication

[147] L. M. Falicov and P. R. Sievert, Theory of the galvanomagnetic effects in metals with magnetic breakdown: semiclassical approach, Phys. Rev., 138 A88 (1965)

[148] The *CGraph* program was written by A. C. Carrington